ODESA ASTRONOMICAL PUBLICATIONS

Volume 38
(2025)

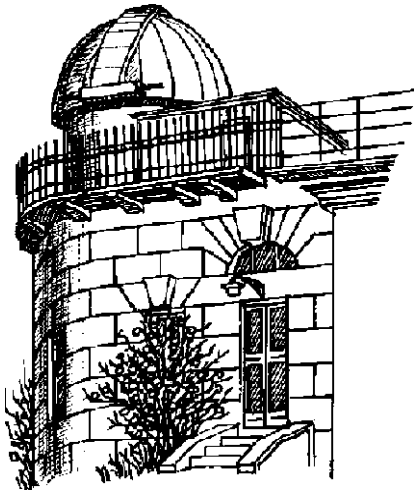

Astronomical Observatory
of Odesa I. I. Mechnikov National University

ODESA ASTRONOMICAL PUBLICATIONS

Volume 38 (2025)

Address:

Astronomical Observatory, Odesa National University,
T. H. Shevchenko Park, Odesa, 65014, Ukraine
Tel.: + 38 048 722-03-96

e-mail: astronomical_observatory@onu.edu.ua
http://www.astro-observ-odessa0.1gb.ua

The electronic version of the journal is available via the link: http://oap.onu.edu.ua

Одеські Астрономічні Публікації
Видається з 1946 року (видання відновлено в 1993 р., № 6)

Згідно з Рішенням Національної ради України з питань телебачення і радіомовлення № 36 від 11.01.2024 р. журнал зареєстрований як друковане медіа з ідентифікатором R30-02636.

Наказом Міністерства освіти та науки України № 1643 від 28.12.2019 р. (Додаток 4) журнал включено до Переліку наукових фахових видань України.

Друкується за рішенням Вченої ради НДІ «Астрономічна обсерваторія» Одеського національного університету імені І. І.Мечникова від 11 листопада 2025 р., протокол № 3.

ISSN 1810-4215 (print) 2786-5215 (online)

ODESA ASTRONOMICAL PUBLICATIONS

Volume 38
(2025)

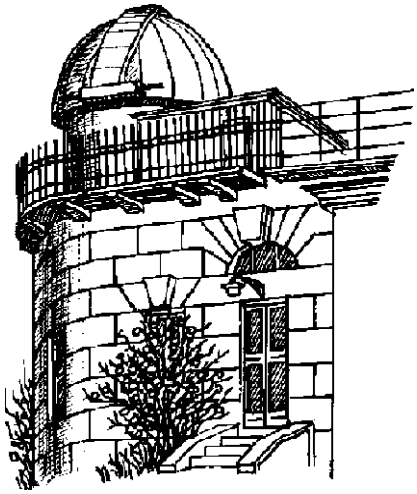

CONTENTS

Cosmology, gravitation, astroparticle physics, high-energy physics

Doikov D., Doikova K.
A NOVEL IMAGE RECONSTRUCTION APPROACH IN THE X- AND γ-RAY DOMAIN 5
Doikov M.
DESIGN AND INVESTIGATION OF A NOVEL GAMMA-RAY SPECTROGRAPH CONFIGURATION IN THE ENERGY RANGE 0.511–5 MEV 12
Kamenshchik A. Yu.
SINGULARITIES AND THEIR CROSSING IN GRAVITY AND COSMOLOGY 20
Panko E. A., Yemelianov S. I. , Lavreniuk D. O.
USING CLUSTER CARTOGRAPHY 2D+ FOR DETECTING SUBSTRUCTURES IN THE 3D GALAXY CLUSTERS 28
Pechko A. K., Panko E. A., Vasylchenko V. V., Mirochnik N. P.
UNISTELLAR EVSCOPE 2: TECHNICAL SPECIFICATIONS, USER COMMUNITY, AND PROSPECTS FOR APPLICATION 32

Astrophysics (stellar atmospheres, interacting binary systems, variable stars)

Achkassova S. E., Nurmakhametova Sh. T., Miroshnichenko A. S., Vaidman N. L., Khokhlov S. A., Agishev D. T., Danford S.
PERIODIC VARIATIONS IN THE OPTICAL SPECTRUM OF THE POST-AGB OBJECT LN HYA 36
Hasanova A. B., Khalilov A. M., Baloglanov A. Sh., Hajiyeva G. M.
VARIATION OF THE Hα LINE PROFILE IN THE SPECTRUM OF THE SUPERGIANT STAR HD 207260 (A2 Iae) 41
Humbatova A. E.
THE DISTRIBUTION OF TEMPERATURE IN THE DETAILS OF JUPITER'S DISK BASED ON THE ABSORPTION LINES OF THE NH3 λ6450 Å BAND 45
Keir L. E., Panko E. A., Pyatnytskyy M. Yu.
THE FEATURES OF FI SGE PHOTOMETRIC VARIABILITY ON TRANSITING EXOPLANET SURVEY SATELLITE OBSERVATIONS 50
Mammadova S. O., Aliyeva V. I., Rustamov B. N.
SPECTRAL STUDY OF THE HERBIG Ae STAR HD 31648. THE Hα AND Hβ EMISSION LINES 54
Milone E. F.
A PERSPECTIVE ON ECLIPSING BINARY STAR STUDIES IN THE POST-GAIA ERA 58
Mishenina T., Gorbaneva T., Pignatari M., Kurtukian-Nieto T.
ENRICHMENT WITH THE FIRST- AND SECOND-PEAK S-PROCESS ELEMENTS IN GALACTIC DISC GIANTS 81
Nurmakhametova Sh. T., Vaidman N. L., Miroshnichenko A. S., Agishev A. T., Khokhlov A. A.
SPECTROSCOPIC STUDY OF THE POST-AGB BINARY HR 4049 86
Rustamova A. B., Mikailov Kh. M., Rustamov B. N.
ORBITAL SPECTRAL VARIABILITIES IN SYMBIOTIC STAR AG PEGASI 91
Rustamova A. B., Mikailov Kh. M., Rustamov B. N.
OPTICAL SPECTROSCOPY OF SYMBIOTIC STAR EG And. Hα ORBITAL VARIABILITIES 96
Samedov Z. A., Aliyeva Z. F., Hajiyeva G. M., Samedova N. H.
DETERMINATION OF THE EFFECTIVE TEMPERATURES AND SURFACE GRAVITIES OF SEVERAL A-TYPE STARS BASED ON PHOTOMETRIC PARAMETERS 100
Usenko I. A., Kaliuzhnyi M. P., Miroshnichenko A. S., Danford S., Turner D. G., Majaess D. J., Balam D. D.
3D IMAGE OF POLARIS FIELD STARS 104

Solar System and space environment

Karastan M., Bazyey O.
DETERMINING THE ORBIT OF THE TEMPORARY EARTH SATELLITE OF ASTEROID 2024 PT5 109
Koshkin N., Kozhukhov O., Shakun L., Bryukhovetskyi O., Korobeynikova E., Melikyants S., Strakhova S., Dragomiretsky V., Ryabov A.
EVOLUTION OF THE ROTATION PARAMETERS OF THE ROCKET'S UPPER STAGE (SPACE OBJECT 1987-074G) 113

Rychahova V. V., Slyusarev I. G.
REFLECTANCE SPECTRA OF DISTINCT SURFACE UNITS IN THE MARCIA CRATER REGION ON VESTA 121
Strautman A., Bazyey O.
ILLUMINATION OF ARTIFICIAL EARTH SATELLITES IN CIRCULAR ORBITS 128

Radio Astronomy

Bubnov I. M., Vaschishyn R. V., Stanislavsky A. A., Konovalenko A. A., Belov A. S., Selin V. Yu., Frantsuzenko A. V., Stanislavsky L. A., Shevchuk M. V., Reznichenko A. M., Ulyanov O. M., Yerin S. M., Shevchenko V. V.
RESTORATION AND DEVELOPMENT OF THE GURT RADIO TELESCOPE NETWORK: OPPORTUNITIES FOR OBSERVATIONS UNDER WARTIME CONDITIONS 133
Melnik V. M., Dorovskyy V. V.
SPECTRAL FEATURES OF A SINGLE TYPE III BURST OBSERVED BY PSP ON 04.06.2020 137
Myrhorod V. I., Bubnov I. M., Selin V. Yu.
VISUALIZATION AND ANALYSIS OF VECTOR NETWORK ANALYZER DATA FOR THE EXPERIMENTAL MODEL OF THE ACTIVE ANTENNA SECTION OF THE GURT RADIO TELESCOPE 142
Zabora D. A., Ryabov M. I., Sukharev A. L.
PREPARING RADIO AND OPTICAL DATA FOR COMPARING BINARY BLACK HOLE CANDIDATES: THE CASE OF OJ 287 146

Sun, solar activity, solar-terrestrial relations and astrobiology

Kondrashova N. N., Pasechnik M. N.
MORPHOLOGICAL FEATURES OF EXTREME GEOMAGNETIC STORM SOURCES 154
Krivodubskij V. N.
NORTH-SOUTH ASYMMETRY OF SUNSPOT ACTIVITY DURING THE MAUNDER MINIMUM 162
Lozitsky V. G., Yakovkin I. I., Pavlichenko U. O., Sheminova V. A.
MAGNETIC FIELD WEAKENING IN DEEP LAYERS OF A SUNSPOT 165
Tsvyk N. O.
JUPITER'S DAM RADIO EMISSION AND SOLAR ACTIVITY: IO-DEPENDENT AND NON-IO SOURCES 170

COSMOLOGY, GRAVITATION, ASTROPARTICLE PHYSICS, HIGH ENERGY PHYSICS

https://doi.org/10.18524/1810-4215.2025.38.340287

A NOVEL IMAGE RECONSTRUCTION APPROACH IN THE X- AND γ-RAY DOMAIN

Dmitri Doikov[1], Katrin Doikova[2]

[1] Dept. of Physics, Medical Laboratory at Baruch Padeh Medical Center, Poriya, Israel, *dmitro.doikov@gmail.com*

[2] Dept. of Radiology, Baruch Padeh Medical Center, Poriya, Israel, *doikovaekaterin@gmail.com*

ABSTRACT. This study examines the consequences of high-energy radiation interactions from X-ray sources with extended astrophysical objects. A comparative analysis is conducted between the spectra of primary radiation sources and those of irradiated absorbing and scattering regions. The limitations of current diagnostic methods are identified, and strategies for enhancing both the sensitivity and informational value of the resulting data are proposed. Signal-to-noise ratios are derived for a gamma-ray detector prototype developed by the authors, under various geometric configurations of emitting and scattering structures. Necessary modifications to the radiation transport equations are suggested, along with instrumental techniques for identifying and registering previously unrecognized astrophysical entities.

Keywords: X-ray spectroscopy and detectors, visualization of chemical anomality's in X-rays, regularization algorithm, Compton spectroscopy.

АНОТАЦІЯ. У роботі розглянуто наслідки взаємодії жорсткого рентгенівського та гамма-випромінювання з протяжними астрофізичними об'єктами та середовищами різної природи. Проведено порівняння спектрів первинного випромінювання з характеристиками поглинаючих і розсіювальних областей, що піддаються опроміненню. Показано, що реконструкція зображень середовищ, які зазнають опромінення, та їх спостереження у прямих і розсіяних компонентах випромінювання потребують нових фізичних підходів, спеціалізованих інструментальних рішень і вдосконалених алгоритмів обробки даних.

Обґрунтовано необхідність використання інформаційного потенціалу розсіяного випромінювання. Доведено, що, всупереч поширеній думці про втрату якості та виникнення спотворень у детектованих проекційних зображеннях опромінюваних об'єктів μ(x, y) та μ(x, y), існують спектральні діапазони, де домінують «чисті» фізичні процеси: поглинання (0,1–10 кеВ) або розсіяння (40–160 кеВ). У проміжному енергетичному інтервалі 10–40 кеВ ці процеси конкурують. Для підвищення наочності та зручності аналізу було обрано рідкі та тверді фази найбільш поширених середовищ: для атмосфер планет – воду та метан, для міжзоряного середовища – тверді силікати й карбонати. Показано, що за діючої концентрації атомів, визначеної відповідно до формули (6), ще можливе використання наближення однократного розсіяння. Доведені можливості реконструкції проекцій $\mu_s(x, y)$ у розсіяному випромінюванні дозволяють охоплювати значно більший за геометричними та фізичними характеристиками об'єм простору. Цей ефект було зафіксовано космічними апаратами на енергіях, де превалює «чисте» поглинання. У таких умовах агентами розсіяння рентгенівського випромінювання є нано-частинки силікатів і карбонатів. Водночас характер розсіяння має дифракційну природу і визначається макроскопічними параметрами пилу, зокрема коефіцієнтом заломлення у рентгенівському діапазоні, який практично дорівнює одиниці.

На основі проведеного аналізу отримано співвідношення сигнал/шум для розробленого авторами детектора гамма-випромінювання за різної геометрії випромінювальних і розсіювальних об'єктів. Запропоновано необхідні модифікації рівнянь переносу та інструментальні методи ідентифікації й реєстрації раніше неідентифікованих об'єктів, що підвищує чутливість та інформативність отримуваних діагностичних даних.

Ключові слова: рентгенівська спектроскопія та детектори, візуалізація хімічних аномалій у рентгенівських променях, алгоритм регуляризації, комптонівська спектроскопія.

1. Introduction

Recent advances in astronomical observations, particularly the discovery of numerous X-ray sources, have opened new avenues for investigating the radiative response of the environments in which these sources are embedded. These environments are typically rarefied interstellar structures composed predominantly of gas and dust. Notable examples include young supernova remnants and active galactic nuclei (AGN). Within the Solar System, analogous media are represented by aerosols in the upper layers of planetary atmospheres,

containing particles of diverse chemical composition subjected to interactions with the high-energy component of cosmic rays. The problem of reconstructing cosmic structures was first introduced in the context of processing radioastronomical images (Bracewell & Riddle, 1967). The data recorded by detector elements (e.g., antennas) correspond to two-dimensional projections of three-dimensional spatial objects located within the radiation field. For subsequent analysis, such projections are denoted by the function *f(x, y)*. The diversity of geometrical configurations of both the radiation sources and the irradiated media enables the extraction of new information on the physical properties of these interacting systems. In laboratory settings, studies in the soft X-ray range are often hindered by the predominance of photoabsorption over scattering processes. Consequently, spectral analysis of spatially distributed objects relies primarily on the registration of the photoelectric effect and the resulting characteristic emission from the irradiated medium. Notably, redistribution of spectral intensities is observed only for allowed transitions to K-shells of atoms starting with beryllium (Jerkstrand et al., 2011). A key objective is to determine the minimum contrast of inhomogeneities required to resolve structural details at a given signal-to-noise ratio. It is observed that, for certain astrophysical objects, the peak of the X-ray energy distribution shifts toward higher energies. This behavior is typical for phenomena such as nova outbursts and X-ray sources, including pulsars in binary star systems. Among the non-compact sources, young supernova remnants–such as SNR 1987A–exhibit radiation from both forward and reverse shock fronts, as well as from radioactive decay of residual material. Emission from active galactic nuclei (AGN) also remains a subject of considerable interest.

In all the aforementioned cases, the radiation transport equation must be supplemented by an integral term accounting for the contribution of scattering. Cross-sections for photoabsorption and scattering across various media types are presented in detail in several previously published studies [see references]. In dense media where multiple scattering events are prominent, the impact of these processes on the stability and accuracy of image reconstruction procedures has been critically analyzed. The present study is restricted to the energy range covered by all modern X-ray observatories, with the exception of *Fermi LAT*, and therefore does not consider photon energies exceeding 10 MeV. Additionally, all radiation sources under consideration are associated with thermonuclear processes, which yield photon energies limited to a few MeV. The structure of the article is as follows. Section 1 provides a general introduction to the problem and the formulation of the research objectives. Section 2 outlines and analyzes the fundamental equations governing X-ray radiation transport in highly absorbing media, with particular focus on the characteristics of atomic emission that constitute the radiative response of the medium. Section 3 is devoted to the formation of detector-plane images f(x, y), incorporating the effects of multiple scattering. Section 4 presents methodologies for reconstructing the original spatial structure of the object from the recorded projections f(x, y). The Discussion offers an interpretation of the results and proposes directions for the development of third-generation spectrographic detectors based on the findings of this work. The Conclusion summarizes the key outcomes, compares the derived detector characteristics with those of first- and second-generation instruments, and highlights the relevance of spectral color indices for probing the chemical state of scattering media.

2. Radiation Transport Equations for X-rays

A key distinction between the interaction of high-energy radiation fields and matter–compared to interactions in optically active media–is the dominance of photoionization (i.e., the atomic photoelectric effect) in the soft X-ray range. In this regime, the process can be described as pure absorption. In the intermediate energy range, approximately from 30 to 130 keV, the photoabsorption cross-section decreases significantly, and beyond a certain energy threshold, Compton scattering becomes the predominant interaction mechanism. In physical media with average photon energies between 30 and 60 keV, multiple scattering events may occur. As photon energy increases further, the Compton scattering cross-section declines, and the probability of single scattering becomes dominant. Taking these phenomena into account, X-ray spectroscopy enables the formation of radiographic images and spectral projections of the irradiated objects. The same principles apply to the gamma-ray domain. Fig. 1 presents a comparative overview of modern space-based telescopes and the energy ranges covered by their respective spectroscopic instruments.

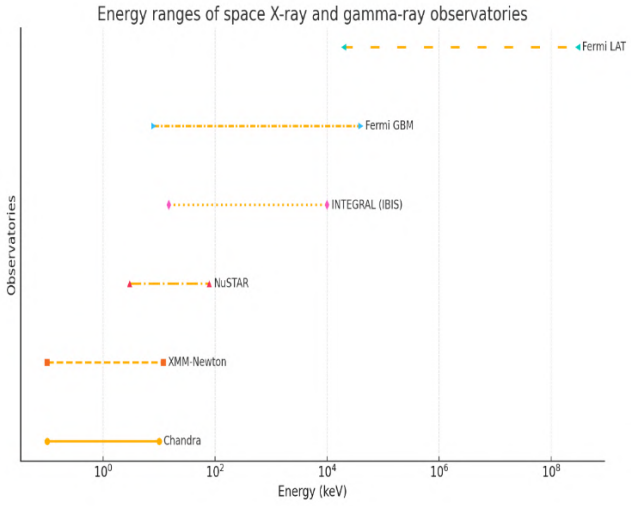

Figure1: Energy range of X- and γ-ray telescopes.

2.1. Physical Characteristics of Matter under High-Energy Radiation Exposure

Let us consider the line integrals of X-ray attenuation through the object.

$$p\ \theta,s\ =\ \int_{-\infty}^{+\infty} f\ x,y\ \delta\ s-x\cdot cos\theta-y\cdot sin\theta\ dxdy, \quad (1)$$

here, f(x, y) denotes the extinction coefficient distribution, while p(θ, s) is its projection–commonly referred to as a sinogram. Reconstruction of f(x, y) is performed using the inverse Radon transform (Yebb, 1989), (Bracewell & Riddle, 1967). In the ideal case:

$$f(x,y)=\int_0^{\pi}\int_{-\infty}^{+\infty} p\ \theta,\omega\ \omega e^{2\pi i\omega t\ s-x\cdot cos\theta-y\cdot sin\theta}\ d\omega\ \ d\theta\ . \quad (2)$$

In practical applications, the filtered back-projection method is used. Prior to its implementation, however, the scattering indicatrix describing X-ray interactions with atomic constituents of the medium must be introduced. Accordingly, the radiative transfer equation is reformulated in a more general framework, with particular emphasis on the geometric features of the target structures.

$$\frac{\mathrm{dI\ r,\Omega}}{\mathrm{ds}}=-\mu_t\ \mathrm{E,r\ I\ r,\Omega}\ +\ \int_{\mathbf{0}}^{\mathbf{4\pi}}\ 4\pi\mu_s\ \mathrm{E,r\ p_{KN}}(\Omega'\rightarrow\Omega)\mathrm{I}(\mathrm{r},\Omega')\mathrm{d}\Omega'\ . \quad (3)$$

The total attenuation coefficient is given by $\mu_t=\mu_a+\mu_s$, where μ_a,μ_s denotes the photo absorption and Compton scattering coefficient, and $p_{KN}(\Omega'\rightarrow\Omega)$ is the Klein–Nishina indicatrix describing the angular probability distribution of scattered photons, normalized over the full solid angle 4π. Physically, this quantity expresses the probability of scattering into a direction defined by the angle θ

$$p_{KN}\ \ \theta\ =\frac{1}{\sigma_{KN}}r_e^2\ \ \frac{E'}{E}\ ^2\ (\frac{E'}{E}+\frac{E}{E'}-sin^2\theta\ )\ , \quad (4)$$

here, E' denotes the energy of the scattered quantum, while σ_{KN} represents the total Klein–Nishina cross-section for a single electron.

$$E'=E/(1+\frac{E_e}{m_ec^2\ 1-cos\theta})\ . \quad (5)$$

The radiation intensity $\mathrm{I\ r,\Omega}$ detected by the observer as a result of single scattering on spherical irregularities V_{irreg} with radius a can be expressed as

$$I_s\ \Omega_s\ \approx I_0\mu_s\ E\ \ \frac{V_{irreg}}{4\pi R_s^2}\cdot p_{KN}(\theta_s)\ e^{-\mu_t(s_1+s_2)}\ . \quad (6)$$

The value $I_0\mu_s\ E\ \ \frac{V_{irreg}}{4\pi R_s^2}$ in equation (5), this quantity is equivalent to the density of scattering electrons, ρ_e, which is correlated with the average mass density of the medium. s_1,s_2 denote the distances from the source to the scattering object and from the object to the observer, respectively. The radiative transfer equation (3) is valid under the assumption of single scattering. To justify the applicability of this approximation, we estimate the mean free path l of an X-ray photon in water. To account for the actual contribution from oxygen atoms, we subtract their effect and retain the effective mean free path for hydrogen atoms alone. Assuming a representative value of $l\approx 8$ cm for X-rays with average energy, we obtain the mean effective number of atoms N_A.

$$N_A=2\cdot\frac{1}{9}\frac{\rho}{\mu_H}N_A\approx 8{,}058\cdot 10^{23}\ cm^{-2}. \quad (7)$$

For most rarefied astrophysical media and the upper layers of the Earth's atmosphere, such an approximation is acceptable. In the following section, we compare scattering degrees derived from modeling with those obtained using this approximation. Having determined N_A, we proceed to the geometry of the inhomogeneities under investigation and relate the scattered radiation from the source to the spatial distribution of average electron density within these structures. It is necessary to select a suitable function $f_s(x,y)$ analogous to the attenuation function, which can be reconstructed from the scattered photons. To do so, we must return to the fundamental question: what physical quantity is actually measured when scattering dominates? If the cone of unscattered (ballistic) rays intersects the observer's detector, then even in scattering-dominated regimes, we simultaneously record attenuation of the primary beam–described by the first term in Equation (3), $I_{prim}\ (\theta,s)$ –and the intensity of the scattered component, $I_{scat}\ \theta,s$, The latter is further refined by specifying the kernel of the double integral:

$$\begin{aligned} I_{prim}\ \ \theta,s\ &=I_0\ exp[-\int\mu\ x,y\ dl]\\ I_{scat}\ (\theta,s)&=\iint f_s\ (x,y)\ P(\psi(x,y\rightarrow s))\ \frac{1}{R^2}\ dxdy \end{aligned} \quad (8)$$

The function $f_s\ (x,y)$ represents the local electron density, i.e., the number of Compton-scattering centers. The angular distribution of scattered photons is described by the indicatrix $P\ \psi\ x,y\rightarrow s\ \ =p_{KN}\ \ \theta$ derived from the Klein–Nishina (KN) theory. Here, R denotes the distance from the scattering point to the detector. The corresponding expression involves a double integral taken over the entire volume of the medium. The scattered signal thus constitutes a convolution-type integral. In the absence of scattering and under dominant photo absorption, the kernel of the direct Radon integral along the ray connecting the primary radiation source and the observer's detector contains a delta function of the form $\delta\ s-x\cdot cos\theta-y\cdot sin\theta$. Numerical results illustrating scattering irregularities, including chemical composition anomalies, are shown in Fig. 3 for a hydrogen–oxygen medium with localized oxygen deficiency. Notably, when the magnitude of the anomaly falls below 3%, the scattered signal becomes indistinguishable from the noise level of the detection system. The energy of the incident photons is 130 keV.

2.2. The Role of Fluorescent X-ray Emission

Essentially, when photo absorption occurs in a gas–dust diffuse medium within the energy range up to 30 keV, all constituent elements with atomic numbers from 1 to 4

undergo only ionization, followed by the capture of free electrons from the medium and subsequent recombination through three-body collisions. The probability of such events in a diffuse environment is extremely low. A rare exception is found in young, dense supernova remnants, where the presence of metals in the inner layers can lead to an increase in electron density [Chevalier & Fransson, 2016). In such cases, photo absorption in elements starting from boron and above results in the formation of K-shell vacancies, the emission of high-energy electrons, and Auger electrons. The filling of K-shell vacancies gives rise to soft X-ray secondary radiation, which is efficiently reabsorbed in the surrounding medium. Therefore, the detection of such quanta provides a means for diagnosing the outer layers of the observed objects. The energy intervals between the absorption edges of these photons are referred to as transparency windows. Visualization of images within these 'windows' enables the characterization of deeper layers through the continuous component of the spectrum. The thermalization of X-ray radiation primarily begins with multiple Compton scatterings, followed by a cascade of energy loss and subsequent photo absorption.

3. The Multiple Scattering Approximation

Multiple scattering of X-ray radiation contributes to two principal effects. First, it reduces the contrast of the contours of observed structures in direct transmission images. On the other hand, in the absence of absorption in equation (3), contrast enhancement relative to the background noise emerges in regions of structural irregularities, as illustrated in Fig. 2. In other words, multiple scattering of X-ray photons gives rise to a diffuse component of the radiation field, which is a fundamental characteristic of the multiple scattering regime. This occurs because the quantities $P\ \psi\ x,y \to s\ \ = p_{KN}\ \ \theta$, derived from equations (3) and (4), can no longer adequately describe the entire scattering system as a whole. In such cases, the Monte Carlo method is employed to address the problem.

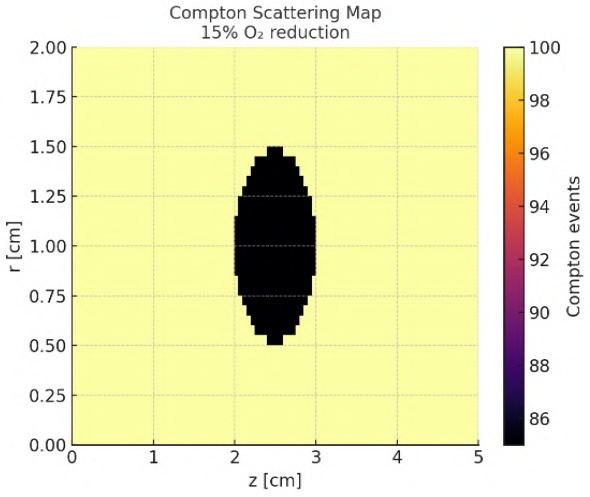

Figure 2: Spatial structure of the X-ray scattering region.

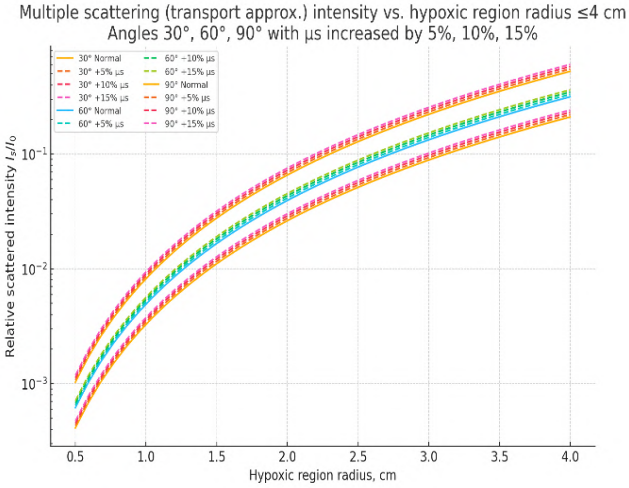

Figure 3: Experimental modeling of multiple scattering in oxygen-deficient liquid environments. The word hypoxic means the oxygen deficiency.

Fig. 3 plots showing scattering angles of 30°, 60°, and 90° under conditions of multiple scattering (transport approximation) for oxygen-deficient regions with radii ranging from 0.5 to 4 cm. At 30°, the intensity level is higher than at 60° and 90° due to the anisotropy of scattering. A 10–15% increase in the scattering coefficient μ_s (x, y) is observed with decreasing oxygen concentration in water, resulting in a noticeable contrast deviation for radii larger than 2 cm. For small regions (less than 1 cm), such differences remain undetectable.

4. Image Reconstruction from X-ray and Gamma-Ray Detector Readings

The inverse problem consists in reconstructing the geometry of a scattering region based on the radiation measured by detectors. The raw data (e.g., in the form of RAW files) are used for the visualization of objects via scattered radiation, a technique known as *scatter imaging*. The key idea is to reconstruct local variations in the attenuation coefficient μ_a (x, y) and the scattering coefficient μ_s (x, y) within the scattering region by analyzing the angular distribution and intensity of lateral scattering. To derive the relations required for solving the inverse problem, we rewrite the second (scattering) term in equation (3) in a more convenient form:

$$I_s\ \ \theta, r_d\ \ = \int_0^V G\ r, r_d, \theta\ \ \mu_s\ \ r\ \ \Phi\ r\ \ dV\,. \qquad (9)$$

Where $\Phi\ r$ denotes the primary radiation fluence at point r, associated with the local scattering coefficient $\mu_s\ \ r$, and $G\ r, r_d, \theta$ is a geometric and transport operator that accounts for attenuation, the scattering indicatrix $p_{KN}\ \ \theta$ and the propagation path to the detector. The measurement process represents a discrete data acquisition scheme, in which the detector readings are recorded in sampled form. In the presence of mmm detector channels, each channel must be mapped to its corresponding angular and spatial coordinates:

$$I_m^{meas} = \ _j K_{mj}\ \mu_{s,j} \ + \ noise\ . \qquad (10)$$

Where K_{mj} is the sensitivity matrix (kernel), $\mu_{s,j}$ is the parameter to be estimated–representing spatial variations of the scattering coefficient μ_s , and *noise* denotes statistical measurement noise.

4.1. Inverse Problem Statement

It is required to determine the fields $\boldsymbol{\Delta\mu_s}\ (\boldsymbol{r})$, that give rise to anomalies in the scattering intensity.

$$\Delta I_m = \ _j K_{mj}\ \Delta\ \mu_{s,j} \qquad (11)$$

Which corresponds to the solution of a linear inverse problem.

$$\Delta I = K\cdot\Delta\ \mu_s\ . \qquad (12)$$

Structure of the Raw Data from Detectors. In X-ray detectors, pixels are arranged in the form of a square matrix, whose dimensions are determined by the manufacturer. Each detector is associated with a two-dimensional matrix and corresponding time series that record the activation time of each pixel following the interaction with an X-ray photon. This structure enables dynamic monitoring of the imaged objects. In classical detectors of the first and second generations, image analysis and reconstruction rely primarily on object projections formed by photon absorption. It is generally assumed that this is sufficient for reconstructing the density distribution of the object. In contrast, our method utilizes projections formed by X-rays scattered by atomic electrons within the object. As shown in Fig. 5 from (Doikov D & Doikov M, 2024), there exists a spectral region in which scattering dominates over photoabsorption.

4.2. Reconstruction Methods

The reconstruction of astronomical images was first introduced in the late 1960s in the context of radio interferometric observations. The primary objective of these studies was to determine the geometric and physical characteristics of observed objects. By comparing regions responsible for absorption and scattering of radio waves during data processing, it became possible to achieve the necessary image contrast. A subsequent development involved obtaining high-contrast optical and infrared images containing fine structural details in planetary atmospheres within the Solar System. In this case, the recorded radiation was affected by Rayleigh molecular scattering. The variation in measured scattered radiation as a function of planetary rotation enabled the association of signals with the angular coordinate θ. Once the intensity distribution of scattered radiation was obtained, a suitable image reconstruction method could be selected. Currently, the following reconstruction approaches are widely used:

1. **Algebraic Methods (ART, SIRT).** A response matrix K is constructed (e.g., via Monte Carlo simulation for a given anomalous medium), and a minimum-norm solution is obtained using a regularization parameter λ:

$$\Delta\mu_s\ = \arg\ min \parallel K\Delta\mu_s\ - \Delta I\ \parallel^2 + \lambda \parallel \Delta\mu_s \parallel . \quad (13)$$

2. **Iterative Reconstruction with Regularization**. Используется Maximum-Likelihood Expectation Maximize**.** An advanced class of reconstruction techniques employs iterative schemes with embedded regularization. One widely used algorithm is Maximum-Likelihood Expectation Maximization (MLEM)**,** which is particularly effective in low-photon-count or Poisson-limited regimes. The algorithm iteratively updates the estimate of the scattering or attenuation distribution μ(r) to maximize the likelihood of observing the measured detector data, while optional regularization terms may be included to stabilize the solution and suppress noise action (MLEM).

3. **Diffusion Approximation / Transport Model Fit.** The scattering process is modeled using a diffusion approximation or a full radiative transport model, with spatially varying parameters $\Delta\mu_s$ and $\Delta\mu_a$ in different regions. The model parameters are adjusted so that the simulated lateral (scattered) signal matches the experimentally measured data. This approach is particularly suitable when multiple scattering dominates and the medium can be approximated as diffusive.

4.3. Stepwise Reconstruction Algorithm

- Data preparation: Convert RAW data into sinograms as a function of projection angle; normalize with respect to angle and photon energy.
- Model calibration: Select a precomputed or experimentally calibrated model using a reference sample to obtain the system response matrix K. Subtract the background signal (scattering from the entire nominal model without anomalies).
- Optimization and inversion: Perform data inversion and parameter estimation using equation (13) in combination with Algebraic Reconstruction Techniques (ART/SIRT) augmented with Total Variation (TV) or Tikhonov regularization.
- Interpretation: Analyze the reconstructed image to obtain a spatial map of $\Delta\mu_s\ (r)$ .representing local deviations in the scattering coefficient.
- Noise suppression and structural enhancement: The highest image quality and feature resolution are achieved using TV regularization, which effectively suppresses noise and reconstructs smoothed or piecewise-constant anomalies:

$$min_x \parallel Kx - \Delta I \parallel^2 + \lambda\, TV(x)\ . \qquad (14)$$

Depending on the nature and characteristics of the measured data, two forms of total variation (TV) regularization can be applied:

Anisotropic or simple form: the absolute differences between neighboring pixel (voxel) values are summed separately along the horizontal and vertical directions. At

this stage, artifacts and noise in the projection signals are partially suppressed.

$$TV\ x\ =\ _{i,j}\ x\ i+1,j\ -x\ i,j\ \ +\ x\ i,j+1\ -\ x\ x\ i,j \tag{15a}$$

Isotropic form: enables smoothing of sharp discontinuities and artifacts that may occur during image acquisition on the detector.

$$TV\ x\ = \ _{i,j}\ \sqrt{x\ i+1,j\ -x\ i,j\ ^{2}+\ x\ i,j+1\ -x\ i,j\ ^{2}} \tag{15b}$$

Here, the gradient is computed at each pixel (in both x and y directions), its norm is taken, and then the result is summed over the entire domain. The first term in equation (14) is based on comparison and alignment with the measured data, while the second term suppresses excessive oscillations. As a result, the solution becomes piecewise constant and more effectively reveals localized anomalies. These anomalies constitute the main objective of the present study. Essentially, by anomalies we refer to rapid lightning formation and various energy bursts occurring under terrestrial and cosmic conditions.

5. Calculation Results

Many problems in astrophysics and planetary astronomy are based on the analysis of spectral flux measurements from extended structures that scatter X-ray radiation originating from point-like sources.

In Fig. 4: Top Left is the baseline phantom (normal oxygen level); Top Center is phantom with a local oxygen deficiency (15% reduction); Top Right is differential sinogram ΔI recorded by lateral detectors. Bottom Left – reconstruction using a SIRT-like method (without filtering); Bottom Center – reconstruction after Total Variation (TV) regularization (the anomaly becomes sharper and more compact); Bottom Right – ground-truth hypoxia mask.

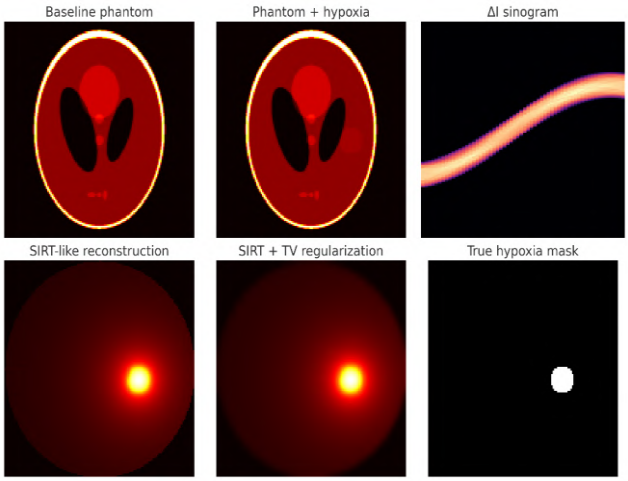

Figure 4: Mapping of a 2D Chemical Inhomogeneity (Shepp-Logan).

The Fig. 4 demonstrates that a local chemical anomaly is successfully recovered as a bright region, even for a weak perturbation (+15%). TV regularization significantly improves spatial localization.

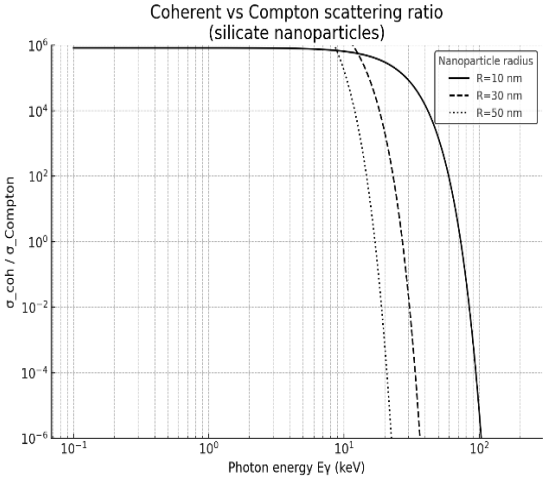

Figure 5: Relative contribution of Compton-type scattering for nanoparticles.

The Fig. 5 demonstrates that a local chemical anomaly is successfully recovered as a bright region, even for a weak perturbation (+15%). TV regularization significantly improves spatial localization.

Discussion. In the coming years, the deployment of next-generation (third-generation) detector-spectrographs is anticipated. The crystals used in these detectors possess a complex spatial structure, imposing constraints on the dimensions of the elementary pixel cells. For applications in X-ray and soft γ-ray spectroscopy, it is essential that the voxel length be no less than 1 cm, while the pixel width should not exceed several tens of nanometers. A potential difference of up to 1000 V is applied across the voxel faces. Therefore, studying the degradation mechanisms of semiconductors incorporating heavy elements is of significant interest.

Materials such as CsPbBr perovskites (Doikov D. & Doikov M., 2024; Liu, Wu, Wei, 2022) fall into this category. In third-generation detectors, the spectra of high-energy radiation are recorded within each voxel. In light of the discussed challenges, the availability of detailed spectra of both scattered and characteristic radiation enhances the resolution of structures with chemical inhomogeneities. At the same time, the likelihood of artifact formation is reduced. In $CsPbBr_3$ semiconductors, the signal-to-noise ratio has reached values of 2–3%, which improves reconstruction quality and expands the capabilities of spectral imaging.

Spectral image reconstruction requires careful use of existing tools. In essence, the method is based on the analysis of scattered high-energy radiation and the reconstruction of object structures from their scattering signatures. Due to the well-known expression for the scattering indicatrix $p_{KN}\ \ \theta$ each atomic species exhibits a characteristic angular distribution that relates the photon scattering angle to its post-collision energy. In other words, the dispersion of the scattered radiation is directly linked to the chemical composition of the medium.

Color Indices. In some cases, the intensity of scattered high-energy radiation is too low to allow for detailed spectral reconstructions. For such scenarios, we propose using integrated flux ratios across selected spectral intervals, analogous to color indices in optical astronomy. In stellar spectroscopy, these color indices have shown sensitivity – and in some cases even correlation – with the metal content of stellar atmospheres. A similar approach may enhance the interpretability of scattering-based chemical imaging.

Spectral Geometry. The reconstruction of investigated objects using spectral analysis enables the extraction of additional structural and compositional details, which are directly related to the medium's radiative response to external irradiation. During the reconstruction process, both artifacts and zones with local physicochemical heterogeneities begin to emerge clearly, as illustrated in Fig. 4, thereby expanding the diagnostic potential of the proposed method.

6. Conclusion

Image reconstruction of irradiated media–based on the analysis of both transmitted and scattered radiation–has necessitated the development of new physical concepts, instrumentation strategies, and computational algorithms. This study substantiates the importance of incorporating scattered radiation into the image reconstruction framework. Contrary to the common belief that scattering leads only to image degradation and loss of diagnostic value, our results demonstrate that certain spectral regions actually provide "clean" dominance of specific interactions:

- Pure absorption: 0.1–10 keV;
- Pure scattering (mainly Compton**)**: 40–160 keV;
- Competitive regime (absorption and scattering): 10–40 keV.

To simplify interpretation and facilitate visualization, we selected both liquid and solid phases of the most abundant cosmic and planetary environments: water and methane for planetary atmospheres, and silicates and carbonates for the interstellar medium. To date, most image reconstructions have been carried out under the pure absorption approximation, which assumes the radiation source is positioned behind the irregular medium along the source–detector axis. In this setup, the projection data corresponds to a 2D distribution of the absorption coefficient $\mu_{\mathrm{a}}\,(x,y)$, which is commonly interpreted as the mass density map ρ_{a} (x,y). However, our findings indicate that such a configuration limits the amount of physical information retrievable from the system and often reduces irregularities to the level of noise in the detector image, thereby compromising contrast.

In regions corresponding to very small scattering angles $\theta \ll 1$, contrast loss due to scattering becomes significant and calls for additional mathematical treatment to restore interpretability. In cases where the effective number of scatterers (atoms) remains within the single-scattering regime (see equation (6)), our study demonstrates that it is feasible to reconstruct spatial distributions of the scattering coefficient $\mu_{s}(x,y)$ based on scattered radiation. This approach dramatically expands the observable volume–both geometrically and physically – compared to absorption-only techniques. Interestingly, such effects have also been observed by X-ray satellites, even in energy domains typically dominated by absorption. In these observations, nanoparticles of silicates and carbonates serve as primary scattering agents. However, under these conditions, scattering is primarily diffraction-based, governed by the macroscopic properties of the dust particles. Specifically, it depends on the refractive index in the X-ray regime, which is typically very close to unity. X-ray observatories have recorded diffraction halos around novae during their peak brightness phases (Drine, 2003). To quantify the contributions of diffraction and Compton scattering, the following spectral classification is applied:

- Soft X-ray halos (0.1–10 keV) dominated by diffraction (coherent scattering, σ_{coh} tipe);
- Intermediate range (10–40 keV) competitive regime (diffraction and Compton scattering);
- Hard X-rays (>40 keV) dominated by Compton scattering.

For an individual particle containing N electrons, the scattering cross section must be computed accordingly to capture the contributions of both coherent and incoherent processes.

$$\frac{\sigma_{coh}}{\sigma_{Compt}} \approx \frac{N^2 |F\ q\ |^2}{N\sigma_{KN}} \tag{16}$$

$$|\,F(q)\,|^2 \approx exp\,-\,qR^{\ 2}\ , q = \frac{4\pi}{\lambda}\sin\theta/2 \tag{17}$$

For the first time, previously invisible shells near novae have been identified based on scattered radiation. We have determined a wavelength interval in which diffraction-based X-ray scattering by dust becomes comparable to–or even exceeds – Compton scattering. By comparing the angular scattering indicatrices associated with the two mechanisms, $\mathrm{p}_{\mathrm{KN}}(\theta_s)$ we found that $\mathrm{p}_{\mathrm{KN}}(\theta_s)$ weaker anisotropy compared to the strongly forward-peaked, needle-like form of $\kappa\ \mathrm{p}_{Difr}(\theta_s)$. The sharp angular structure of $\kappa\ \mathrm{p}_{Difr}(\theta_s)$. makes it particularly suitable for both forward and inverse Radon transform techniques.

Author Contributions: D.D. developed the physical model presented in Section 2-4. The *Introduction*, problem Formulation, *Discussion*, and *Conclusion* were co-written.

References

Bracewell R.N., Riddle A.C.: 1967, *Astroph. J.*, **150**, 427. DOI: 10.1086/149346

Chevalier R.A., Fransson C.: arXiv.1612.07459v1 [astro-ph.He], 22 Dec 2016.

Costantini E., Corrales L.: 2022, aanda.org+5edoc.ub.uni-muenchen.de+5cxc.harvard.edu+5arXiv.

Doikov M.: 2024, *OAP*, **37**, 11-14. DOI: 10.18524/1810-4215.2024.37.312675

Doikov D.N., Doikov M.D.: 2024, *OAP*, **37**, 5-10. DOI: 10.18524/1810-4215.2024.37.312680

Draine B.T.: 2003, aanda.org+15cxc.harvard.edu+15arXiv+15.

Jerkstrand A., Fransson C., Kozma C.: 2011, *A&A*, **530**, A45, 1-23.

Lee J.C.: 2011, *Space Sci. Rev.*, **157**, 93–101. https://doi.org/10.1007/s11214-010-9723-2

Liu Fangze, Wu Rong, Wei Jing, Ni Wanyi et. al.: 2022, *ACS Energy Lett.*, **7**, 1066–1085, https://doi.org/ 10.1021/acsenergylett. 2c00031.

The Physics of Medical Imaging: 1991 / Ed. by Steve Webb. IOP Publishing Ltd. pp. 138-171.

https://doi.org/10.18524/1810-4215.2025.38.340350

DESIGN AND INVESTIGATION OF A NOVEL GAMMA-RAY SPECTROGRAPH CONFIGURATION IN THE ENERGY RANGE 0.511–5 MEV

Marko Doikov

Paisii Hilendarski University of Plovdiv, Faculty of Physics and Technology,
Tzar Asen St, 4000 Plovdiv, Bulgaria, *marik.doikov@gmail.com*

ABSTRACT. A novel composite gamma-ray detector based on three $CsPbBr_3$ crystals is proposed for the registration of quanta in the 0.1–5.0 MeV energy range. The central crystal simultaneously performs two functions: direct detection of gamma photons with energies up to 0.6 MeV and detection of annihilation-induced radiation in the 1.022–5.0 MeV range. The induced radiation is additionally recorded by two symmetrically positioned side crystals.

Monte Carlo simulations of gamma-ray transport within the primary crystal were performed to determine the detector response function and the angular scattering angular distribution. The secondary radiation yield and its detectability by the side detectors were quantified. Characteristic time constants of the detection processes and saturation regimes were identified. Furthermore, the economic feasibility of the proposed detector configuration was assessed, demonstrating its potential for practical implementation in advanced gamma-ray spectrographs.

Keywords: gamma-ray spectroscopy, $CsPbBr_3$ detector, positron annihilation, Monte Carlo simulation, composite detector design.

АНОТАЦІЯ. Запропоновано новий комбінований гамма-детектор на основі трьох кристалів $CsPbBr_3$ для реєстрації квантів у діапазоні енергій 0,511–5,0 МеВ. Центральний кристал виконує одночасно дві функції: безпосередню реєстрацію гамма-фотонів з енергіями до 0,6 МеВ та детекцію випромінювання, індукованого анігіляцією, у діапазоні 1,022–5,0 МеВ. Індуковане випромінювання додатково реєструється двома симетрично розташованими бічними кристалами.

Було виконано моделювання транспорту гамма-квантів у первинному кристалі методом Монте-Карло для визначення функції відгуку детектора та індикатриси кутового розсіяння. Оцінено вихід вторинного випромінювання та його реєстрація бічними кристалами. Визначено характерні часові константи процесів детектування та режими насичення. Додатково проведено аналіз економічної доцільності запропонованої конфігурації детектора, що демонструє її потенціал для практичного впровадження у сучасній гамма-спектрографії. Були визначені критичні режими роботи та розрахована реакція системи у вигляді імпульсів струму – дані, необхідні для проектування електронного інтерфейсу.

Ключові слова: гамма-спектроскопія, детектор $CsPbBr_3$, анігіляція позитронів, моделювання Монте-Карло, комбінована конструкція детектора.

1. Introduction

Detailed gamma-ray spectra became widely accessible to a broad range of specialists with the advent of semiconductor crystals possessing average atomic numbers Z in the range of 50–60 (Doikov, 2022). The high accuracy of the acquired spectral data, combined with the absence of a need for cryogenic cooling of gamma spectrographs, has significantly enhanced their availability and reduced production costs. Crystals and powders of $CsPbBr_3$ are now commercially available. γ- radiation with energies not exceeding 0.6 MeV can be efficiently detected using a crystal with a volume of ~1 cm^3. Under these conditions, γ-quanta in the intermediate energy range of 0.6–1.022 MeV require additional considerations for signal formation, as they are only partially absorbed within the crystal. Consequently, the efficiency of converting the absorbed photon energy into a current pulse is reduced.

The dominant interaction mechanism for γ-quanta, as illustrated in the figures presented in this study, is Compton scattering. For example, a single scattering event of an X-ray quantum with energy 50 keV results in a maximum energy transfer of approximately 5 keV. After undergoing multiple scattering events, low-energy X-ray and γ-quanta ($E_\gamma \leq 10$ keV) are subject to enhanced photo absorption (Liu et al, 2022; Weber) For effective absorption of γ-quanta in the range 0.6 MeV $\leq E_\gamma \leq$ 1.022 MeV, it is necessary to increase the thickness of the $CsPbBr_3$ absorber crystal. However, this approach contradicts the requirements for the miniaturization of gamma spectrographs. In this energy region, Compton scattering events become rarer, yet the resulting current pulse amplitude is significantly larger than that produced by absorbed photons in the lower-energy range 0.1 MeV $\leq E_\gamma \leq$ 0.6 MeV.

The present work is devoted to a novel method for recording gamma-ray spectra in the energy interval 1.022 MeV $\leq E_\gamma \leq$ 5 MeV. The implementation of this method is structured into three main stages, described in

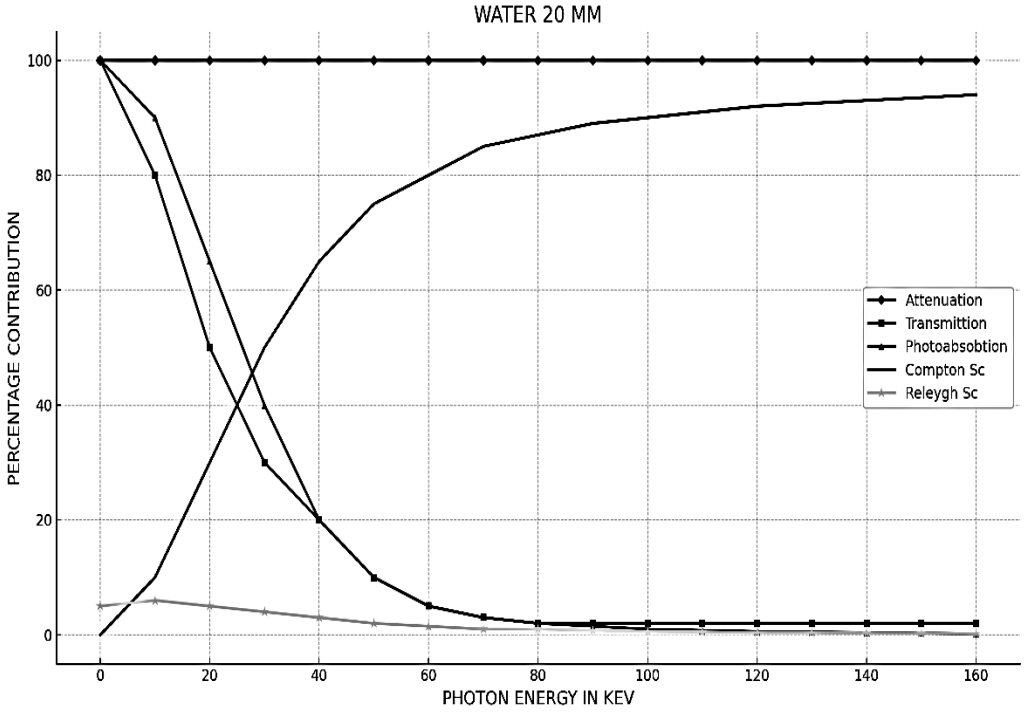

Figure 1: Interaction X-ray and γ-quanta with water

separate sections. Section 2 presents calculations of Compton scattering diagrams and the resulting angular distributions of γ-quanta, based on the Klein–Nishina formalism. Section 3 focuses on the calculation of cross-sections for electron–positron pair production in the vicinity of atomic nuclei in soft tissues. Importantly, the proposed method does not require increasing the thickness of the detector's absorbing layer. Section 4 discusses the detector design and its electronic interface. Sections 5 and 6 contain the Discussion and Conclusion, respectively, including a comparison of the developed device with previously reported detectors and the presentation of model gamma spectra.

2. Compton Scattering of γ-quanta in $CsPbBr_3$ Crystals

The propagation of X-ray and γ-quanta in matter is accompanied by photo absorption, collisions, and scattering processes, primarily Compton and Rayleigh scattering on atomic electrons (Weber; Incerti et al., 2010). Figure 1 illustrates the relative contributions of these interaction mechanisms during photon transport in soft tissues.

Photo absorption is most effective in the soft X-ray energy range. In the soft to intermediate gamma-ray range, inelastic Compton scattering dominates. From the Klein–Nishina equation, the angular scattering distribution (angular distribution) of γ-quanta can be derived.

$$\frac{d\sigma}{d\Omega} = \frac{r_0^2}{2}\left(\frac{E'}{E}\right)^2\left(\frac{E'}{E} + \frac{E}{E'} - sin\theta\right) \quad (1)$$

Here, θ denotes the scattering angle relative to the initial photon propagation direction. E' and E represent the energies of the scattered and incident photons, respectively, while r_0 is the classical electron radius. The angle θ also characterizes the electron scattering geometry.

The mean free path of X-ray quanta increases with photon energy. For photons with an energy of approximately 50 keV, the mean free path is about 8 cm. When compared to the dimensions of the phantom–represented here by a standard water phantom of 10^3 cm^3 volume – it can be concluded that, on average, a single scattering event occurs.

As shown in Table 1, approximately 30–40% of the scattered quanta possess a lateral, in particular perpendicular, component. For a soft-tissue thickness of 10 cm, the resulting fractional distribution is as follows: 70–80% of the photons remain unattenuated and do not interact, 10–20% undergo photo absorption, and among all scattered photons, 30–40% are deflected laterally. This corresponds to about 3–8% of the total photon flux. With increasing photon energy E, the scattering angular distribution E' becomes more strongly localized around the original photon propagation direction, as illustrated in Figure 2.

Table 1: Single scattering in soft tissues (water) at an X-ray energy of E = 50 keV. Percentage of scattered radiation:

Scattering angle θ (degrees)	Normalized $d\sigma/d\Omega$
0° (forward)	1.0
45°	0.70
90° (lateral)	0.40
135° (backward)	0.15
180° (backward)	0.05

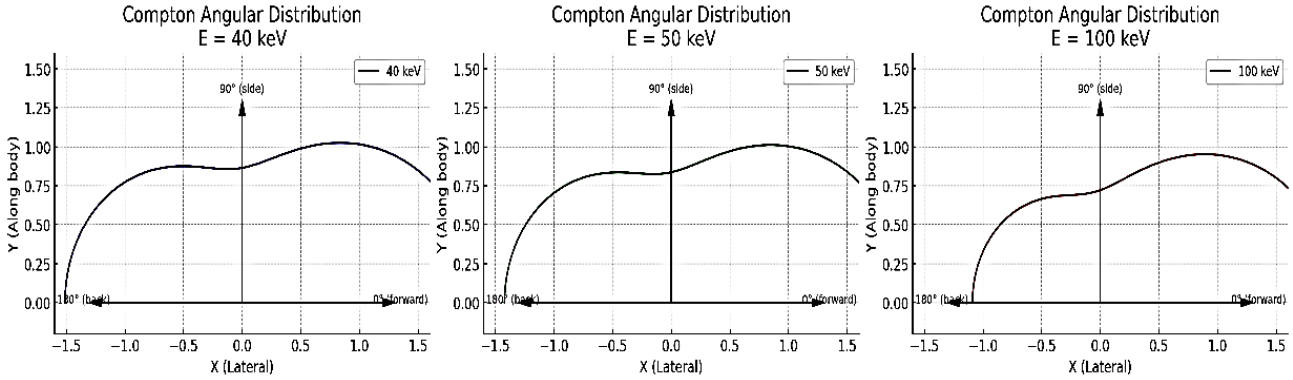

Figure 2: Scattering angular distribution of photons with different energies in the soft gamma-ray and hard X-ray range. The length of the line connecting the origin to a point on the diagram is proportional to the scattering probability.

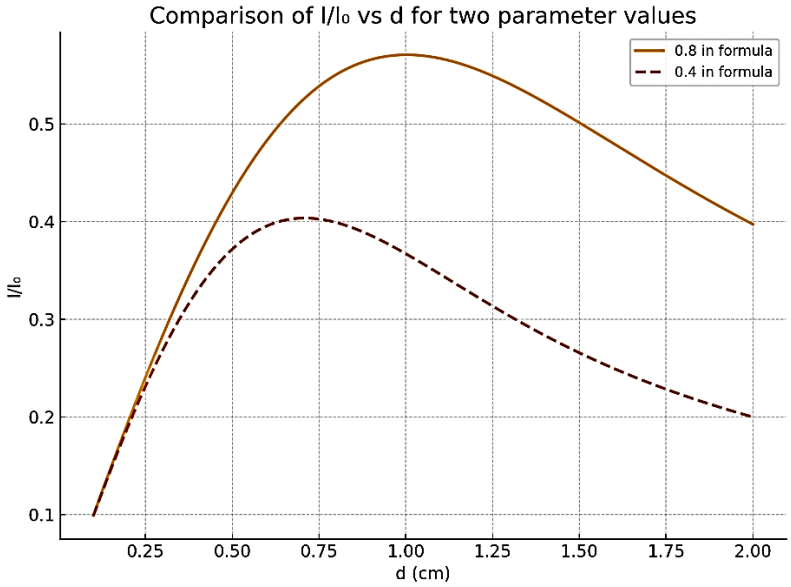

Figure 3: Dependence of $\frac{I}{I_0}$ on the crystal thickness d, calculated using the Hurst relation for characteristic potential differences V=500 V and V=1000 V $\mu\tau V = 0.4\ and\ 0.8$ in free dimension units).

The fraction of photons scattered in the forward direction increases with rising energy E. To calculate the current pulse, it is necessary to determine the energy $\Delta E_c = E - E' \approx (5-10)\ keV$. Let the band gap width of the $CsPbBr_3$ semiconductor be denoted as ΔE_{forb}. Then, the total number of electrons transferred from the valence band to the conduction band after a single inelastic scattering event is given by the expression:

$$N_{fr} = \Delta E_c / \Delta E_{forb}. \quad (2)$$

To calculate the amplitude of the current pulse, the relations provided in (Doikov, 2022, 2023), which are also relevant for the present study, were employed:

$$N_{fr} = \frac{\Delta E_c\left(1-exp\left(-k_\gamma d\right)\right)}{\Delta E_{forb}} \quad (3)$$

In the exponent, it is more convenient to replace the extinction coefficient of gamma or X-ray radiation k_γ with the mass extinction coefficient $k_\gamma(m)$. The value of $k_\gamma(m)$ allows one to evaluate the percentage contribution of various scattering and absorption mechanisms to the total extinction, for example, in soft tissues (see Fig. 1). For semiconductor crystals of $CsPbBr_3$, the effective average atomic number is $M_\mu = 57.35$. The mean mobility–lifetime product of electron–hole pairs is $\mu\tau = 8 \cdot 10^{-4} cm^2/V$ where V denotes the potential difference between the electrodes of the $CsPbBr_3$ crystal. The signal-to-noise ratio, in the first approximation, can be expressed by the Hurst relation, which is useful for physical analysis:

$$\frac{I}{I_0} = \frac{\mu\tau V}{d}\left(1 - exp\left(-\frac{d^2}{\mu\tau V}\right)\right) \quad (4)$$

or alternatively, by incorporating the semi-empirical data reported in (Zhang,Zhou, 2020; Liu, Wu, Wei, et al., 2022; López, Abia, Consuelo et al., 2020).

$$\frac{I}{I_0} \approx \frac{0.8}{d}\left(1 - exp\left(-\frac{d^2}{0.8}\right)\right) \quad (5)$$

Here, the quantity on the left-hand side of the equation, $\frac{I}{I_0}$, represents the relative reduction (or change) in the current when passing through a layer of thickness d. This ratio describes the attenuation of current (or radiation, or signal) due to the presence of a material layer into which charges, photons, or ions penetrate. In detector physics (for example, in scintillation layers), the ratio $\frac{I}{I_0}$ can be associated with the particle detection efficiency as a function of the active layer thickness.

Numerous measurements of the aforementioned parameters have demonstrated that the optimal thickness d of $CsPbBr_3$ crystals corresponds to the values at which the plotted function reaches its maximum. This fact determines the characteristic dimensions of commercially available detector-grade crystals. The signal-to-noise ratio in modern $CsPbBr_3$ based detectors typically ranges from 80 to 100, making them competitive with more expensive counterparts based on other crystals containing heavy elements. Asymptotic behavior: when $d \ll \lambda$, where $\lambda = \mu\tau V$, almost the entire intensity is transmitted. For $d \gg \mu\tau V$, $\frac{I}{I_0} \approx \frac{\mu\tau V}{d}$ i.e., the intensity decreases inversely with thickness.

3.1. Quantitative estimates of elementary processes within the specified energy range

3.1.2. Expected current response. We introduce the following notation:

- Q – the charge of the electron cloud generated by the passage of a single ionizing gamma or X-ray quantum. The value of Q includes secondary electrons and holes (the avalanche multiplication is ensured by the high potential difference V applied to the contacts, typically (500–1000 V).
- τ_{drift} – the charge drift time in the $CsPbBr_3$ crystal, with $\tau_{drift} \approx 10\ ns$, E_{dep} – the absorbed energy corresponding to the four primary interaction mechanisms,

$$E_{dep} \approx 1.022 MeV - 6\ MeV \approx (1.022 - 6) \cdot 10^6\ eV \quad (6)$$

- $\Delta E_{el+dot} \approx 10\ eV - 25\ eV$ – the average energy required to generate an electron–hole pair (including possible trapping states).

Under these assumptions, the current response induced on the electrodes can be estimated for the given ionization parameters as:

$$E_{dep} \approx 5 \cdot 10^6\ eV; Q = \frac{E_{dep}}{\Delta E_{el+dot}} =$$
$$= 4 \cdot 10^{-14}\ Ql;\ \ I(\tau_{drift}) = \frac{Q}{\tau_{drift}} \approx 4\ \mu A \quad (7)$$

The obtained results are essential for evaluating the amplitude of the current pulse. Within a single significant order of magnitude, the values of the maximum amplitudes $I(\tau_{drift})$ vary. An analysis of the current amplitudes shows that $I(\tau_{drift})$ deviates significantly from a symmetric signal shape (Doikov, 2023). This demonstrates the practicality of integrating the pulse and subsequently discretizing it by the total charge Q. In this case, the current pulse is transformed into a standard rectangular shape and further converted into a potential pulse. The output values of the processed gamma spectrum exhibit high physical reliability.

With complete absorption of a γ-quantum with an energy of 5 MeV via pair production, a $CsPbBr_3$ detector can generate a peak current on the order of 4–8 μA, with a duration of approximately 10–20 ns, depending on the carrier mobility and the applied electric field. Let us examine in more detail the absorption capability of $CsPbBr_3$ crystals and soft tissues in connection with the need to address a range of applied problems. Water-containing aerosols in thunderclouds actively interact with gamma radiation. The deceleration of electrons in the fields of oxygen, nitrogen, and hydrogen atoms leads to the emission of continuous gamma quanta of sufficiently high energies. The electric potential of a lightning discharge can reach about 200 MeV. Therefore, the flux of gamma quanta is sufficient to produce electron–positron pairs in the electric field of a thunderstorm discharge (in water vapor). At lightning branch points, synchrotron X-ray and, more rarely, gamma radiation have also been observed. Thus, lightning provides conditions for bursts of direct gamma radiation. After interacting with nuclear fields, such gamma quanta with $E_\gamma \geq 1.022\ MeV$ E vanish, resulting in the creation of electron–positron pairs.

Fig. 4 also shows the current response of a $CsPbBr_3$ crystal in the energy range 1.022–5 MeV. The following contributions are taken into account: Direct ionization (a gradual increase with energy); Pair production (a sharp quadratic rise above 1.022 MeV); Total signal, which becomes increasingly dominated by the pair-production contribution at energies above approximately 2.5 MeV. The comparative contribution of electron–positron pair production to the formation of the current pulse is presented in Fig. 5. The ionization losses from the creation of electron–positron pairs are formed by the beta electron of the pair, the positron, and two annihilation γ-quanta with energies of 0.511 MeV, which in turn contribute to the current pulse. From the law of energy conservation, the residual kinetic energy of the produced particle pair must also be taken into account.

The dashed curve represents the current from the two 511 keV γ-quanta produced during positron annihilation (this contribution remains constant above the 1.022 MeV threshold). The black dash-dot curve shows the total detector response, taking into account: direct ionization, pair production, annihilation radiation. This contribution is particularly noticeable in the 1.5–2.5 MeV region, before the main energy losses from the electron–positron pairs themselves become dominant.

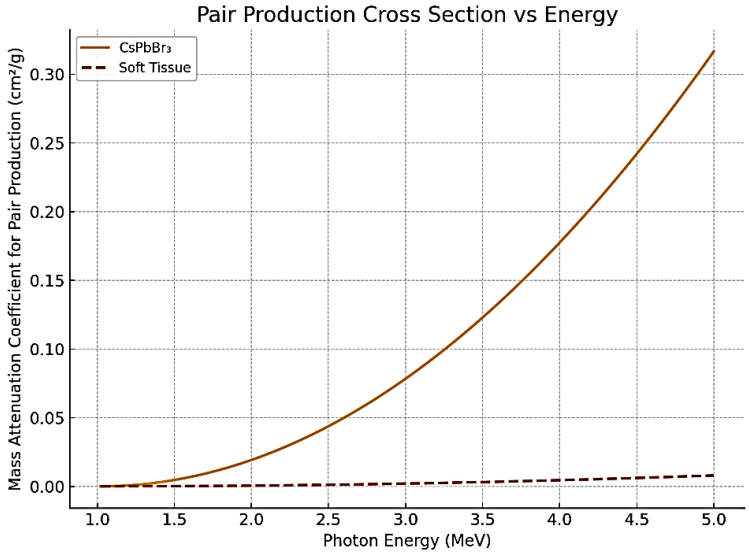

Figure 4: Extinction of gamma quanta with $1.022\ MeV \leq E_\gamma \leq 5\ MeV$ in soft tissues (Water) and in $CsPbBr_3$ crystals.

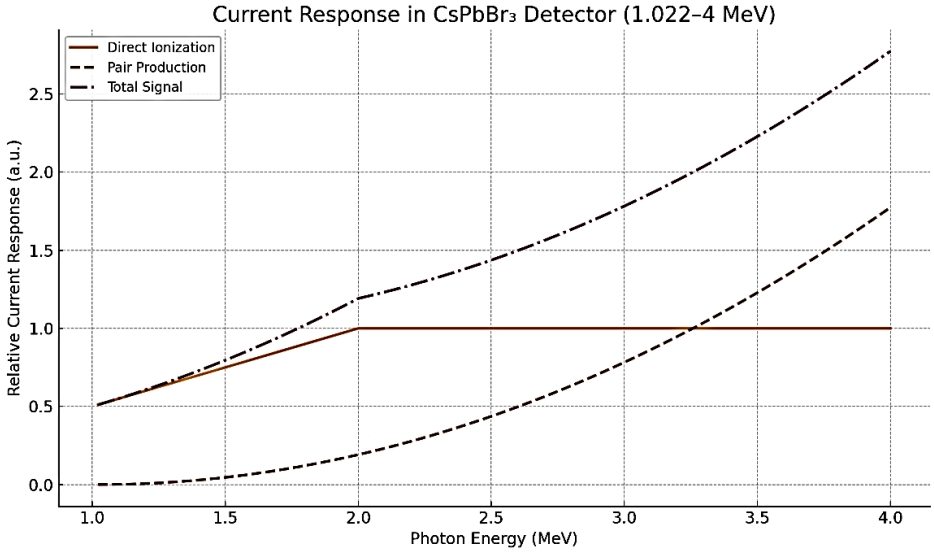

Figure 5: Relative contribution of annihilation to the resulting current response.

3.1.3. Accounting for incomplete absorption of annihilation-induced quanta. Consider a $CsPbBr_3$_33 crystal irradiated by γ-quanta with energies from 1.022 MeV to 4 MeV. The crystal volume is 1 cm³. We aim to determine the relative fraction of emitted γ-quanta generated as a result of electron–positron pair production near the nuclei constituting the crystal. To evaluate the relative yield of annihilation γ-quanta (511 keV) produced during the creation of electron–positron pairs in a $CsPbBr_3$ crystal of volume 1 cm³, we define the percentage of γ-quanta escaping the crystal – i.e., those not absorbed after positron annihilation – as a function of the energy of the primary γ-quantum that initiated the pair production process.

Material: $CsPbBr_3$, density ≈4.9 g/cm³, geometrical shape – cube of 1 cm³. The mass extinction coefficient is $\frac{\mu_{ext}}{\rho} = 0.25\ cm^2/g$. Thus, the linear extinction coefficient is $\mu_{ext} \approx 0{,}25 \cdot 4{,}9 \approx 1{,}225\ cm^{-1}$. The mean free path is therefore λ=1/μ≈0.816 см. The final step is to calculate the survival (escape) probability – P_{esc} of a γ-quantum with energy $E_\gamma = 0{,}511$ MeV:

$$P_{esc} = \frac{1}{6}\int_0^1 exp\left(-\frac{x}{\lambda}\right)dx = \lambda\left(1 - exp\left(-\frac{1}{\lambda}\right)\right) \approx 0{,}293 \quad (8)$$

Conclusions for this section. Approximately 29.3% of the annihilation γ-quanta generated within a 1 cm³ volume of $CsPbBr_3$ escape the crystal without being absorbed.

Approximately 80% of the total number of annihilated quanta, as well as the resulting combined contribution to the detector pulse. In the final figure, it is taken into account that about 29.3% of the annihilation γ-quanta generated within a 1 cm³ volume of $CsPbBr_3$ escape the crystal without being absorbed. Having obtained the final results (Fig. 7), we now proceed to the development and modeling of a combined gamma detector.

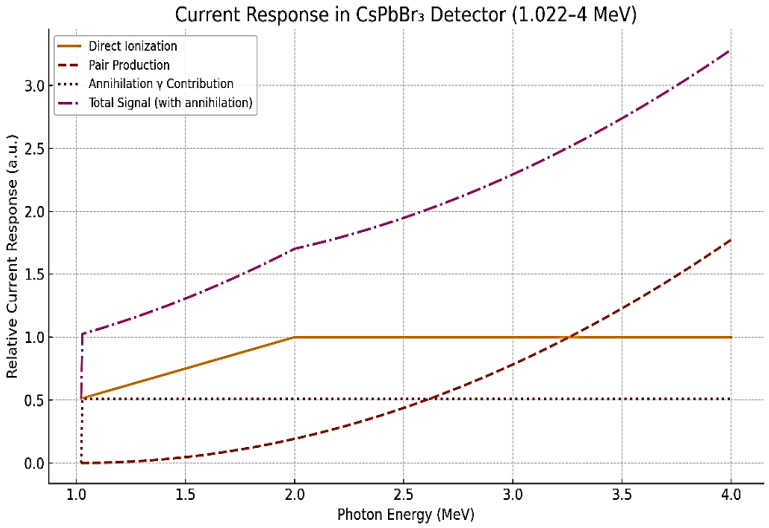

Figure 6: Current response of the detector accounting for direct ionization, electron–positron pair production, annihilation, and the resulting combined contribution to the detector pulse.

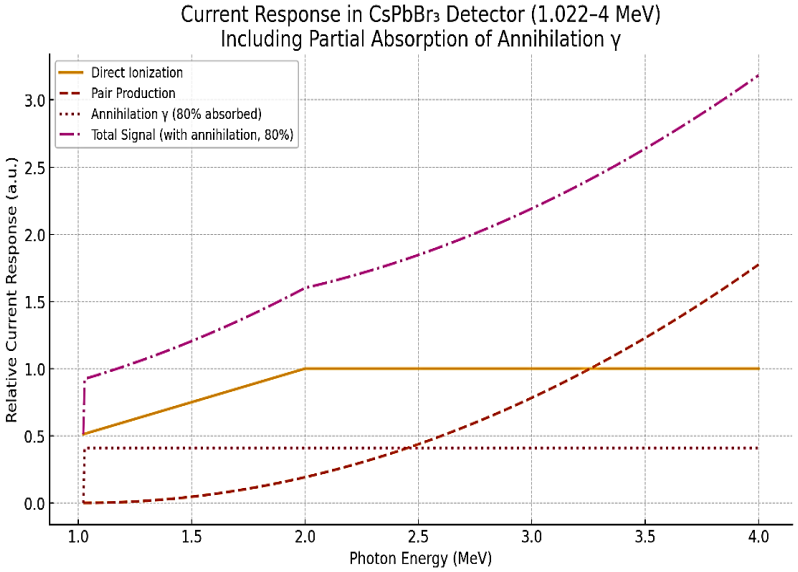

Figure 7: Current response of the detector accounting for direct ionization, electron–positron pair production, and annihilation.

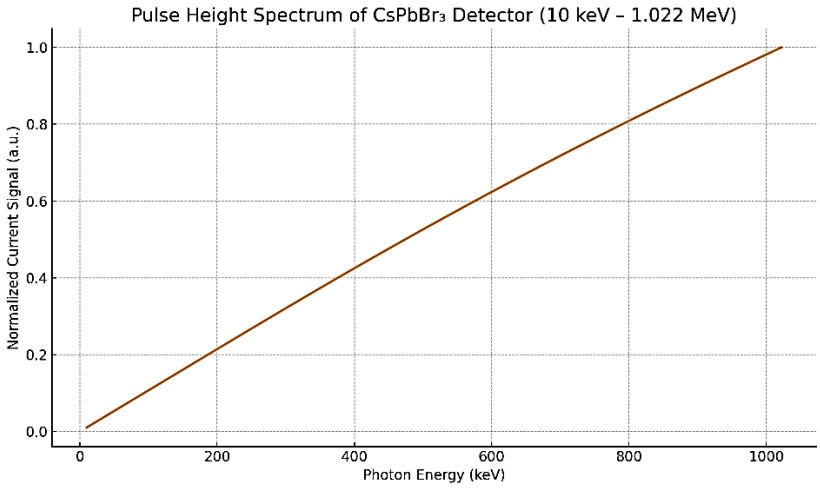

Figure 8: I(t)[a.u.] = Q(t)/Qmax – normalized current signal.

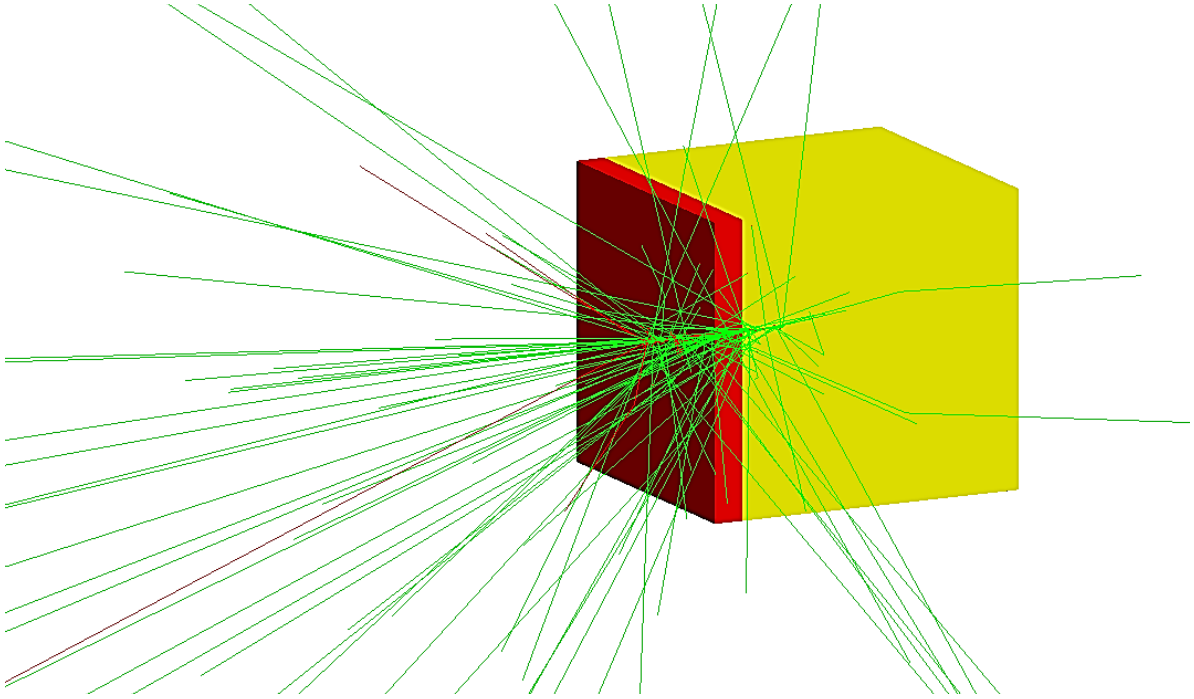

Figure 10: Simulation of a $CsPbBr_3$ crystal detector with a beam of 1000 γ-quanta.

4. Design of a combined detector

In this section, the most technically challenging task is the development of a gamma detector capable of reconstructing the spectra of investigated objects in the energy interval 0.511–1.022 MeV. Within this range, only ionization losses caused by Compton scattering need to be considered. Figure 4 presents the results of quantitative calculations of the total absorption coefficient. It should be noted that most radioactive isotopes exhibit their activity in the form of both discrete (line) spectra and Compton continua, analogous to the presence of discrete spectral lines superimposed on a continuous background in classical optics. The graph shows the spectrum of current pulses from a $CsPbBr_3$ – based detector with a volume of 1 cm^3 when interacting with γ-quanta with energies from 10 keV to 1.022 MeV.

The key features of the normalized current pulse dependence are determined by the efficiency of gamma-quantum extinction mechanisms, more precisely by the slope of the curve in Fig. 4. In particular: At low energies (up to ~100 keV), the current is small due to the high probability of transmission without interaction. In the range 200–600 keV, the response increases sharply due to more efficient absorption, primarily through the photoelectric effect. As the energy approaches 1 MeV, the current continues to grow but with a reduced slope, as the interaction probability begins to decrease. This spectrum represents not an energy-dispersive response, but rather the current (pulse) response. When gamma spectra need to be studied, a practical solution would involve considering both the intrinsic energy resolution of the detector and the spectrum of the incident radiation.

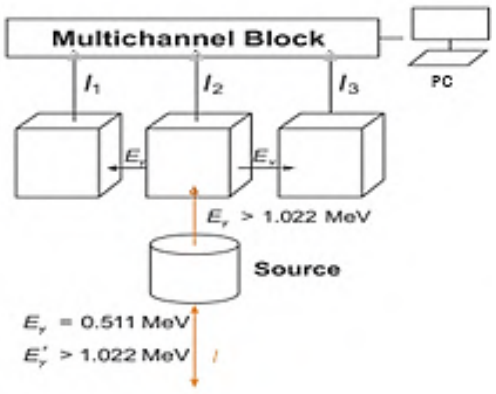

Figure 9: Schematic view of the gamma spectrograph for induced radiation.

5. Discussion

The diagnostics of physical media using next-generation high-precision gamma and X-ray spectrographs significantly expands the range of solvable problems in medicine, meteorology, and astrophysics. γ-quanta are formed by two independent mechanisms. For example, in Fig. 6, 7 a directed flux of beta particles and Gamma rays is emitted from a shielded cylindrical container. The device incorporates three independent detectors: the central detector records the direct radiation, while the lateral crystal semiconductor detectors register induced γ-quanta of strictly defined energy - 0.511 MeV.

For the "purity" of the experiment, it is necessary to determine the fraction of the scattered component of the flux that reaches the lateral detectors. For this purpose, the

results of standard modeling of multiple scattering of quanta within a CsPbBr3 crystal are used. It should be noted that the fraction of scattered quanta increases with decreasing energy of the incident quanta. When the photon energy Eγ increases such that $E_\gamma \gg 0.1$ MeV, the angular distribution becomes dominated by forward Compton scattering, as is evident in Fig. 2 for $E_\gamma =$ 0.1 MeV. Therefore, the effect of induced emission of gamma quanta can be considered "free" of scattered quanta from the direct flux.

In comparison with traditional CdZnTe and $LaBr_3$(Ce) detectors, the proposed $CsPbBr_3$ configuration provides the same or even better energy resolution (~1–2% FWHM at 662 keV) and higher detection efficiency in the 0.511–5 MeV range due to active capture of annihilation photons and operation at room temperature without cryogenic cooling. $CsPbBr_3$ crystals are inexpensive and readily available, and their composite geometry (central and side crystals) allows for efficient detection of 511 keV photons, eliminating escape peaks and expanding the measurable energy range. Thus, this design combines the resolution of semiconductors, the efficiency of scintillators, and low cost, representing a new generation of compact gamma spectrographs. The maximum permissible flux of gamma quanta is limited to approximately $10^6 \text{см}^{-2} s^{-1}$. At this level, the detection system is unable to fully relax to its initial state between successive events. To calculate the response curve of $CsPbBr_3$ and predict the pulse shape generated by individual gamma or X-ray quanta, we employed the open-source Geant4-DNA v11.2 simulation toolkit (Incerti et al., 2010), as utilized during participation in the International Geant4 School, Pavia, Italy (January 11–19, 2024).The trajectory of each quantum within the $CsPbBr_3$ crystal is governed by its chemical structure and by fundamental processes such as absorption, scattering, and pair production. The Monte Carlo method implemented in Geant4 regulates the elementary interactions of photoabsorption, Compton and Rayleigh scattering, and electron–positron pair creation. The absorbed dose – resulting from both the primary quanta and the secondary photons and particles they generate – forms a current pulse in both the primary and secondary detectors. According to the performed calculations, the amplitude and shape of the current pulse within the principal operational range of radiation fluxes exhibit a linear dependence on the absorbed dose. The proposed combined detector allows separate construction of spectra for primary and secondary radiation components. Solving this problem by alternative analytical methods is practically impossible.

6. Conclusion

The gamma spectrograph for induced radiation has made it possible to broaden the range of applied tasks. This work proposed new configurations, structural elements, and physical principles that allow the exploitation of detectors composed of atoms with high atomic weights. The absence of a need for deep cooling and the commercial availability of $CsPbBr_3$ crystals make their mass production feasible and enable their wide implementation in nuclear medicine and geophysics. A complete set of simulations of the expected parameters of the developed detectors was carried out with the goal of fabricating a prototype. Critical operating modes were determined, and the system response in the form of current pulses was calculated—data necessary for the design of the electronic interface.

Acknowledgment. The author expresses sincere gratitude to Senior Researcher of INFN Luciano Pandola for his support of the present work, to Prof. V. Ya. Gotsulski for his critical remarks, to Prof. Slavi Ljubomirov (Plovdiv University, Bulgaria), and to Prof. Dmitri Doikov (Department of Physics, Medical Laboratory, Medical Center Tzafon, Poria, Israel) for their guidance and supervision of the study.

References

Doikov M.: 2022, *OAP*, **35**, 24. DOI: 10.18524/1810-4215.2022.35.268000

Doikov M.: 2023, *OAP*, **36**, 42. DOI: 10.18524/1810-4215.2023.36.290774

Incerti S. et al.: 2010, *IntJModSimulSciCom*, **01**, 02, 157. https://doi.org/10.1142/S179396231000012

Liu Fangze et al.: 2022, *ACSEnL*, **7**, 1066. https://doi.org/10.1021/acsenergylett.2c00031

López Carlos A. et al.: 2020, *ACSOmega*, **5**, **11**, 5931. DOI: 10.1021/acsomega.9b04248.

Weber G. https://web-docs.gsi.de/~stoe_exp/web_programs/x_ray_absorption/index.php

Zhang Huan, Zhou YouHe: 2020, *NatCo*, 11, id. 5072 https://www.nature.com/articles/s 41467020187590

https://doi.org/10.18524/1810-4215.2025.38.340259

SINGULARITIES AND THEIR CROSSING IN GRAVITY AND COSMOLOGY

A. Yu. Kamenshchik

Department of Physics and Astronomy "Augusto Righi", University of Bologna, National Istitute for Nuclear Physics, Bologna, Italy, *kamenshchik@bo.infn.it*

ABSTRACT. We discuss the problem of singularity crossing in isotropic and anisotropic universes. First, we consider the so called soft or sudden singularities and, in particular the Big Brake singularity. This singularity was discovered in a particular tachyon cosmological model and it was also shown that this kind of singularity arises in a very simple model, where matter is represented by the anti-Chaplygin gas. At the encounter with the Big Brake singularity the universe has a finite scale factor, a vanishing expansion velocity and an infinite deceleration. The Christoffel symbols also vanish the geodesics are regular and the universe easily can cross such a singularity. Adding to the anti-Chaplygin gas or to the tachyon matter some amount of dust we see that the Big Brake singularity is substituted by a more general soft singularity, its crossing implies a certain transformation of the properties of matter. The crossing of the Big Bang – Big Crunch singularity is more counter-intuitive. However, we describe it for both Friedmann universe and Bianchi-I universe using the field reparametrization of the variables present in models (a scalar field and the metric). Then we consider the Wheeler-DeWitt equation and show that the probability for the universe to find itself at the soft singularity is different from zero, while the encounter with the Big Bang – Big Crunch singularity is suppressed. We analyze the possibility to construct Fock spaces of quantum particles at the vicinity of different cosmological singularities and see when it is possible and when it is not possible. Finally, we present some attempts to develop general approach to the connection between the field reparametrization and the elimination of singularities.

Keywords: gravitation; cosmology; singularities.

АНОТАЦІЯ. Ми обговорюємо проблему перетину сингулярності в ізотропних та анізотропних всесвітах. Спочатку ми розглянемо так звані м'які або раптові сингулярності та, зокрема, сингулярність Великого Гальма. Ця сингулярність була виявлена в певній тахіонній космологічній моделі, і було також показано, що цей тип сингулярності виникає в дуже простій моделі, де матерія представлена античаплигінським газом. При зіткненні з сингулярністю Великого Гальма Всесвіт має скінченний масштабний коефіцієнт, зникаючу швидкість розширення та нескінченне уповільнення. Символи Крістоффеля також зникають, геодезичні є регулярними, і Всесвіт може легко перетнути таку сингулярність. Додаючи до античаплигінського газу або тахіонної матерії певну кількість пилу, ми бачимо, що сингулярність Великого Гальма замінюється більш загальною м'якою сингулярністю, її перетин передбачає певну трансформацію властивостей матерії. Перетин сингулярності Великого Вибуху – Великого Стиснення є більш контрінтуїтивним. Однак, ми описуємо це як для Всесвіту Фрідмана, так і для Всесвіту Б'янкі-I, використовуючи репараметризацію поля змінних, присутніх у моделях (скалярне поле та метрика). Потім ми розглядаємо рівняння Уілера-Девітта і показуємо, що ймовірність того, що Всесвіт опиниться в м'якій сингулярності, відрізняється від нуля, тоді як зустріч із сингулярністю Великого вибуху – Великого стиснення виключається. Ми аналізуємо можливість побудови просторів Фока квантових частинок поблизу різних космологічних сингулярностей та бачимо, коли це можливо, а коли ні. Нарешті, ми представляємо деякі спроби розробити загальний підхід до зв'язку між репараметризацією поля та усуненням сингулярностей.

Ключові слова: гравітація; космологія; сингулярність.

1. Introduction

Appearance of singularities is one of the most important phenomena in General Relativity and in its generalizations and modifications. The singularities were first discovered in such simple geometries as those of Friedmann and Schwarzschild and later their general character was established in (Penrose, 1965; Hawk-

ing, 1966; Gorini et al., 2004). The investigation of the oscillatory approach to the cosmological singularity (Belinsky, Khalatnikov & Lifshitz, 1970) known also as Mixmaster universe (Misner, 1969) has opened the way to the birth of a new branches of the mathematical physics – chaotic cosmology (Khalatnikov, Lifshitz, Khanin et al., 1985) and its relation tohyperbolic Kac-Moody algebras (Damour, Henneaux & Nicolai, 2003).

While some researchers try to exclude cosmological singularities and singularities hidden inside black holes, constructing some involved models, the idea that the singularities are not a drawback of the General Relativity but is natural and fundamental feature becomes more popular during new millennium. Remarkably this idea was advocated by Misner (Misner, 1969a) as early as in 1969. Let us give some direct citations from his enchanting paper.

"I prefer a more optimistic viewpoint ("Nature and Einstein are subtle but tolerant") which views the initial singularity in cosmological theory not as a proof of our ignorance, but as a source from which we can derive much valuable understanding of cosmology."

"Thus, while I presume that relativity, like other physical theories, will be improved from time to time, I do not see that these changes need bear directly on the problem of cosmological singularity."

"We should stretch our minds, find some more acceptable set of words to describe the mathematical situation, now identified as "singular", and then proceed to incorporate this singularity into our physical thinking until observational difficulties force revision on us."

"The concept of a true initial singularity (as distinct from an indescribable early era at extravagant but finite high densities and temperatures) can be a positive and useful element in cosmological theory.

The Universe is meaningfully infinitely old because infinitely many things have happened since the beginning."

Inspired by this spirit of treatment of the singularities as something natural, one can try to study the opportunity to cross them. In this paper, based on my talk at the XXV Gamov International Astronomical Conference, I shall review different aspects of the singularity crossing in gravity and cosmology. The structure of the paper is the following: the second section is devoted to the description of the so called soft or sudden singularities; in the third section we treat the more traditional Big Bang – Big Crunch singularity; the fourth section is devoted to quantum cosmology; in the fifth section we discuss what happens with quantum particles at the singularity crossing; in the sixth section we describe attempts to develop a general approach to the description of the singularity crossing; the last section contains conclusive remarks.

2. The Big Brake cosmological singularity, more general soft singularities and their crossing

We start this section with the consideration of a very particular toy model (Gorini, Kamenshchik, Moschella et al., 2004). A flat Friedmann universe with the metric

$$ds^2 = dt^2 - a^2(t)dl^2$$

is driven by the so called tachyon field (Sen 2002) with the Lagrange density

$$L = -V(T)\sqrt{1-\dot{T}^2}.$$

The energy density is

$$\rho = \frac{V(T)}{\sqrt{1-\dot{T}^2}},$$

the pressure is

$$p = -V(T)\sqrt{1-\dot{T}^2}.$$

The Friedmann equation has the following form:

$$H^2 \equiv \frac{\dot{a}^2}{a^2} = \rho.$$

The equation of motion for the tachyon field is

$$\frac{\ddot{T}}{1-\dot{T}^2} + 3H\dot{T} + \frac{V_{,T}}{V} = 0.$$

In our model the potential is

$$V(T) = \frac{\Lambda}{\sin^2\left[\frac{3}{2}\sqrt{\Lambda\,(1+k)}\;T\right]} \times\sqrt{1-(1+k)\cos^2\left[\frac{3}{2}\sqrt{\Lambda\,(1+k)}\,T\right]}\;,$$

where k and $\Lambda > 0$ are the parameters of the model. The case $k > 0$ is more interesting. Indeed, in this case some trajectories (cosmological evolutions) finish in an infinite de Sitter expansion. In other trajectories the tachyon field transforms into a pseudotachyon field with the Lagrange density, energy density and positive pressure (Gorini et al., 2004):

$$L = W(T)\sqrt{\dot{T}^2-1},$$
$$\rho = \frac{W(T)}{\sqrt{\dot{T}^2-1}},$$
$$p = W(T)\sqrt{\dot{T}^2-1},$$
$$W(T) = \frac{\Lambda}{\sin^2\left[\frac{3}{2}\sqrt{\Lambda\,(1+k)}\;T\right]} \times\sqrt{(1+k)\cos^2\left[\frac{3}{2}\sqrt{\Lambda\,(1+k)}\,T-1\right]}$$

What happens to the Universe after the transformation of the tachyon into the pseudotachyon ? It encounters the Big Brake cosmological singularity.

The Big Brake cosmological singularity has the following characteristics:

$$t \to t_{BB} < \infty,$$

$$a(t \to t_{BB}) \to a_{BB} < \infty,$$

$$\dot{a}(t \to t_{BB}) \to 0,$$

$$\ddot{a}(t \to t_{BB}) \to -\infty,$$

$$R(t \to t_{BB}) \to +\infty,$$

$$\rho(t \to t_{BB}) \to 0,$$

$$p(t \to t_{BB}) \to +\infty.$$

If $\dot{a}(t_{BB}) \neq 0$ it is a more general soft singularity.

At the Big Brake singularity the equations for geodesics are regular, because the Christoffel symbols are regular (moreover, they are equal to zero). We can ask ourselves if it is possible to cross the Big Brake singularity (Gorini et al., 2004). Let us study the regime of approaching to the Big Brake. On analyzing the equations of motion we find that on approaching the Big Brake singularity the tachyon field behaves as

$$T = T_{BB} + \left(\frac{4}{3W(T_{BB})}\right)^{1/3} (t_{BB} - t)^{1/3}.$$

Its time derivative $s \equiv \dot{T}$ behaves as

$$s = -\left(\frac{4}{81W(T_{BB})}\right)^{1/3} (t_{BB} - t)^{-2/3},$$

the cosmological radius is

$$a = a_{BB} - \frac{3}{4} a_{BB} \left(\frac{9W^2(T_{BB})}{2}\right)^{1/3} (t_{BB} - t)^{4/3},$$

its time derivative is

$$\dot{a} = a_{BB} \left(\frac{9W^2(T_{BB})}{2}\right)^{1/3} (t_{BB} - t)^{1/3},$$

and the Hubble variable is

$$H = \left(\frac{9W^2(T_{BB})}{2}\right)^{1/3} (t_{BB} - t)^{1/3}.$$

All these expressions can be continued into the region where $t > t_{BB}$, which amounts to crossing the Big Brake singularity. Only the expression for s is singular at $t = t_{BB}$ but this singularity is integrable and not dangerous.

Once reaching the Big Brake, it is impossible for the system to stay there because of the infinite deceleration, which eventually leads to a decrease of the scale factor. This is because after the Big Brake crossing the time derivative of the cosmological radius and Hubble variable change their signs. The expansion is then followed by a contraction, culminating in the Big Crunch singularity.

One of the simplest cosmological models revealing a Big Brake singularity is the model based on the anti-Chaplygin gas with an equation of state

$$p = \frac{A}{\rho}, \quad A > 0.$$

Such an equation of state arises in the theory of wiggly strings (Carter, 1989; Vilenkin, 1990). Here

$$\rho(a) = \sqrt{\frac{B}{a^6} - A}.$$

At $a = a_* = \left(\frac{B}{A}\right)^{1/6}$ the universe encounters the Big Brake singularity.

What happens in a universe filled with an anti-Chaplygin gas and dust (Keresztes et al., 2013; Gorini et al., 2004)? The energy density and the pressure are

$$\rho(a) = \sqrt{\frac{B}{a^6} - A} + \frac{M}{a^3}, \quad p(a) = \frac{A}{\sqrt{\frac{B}{a^6} - A}}.$$

Due to the dust component, the Hubble parameter has a non-zero value at the encounter with the singularity, therefore the dust implies further expansion. However, with continued expansion however, the energy density and the pressure of the anti-Chaplygin gas would become ill-defined. The abrupt transition from the expansion to the contraction of the universe does not look natural. One can try to change the equation of state of the anti-Chaplygin gas on passing the soft singularity. There is some analogy between the transition from an expansion to a contraction of a universe and the perfectly elastic bounce of a ball from a wall in classical mechanics. There is also an abrupt change of the direction of the velocity (momentum). However, we know that in reality the velocity is changed continuously due to the deformation of the ball and of the wall. The pressure of the anti-Chaplygin gas

$$p = \frac{A}{\sqrt{\frac{B}{a^6} - A}}$$

tends to $+\infty$ when the universe approaches the soft singularity. Requiring the expansion to continue into the region $a > a_S$, while changing minimally the equation of state, we assume

$$p = \frac{A}{\sqrt{|\frac{B}{a^6} - A|}},$$

$$p = \frac{A}{\sqrt{A - \frac{B}{a^6}}}, \text{ for } a > a_S.$$

This implies the energy density

$$\rho = -\sqrt{A - \frac{B}{a^6}}.$$

The anti-Chaplygin gas transforms itself into Chaplygin gas with negative energy density. The pressure remains positive, expansion continues. The spacetime geometry remains continuous. The expansion stops at $a = a_0$, where

$$\frac{M}{a_0^3} - \sqrt{A - \frac{B}{a_0^6}} = 0.$$

Then the contraction of the universe begins. At the moment when the energy density of the Chaplygin gas becomes equal to zero (again a soft singularity), the Chaplygin gas transforms itself into the anti-Chaplygin gas and the contraction continues culminating in an encounter with the Big Crunch singularity. Analogous effects arise in the model with the tachyon field and dust. The Lagrangian of the Born-Infeld like field changes its form.

We conclude this section by mentioning that the soft (sudden) cosmological singularities were firstly studied in (Barrow, Galloway & Tipler 1986). The conditions of the singularity crossing were studied in (Fernandez-Jambrina & Lazkoz 2004). Interesting tachyon cosmological models were suggested in (Feinstein 2002) and (Padmanabhan 2002).

3. Big Bang – Big Crunch singularity crossing

The idea that the Big Bang – Big Crunch singularity can be crossed appears very counterintuitive (Gorini et al., 2004). Some approaches to the description of this crossing were elaborated during the last two decades (Bars et al., 2012; Wetterich, 2014; Dominis Prester, 2016). There is an analogy with the horizon which arises due to a certain choice of the spacetime coordinates: the singularity arises because of some choice of the field parametrization. On choosing some convenient field parametrization one can provide a matching between the characteristics of the universe before and after the singularity crossing. One can trace an analogy to the Kruskal coordinates for the Schwarzschild metric. On choosing appropriate combinations of the field variables we can describe the passage through the Big Bang – Big Crunch singularity, but this does not mean that the presence of such a singularity is not essential. Indeed, extended objects cannot survive this passage.

Let us consider a flat Friedmann universe filled with a conformally coupled scalar field (Kamenshchik, Pozdeeva, Tronconi et al., 2016).

$$S = \int d^4x\sqrt{-g}\left[U(\sigma)R - \frac{1}{2}g^{\mu\nu}\sigma_{,\mu}\sigma_{,\nu} + V(\sigma)\right],$$

$$U(\sigma) = U_0 - \frac{1}{12}\sigma^2.$$

Let us apply the conformal transformation of the metric

$$g_{\mu\nu} = \frac{U_1}{U}\tilde{g}_{\mu\nu}.$$

A new scalar field ϕ is

$$\frac{d\phi}{d\sigma} = \frac{\sqrt{U_1(U + 3U'^2)}}{U} \Rightarrow \phi = \int \frac{\sqrt{U_1(U + 3U'^2)}}{U} d\sigma.$$

$$\phi = \sqrt{3U_1}\ln\left[\frac{\sqrt{12U_0} + \sigma}{\sqrt{12U_0} - \sigma}\right]$$

$$\sigma = \sqrt{12U_0}\tanh\left[\frac{\phi}{\sqrt{12U_1}}\right].$$

The action then becomes the action for a minimally coupled scalar field:

$$S = \int d^4x\sqrt{-\tilde{g}}\left[U_1 R(\tilde{g}) - \frac{1}{2}\tilde{g}^{\mu\nu}\phi_{,\mu}\phi_{,\nu} + W(\phi)\right],$$

$$W(\phi) = \frac{U_1^2 V(\sigma(\phi))}{U^2(\sigma(\phi))}.$$

This is called the transformation from the Jordan frame to the Einstein frame.

In a flat Friedmann universe

$$ds^2 = N^2 d\tau^2 - a^2 dl^2,$$

$$d\tilde{s}^2 = \tilde{N}^2 d\tau^2 - \tilde{a}^2 dl^2.$$

$$\tilde{N} = \sqrt{\frac{U}{U_1}}N,\ \tilde{a} = \sqrt{\frac{U}{U_1}}a,\ t = \int\sqrt{\frac{U_1}{U}}d\tilde{t},$$

where t and $\tilde{t}$ are the cosmic time parameters in the Jordan and the Einstein frames.

$$a = \tilde{a}\sqrt{\frac{U_1}{U_0}}\cosh\left(\frac{\phi}{\sqrt{12U_1}}\right).$$

In the vicinity of the singularity in the Einstein frame:

$$\tilde{a} \sim \tilde{t}^{\frac{1}{3}} \to 0, \text{ when } \tilde{t} \to 0.$$

However, in the Jordan frame one has

$$a \sim \tilde{t}^{\frac{1}{3}}\left(\tilde{t}^{\frac{1}{3}} + \tilde{t}^{-\frac{1}{3}}\right) \to \text{const} \neq 0.$$

Meanwhile, the scalar field σ crosses the value $\pm\sqrt{12U_0}$ and the coupling function U changes its sign. Thus, the evolution in the Jordan frame is regular, and we can use this fact to describe the crossing of the Big Bang – Big Crunch singularity in the Einstein frame. If one considers the expansion of the universe from the Big Bang with normal gravity driven by the standard scalar field, the continuation backward in time shows that it was preceded by the contraction towards a Big Crunch singularity in the antigravity regime, driven by a phantom scalar field with a negative kinetic term.

The possibility of a change of sign of the effective gravitational constant in the model with a conformably coupled scalar field was analyzed in (Starobinsky, 1981; Gorini et al., 2004). It was shown that in a homogeneous and isotropic universe, one can indeed cross the point where the effective gravitational constant changes sign. However, the presence of anisotropies changes the situation: these anisotropies grow indefinitely when this constant is equal to zero. To describe the Big Bang – Big Crunch singularity crossing in anisotropic universes it is necessary to use another methods. We have done it for the Bianchi-I universe (Kamenshchik, Pozdeeva, Tronconi et al 2017, Kamenshchik, Pozdeeva, Starobinsky et al., 2018). The idea was the following. Introducing the new "radial" variable

$$r \sim a^{3/2}$$

and treating the scalar field as an angular variable, we obtain an effective Lagrangian

$$L = \frac{1}{2}\dot{r}^2 - \frac{1}{2}r^2\dot{\phi}^2,$$

or, in Cartesian coordinates

$$L = \frac{1}{2}\dot{x}^2 - \frac{1}{2}\dot{y}^2.$$

Solving the equations of motion one can describe the singularity crossing. Introduction of the anisotropy factors for the Bianchi-I model is reduced to the modification of the kinetic term for the massless scalar field.

4. Quantum cosmology and singularities

Speaking about quantum cosmology and singularities people mean two different approaches. One can consider a modification of the Friedmann equation, taking into account the quantum corrections to the effective action of the theory:

$$\frac{\dot{a}^2}{a^2} + \frac{k}{a^2} = \rho_{\text{matter}} + \rho_{\text{quantum corrections}}.$$

One can hope that these correction change the dynamics of the universe evolution, implying an appearance of some kind of bounce and avoing an encounter with the singularity. Another approach is based on the study of the Wheeler-DeWitt equation and the prospective of vanishing of the quantum state of the universe at the singular configurations of the geometry (DeWitt 1967):

$$\Psi(\text{geometry} + \text{matter})_{\text{geometry is singular}} = 0.$$

The wave function of the Universe Ψ satisfies the Wheeler-DeWitt equation

$$\hat{\mathcal{H}}\Psi = 0,$$

where $\hat{\mathcal{H}}$ is the so called super-Hamiltonian. There are two major questions, concerning this equation. It looks like the very notion of time disappears here. Then, it is not clear how the notion of the probability can be determined. There is rather a vast literature devoted to treatment of these problems (see e.g. (Barvinsky 1993)). The general recipe for their treatment can be formulated as follows: a time can be defined as a certain function of geometrical variables. After that the wavefunction describing matter variables satisfies an effective Schrödinger equation. The singularity is associated with such values of the matter variables when this singularity arises in the classical theory. Our analysis of some simple models tells that the probability of the arising of soft singularities is not suppressed by the wave function of the universe (Kamenshchik, Kiefer & Sandhofer 2007, Kamenshchik and Manti 2012, Kamenshchik, Kiefer & Kwidzinski 2016). At the same time the probability of Big Bang – Big Crunch singularity tends to zero. The suppression of the Big Bang – Big Crunch singularity follows from the requirement of the normalizability of the wave function of the Universe (Barvinsky & Kamenshchik 1990). Indeed, we require that

$$\int d\phi \bar{\Psi}(\phi)\Psi(\phi) < \infty,$$

where ϕ is a scalar field, driving the evolution of the universe. When $|\phi| \to \infty$, the probability density $\bar{\Psi}\Psi$ should tend to zero rapidly. If $|\phi| \to \infty$ corresponds to Big Bang – Big Crunch singularity, when this singularity is suppressed.

5. Particles, fields and singularities

We can ask ourselves what happens with particles (in quantum field theoretical sense) when the universe passes through the cosmological singularity (Galkina & Kamenshchik 2020). We consider only particles connected with a scalar field. The scalar field in the flat Friedmann universe satisfies the Klein-Gordon equation:

$$\Delta\phi + V'(\phi) = 0,$$

where Δ is the D'Alambert operator. One can consider a spatially homogeneous solution of this equation ϕ_0, depending only on time t as a classical background. A small deviation from this background solution can be represented as a sum of Fourier harmonics satisfying linearized equations

$$\ddot{\phi}(\vec{k},t) + 3\frac{\dot{a}}{a}\dot{\phi}(\vec{k},t) + \frac{\vec{k}^2}{a^2}\phi(\vec{k},(t)) + V''(\phi_0(t))\phi(\vec{k},(t)) = 0.$$

The corresponding quantized field is

$$\hat{\phi}(\vec{x},t) = \int d^3\vec{k}(\hat{a}(\vec{k})u(k,t)e^{i\vec{k}\cdot\vec{x}} + \hat{a}^+(\vec{k})u^*(k,t)e^{-i\vec{k}\cdot\vec{x}}),$$

where the creation and the annihilation operators satisfy the standard commutation relations:

$$[\hat{a}(\vec{k}), \hat{a}^+(\vec{k}')] = \delta(\vec{k} - \vec{k}').$$

The basis functions should be normalized so that the canonical commutation relations between the field ϕ and its canonically conjugate momentum $\hat{\mathcal{P}}$ were satisfied

$$[\hat{\phi}(\vec{x},t), \hat{\mathcal{P}}(\vec{y},t')] = i\delta(\vec{x} - \vec{y}).$$

$$u(k,t)\dot{u}^*(k,t) - u^*(k,t)\dot{u}(k,t) = \frac{i}{(2\pi)^3 a^3(t)}.$$

The linearized Klein-Gordon equation has two independent solutions. To define a particle it is necessary to have two independent non-singular solutions. It is a non-trivial requirement in the situations when a singularity or other kind of irregularity of the spacetime geometry occurs. It is convenient also to construct explicitly the vacuum state for quantum particles as a Gaussian function of the corresponding variable. Let us introduce an operator

$$\hat{f}(\vec{k},t) = (2\pi)^3(\hat{a}(\vec{k})u(k,t) + \hat{a}^+(-\vec{k})u^*(k,t)).$$

Its canonically conjugate momentum is

$$\hat{p}(\vec{k},t) = a^3(t)(2\pi)^3(\hat{a}(\vec{k})\dot{u}(k,t) + \hat{a}^+(-\vec{k})\dot{u}^*(k,t)).$$

We can express the annihilation operator as

$$\hat{a}(\vec{k}) = i\hat{p}(\vec{k},t)u^*(k,t) - ia^3(t)\hat{f}(\vec{k},t)\dot{u}^+(k,t).$$

Representing the operators $\hat{f}$ and $\hat{p}$ as

$$\hat{f} \to f, \quad \hat{p} \to -i\frac{d}{df},$$

one can write down the equation for the corresponding vacuum state in the following form:

$$\left(u^*\frac{d}{df} - ia^3\dot{u}^* f\right)\Psi_0(f) = 0.$$

Its solution is

$$\Psi_0(f) = \frac{1}{\sqrt{|u(k,t)|}}\exp\left(\frac{ia^3(t)\dot{u}^*(k,t)f^2}{2u^*(k,t)}\right).$$

In the case of the Big Bang – Big Crunch singularity, one of the basis functions in the vicinity of the singularity becomes singular and it is impossible to construct a Fock space. In the case of the Big Rip singularity, when in finite interval of time the universe achieves an infinite volume and infinite time derivative of the scale factor, the Fock space can be constructed for a spectator scalar field, but it does not exist for the phantom scalar field driving the expansion. In the case of the model with tachyon field, presented above, we have considered three situations. First of them is the non-singular transformation of the tachyon into pseudo-tachyon. In this case both the basis functions are regular and hence the operators of creation and annihilation are well defined. However, at the moment of the transformation the dispersion of the Gaussian wave function of the vacuum becomes infinite and then becomes finite again. In the vicinity of the Big Brake singularity it is impossible to define a Fock vacuum. However, if we add to the universe dust, the character of the soft singularity is slightly changed and then the presence of the Fock vacuum is restored.

6. Covariant approach to singularities

We have already told that the crossing of the Big Bang – Big Crunch singularities looks rather counterintuitive. However, it can be sometimes described by using the reparametrization of fields, including the metric. One can say that to do this, it is necessary to resort to one of two ideas, or a combination thereof. One of these ideas is to employ a reparameterization of the field variables which makes the singular geometrical invariant non-singular. Another idea is to find such a parameterization of the fields, including, naturally, the metric, that gives enough information to describe consistently the crossing of the singularity even if some of the curvature invariants diverge. The application of these ideas looks in a way as a craftsman work. Our goal was to develop a general formalism to distinguish "dangerous" and "non-dangerous" singularities, considering the field variable space of the model under consideration. In other words, we try to understand when the spacetime singularities can be removed by a reparametrization of the field variables (Casadio, Kamenshchik & Kuntz, 2021; Casadio, Kamenshchik & Kuntz, 2022; Kuntz, Casadio & Kamenshchik, 2022).

Our hypothesis was the following: when the geometry of the space of the field variables is non-singular, one can describe the singularity crossing. The field space $\mathcal{S}$ was developed in order to treat on the same (geometrical) footing both changes of coordinates in

the spacetime $\mathcal{M}$ and field redefinitions in the functional approach to quantum field theory (Vilkovisky, 1984; DeWitt, 1987).

This approach requires introducing a local metric G in field space $\mathcal{S}$ and computing the associated geometric scalars by defining a covariant derivative which is compatible with G. G is actually determined by the kinetic part of the action and its dimension depends on the field content of the latter. After some cumbersome calculations in the functional space, we have shown that the Kretschmann scalar

$$\mathcal{K} = \mathcal{R}_{ABCD}\,\mathcal{R}^{ABCD}$$

is finite in every theory of pure gravity

$$\mathcal{K} = \frac{n}{8}\left(\frac{n^3}{4} + \frac{3n^2}{4} - 1\right),$$

where n is the spacetime dimension. It can be interpreted as a statement that all the singularities in empty universe can be crossed.

We have considered also another hypothesis connected to quantum effective action and to the homotopy group. Let us introduce the functional

$$\psi[\varphi] = e^{i\,\Gamma[\varphi]},$$

where $\Gamma[\varphi]$ is the effective action. We shall call $\psi[\varphi]$ the functional order parameter because ψ plays the analogous role to the order parameter in the theory of phase transitions in ordered media or cosmology.

The field space $\mathcal{M}$ can be thought of as the ordered medium itself, whereas functional singularities correspond to topological defects.

The functional order parameter ψ defines the map

$$\psi : \mathcal{M} \to S^1,$$

from the field space to the unit circle, the latter playing the role of the order parameter space. The singularities can be characterized by the fundamental group (first homotopy group). If this group is trivial the singularity can be removed. We have checked on the example of some simple systems with removable singularity that the corresponding homotopy group is indeed trivial.

7. Conclusions

In this paper we have tried to present some arguments and results telling that the appearance of the singularities in the cosmological and other gravitational systems is not drawback of models or theories but is instead their distinguishing feature. Thus, to our mind rather than avoid singularities, it is better to study how their presence influences the non-singular quantities (just like in quantum field theory). Further details and references can be found in the review papers (Gorini et al., 2004; Kamenshchik, 2013; Kamenshchik, 2018; Kamenshchik, 2024).

Acknowledgements. The author is thankful to the organizers of the XXV Gamov International Astronomical Conference for their kind invitation to give a talk.

References

Barrow J.D., Galloway J.G. & Tipler F.J.: 1986, *Mon. Not. R. Astron. Soc.,* **223**, 835.

Bars I., Chen S.H., Steinhardt P.J. et al.: 2012, *Phys. Lett. B,* 715, 278.

Barvinsky A.O.: 1993, *Phys. Rep.,* **230**, 237.

Barvinsky A.O. & Kamenshchik A.Yu.: 1990, *Class. Quantum Grav.,* **7**, L181.

Belinsky V.A., Khalatnikov I.M. & Lifshitz E.M.: 1970, *Adv. Phys.,* **19**, 525.

Carter B.: 1989, *Phys. Lett. B,* **224**, 61.

Casadio R., Kamenshchik A. & Kuntz I.: 2021, *Nucl. Phys. B,* **971**, 115496.

Casadio R., Kamenshchik A. & Kuntz I.: 2022, *Int. J. Mod. Phys. D,* **31** 01, 2150130.

Damour T., Henneaux, M. & Nicolai H.: 2003, *Class. Quantum Grav.,* **20**, R 145.

DeWitt B.S.: 1967, *Phys. Rev.,* **160**, 1113.

DeWitt B.S.: 1987, in Quantum field theory and quantum statistics: essays in honour of sixteeth birthday of E. S. Fradkin, eds. I. A. Batalin, C. J. Isham and G. A. Vilkovisky. Adam Hilger, Bristol, UK.

Dominis Prester P.: 2016, *Adv. Math. Phys.,* **2016**, 6095236.

Feinstein A.: 2002, *Phys. Rev. D,* **66**, 063511.

Fernandez-Jambrina, L. & Lazkoz, R.: 2004, *Phys. Rev. D,* **70**, 121503.

Galkina O. & Kamenshchik A.Yu.: 2020, *Phys. Rev. D,* **102**, 2, 024078.

Gorini V., Kamenshchik A.Y., Moschella U. et al.: 2004, *Phys. Rev. D,* **69**, 123512.

Hawking S.W.: 1966, *Phys. Rev. Lett.,* **17**, 444.

Kamenshchik A.Y.: 2013, *Class. Quantum Grav., 30*, 173001.

Kamenshchik A.Yu.: 2018, *Found. Phys.,* **48**, 10, 1159.

Kamenshchik A.: 2024, *Gen. Relat. Grav.,* **56**, 11, 133.

Kamenshchik A.Yu., Kiefer C. & Sandhofer B.: 2007, *Phys. Rev. D,* **76**, 064032.

Kamenshchik A.Yu. & Manti S.: 2012, *Phys. Rev. D,* **85**, 123518.

Kamenshchik A., Kiefer C. & Kwidzinski N.: 2016, *Phys. Rev. D,* **93**, 8, 083519.

Kamenshchik A.Yu., Pozdeeva E.O., Tronconi A. et al.: 2016, *Phys. Rev. D,* **94**, 063510.

Kamenshchik A.Y., Pozdeeva E.O., Vernov S.Y. et al.: 2017, *Phys. Rev. D,* **95**, 083503.
Kamenshchik A.Y., Pozdeeva E.O., Starobinsky A.A. et al.: 2018, *Phys. Rev. D,* **97**, 2, 023536.
Keresztes Z., Gergely, L.A., Kamenshchik A.Yu. et al.: 2013, *Phys. Rev. D,* **88**, 023535.
Khalatnikov I.M., Lifshitz E.M., Khanin K.M. et al.: 1985, *J. Stat. Phys.,* **38**, 97.
Kuntz I., Casadio R. & Kamenshchik A.: 2022, *Mod. Phys. Lett. A,* **37**, 10, 2230007.
Misner C.W.: 1969, *Phys. Rev. Lett.,* **22**, 1071.
Misner C.W.: 1969a, *Phys. Rev.,* **186**, 1328.
Padmanabhan P.: 2002, *Phys. Rev. D,* **66**, 021301.
Penrose R.: 1965, *Phys. Rev. Lett.,* **14**, 57.
Sen A.: 2002, *JHEP,* **04**, 048.
Starobinsky A.A.: 1981, *Sov. Astron. Lett.,* **7**, 36.
Vilenkin A.: 1990, *Phys. Rev. D,* **41**, 3038.
Vilkovisky G.A.: 1984, *Nucl. Phys. B,* **234**, 125.
Wetterich C.: 2014, *Phys. Rev. D,* **89**, 024005.

https://doi.org/10.18524/1810-4215.2025.38.343162

USING CLUSTER CARTOGRAPHY 2D+ FOR DETECTING SUBSTRUCTURES IN THE 3D GALAXY CLUSTERS

E. A. Panko[1], S. I. Yemelianov[2], D. O. Lavreniuk[1]

[1] Odesa I. I. Mechnikov National University, Odesa, Ukraine, *panko.elena@gmail.com*
[2] Mykolaiv National Agrarian University, Mykolaiv, Ukraine, *sviatoslavem@gmail.com*

ABSTRACT. In our detailed study of the inner structure of PF galaxy clusters, we found different kinds of substructures in these objects. Most of the detected substructures are quite common. In addition to the classical filamentary features described by Rood and coauthors' papers, we include complex cross-shaped substructures and short dense chains of galaxies as regular. We suppose that regular substructures are connected with the Large-Scale Structure of the Universe elements, which form the parent cluster node. Our previous studies were based on the list of galaxies of the Muenster Red Sky Survey, which has no redshifts. It allowed us to study only the 2D distribution of galaxies inside the cluster. Modern data, such as the Sloan Digital Sky Survey, the VIMOS Public Extragalactic Redshift Survey, the Euclid Wide Survey, and others, give us the opportunity for 3D studies of these objects.

We improved the base online version of the "Cluster Cartography 2D" tool (*https://clustercartography.github.io/*) into the "Cluster Cartography 2D+" tool. It allows to apply the algorithms developed for 2D version to the detection of regular substructures on a statistically significant level for the 3D distribution of galaxies in the rectangular projections. We tested this opportunity on artificial galaxy clusters with different kinds of substructures. We have shown that using 2D projections allows us to detect the 3D regular substructures, and to restore their real shapes and directions.

Keywords: Universe, LSC: galaxy clusters: morphology: inner structure, substructures; data analysis.

АНОТАЦІЯ. В наших попередніх роботах, що присвячені детальному дослідженню внутрішньої будови скупчень галактик каталогу PF, були виявлені різні види підструктур у цих об'єктах. Більшість виявлених підструктур зустрічаються досить часто. На додаток до класичних філаментарних особливостей, що були описані ще у статтях Руда та співавторів, ми включаємо до регулярних підструктур складні хрестоподібні утворення та короткі щільні ланцюжки галактик. Таки підструктури, скоріше за все, пов'язані з елементами Великомасштабної Структури Всесвіту, що формють вузол, в якому виникає скупчення галактик. Наше дослідження базувалося на списку галактик Мюнстерського огляду червоного неба (Muenster Red Sky Survey), який дозволяє нам вивчати лише 2D розподіл галактик всередині скупчення. Сучасні дані, такі як Sloan Digital Sky Survey, VIMOS Public Extragalactic Redshift Survey, Euclid Wide Survey та інші, дають можливість 3D досліджень для цих об'єктів.

Ми вдосконалили базову онлайн-версію програми Cluster Cartography (*https://clustercartography.github.io*) до 2D рівня Cluster Cartography 2D+. Це дозволяє застосовувати алгоритми, які було розроблено та протестовано у 2D версії, до виявлення регулярних субструктур на статистично значущому рівні для 3D розподілу галактик у прямокутних проекціях. Ми перевірили ці можливості на штучних скупченнях галактик з різними видами субструктур. Ми показали, що використання 2D проекцій дозволяє нам виявляти 3D регулярні підструктури та відновлювати їх реальні форми та орієнтації.

Ключові слова: Всесвіт, Великомасштабна структура: скупчення галактик: морфологія: внутрішня будова, субструктури; аналіз даних.

1. Introduction

The elements of the Large Scale Structure of the Universe (LSS) evolve in interaction with its surroundings. The co-evolution of LSS elements was established in the base theoretical works like Silk (1968), Peebles (1969), Peebles & Yu (1970), Zeldovich (1970), and most recently. The initial fluctuations of the density and Hubble flow produce the different variants

of expansion/contraction: 3D contraction gives spherical or ellipsoidal structures, 2D leads to filaments, and the walls are formed due to 1D contraction. According to modern scenarios, the evolution of the elements of LSS occurs in interaction with its surroundings. This co-evolution of LSS elements was established in the base theoretical works like Silk (1968), Peebles (1969), Peebles & Yu (1970), Zeldovich (1970), and most recently. The initial fluctuations of the density and Hubble flow produce the different variants of expansion/contraction: 3D contraction gives spherical or ellipsoidal structures, 2D leads to filaments, and the walls are formed due to 1D contraction. The numerical simulations from the first (Klypin & Shandarin, 1983) to the latest (Springel et al., 2005, Vogelsberger et al., 2014, Artale et al., 2017, Cui et al., 2018, Tomoaki et al., 2021) showed that the multi-speed expansion leads to the arising Cosmic web nodes in the crossing filaments and walls, and the largest LSS elements, such as galaxy clusters or superclusters, occur in the nodes of the cosmic web. It corresponds to the results of the observations (Wen et al., 2009, Dietrich et al., 2012, Parekh et al., 2020). Tracing the cosmic web in the densest nodes allows us to detail the constraints of the cosmological models. The number of filaments connected to a given node is attributed as the node connectivity or multiplicity. Theory and simulations show that connectivity and multiplicity can be expected to increase with node mass or environmental density (Aragón-Calvo et al., 2010, Codis et al., 2018, Gouin et al., 2021; Kraljic et al., 2022, Malavasi et al., 2023). In observations, connectivity multiplicity in relation to its mass, dynamical status, and galaxy population was explored at galaxy cluster scales in Sarron et al. (2019), Darragh Ford et al., (2019), Lee et al. (2019). Probably, the node's connectivity at galaxy cluster scales must manifest inside the cluster as corresponding substructures at the same stage of evolution according to Struble & Rood (1987).

Our previous research was directed to the study of substructures in galaxy clusters in fields with different densities, from the richest regions (Panko et al., 2021) to isolated galaxy clusters (Panko et al., 2022). In all cases, we detected the different kinds of regular substructures, such as linear ones from wide bands to thin filaments, crosses and semi-crosses, and short dense curve stripes in the 2D distribution of galaxies for PF galaxy clusters (Panko & Flin, 2006). Our approach was described in Panko (2025), and Yemelyanov & Panko (2021) papers. We detected substructures in the clusters, which are probably footprints of the filaments connected to the parent cluster node.

"Cluster Cartography 2D" tool, CC 2D further, https://clustercartography.github.io/ is used to study substructures on galaxy clusters for 2D input data. The improved "Cluster Cartography 2D+" tool, on the same web page, allows us to detect substructures in 3D data. In the paper, we discussed the perspectives of the improved tool for the 3D study of galaxy clusters, using a simulated distribution of galaxies in the cluster. In the future, the CC 2D+ tool can be used for modern data of the Sloan Digital Sky Survey (SDSS, York et al., 2000),, the VIMOS Public Extragalactic Redshift Survey (VIPERS, Scodeggio et al., 2018), or the Euclid Wide Survey (EWS, Euclid Collaboration: Scaramella et al., 2022).

2. "Cluster Cartography 2D+"

Web version of CC 2D tool contains functions for processing data, calculating statistics, and plotting maps, histograms, and graphics, which are built using different parameters, such as the radii and widths of the rings in determining the degree of the concentration to the center, the widths of the bands in determining of the degree of the concentration in the linear substructures, the presence of the Binggeli effect (Binggeli, 1982) both for all galaxies and separated substructures, etc. (Yemelyanov & Panko, 2021). We can search for the position of the greatest density of galaxies in the cluster field, detect the regular linear and cross-type substructures, study the rope of the brightest galaxies, and analyze the shape of the members of the cluster based on the algorithms described in Panko (2025) paper. We can also create a list of galaxies forming the regular substructures.

The difference in the CC 2D+ input file is the 3rd coordinate placed in the last column. All the capabilities of the CC 2D+ version was retained and can be used for various projections of 3D data. The RA and Dec data correspond to the X and Y coordinate axes, and the distance or redshift z corresponds to the Z axis. If we have no distance or need to analyze the 2D data, the last column is not considered.

In the CC 2D+, the RA and Dec coordinates of galaxies are shown as the projection of one from our test cluster onto the celestial sphere (Fig. 1*a*). The 2D+ tool allows us to create the 3D color map of the cluster, where the color of the symbol illustrates the galaxy distance from the cluster center. CC 2D+ gives the possibility to rotate the cluster and to create cluster maps in the other projections XZ and YZ, where Z is the distance/redshift of the galaxy (Fig. 1*b, c*). Thus, we can study the 3D distribution of galaxies in three rectangular projections: RA and Dec, RA and z, Dec. and z. The ability to rotate the cluster to an arbitrary angle also allows us to find the best orientation for visibility of the substructure. It is illustrated in Fig. 2. The initial view of the cluster is shown in Fig. 2*a*, while the turned cluster in Fig. 2*b* shows all linear elements of the compound cross.

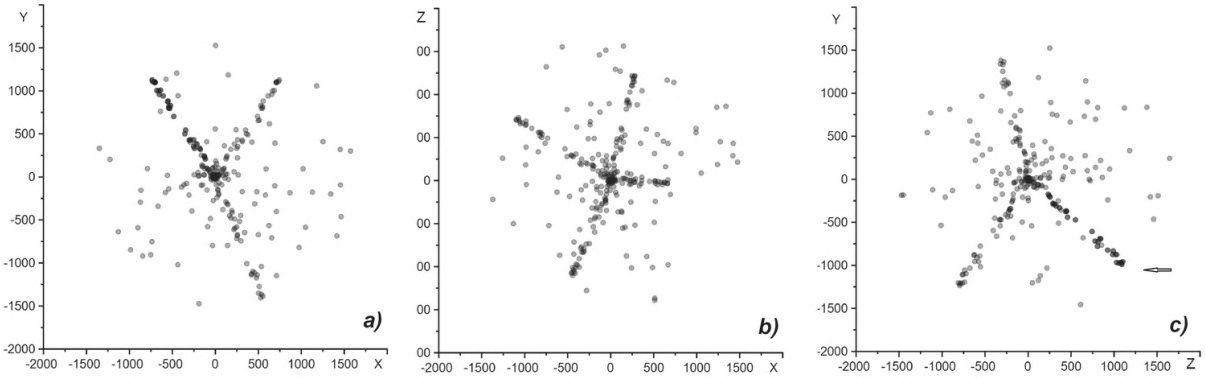

Figure 1: Artificial open cluster with 3D compound cross-type substructure in the different projections: *a*) for RA and Dec. axes, *b*) for RA and *z* axes, and *c*)for Dec. and *z* axes, arrow points to 2 stripes of the cross combined in Dec− *z* projection

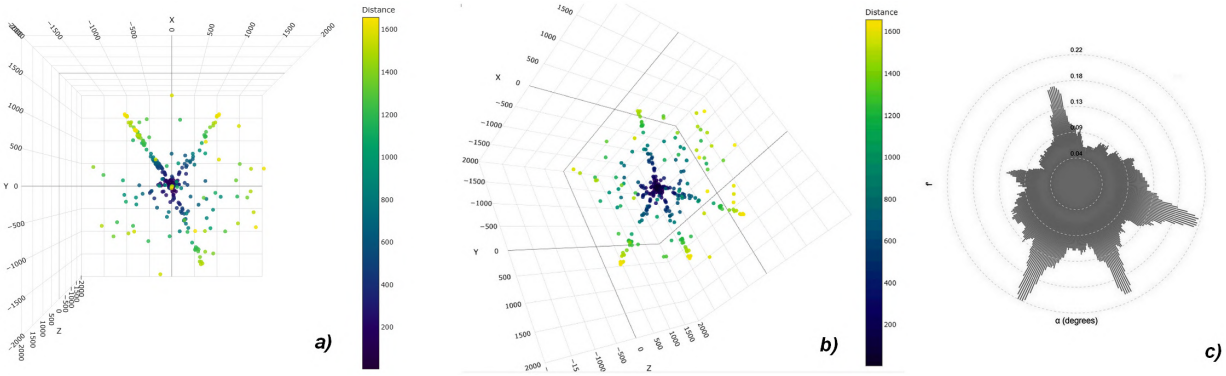

Figure 2: The 3D map of the artificial cluster with compound cross: *a*) initial view, *b*) turned map, all components of the compound cross are clearly seen, *c*) radial LightHouseBeam diagram fir the turned map

3. 3D substructures search discussion

For testing the CC 2D+ tool, we create a set of artificial galaxy clusters with different morphologies and substructure' types. We constructed the next types of distribution of galaxies:

- the cluster open type as a base element for the next steps;
- the cluster with the spherical or ellipsoidal core;
- the open cluster with the wall;
- the open cluster with the single filament;
- the open cluster having a compound 3D substructure cross-type.

All simulated features were constructed based on an open cluster with additional elements. The distributions of the galaxies in a thin wall or filaments were constructed using the Box - Miller transformation.

Obviously, the degree of concentration of galaxies toward the cluster center does not depend on the projection. Nevertheless, such clusters we must consider in the three projections for the estimation of the real core shape and orientation.

The filament inside the cluster looks like linear substructure in all projections, except for the case of special orientation: when the filament directs along the line of sight, it will be seen as a concentration towards the cluster center, and we obtain the false morphological classification as "Concentrated cluster". If the angle between the linear substructure and the line of sight is small, we detect it as a dense short chain. They are rare special cases. However, we must take into account these.

Another rare special case is the wall-type substructure, which is seen as a filament. But, in some projections, we can lose such a substructure in the background of other cluster members. The 2D+ tool allows us to rotate the 3D cluster map. It gives the possibility

of confident detection for all filaments and walls with visual control.

The last test artificial cluster with the compound cross connecting 4 different filaments, is shown in Fig. 1 in all projections. The some cross elements can be lost in projections, as in Fig 1*c*. The initial 3D color map of the test cluster is shown in Fig. 2*a*. It's like to RA–Dec. projection map (Fig. 1*a*). The optimal view of the substructure is shown in Fig. 2*b*, and the corresponding radial LightHouseBeam diagram is present in Fig. 2*c*. The diagram was created on the 2D projection of the rotated cluster. This diagram is the visualization of LightHouseBeam analysis, which shows all linear elements of the compound cross.

The reliability of the real substructures identification is confirmed by both the observed distribution of bright galaxies in the cluster and the alignment of galaxies relative to substructures in accordance with the work of Joachimi et al. (2015). For the PF clusters we have the 2D position and orientations for galaxies from Muenster Red sky Survey (Ungrue at al., 2003) Unfortunately, in 3D we have no space alignment of galaxies, even if we have the distances. So, in the 3D case, we can confirm the reliability of the substructure only by the brightest galaxies' positions.

The observational data for our further research can be selected in the NASA/IPAC Extragalactic Database (https://www.ipac.caltech.edu/project/ned, https://ned.ipac.caltech.edu/), where some PF Galaxy Clusters (Panko & Flin, 2006) are present too.

4. Conclusion

We created the "Cluster Cartography 2D+" tool, which allows the detection of regular substructures in 3D data for galaxy clusters. All types of substructures, such as planes, filaments, and complex crosses, can be detected in three projections: RA and Dec., RA and z, and Dec. and z, using corresponding well-tested algorithms. In the CC 2D+ tool, we can also create 3D maps and turn them for an arbitrary angle for the best visibility of the substructure. The CC 2D+ tool is advisable for estimating the central core shape and orientation, too. We plan to create the Spherical Density Chart (3D analog of the Polar Density Chart in LightHouseBeam analysis) and use our tool to study the galaxy clusters in modern 3D data.

Acknowledgments. The authors express their sincere gratitude to the independent referee, Dr. Dominique Proust, for helpful comments on our paper.

This research has made use of NASA's Astrophysics Data System. This research has made use of the NASA/IPAC Extragalactic Database, which is funded by the National Aeronautics and Space Administration and operated by the California Institute of Technology.

References

Aragón-Calvo M. A., van de Weygaert R. & Jones B. J. T.: 2010, *MNRAS*, **408**, 2163.
Binggeli B.: 1982, *A&A*, **107**, 338.
Codis S., Pogosyan D., & Pichon C.: 2018, *MNRAS*, **479**, 973.
Cui W., Knebe A., Yepes G., et al.: 2018, *MNRAS*, **473**, 68.
Darragh Ford E., Laigle C., Gozaliasl G., et al.: 2019, *MNRAS*, **489**, 5695.
Dietrich J. P., Werner N., Clowe D., et al.: 2012, *Nature*, **487**, 202.
Gouin C., Bonnaire T., & Aghanim N.: 2021, *A&A*, **651**, A56.
Joachimi B., Cacciato M., Kitching T. D., et al.: 2015, *Space Sci. Rev.*, **193**, 1.
Klypin A.A. & Shandarin S.F.: 1983, *MNRAS*, **204**, 891.
Kraljic K., Laigle C., Pichon C., et al.: 2022, *MNRAS*, **514**, 1359.
Lee S.-K., Im M., Hyun M., et al.: 2019, *MNRAS*, **490**, 135.
Malavasi N., Sorce J. G., Dolag K., & Aghanim N.: 2023, *A&A*, **675**, A76.
Panko E. A.: 2025, *Universe*, **11**, 7, id.238.
Panko E. A. & Flin P.: 2006, *J. Astron. Data*, **12**, 1.
Panko E., Yemelianov S., Korshunov V., et al.: 2021, *Astron. Rep.*, **65**, 1002.
Panko E. A., Yemelianov S., Sirginava A., & Pysarevskyi Z.: 2022, *ComBAO*, **69**, 256.
Parekh V., Lagana T. F., Tho K., et al.: 2020, *MNRAS*, **491**, 2605.
Peebles P.: 1969, *AJ*, **155**, 393.
Peebles P. J. E. & Yu J. T.: 1970, *ApJ*, **162**, 815.
Sarron F., Adami C., Durret F., & Laigle, C.: 2019, *A&A*, **632**, A49.
Scaramella R., Amiaux J., Mellier Y.,at al.: 2022, *A&A*, **662**, A112.
Scodeggio M., Guzzo L., Garilli B., et al.: 2018, *A&A*, **609**, A84.
Silk J.: 1968, *ApJ*, **151**, 459.
Springel V., White S. D., Jenkins A., et al.: 2005, *Nature*, **435**, 629.
Struble M. F. & Rood H. J.: 1987, *ApJSS*, **63**, 555.
Tomoaki A. A., Francisco P., Klypin A. A., et al.: 2021, *MNRAS*, **506**, 4210.
Ungrue R., Seitter W. C., Duerbeck H. W.: 2003, *J. Astron. Data*, **9**, 1.
Vogelsberger M., Genel S., Springel V., et al.: 2014, *MNRAS*, **444**, 1518.
Wen Z.L., Han J.L. & Liu A.C.: 2009, *ApJSS*, **183**, 197.
Yemelyanov S. I. & Panko E. A.: 2021, *OAP*, **34**, 35.
York D. G., Adelman J., Anderson John E. J., et al.: 2000, *AJ*, **120**, 1579.
Zeldovich Y. B.: 1970, *A&A*, **5**, 84.
Zeldovich Y., Einasto J. & Shandarin S.: 1982, *Nature*, **300**, 407.

https://doi.org/10.18524/1810-4215.2025.38.343163

UNISTELLAR EVSCOPE 2: TECHNICAL SPECIFICATIONS, USER COMMUNITY, AND PROSPECTS FOR APPLICATION

A. K. Pechko[1], E. A. Panko[2], V. V. Vasylchenko[3,4], N. P. Mirochnik[3,4]

[1] Odesa I. I. Mechnikov National University, Odesa, Ukraine, *pechko.anastasi@stud.onu.edu.ua*
[2] Odesa I. I. Mechnikov National University, Odesa, Ukraine, *panko.elena@gmail.com*
[3] Anatolii Lyhun Scientific Lyceum of Kamianske City Council, Kamianske, Dnipropetrovsk region, Ukraine
[4] National Centre "Junior Academy of Sciences", under the auspices of UNESCO, Kamianske, Dnipropetrovsk region, Ukraine

ABSTRACT. The Unistellar eVscope 2 represents a new generation of compact astronomical instruments that combine portability, automation, and digital networking to empower both professional and citizen astronomers. This study evaluates the telescope's technical performance, educational potential, and scientific applications, particularly in exoplanet transit photometry. Based on the comparison of our observational data obtained within the Unistellar global network and professional OGLE data, we showed the great possibility of this approach. Our results demonstrate that high-quality light curves can be produced even under sub-optimal conditions, and compact digital telescopes can play an essential role in expanding observational coverage and in training the next generation of astronomers. The Unistellar network model, combining technological innovation, social participation, and data integrity, stands as a powerful example of how future astronomy will operate at the intersection of professional and citizen science.

Keywords: exoplanets: observations: photometry: transits; citizen astronomy: Unistellar.

АНОТАЦІЯ. Телескопи Unistellar представляють нове покоління компактних астрономічних приладів, які поєднують портативність, автоматизацію та цифрові мережі, та розширюють можливості як професійних, так і цивільних астрономів. Наше дослідження оцінює технічні можливості телескопу Unistellar eVscope2, його освітній потенціал та наукове застосування, зокрема у фотометрії транзитів екзопланет. На основі порівняння наших спостережень, отриманих у співпраці з глобальною мережею Unistellar, та професійних даних проєкту OGLE, ми продемонстрували великий потенціал такого підходу. Ми показали, що спостережні дані, які отримують при взаємодії у спільноті Unistellar Global Network, навіть за ненайкращих умов, дозволяють будувати високоякісні криві блиску при змінах по току від зорі на рівні 1–2%, тому компактні цифрові телескопи можуть відігравати важливу роль в отриманні якісних спостережних даних, у навчанні наступного покоління астрономів підвищенн інтересу до астрономії та розширенні кола непрофесійних спостерігачів. Ми підтвердили ефективність eVscope2 як інструмента для наукових досліджень, освітніх проєктів та міжнародної співпраці.

Окрім основних спостережних можливостей, Unistellar eVscope2 демонструє перехід до моделі розподіленої спостережної екосистеми, у межах якої тисячі малих інструментів колективно створюють науково цінні результати, що служать базою для професійних досліджень. Поєднання спостережень у режимі реального часу, автоматичного розпізнавання подій і інтеграції з науковими базами даних робить такі інструменти потужним ресурсом не лише для досліджень транзитів екзопланет, але й для більш широкого кругу задач, таких, як астрономічний моніторинг змінних зір, термінові спостереження несподіваних астрономічних явищ, спільні наукові спостережні кампанії тощо. Демократизуючи доступ до неба, телескопи та спільнота Unistellar сприяють науковій грамотності, дозволяючи навіть аматора і студентам брат участ глобальни дослідницьких ініціативах. Таким чином, він стимулює міжпоколінну співпрацю й формування нової моделі наукового колективу – синергії між науковцями, освітянами та ентузіастами, спрямованої на розвиток сучасної культури науки.

Результати нашого дослідження показують, що компактні малоапертурні цифрові телескопи можуть відігравати значущу роль у формуванні майбутнього покоління астрономів і дослідників. Мережа Unistellar, яка поєднує технологічні інновації, соціальну участь і цивільну науку, демонструє реальний приклад того, як майбутня астрономія функціонуватиме на межі професійної та аматорської діяльності.

Ключові слова: екзопланети: спостереження: фотометрія: транзити; цивільна астрономія: Unistellar.

1. Introduction

The modern approach to observational astronomy allows for obtaining significant results using small telescopes. Many tasks require a large number of individual measurements of magnitudes by standard methods. The Unistellar program and community are a great example of productive collaboration between professionals and citizen science in the direction of exoplanet transits observations, in particular (Bonney et al., 2014).

The search for exoplanets is one of the most dynamic areas of modern astrophysics, offering insights into planetary formation, orbital dynamics, and habitability beyond the Solar System. Among the observational methods, transit photometry - the measurement of periodic dips in stellar brightness as a planet passes in front of its host star has proven exceptionally productive (Winn & Fabrycky, 2015). The most interest light curves allowed detecting compound transits, like as VLT observations of the light curve of TRAPPIST-1 during the triple transit of 11 December 2015 (Gillon et al., 2016), Kepler observations of the Kepler-1625b super-Jupiter and it's Neptune-sized exomoon, orbiting of the planet (Teachey & Kippin, 2018), and exotic light curve BD+05 4868 Ab, which arose due to disintegration of the exoplanet (Hon et al., 2025). In the all cases the dept of the transit is on the level of $0.05-0.12$ form common flux.

While large professional surveys such as Kepler, TESS, and PLATO dominate the field, smaller instruments increasingly contribute through citizen-science initiatives. The Unistellar eVscope 2, with its integrated sensor, automated pointing, and mobile-app control, demonstrates how distributed telescope networks can enhance temporal coverage and community engagement in real research.

2. Instrument Specifications and Methodology

The Unistellar eVscope 2 is a compact digital reflector telescope with the following base parameters:

- Mirror diameter: 114 mm;
- Focal length: 450 mm $(f/4)$;
- optical tube length 549 mm;
- Sensor: Sony IMX347, 7.7 MP;
- Limiting magnitude 18.2^m;
- Field of view: $34.2 \times 45.6\, arcmin$;
- Scale $1.33''/pix$;
- Weight: $\approx 9\, kg$;
- Motorized ALT-AZ mount;
- Slew speeds max $4^\circ/s$;
- Control: Smartphone application;
- Capabilities: battery autonomy ≈ 9 h, storage 64 GB, automatic alignment, live stacking, and transit photometry.

Observations were performed through the Unistellar citizen-science network, which connects professional astronomers, educators, and amateurs worldwide. Uniform optical properties of the Unistellar telescope family provide a consistent combination of the network observations; it was studied in Perrocheau et al. (2022), Graykowski et al. (2023), Peluso et al. (2023), and Sgro et al. (2023).

Each participant of the Unistellar community contributes calibrated photometric data that can be merged and cross-validated with professional databases. The observer can process the individual frames (in the *fits* format) and obtain the light curve by himself. However, the best results are obtained in the centralized standard analysis, which includes the comparison with model systems also.

Our test frames, obtained before the transit observations, showed that the limiting magnitude for our Unistellar eVscope 2, is 16^m. It agrees with the limiting magnitude in the base parameters, because 18.2^m value was obtained in countryside mode with longer exposure. Nevertheless, for our tasks 16^m is sufficient: in the frames received at altitudes of more 45°, we detected weaker stars confidently. The main part of the program stars have magnitudes at level $12 - 14^m$, so using Unistellar is valid.

Anastasia Pechko was a leading observer of our team. We obtained transit light curves for 2 confirmed exoplanets: TOI-2046b, created in 2020, and TrES-3b (TOI-2126.01), created in 2007; transit light for 2 candidate planets: TOI-7343.01 TOI, created in April of 2025, and TOI-7425.01 created in May 2025-05-01.

The information about our objects from the TOI list was obtained from the NASA Exoplanet Archive (Street et al., 2024). For all transits, we determined the mid-transit time, the duration and depth of the transit, and the duration of the magnitude decrease/increase.

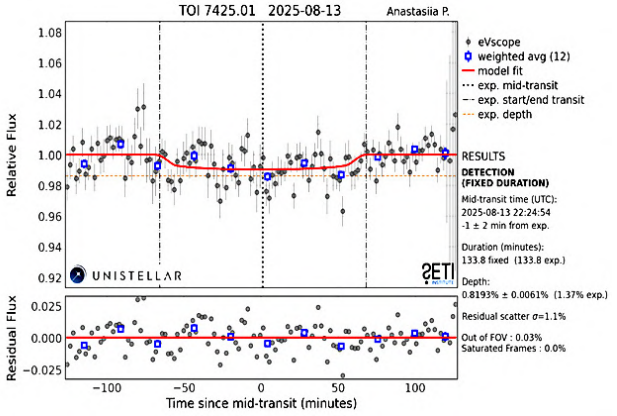

Figure 1: Transition light curve for TOI-7425.01 with the weakening of flux on the level 0.82%. The upper panel with relative flux: individual data are shown as grey dots with corresponded error bars, weighted average points are shown as squares and the synthetic light curve is a solid line. The bottom panel residual flux: the average value is zero. The legend is shown on the right

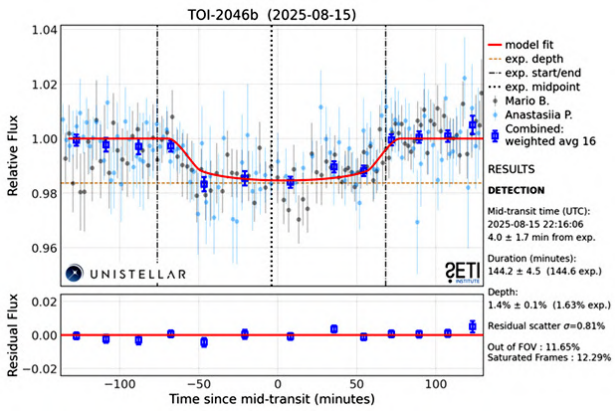

Figure 2: Transition light curve for TOI-2046b, reduced by 2 different observers. The legend as in Fig. 1

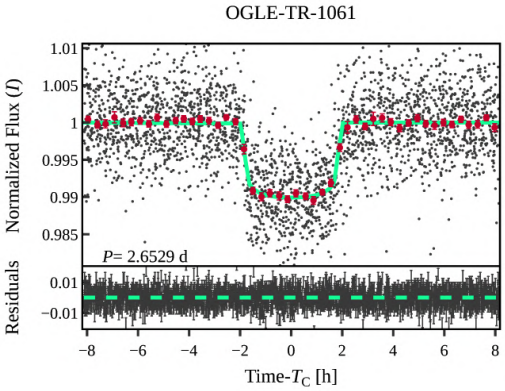

Figure 3: Transition light curve for OGLE-TR-1061

In all four transits, the parent star magnitudes were about 12^m, the individual error for current magnitude was at the level about 0.007 of the relative flux, and the depths of the transit were from 0.82% to 1.97% of the full flux. The accuracy of the transit's time frames is on the level of 2% and is in good agreement with the TOI forecast. The transit light curve with the least weakening of flux for our observations (0.82%) is presented in Fig. 1.

15^{th} on August 2025, Anastasia Pechko and our team conducted exoplanet transit observations, later combined in the Unistellar Community with independent data from another observer. The combined light curve was generated through weighted averaging, which effectively reduced noise and increased the signal-to-noise ratio. It is shown in Fig. 2. The comparison of data from two geographical locations confirmed consistency within measurement uncertainties. The improvement in curve smoothness demonstrates the power of collaborative photometry, where multiple observers contribute to a single scientifically robust data set.

The combined light curve shows a flux decrease of about $1 - 1.5\%$, typical for hot Jupiter type planets, and a duration close to two hours. The agreement between independently reduced data sets verifies the reliability of the Unistellar calibration pipeline and emphasizes the efficiency of data stacking and noise reduction. Even under moderate light pollution, the resulting signal-to-noise ratio was sufficient to clearly detect the ingress and egress phases.

3. The comparison with OGLE transits and discussion

In our observation we obtained the typical values of the transit light curve parameters. The OGLE data base (*https://ogledb.astrouw.edu.pl/*) contains higher quality photometry data for different variables. One section in the OGLE contains 99 transiting planet candidates in the Galactic bulge (Mróz et al., 2023), with the probability ranging from 0.80 to 1.00. We select 4 transit light curves for comparison with our results. The typical OGLE transit for OGLE-TR-1061b is present in Fig. 3, from *https://ogledb.astrouw.edu.pl/*.

We see the transit depth at about the 1% level, but the scatter of individual points is practically the same as in our observations. We can also point out that the data in Fig. 3 were collected over 10 years. So, our one-night data gives comparable results with long-time observations. More, the OGLE data were obtained using a fully automated 1.3 *m* Warsaw University Telescope Las Campanas Observatory, Chile. It's an excellent place for photometry, and the excellent equipment;

however, due to modern methods of data reduction, we have the results on eVscope 2 practically on the same level. So, the obtained results confirm that compact automated telescopes can achieve scientifically valuable photometric precision even under light-polluted urban conditions.

Over the past decade, small-aperture telescopes have become effective tools for observing transits. Wide Angle Search for Planets, WASP program is two successful robotic observatories. The base equipment of the WASP program is lenses with an aperture of 111 *mm* (Pollacco et al., 2016). The Unistellar telescopes, having practically the same aperture, can provide wide support for professional observations. Examples of the successful work of the eVscope are observations of the comets 12P/Pons-Brooks and C/2023 A3 (Tsuchinshan-ATLAS) 11, when their magnitudes were greater than 16^m (Graykowski et al., 2024).

4. Conclusion

The quality of the Unistellar eVscope 2 and modern methods of data reduction allow us to use this telescope and analogs as an effective tool for research, outreach, and international collaboration. The hundreds of Unistellar users, distributed across all continents, excluding Antarctica, open new possibilities for:

- Long-term exoplanet monitoring, including transit-timing-variation (TTV) analysis and orbital refinement.
- Asteroid occultation studies, contributing to the characterization of small Solar System bodies.
- Rapid follow-up of transient phenomena such as supernovae and comets.
- Educational engagement, allowing students and teachers to participate in authentic scientific research.
- Citizen science integration, supplying complementary datasets to major space missions (TESS, Kepler, PLATO).

We showed the Unistellar eVscope 2 provides reliable exoplanet light curves, validating its use in scientific and educational contexts. Collaborative data merging within the Unistellar community significantly improves measurement accuracy and minimizes systematic errors. The study demonstrates that citizen science networks can meaningfully contribute to professional astrophysical research.

Acknowledgments. The authors express their sincere gratitude to Dr. Franck Marchis and Taisiia Karasova for their valuable guidance, encouragement, and support throughout this project.

This research has made use of NASA's Astrophysics Data System. This research has made use of the NASA Exoplanet Archive, which is operated by the California Institute of Technology, under contract with the National Aeronautics and Space Administration under the Exoplanet Exploration Program.

The authors express their sincere gratitude to the anonymous referee for constructive comments.

References

Bonney R., Shirk J. L., Phillips T. B., et al.: 2014, *Science*, **343**, 6178, 1436.

Gillon M., Jehin E., Lederer S. et al.: 2016, *Nature*, **533**, 221.

Graykowski A., Lambert R. A., Marchis F., et al.: 2023, *Nature*, **616**, 461.

Graykowski A., Hemmelgarn S., Esposito T. M.: 2024, *Research Notes of the AAS*, **8**, Iss. 2, id. 41.

Marc Hon M., Rappaport S., Shporer A., et al.: 2025, *ApJ Letters*, **984**, L3.

Street R. A., Bachelet E., Tsapras. Y., et al.: 2024, *PASP*, **136**, id. 064501M.

Mróz M., Pietrukowicz P., Poleski R., et al.: 2023, *Acta Astron.*, **73**, 127.

Pollacco D. L., Skillen I., Collier Cameron A., et al.: 2016, *PASP*, **118**, 1407.

Peluso D. O., Esposito T. M., Marchis F., et al.: 2023, *PASP*, **135**, 1043, id. 015001.

Perrocheau A., Esposito T. M., Dalba P. A., et al.: 2022, *ApJ Letters*, **940**, L39.

Sgro L. A., Esposito T. M., Blaclard G., et al.: 2023, *Research Notes of the AAS*, **7**, id. 141.

Teachey A. & Kipping D. M.: 2018, *Science Advances*, **4**, 10, 1.

Winn J. N., Fabrycky D. C.: 2015, *Ann. Rev. Astron.& Astrophys.*, **53**, 409.

ASTROPHYSICS

(stellar atmospheres, interacting binary systems, variable stars)

https://doi.org/10.18524/1810-4215.2025.38.343166

PERIODIC VARIATIONS IN THE OPTICAL SPECTRUM OF THE POST-AGB OBJECT LN HYA

S. E. Achkassova[1], Sh. T. Nurmakhametova[1], A. S. Miroshnichenko[1,2,3], N. L. Vaidman[2,1], S. A. Khokhlov[2,1], D. T. Agishev[1], S. Danford[3]

[1] Al-Farabi Kazakh National University, Al-Farabi Ave, 71, 050040, Almaty, Kazakhstan, *snezhanachkasova29@gmail.com*; *shahidanurmahametova@gmail.com*; *agishev.pluto@gmail.com*

[2] Fesenkov Astrophysical Institute, Observatory, 23, 050020 Almaty, Kazakhstan, *nva1dmann@gmail.com*; *skhokh88@gmail.com*

[3] Department of Physics and Astronomy, University of North Carolina at Greensboro, Greensboro, NC 27402-6170, USA, *a_mirosh@uncg.edu*; *danford@uncg.edu*

ABSTRACT. LN Hya (BS 4912; HD 112374) has long been regarded as a post-AGB F-type supergiant, located at a high Galactic latitude ($b = +36\overset{\circ}{.}3$). Earlier studies relied on limited spectroscopic and photometric material. We present a new data set comprising 73 medium-resolution ($R \approx 12{,}000$) optical spectra obtained at the 0.81-meter telescope of the Three College Observatory (North Carolina, USA) in 2021—2025. We found regular variations in the radial velocities (RV) of absorption lines with a period of 148.63 ± 0.09 days. Our observations cover 10 most recent variability cycles and suggest that LN Hya is a binary system with an eccentric orbit ($e = 0.19 \pm 0.02$). In this paper, we describe the data reduction and analysis process as well as some spectral features of the system. Future plans for a deeper study of LN Hya that include analyzing existing photometric data and correlating them with the spectral variability are outlined.

Keywords: post-AGB stars; binary systems; spectroscopic orbits; radial velocities; stellar variability.

АНОТАЦІЯ. LN Hya (BS 4912; HD 112374) довгий час вважався надгігантом типу F після AGB, розташованим на високій галактичній широті ($b = +36\overset{\circ}{.}3$). Раніше дослідження спиралися на обмежений спектроскопічний та фотометричний матеріал. Ми представляємо новий набір даних, що містить 73 оптичні спектри середньої роздільної здатності ($R \approx 12\ 000$), отримані на телескопі діаметром 0,81 м Обсерваторії Трьох Коледжів (Північна Кароліна, США) у 2021—2025 рр. Ми виявили регулярні варіації радіальних швидкостей (RV) ліній поглинання з періодом $148{,}63 \pm 0{,}09$ днів. Наші спостереження охоплюють 10 останніх циклів змінності та свідчать, що LN Hya є подвійною системою з ексцентричною орбітою ($e = 0{,}19 \pm 0{,}02$). У цій роботі ми описуємо процес редукції та аналізу даних, а також деякі спектральні особливості системи. Окреслено плани подальшого детальнішого дослідження LN Hya, що включають аналіз наявних фотометричних даних і їх кореляцію зі спектральною варіабельністю.

Ключові слова: зорі після AGB; подвійні системи; спектроскопічні орбіти; радіальні швидкості; зоряна змінність.

1. Introduction

Post-AGB stars are evolved low- and intermediate-mass objects (initial masses 0.8–8 $M_\odot$). They represent a short-lived ($\sim 10^3$–10^4 yr) transitional stage between the asymptotic giant branch (AGB) and the planetary nebula. During this phase, the star loses most of its extended outer envelope, which forms a circumstellar shell rich in gas and dust. As the envelope disperses, the star evolves toward higher effective temperatures on the Hertzsprung–Russell diagram. It contracts and heats up while still retaining the luminosity characteristic of a cool supergiant. The effective temperature ($T_{\rm eff}$) increases from ~5,000 K to as high as 30,000–200,000 K for the hottest remnants (Miller Bertolami 2016). Meanwhile, the core temperature remains on the order of 10–100 MK. This evolutionary stage typically ends with the star becoming the central star of a planetary nebula and, ultimately, a white dwarf (Van Winckel 2003; Herwig 2005).

One of the brightest stars in its class is LN Hya (BS 4912, HD 112374). It is located at a high Galactic

latitude of $b = +36.4°$ and exhibits a noticeable metal deficiency, which confidently places it among the old stellar population, likely belonging to the thick disk or Galactic halo. Its bolometric luminosity, estimated as $\log(L/L_\odot) = 4.0$, along with $T_{\rm eff} \simeq 6000$ K, places LN Hya close to the post-AGB evolutionary track with a core mass $M_{\rm core} \approx 0.6\,M_\odot$ in the models of Miller Bertolami (2016), consistent with other similar post-AGB objects (e.g., Klochkova, Panchuk 2012).

The optical spectrum of LN Hya corresponds to an F-type luminous supergiant (F3 Ia). It shows typical characteristics of low-mass, post-AGB "high-latitude supergiants". One notable feature is the Hα line profile, which usually displays emission components superimposed on a broad absorption. Among post-AGB stars, the Hα line is commonly observed to exhibit a double-peaked emission profile, a hallmark of a rotating circumstellar structure. In some systems, the emission arises in material gravitationally bound to the primary star and situated outside its orbit. It likely forms in a circumbinary disk and varies with the orbital phase (e.g., Nurmakhametova et al. 2025). In other cases, the Hα profile appears as a deep absorption core partially filled in by emission wings. Such profiles are commonly interpreted as evidence of a long-lived reservoir of the circumstellar gas distributed in a rotating disk or an extended envelope (e.g., Klochkova, Panchuk 2012).

Post-AGB binaries with long-lived circumbinary dusty disks form a well-studied class: their SEDs show stable near-IR excesses from compact Keplerian disks, now resolved interferometrically and modeled as dust-sublimation–truncated rims (De Ruyter et al. 2006; Hillen et al. 2017; Kluska et al. 2019). Their orbital periods span $\sim 10^2$–10^3 days and frequently retain significant eccentricities, likely sustained or re-excited by disk–binary interactions (Dermine et al. 2013; Oomen et al. 2018). In this context, LN Hya's RV period, Hα phenomenology, and other spectral properties place it among the disk-bearing post-AGB binaries, where binarity, mass loss, and disk dynamics are coupled.

Luck et al. (1983) found the following fundamental parameters of LN Hya: $T_{\rm eff} \simeq 6000$K, a surface gravity of $\log g = 0.4$ - 0.8 and a significantly reduced metallicity of [Fe/H] = –1.2, accompanied by a nitrogen overabundance of [N/Fe] = +0.5.

Despite previous observations, LN Hya remains an object of a considerable interest due to its atmospheric instability, variable emission characteristics, and unusual chemical abundance patterns, characterized by a significant depletion of refractory elements (e.g., Fe, Ca, Ti) and an enhancement of nitrogen ([Fe/H] ≈ –1.2, [N/Fe] ≈ +0.5). Such selective abundance anomalies are typical of post-AGB binaries with circumbinary disks, where refractory elements condense into dust grains while volatile species are re-accreted onto the stellar atmosphere. Previous investigations of LN Hya were hampered by the scarcity of high-resolution, homogeneous spectroscopic material and the absence of a long-term RV monitoring.

Revealing the binary nature of LN Hya is crucial for understanding the origin of its circumstellar matter, the mass-loss mechanisms, and the role of binarity in the post-AGB evolution. In this context, our new multi-year spectroscopic campaign provides the first opportunity to derive a coherent orbital solution and directly test the binary hypothesis.

The primary aim of this work is to perform a high-resolution spectroscopic and photometric analysis of LN Hya, focusing on the temporal behavior of key spectral lines, particularly Hα, as well as RV variations that may reflect atmospheric pulsations or dynamical instabilities. In addition, we aim to derive the orbital parameters of the system by analyzing long-term RV data, with the goal of verifying the possible binary nature of LN Hya and detecting a potential secondary component. Photometric observations will also be used to study brightness variations and light curve morphology, offering further insights into the physical processes governing the evolution and variability of this post-AGB object.

2. Observations

Spectroscopic monitoring was carried out with the 0.81 m telescope at the Three College Observatory using the échelle spectrograph eShel (Shelyak Instruments[1]) between 19 May 2021 and 2 June 2025. In total, 73 spectra were obtained. Because the target remains low at the site (latitude $+35°56'$), typical total integrations were 1-2 hours, composed of individual 25–40–minute exposures.

The data reduction did not include overscan removal or dark-frame subtraction. Dark frames were used only to identify and map detector pixels that show abnormal responses, producing artificial narrow emission-like features. These "bad" pixels were recorded into a mask and corrected during the initial processing using the fixpix task in the ccdproc package, which proved to be more efficient and stable than traditional dark subtraction. The remaining steps of the procedure comprised scattered-light suppression, order tracing and optimal extraction, wavelength calibration with ThAr-lamp spectra, heliocentric correction, and continuum normalization with masking of strong spectral features. Flat-field frames were not applied because the detector's pixel-to-pixel sensitivity variations are $\leq 1.5\%$, and the flat-field lamp does not illuminate the full extracted spectral range. The typical accuracy of the wavelength solution is on the order of a few $10^2\,{\rm m\,s^{-1}}$ ($\approx 300\,{\rm m\,s^{-1}}$).

[1] https://shelyak.com

3. Methods

RVs were measured by cross-correlation in the spectral window λ = 5046–5163 Å, which is rich in narrow metallic lines and minimally affected by emission or telluric contamination. Before computing the CCF, residual outliers were removed, the continuum was normalized, and problematic segments were masked. The cross-correlation peak was fitted with a Gaussian; the centroid yields the RV, while the width and contrast provide the internal uncertainty. To account for excess scatter beyond the formal errors, we introduced an additive jitter term, σ_j, as a free parameter in the Markov-Chain Monte Carlo (MCMC) analysis. This approach provides a robust, fully Bayesian estimation of the orbital parameters, properly propagating non-Gaussian uncertainties and correlations between parameters such as P, e, and K_1. This method yields posterior probability distributions rather than single best-fit values, allowing realistic credible intervals for each element of the orbit. This term, typically 0.4–0.8 km s^{-1}, absorbs additional astrophysical or instrumental variability. A systematic error floor of the same order was also adopted to reflect instrumental stability. The RV zero point was monitored via stable spectral regions and inter-night consistency checks.

As a reference template for cross-correlation, we used our spectrum of LN Hya obtained on 2021/05/19 (see Fig. 1), which has a S/N ratio of $\sim$ 200 in the continuum of the chosen region. The orbital RV for the template spectrum was determined by cross-correlating the mentioned spectral region with that of a constant RV star α Persei (RV$_{\rm hel} = -2.1$ km s^{-1}) obtained with the same equipment. This way the RV scale was translated into the heliocentric frame (see Fig. 2).

RVs were analysed with a reproducible analysis pipeline implemented in Python. First, we determined the period from the RV time series using the Lomb–Scargle algorithm, which is appropriate for uneven sampling and highlights the dominant periodicity. Next, we modelled the RV curve with a single-lined Keplerian profile and inferred the orbital elements by Bayesian Markov-chain Monte Carlo sampling using the affine-invariant ensemble sampler implemented in the `emcee` package (Foreman-Mackey et al., 2013).

We used weakly informative priors, initialized chains near the periodogram solution, discarded burn-in, and checked convergence with standard diagnostics. Final values for the period, systemic velocity, semi-amplitude, eccentricity, and argument of periastron are reported as posterior medians with 16th–84th percentile credible intervals. The workflow follows our previously published RV+MCMC analyses and is implemented in Python. This method was also employed in Vaidman et al. (2025a) and in Nurmakhametova et al. (2025); see also Vaidman et al. (2025b) for methodological details.

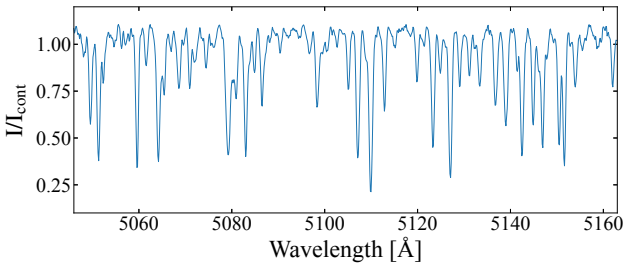

Figure 1: Part of the TCO spectrum of LN Hya in the wavelength range 5046–5163 Å obtained on 2021/05/19 and used as a template for cross-correlation.

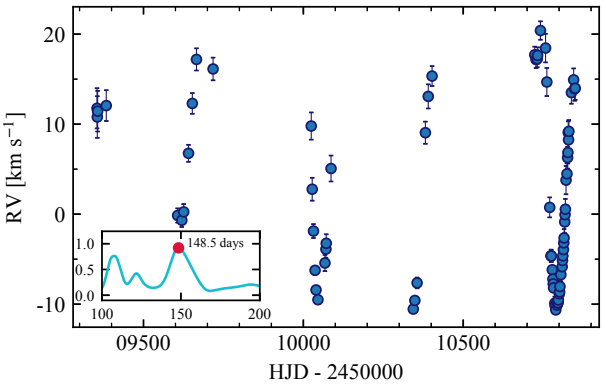

Figure 2: RV measurements in the heliocentric frame as a function of HJD. The inset shows the periodogram, indicating a detected period of 148.5 days.

4. Results

The LS periodogram (inset in Fig. 2) shows a single dominant peak at a period of 148.5 days with a very low false-alarm probability; weaker aliases are negligible. Folding the RVs on this period produces a phase-coherent curve with minimal scatter, consistent with the modulation seen in the long-term photometry. This establishes the characteristic timescale of the system and underpins the orbital solution reported below. The phase-folded RV curve (Fig. 3) for the first time demonstrates that LN Hya is a spectroscopic binary. The smooth line approximating the data points is the best-fitting single-lined Keplerian (SB1) model, computed from the MCMC posterior-median orbital elements listed in Table 1.

The phase–coherent RV curve establishes a well-constrained single–lined spectroscopic orbit for LN Hya (Table 1). The solution indicates a moderate eccentricity with a well–constrained argument of periastron, a stable systemic velocity across all seasons, and a precisely measured semi–amplitude of the visible

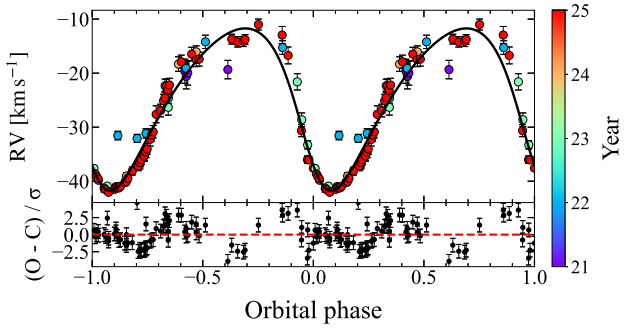

Figure 3: Radial velocity of LN Hya in the 10 latest orbital cycles ($\sim$ 1,500 days). RVs were measured in the TCO spectra by cross-correlation in a spectral range λ = 5046–5163 Å. The colour scale indicates the year of observation.

Table 1: Orbital parameters of LN Hya.

No.	Parameter	Value
1	P (days)	148.63 ± 0.09
2	T_0 (HJD)	2459291.31 ± 1.83
3	e	0.19 ± 0.02
4	ω (degrees)	106.85 ± 0.23
5	γ (km s^{-1})	-24.29 ± 0.34
6	K_1 (km s^{-1})	14.979 ± 0.44
7	$f(m)$ ($M_\odot$)	0.049 ± 0.004
8	N	73

Notes. (1) Orbital period; (2) periastron epoch for the elliptical orbit and time of superior conjunction (at γ RV) for the circular orbit; (3) eccentricity; (4) argument of the periastron; (5) systemic RV; (6) semi-amplitude of the RV variation of the visible component; (7) mass function; (8) number of spectra used in the orbit calculation.

component. This is the first self–consistent orbital solution for LN Hya solely based on a homogeneous RV data set. It determines the system's dynamical timescale and geometry for subsequent analysis.

5. Conclusions and Discussion

We present the first self-consistent spectroscopic orbit for LN Hya based solely on medium-resolution RVs. Our homogeneous data set and uniform Bayesian analysis yield a stable, repeatable single-lined solution; the derived elements are internally consistent and robust, fixing the system's dynamical timescale and geometry for the first time. The $\sim$148.5 days period inferred from the RV curve is too long for a classical pulsating Cepheid at the star's temperature and luminosity, favouring the orbital interpretation. The variability can plausibly arise from geometric and atmospheric effects within the binary (e.g., shallow eclipses and/or phase-dependent heating of the visible component).

A phase-coherent orbit enables: (i) mass-function limits on the unseen component and a pathway to dynamical masses once the inclination is constrained; (ii) predictive ephemeris to phase-tag follow-up spectroscopy and interferometry; (iii) separation of orbital signals from low-amplitude atmospheric pulsations; and (iv) phase-dependent modelling of circumbinary gas and dust within a self-consistent geometry.

Future directions. We will (i) extend and densify the RV monitoring to refine the orbital elements and mass function, especially near periastron; (ii) obtain higher-resolution spectra to search for weak features of the secondary and to improve line-profile modelling; and (iii) constrain the inclination via long-baseline (spectro-)interferometry and $v \sin i$ constraints to enable dynamical masses. These steps will deliver a more accurate orbital solution and provide deeper insights into the origin of the system.

Funding. This research was funded by the Science Committee of the Ministry of Science and Higher Education of the Republic of Kazakhstan (Grant No. AP23484898).

Acknowledgements. This research has made use of the SIMBAD database, operated at CDS, Strasbourg, France; SAO/NASA ADS, ASAS, and Gaia data products. This paper is based on observations obtained at the 0.81 m telescope of the Three College Observatory (North Carolina, USA). A.M. and S.D. acknowledge technical support from Dan Gray (Sidereal Technology Company), Joshua Haislip (University of North Carolina Chapel Hill), and Mike Shelton (University of North Carolina Greensboro), as well as funding from the UNCG College of Arts and Sciences and Department of Physics and Astronomy.

References

Arkhipova V.P., Ikonnikova N.P., Noskova R.I., Komissarova G.V.: 2001, *Astron. Lett.*, **27**, 156–168.

Dermine T., Izzard R.G., Jorissen A., Van Winckel H.: 2013, *Astron. Astrophys.*, **551**, A50.

Foreman-Mackey D., Hogg D.W., Lang D., Goodman J.: 2013, *Publ. Astron. Soc. Pac.*, **125**, 306.

Henson G.D., Deskins W.R.: 2009, *ASP Conf. Ser.*, **412**, 229.

Herwig F.: 2005, *Annu. Rev. Astron. Astrophys.*, **43**, 435–479.

Hillen M., Van Winckel H., Menu J., Manick R., Debosscher J., Min M., de Wit W.-J., Verhoelst T., Kamath D., Waters L.B.F.M.: 2017, *Astron. Astrophys.*, **599**, A41.

Klochkova V.G., Panchuk V.E.: 2012, *Astron. Rep.*, **56**, 104–115.

Kluska J., Van Winckel H., Hillen M., et al.: 2019, *Astron. Astrophys.*, **631**, A108.

Luck R.E., Lambert D.L., Bond H.E.: 1983, *Publ. Astron. Soc. Pac.*, **95**, 413–421.

Miller Bertolami M.M.: 2016, *Astron. Astrophys.,* **588**, A25.

Nurmakhametova S.T., Vaidman N.L., Miroshnichenko A.S., Khokhlov A.A., Agishev A.T., Yermekbayev B.S., Danford S., Aarnio A.N.: 2025, *Galaxies,* **13**, 26.

Oomen G.-M., Van Winckel H., Pols O., Nelemans G., Escorza A., Manick R., Kamath D., Waelkens C.: 2018, *Astron. Astrophys.,* **620**, A85.

De Ruyter S., Van Winckel H., Maas T., Lloyd Evans T., Waters L.B.F.M., Dejonghe H.: 2006, *Astron. Astrophys.,* **448**, 641–653.

Vaidman N.L., Miroshnichenko A.S., Zharikov S.V., Khokhlov S.A., Agishev A.T., Yermekbayev B.S.: 2025a, *Galaxies,* **13**, 3, 47.

Vaidman N.L., Nurmakhametova S.T., Miroshnichenko A.S., Khokhlov S.A., Agishev A.T., Khokhlov A.A., Ashimov Y.K., Yermekbayev B.S.: 2025b, *Galaxies,* **13**, 5, 101.

Van Winckel H.: 2003, *Annu. Rev. Astron. Astrophys.,* **41**, 391–427.

https://doi.org/10.18524/1810-4215.2025.38.341536

VARIATION OF THE Hα LINE PROFILE IN THE SPECTRUM OF THE SUPERGIANT STAR HD 207260 (A2 Iae)

A. B. Hasanova, A. M. Khalilov, A. Sh. Baloglanov, G. M. Hajiyeva

Shamakhi Astrophysical Observatory named after Nasraddin Tusi, Ministry of Science and Education of the Republic of Azerbaijan, Shamakhi, Azerbaijan

aynura.hasanova@shao.science.az

ABSTRACT. We present the results of a detailed spectroscopic investigation of the supergiant HD 207260 (A2 Iae), based on high-resolution echelle spectra obtained in 2018 with the 2-meter telescope at the Shamakhi Astrophysical Observatory. The focus is on the variability of the Hα line, which exhibits a complex and variable profile, consisting of both an absorption and an emission component. The intensity of the emission component and its radial velocity were found to vary significantly across different epochs. These changes were accompanied by synchronous variations in the radial velocity of the absorption and in the equivalent width of the line. Such behavior suggests a dynamical origin for the emission component, possibly related to instabilities in the upper atmosphere or episodic mass loss processes.

Fourier analysis of the radial velocity variations reveals with an approximate of 35–40 days. This periodicity is consistent with the presence of radial or non-radial pulsations, which may drive structured outflows in the upper layers of the stellar atmosphere.

It is assumed that the change in the Hα line profile, the change in the radial velocity and the equivalent width of the absorption and emission components of the Hα line profile occur as a result of the interaction of the stellar atmosphere with the circumstellar envelope as a result of the pulsation of the star.

Keywords: supergiant stars, Hα line profile, radial velocity, spectral variability, stellar pulsations.

АНОТАЦІЯ. Ми представляємо результати детального спектроскопічного дослідження надгіганта HD 207260 (A2 Iae), що базується на високодисперсних ешель-спектрах, отриманих у 2018 році за допомогою 2-метрового телескопа Шамахинської астрофізичної обсерваторії. Основна увага приділяється варіабельності лінії Hα, яка демонструє складний і змінний профіль, що складається як з абсорбційного ядра, так і з емісійної компоненти. Було встановлено, що інтенсивність емісії та її променева швидкість значно змінюються в різні епохи. Ці зміни супроводжувалися синхронними варіаціями радіальної швидкості та еквівалентної ширини поглинальної складової лінії. Така поведінка свідчить про динамічне походження емісійної компоненти, можливо повязане з нестабільностями у верхніх шарах атмосфери або з епізодичними процесами втрати маси.

Фур'є-аналіз радіальної швидкості показує приблизний період у 35–40 днів. Ця періодичність узгоджується з наявністю радіальних або нерадіальних пульсацій, які можуть спричиняти структуровані потоки у верхніх шарах зоряної атмосфери.

Передбачається, що зміна профілю лінії Hα, зміна радіальної швидкості та еквівалентної ширини поглинальної та емісійної складових профілю лінії Hα відбуваються в результаті взаємодії зоряної атмосфери з навколозоряною оболонкою внаслідок пульсації зірки.

Ключові слова: надгіганти, профіль лінії Hα, радіальна швидкість, спектральна варіабельність, зоряні пульсації.

1. Introduction

B- and A-type supergiant stars represent the brightest stellar population in both spiral and irregular galaxies that are undergoing active star formation. These stars are young and predominantly located within the galactic plane. Due to their high luminosity, they can be observed at large distances, providing a unique opportunity to study the distribution of chemical elements and to trace the chemical evolution of the Milky Way as well as other galaxies. Furthermore, these stars are extensively used to investigate the spiral structure of galaxies and to determine their morphological parameters.

HD 207260 (A2 Iae), as a typical representative of this class of supergiants, is therefore of particular interest for studies related to stellar evolution. To this end, high-resolution spectra of HD 207260 were obtained with the 2-meter telescope at the Shamakhi Astrophysical Observatory. Based on these observations, the variability of the Hα line profile was analyzed, including measurements of its characteristic parameters and changes in the profile shape over time.

The supergiant star ν Cep (HD 207260 = HR 8334) has a visual magnitude of V=4.29 (Ducati, 2002) and a spectral type of A2 Iae (Gray & Garrison, 1987). In the Galactic coordinate system, its position is l=102°.3, b=+5°.93 (Pan et al., 2004), and its distance is 2083 pc (π=0.00048; Van Leeuwen, 2007).

In the work by Samedov et al. (Samedov et al., 2020) investigated the supergiant HD 207260. Atmospheric parameters were determined: T_{eff} =9200±200K; logg = 1.4

± 0.2; ξt = 6.0±0.5 km/s; logε(Fe)=7.55±0.1; [Fe/H]=0.08. Chemical composition analysis has revealed that the carbon abundance in ν Cep is lower than the solar value, while nitrogen is overabundant. The abundances of Sc, Ti, V, Cr, Fe, Ni, Sr, Zr, and Ba are close to solar values. These results indicate that ν Cep and the Sun formed from material with similar overall chemical composition, and evolutionary processes have modified the initial carbon and nitrogen abundances while other elements relatively unchanged. The observed chemical abundances are consistent with stellar evolution theory (Hajiyeva, 2020).

2. Magnetic Field in the Supergiant Star HD 207260

Between 1975 and 1979, Scholz and Gerth (1980) conducted observations of νCep at the Karl Schwarzschild Observatory (Tautenburg, Germany) in the 4000–4600 Å spectral range, obtaining 55 Zeeman spectra. Based on these observations, they investigated the star's magnetic field and the line profiles of the hydrogen Balmer series, specifically Hβ and Hδ, as well as the radial velocity variations.

The magnetic field was found to vary weakly between several hundred gauss during 1975–1978, but in 1978 it increased sharply to approximately +2000 gauss. Radial velocity variations exhibited both slow and rapid changes similar to the magnetic field. A quasi-periodicity of 39.9 days in radial velocity was detected, which the authors attributed to stellar rotation. Differences in radial velocity between H_β, H_γ, and H_δ lines were explained by the presence of an extended circumstellar envelope. Additionally, various neutral and ionized spectral lines showed radial velocity variations in the range of 1–4 km s^{-1}. During 1975–1976, radial velocities displayed inconsistent and contradictory values ranging from ~−18 to ~25 km s^{-1}. Scholz and Gerth suggested that ν Cep might be a binary system (Scholz & Gerth, 1980).

Previous studies provide some information on the spectral and photometric parameters characterizing HD 207260. However, details regarding non-stationary processes in the stellar atmosphere and the spectral lines that trace these phenomena remain largely unexplored. Therefore, investigating the Hα line of hydrogen and other lines that characterize atmospheric non-stationary processes is timely and of significant importance.

3. Observations, data reduction, and discussion

Spectroscopic observations of HD 207260 were carried out between 2015 and 2019 using the 2-m telescope at the Shamakhi Astrophysical Observatory named after N. Tusi. Until 2016, spectra were obtained in the Cassegrain focus with the UAGS spectrograph equipped with a 530×580-pixel CCD camera at a spectral resolution of R=14000, covering the 3960–6600 Å spectral range (Mikaillov et al., 2005).

After 2016, spectra were acquired using the fiber-fed Cassegrain echelle spectrograph with a 4000×4000-pixel CCD camera at spectral resolutions of R=28000 and R=56000, spectral region are 3700-8500 ÅÅ. Daytime sky spectra were used for dispersion curve calibration. Typically, 2–3 spectra of the star were obtained per night. Since no significant short-term variability was observed within a single night, these spectra were averaged to improve the signal-to-noise ratio.

The obtained spectra were reduced using the IRAF software package (Hasanova & Rustamova, 2023; Hasanova, 2024). It should be noted that the spectra of HD 207260 had previously been processed using the DECH software packages (DECH-20, DECH-20T, and DECH-30T) developed by Galazutdinov (1992). In the present study, the spectra were reprocessed with IRAF, and the results are in good agreement with those obtained using DECH, confirming the reliability of the reduction and analysis procedures. The uncertainty in the measurement of equivalent widths does not exceed 5%, while the error in radial velocity determinations is less than 1 km s^{-1}. A detailed description of the observational material and the data reduction methodology is provided in our previous works (Hasanova & Rustamova, 2023; Hasanova, 2024).

A total of 25 high-resolution spectra of the HD 207260 star were obtained during the 2016–2019 observational campaigns. In this study, we used the spectra obtained in 2018. A comparative analysis of the emission and absorption components of the Hα line profiles reveals that both the shape and structure of the profile, as well as the spectral parameters characterizing it, exhibit significant variability.

The Hα line profiles are observed in the following forms (Figure 1):

a) Fully absorption profile;

b) Normal P Cyg-type profile – absorption with emission component in the red wing.

The Hα line profiles observed in the spectrum of the hypergiant star HD 207260 at different epochs were constructed (Figure 1). As seen in Figure 1, both the shape of the Hα line profile and its spectral parameters vary over a time interval of seven days or less. The intensity of the emission component observed in the red wing of the Hα line changes with time; occasionally, the Hα line exhibits a P Cyg-type profile. At other times, the emission component completely disappears, resulting in a fully absorption profile.

For instance, on 16 August 2018, the emission component in the red wing of the Hα line in the spectrum of HD 207260 was almost entirely absent. During this epoch, the equivalent width of the absorption component increased abruptly ($\Delta W \approx 540$ mÅ), reaching a maximum value of W = 1662 mÅ. No significant variations in the radial velocity of the emission component were detected.

Based on the performed measurements, a plot showing the temporal variations of the radial velocities of the absorption and emission components of the Hα line, as well as the equivalent width of the absorption component, was constructed (Figure 2).

The plot demonstrates that both the radial velocities of the absorption and emission components and the equivalent width of the absorption component vary with a period of approximately 35–40 days.

An increase in the absolute value of the radial velocity of the absorption component is observed simultaneously with a decrease in both the equivalent width and the intensity of the emission component. In other words, these variations occur synchronously. It is suggested that these changes occur as a result from pulsations of the star, leading to interactions between the stellar atmosphere and the circumstellar envelope.

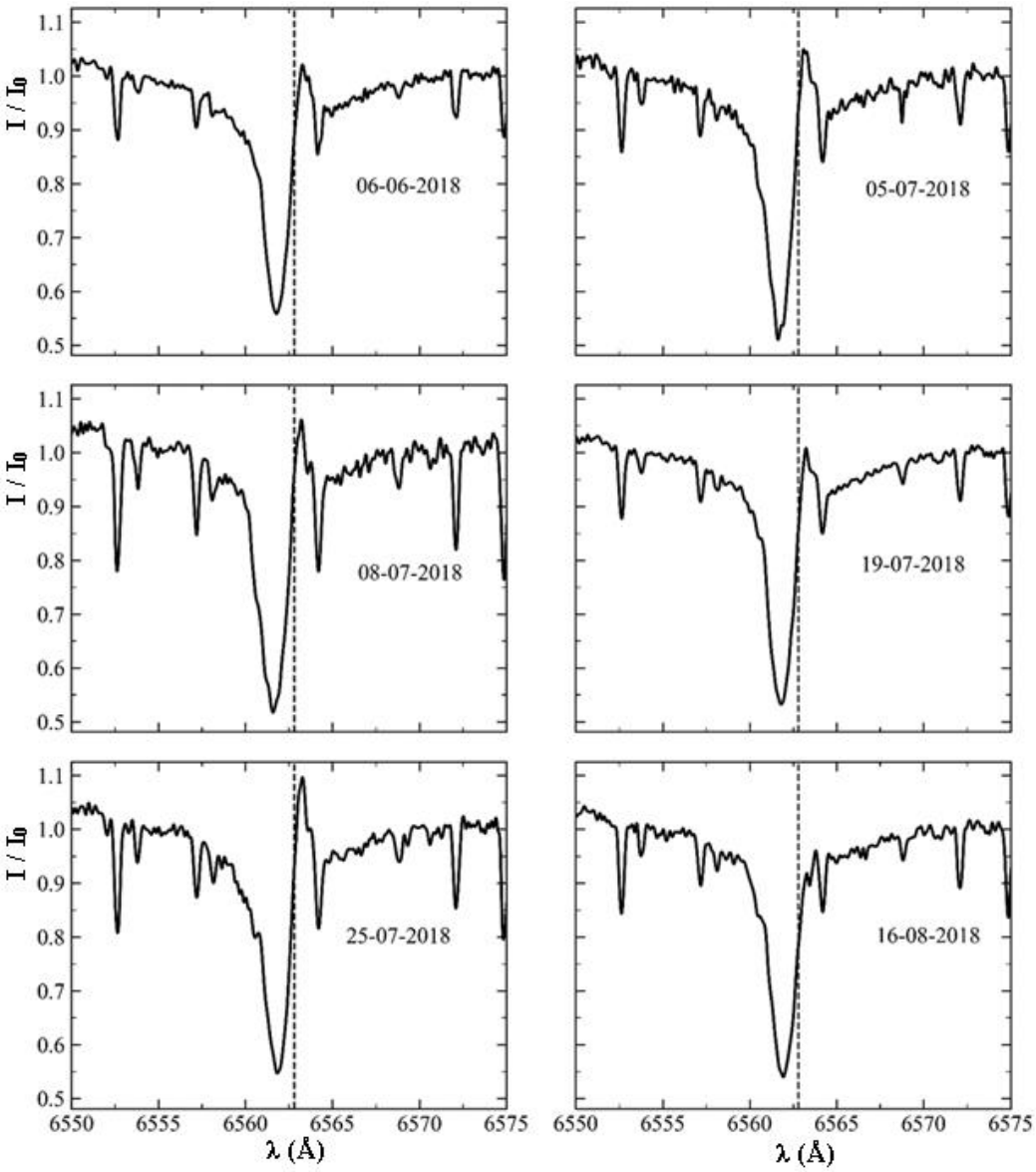

Figure 1: Profiles of the Hα line observed at different epochs in the spectrum of the HD 207260 supergiant star. The dashed line corresponds to the wavelength λ(Hα) = 6562.816 Å.

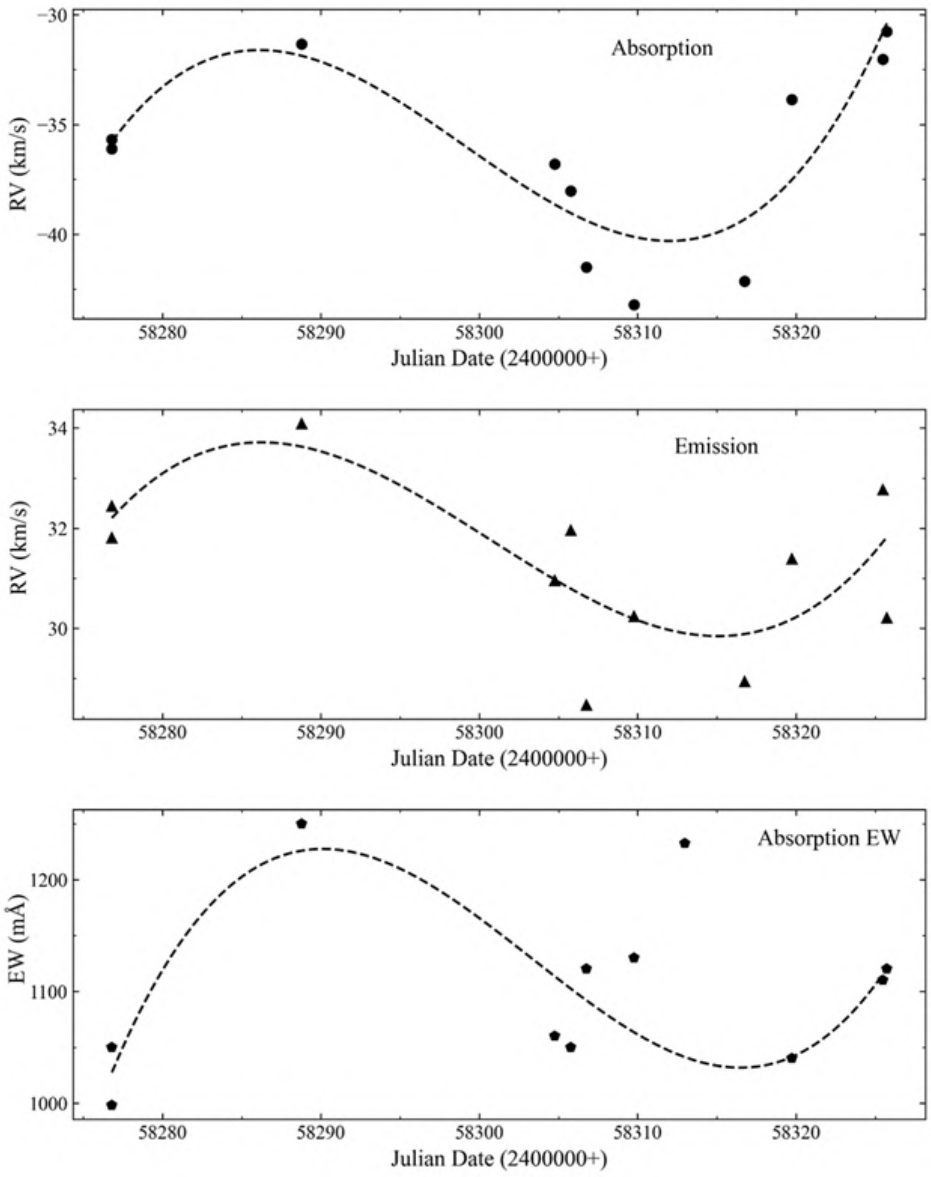

Figure 2: Temporal variations of the radial velocities of the absorption and emission components of the Hα line profile, as well as the equivalent width of the absorption component, observed in the spectrum of the HD 207260 supergiant star.

4. Conclusions

Based on the comparative study of the Hα line profiles in the spectra of the supergiant star HD 207260 obtained in 2018, the following conclusions can be drawn:

The analysis of the Hα line profiles revealed that they generally exhibit a P Cyg-type profile, consisting of an absorption component and an emission component in the red wing. The radial velocities of these components, as well as the equivalent width of the absorption component, vary over time.

It was found that the radial velocities of the absorption and emission components, together with the equivalent width of the absorption component, vary synchronously (Figure 2). These variations occur with a period of approximately 35–40 days.

These results can be utilized in constructing a theoretical model of the star.

References

Ducati J.R.: 2002, *yCat (*CDS/ADC Collection of Electronic Catalogues), **2237**.

Galazutdinov G.A.: 1992, Stellar echelle spectra processing system. (Nizhniy Arkhyz), 52.

Gray R.O. & Garrison R.F.: 1987, *ApJS*, **65**, 581.

Hajiyeva G.M.: 2020, *ProcANAS, Series of Physical and Technical Sciences*, **XL**, 2, 199.

Hasanova A.B. & Rustamova A.B.: 2023, *NewsAzNAS, Physics and Astronomy*, **2**, 135.

Hasanova A.B.: 2024, *NewsAzNAS, Physics and Astronomy*, **2**, 89.

Mikaillov Kh.M., Khalilov V.M. & Alekberov I.A.: 2005, *TsirkShAO*, **109**, 21.

Pan K., Federman S.R., Cunha K. et al.: 2004, *ApJS*, **151**, 313.

Samedov Z.A., Khalilov A.M., Hajiyeva G.M. & Rajabova S.Sh.: 2020, *AzAJ*, **XV(1)**, 54.

Scholz G. & Gerth E.: 1980, *AN*, **301**, 211.

Van Leeuwen F.: 2007, *A&A*, **474**, 653.

https://doi.org/10.18524/1810-4215.2025.38.340271

THE DISTRIBUTION OF TEMPERATURE IN THE DETAILS OF JUPITER'S DISK BASED ON THE ABSORPTION LINES OF THE NH_3 λ6450 Å BAND

A. E. Humbatova

Shamakhi Astrophysical Observatory named after Nassradin Tusi of the Ministry of Science and Education of the Republic Azerbaijan, AZ-5626, Azerbaijan Republic, Shamakhi District, Y. Mammadaliyev Settlement

emineenver23@gmail.com

ABSTRACT. In order to understand significant meteorological processes occurring in Jupiter's atmosphere, studies were carried out on ammonia NH_3 absorption lines, whose relative amount is small but whose influence could be comparable to water vapor in Earth's atmosphere. These observations were performed using a high spectral resolution échelle spectrometer installed at the Cassegrain focus of the 2-meter telescope at Shamakhi Astrophysical Observatory. Variations in the intensity of NH_3 absorption lines in the NH_3 λ 6475Å band were studied in different regions of Jupiter's disk and at the center of Saturn's disk. In this spectral region, 20 lines were selected for the center, 14 lines for the northern zone, and 11 lines for the southern zone. The obtained data were processed using the DECH 95 and DECH 30 programs. The spectrophotometric characteristics of these spectral lines, including their equivalent widths and half-widths, were determined. Based on the observational data obtained, Jupiter's rotational temperature was determined from different line pairs. The calculated temperatures vary between approximately 180 K and 80 K. The observed variations in temperature could be attributed to lightning events within these layers. Summarizing the obtained results, the average temperature in the details of Jupiter's disk was determined to be approximately 127 K, aligning well with findings reported by other authors.

Keywords: Jupiter, NH_3, λ6450 Å absorption lines, rotational temperature.

АНОТАЦІЯ. Для розуміння значущих метеорологічних процесів, що відбуваються в атмосфері Юпітера, були проведені дослідження ліній поглинання аміаку NH_3, відносна кількість яких невелика, але вплив яких може бути порівнянним з водяною парою в атмосфері Землі. Ці спостереження проводилися за допомогою ешель-спектрометра з високою спектральною роздільною здатністю, встановленого у фокусі Кассегрена 2-метрового телескопа в Шамахинській астрофізичній обсерваторії. Варіації інтенсивності ліній поглинання NH_3 у смузі NH_3 λ 6475 Å досліджувалися в різних областях диска Юпітера та в центрі диска Сатурна. У цій спектральній області було відібрано 20 ліній для центру, 14 ліній для північної зони та 11 ліній для південної зони. Отримані дані були оброблені за допомогою програм DECH 95 та DECH 30. Визначено спектрофотометричні характеристики цих спектральних ліній, включаючи їх еквівалентні ширини та напівширини. На основі отриманих даних спостережень було визначено температуру обертання Юпітера за різними парами ліній. Розраховані температури коливаються приблизно від 180 K до 80 K. Спостережувані коливання температури можна пояснити блискавками в цих шарах. Підсумовуючи отримані результати: середня температура в деталях диска Юпітера була визначена приблизно на рівні 127 K, що добре узгоджується з висновками інших авторів.

Ключові слова: Юпітер, NH_3, лінії поглинання λ6450 Å, обертальна температура.

1. Introduction

The condensation of atmospheric gases and the formation of clouds on Jupiter indicate that in the observable part of its atmosphere, at least in the lower layers, temperature decreases with increasing altitude. Until now, the temperature of Jupiter's atmosphere has been determined using various methods. For example, the rotational temperature of CH_4 and the saturation temperature of NH_3. These, of course, correspond to the deepest layers. The brightness temperature determined in the infrared range, on the other hand, characterizes the higher layers. The distribution of temperature depends on the absorption of solar radiation and the planet's own radiation at different altitudes and in various spectral regions. At the observed partial pressures and temperatures in Jupiter's atmosphere, methane does not undergo condensation, whereas H_2O, on the contrary, exists as low-pressure saturated vapor. It is not excluded that water and ice clouds form in the deep, unobservable layers of the atmosphere. The distribution of temperature depends on the absorption of solar radiation and the planet's own radiation at different altitudes and in various spectral regions.

2. The calculation of the rotational temperature

The determination of rotational temperature on Jupiter has been conducted using various molecules. For example, Zabriskie (1962) determined a rotational temperature of T_{rot}= 170K based on the relative intensities of the lines in the H_2 (3-0) band. Spinrad and Trafton (Spinrad,1963) reported a range of 120–170K; however, Spinrad later refined this value, stating that it was 120 K

The calculation of rotational temperature based on CH_4 and NH_3 lines encounters certain difficulties. This is because these molecules are non-linear and their bands have complex structures. For instance, due to its symmetry (tetrahedral), the methane molecule exhibits spherical rotation. It has four fundamental frequencies, two of which (ν_3 and ν_4) are active in the infrared region. When two or more frequencies or their overtones combine, they form combination bands. Pure overtones are distinguishable only for the ν_3 and ν_4 frequencies.

Another challenge arises from the fact that the fundamental inactive frequencies are quite close to ν_3 and ν_4. As a result, rotational levels undergo Coriolis excitation, leading to the splitting of rotational lines, which further complicates the bands. Unfortunately, nearly all CH_4 bands located in the high-resolution spectroscopy region are combination bands. Consequently, their fine structures are extremely difficult to analyze. The intensity of rotational lines depends on three quantities: transition amplitude, the statistical weight of the upper state, and the Boltzmann factor. If the molecule undergoes true spherical rotation, the distribution of rotational levels is given by the following formula:

$$N_k \sim (2k+1)^2 \, e^{-\frac{Bk(k+1)hc}{kT_r}} \quad (1)$$

If the molecule undergoes spherical rotation due to symmetry, then the ratio in equation (1) is not real, and the statistical weight for each rotational level must be calculated taking into account the spin of the nucleus. This is applicable in the case of CH_4. The intensity of rotational lines depends on three quantities: transition amplitude, the statistical weight of the upper state, and the Boltzmann factor. The intensity,

$$I_k \sim A_{k^s k} e^{-\frac{Bk(k+1)hc}{kT_r}} \quad (2)$$

Here, A_k is the transition amplitude, and S_k is the statistical weight.

$$A_{k^s k} = (2K+3)(5a+2b+3c) \quad (3)$$

Here, a, b, and c are the quantities of rotational levels corresponding to the modifications of A, E, and F for a given K. Using the ratios in (1) and (2), the relative intensity of rotational lines in the T_r function can be presented in a table, and by selecting the ratios that better match the observations, the T_r-rotational temperature can be determined. Ouen (1968) determined that using this method, for the $3\nu_3$ band with K=3,4,5,6 lines, the Tr temperature is 200±25.

The rotational temperature determined by Ouen is close to the melting point of NH_3 (195K). It is likely that the lower boundary of the observable part of Jupiter's atmosphere is determined by the level of dense clouds composed of liquid ammonia. Interestingly, the rotational temperature is close to the brightness temperature in the shadow cast by the moons. A comparison of ammonia line spectra at different locations on Jupiter shows a strong variation in their intensities. This indicates horizontal inhomogeneity in the disk of Jupiter at the depths of the cloud layers that produce the observed absorption lines of ammonia. This observational data allows for the calculation of rotation. For the NH_3 λ6451.12 Å line, according to our data, the profile of this line has been constructed using approximate formulas, taking into account the instrumental profile.

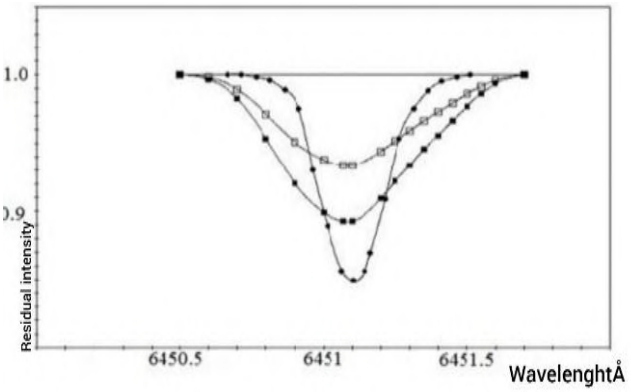

Figure 1: The profile of the NH_3 λ6451.12 Å absorption line in the spectrum of Jupiter, obtained in the SAO. (Equatorial belt – open squares – without considering the instrumental profile, black squares – with the instrumental profile taken into account) and Smith's observation (Ouen 1968) (black circles at the center of the planet's disk)

3. Calculation of the equivalent widths and half-widths of spectral lines

Long-term observations show that Jupiter's atmosphere is heterogeneous (Carlson et.al, 1987). This heterogeneity is also unstable – it changes over time. These variations are manifested in the changes in the intensity of the absorption bands observed in the molecular gas spectrum in the visible and infrared regions. These absorption lines and bands originate at different depths of the gas and cloud layers. The formation of ammonia absorption bands observed in the visible and near-infrared spectral regions occurs primarily within a multilayered cloud structure through the process of multiple scattering and in purely gaseous gaps between cloud layers. Therefore, visible variations in the intensity of NH_3 absorption bands can be interpreted as a consequence of changes in the structural characteristics of the clouds, as well as in the size and concentration of cloud particles. All of these factors are expected to influence the relative abundance of gaseous ammonia in different regions of Jupiter. In 2023, these variations were most clearly observed in the NH_3 absorption band at 6450 Å (Vdovichenko et al., 2025) Based on the intensity of spectral bands, it is possible to assess the physical conditions on the planet. In planetary physics, the study of the heterogeneity of temperature and its dependence on time is of great importance.

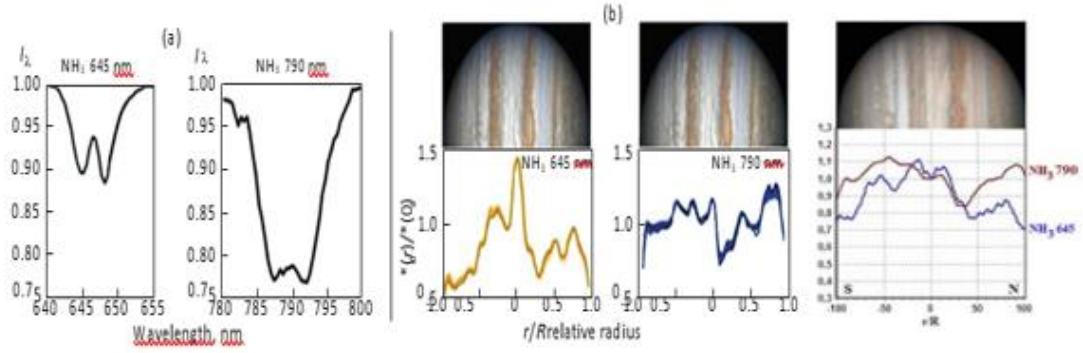

Fiqure 2: Variations in the meridional course of ammonia absorption in two absorption bands at 645 and 790 nm; ammnia absorption bands at 645 and 790 nm: (a) profiles.

Spectrograms of Jupiter in the λ 5200-7000 Å region were obtained by N.B. Ibrahimov at the Shamakhi Astrophysical Observatory, named after N. Tusi, using a two-meter reflector with a dispersion of 6 Å/mm (0.15 resolution) during 1970-71 (10 spectrograms) (Ibrahimov, 1975). These materials were processed and published for the central disk. In this work, spectral data from the NH_3 λ 6450 Å absorption band were used for the central equatorial zone (EZ), the northern equatorial band, and the southern equatorial band. This spectral material was obtained on 22.05.2023, using the 2-meter telescope of the N.Tusi Shamakhi Astrophysical Observatory with a CCD-matrix equipped Echelle spectrometer at a dispersion of 4 Å/mm. For this band, 20 lines were selected for the center, 14 for the northern band, and 11 for the southern band. The acquired data were processed using the DECH 95 and DECH 30 (http://www.gazinur.com/DECH-software.html) programs, and the equivalent widths and half-widths of the spectral lines were calculated. The obtained results are presented in the table below.

As seen, the equivalent width and half-width of the spectral lines are the largest at the center, and are larger in the southern region compared to the northern region. Based on the obtained results, it is possible to assess the physical conditions on Jupiter. For planetary atmospheres, the absorbing atmospheric model assumes that the formation of absorption bands or lines occurs in a uniformly mixed medium of absorbing gas and scattering aerosol. In such a medium, lines of varying intensities and different parts of the absorption band arise at different depths. Undoubtedly, this corresponds to various structural forms. In this case, the volume concentration of the gas and the volume scattering coefficient of the aerosol do not change with depth according to the same law. Even if we use a homogeneous atmospheric model for the analysis of spectrophotometric observations, in the case of actual inhomogeneity, we would obtain different values for the physical characteristics of the gas-aerosol medium depending on the intensity of the given absorption band. In real conditions, the rotational temperature is one such characteristic. The average temperature on Jupiter's disk has been determined by various authors since 1924. For instance, Zabriskie F.R. established that the temperature at the depth where hydrogen's S(0) and S(1) quadrupole lines form varies within the range of T = 170–200K, based on the intensities of these lines.

Although significant data on the study of planetary atmospheres can be obtained through Earth-based observations, results are also derived based on data provided by space probes. The data obtained from space probes have been compared with the results acquired from Earth-based observations (Simon-Miller A. et.al, 2006). It has been determined that temperature variations in the planet's lower latitudes and troposphere are associated with seasonal changes

Due to the sharp decrease in the saturated vapor pressure of ammonia, it can be assumed that the NH_3 concentration in Jupiter's outer atmosphere above the cloud layer is extremely low. The observed weak lines are practically formed within the cloud layer and are determined using the formula

$$T = \frac{E_2 - E_1}{\ln\frac{\beta_1}{\beta_2} + \ln\frac{a_1}{a_2} + \ln\frac{S_2}{S_1} + \frac{E_2 - E_1}{T_0}} \qquad (4)$$

Here, E_1 and E_2 correspond to the energy of the first and second spectral lines, respectively. α_1 represents the Lorentz half-width of the first spectral line, while α_2 represents that of the second spectral line. S_1 is the relative integral absorption coefficient of the first line, and S_2 is that of the second line. T_0 denotes room temperature and is assumed to be $T_0 = 294K$. β represents the difference between the reciprocal values of the single scattering albedo in the line and the continuous spectrum. Based on the obtained materials, the temperature has been determined for various pairs of spectral lines and is presented in the following table. The selection of spectral lines with equal intensity across different regions of the planetary disk allows for a more accurate and stable determination of physical parameters, particularly temperature. In the calculation of rotational temperature, it is crucial that the ratios of line intensities and the associated optical depths (τ) remain constant. If the intensities differ, the resulting temperature will be incorrect. For temperature determination from observed spectra, selecting regions with equal intensities is essential to correctly model the atmospheric structure and conditions. This approach ensures that the temperature estimations are not biased by local variations

Table 1: Equivalent Widths and Half-widths of Spectral Lines

center			north			south		
λ, Å	W, Å	$\Delta\lambda 1/2$, Å	λ, Å	W, Å	$\Delta\lambda 1/2$, Å	λ, Å	W, Å	$\Delta\lambda 1/2$, Å
6327,760	0,053	0,245	-	-	-	6327,704	0,047	0,264
6433,631	0,063	0,423	6433,665	0,025	0,222	-	-	-
6435,157	0,051	0,445	6435,125	0,018	0,235	6435,139	0,020	0,376
6444,792	0,070	0,205	-	-	-	-	-	-
6445,689	0,086	0,469	6445,686	0,024	0,21	6445,667	0,040	0,303
6446,574	0,091	0,852	6446,593	0,036	0,319	6446,536	0,043	0,304
6451,236	0,087	0,494	6451,233	0,046	0,299	-	-	-
6454,522	0,052	0,312	6454,547	0,034	0,366	6454,500	0,040	0,319
6457,290	0,091	0,574	6457,255	0,064	0,337	-	-	-
6457,292	0,087	0,574	6457,276	0,075	0,36	6457,274	0,067	0,324
6459,271	0,033	0,346	6459,249	0,020	0,335	-	-	-
6460,669	0,029	0,285	6460,628	0,016	0,176	6460,634	0,026	0,247
6464,858	0,019	0,327	-	-	-	6464,771	0,018	0,277
6465,515	0,046	0,331	6465,535	0,036	0,262	-	-	-
6470,867	0,036	0,349	6470,817	0,020	0,244	6470,872	0,025	0,244
6474,388	0,065	0,366	6474,417	0,045	0,399	6474,366	0,047	0,303
6478,548	0,021	0,442	6478,552	0,019	0,319	6478,580	0,015	0,297
6489,965	0,040	0,309	-	-	-	-	-	-
6490,028	0,041	0,306	-	-	-	-	-	-
6490,037	0,048	0,305	-	-	-	-	-	-
6501,852	0,034	0,906	6501,454	0,011	0,128	6501,779	0,049	0,277

Table 2: Calculated temperature values based on selected pairs of NH_3 lines

λ(Å)	**J**	**K**	**E_{inv}**	**hc/k**	**A**	**B**	**k**	**E**	**a**	**S**	**T (K)**
6444,792	3	1	-11,7	1,43391	5,93	10,265	1,4E-16	162,025	0,178	3,28	183,09
6451,236	2	0	-10,1	1,43391	5,93	10,265	1,4E-16	81,0734	0,152	1,8	
6444,792	3	1	-11,7	1,43391	5,93	10,265	1,4E-16	162,025	0,178	3,28	148,8
6465,515	3	3	-13,1	1,43391	5,93	10,265	1,4E-16	111,293	0,176	3,68	
6445,689	3	-2	-12,7	1,43391	5,93	10,265	1,4E-16	142,66	0,126	4	79,81
6465,515	3	3	-13,1	1,43391	5,93	10,265	1,4E-16	111,293	0,176	3,68	
6446,574	3	3	-13,1	1,43391	5,93	10,265	1,4E-16	111,293	0,152	4,8	116,82
6457,290	1	0	9,8	1,43391	5,93	10,265	1,4E-16	36,4644	0,178	4,61	
6446,574	3	3	-13,1	1,43391	5,93	10,265	1,4E-16	111,293	0,152	4,8	78,14
6459,271	4	-4	-12,6	1,43391	5,93	10,265	1,4E-16	185,892	0,213	1,89	
6451,236	2	0	-10,1	1,43391	5,93	10,265	1,4E-16	81,0734	0,152	1,8	104,19
6460,669	3	-3	13,1	1,43391	5,93	10,265	1,4E-16	130,077	0,158	1,94	
6459,271	4	-4	-12,6	1,43391	5,93	10,265	1,4E-16	185,892	0,213	1,89	179,09
6465,515	3	3	-13,1	1,43391	5,93	10,265	1,4E-16	111,293	0,176	3,68	

in cloud thickness, or instrumental effects, thereby improving the reliability of atmospheric diagnostics.

As can be seen, the variation in temperature for different line pairs may be caused by lightning occurring in those layers. Under such conditions, the amount of ammonia gas increases, or a thin layer consisting of ammonia ice crystals passes into a gaseous state. Calculations indicate that the temperature on Jupiter's disk is approximately 127 K, which is consistent with the results obtained by other researchers.

4. Conclusion

1. In the presented work, the lines of the λ6450Å band in the spectrum of the planet Jupiter have been studied. Spectral material obtained with a 2-meter telescope at the observatory, using a CCD matrix and a 4 Å/mm dispersion echelle spectrometer, was analyzed. In this spectral region, 20 lines for the center, 14 lines for the northern zone, and 11 lines for the southern zone were selected. The obtained data were processed using the DECH 95 and DECH 30 programs.
2. The spectrophotometric characteristics of these spectral lines, including their equivalent widths and half-widths, have been determined. The results obtained are presented in tables.
3. Based on the obtained observational data, the rotation temperature in the details of Jupiter's disk has been determined for various pairs of spectral lines. As seen, the temperature varies between approximately 180 K and 80 K for different line pairs. Such temperature changes could be caused by lightning occurring in those layers. These findings are important for understanding the dynamic and non-homogeneous nature of Jupiter's atmospheric layers.
4. By summarizing the obtained results, the average temperature in the details of Jupiter's disk is found to be approximately 127 K, which is consistent with the results obtained by other authors.

Acknowledgements. The author expresses sin- cere gratitude to the reviewer and the scientific editor for their interest in the article, for their careful review of its content, and for their highly constructive comments, which have contributed to better structuring the paper and significantly improving its clarity and comprehensibility.

References

Carlson B.E., Prather H.J., Rossow W.B.: 1987, *ApJ*., **322**, 559.

Galazutdinov G.: http://www.gazinur.com/DECH-software.html

Ibragimov N.B.: 1975, *AZh*, **52**, 4, 895.

Owen T., Woodman J. H.: 1968, *ApJ*, **154**, L21.

Simon-Miller Amy A., Conrath Barney J., Gierasch Peter J. et al.: 2006, *Icar*, **180**, 98.

Smith W.H., Macy W., Cochran W.: 1980, *Icar*, **42**, 93.

Spinrad H., Trafton L.: 1963, *Icar*, **2**, 19.

Vdovichenko V.D., Karimov A.M., Lysenko P.G. et al.: 2025, *SoSyR*, 59, 57. https://doi.org/10.1134/S0038094624601750

Zabriskie F.R.: 1962, *AJ*, **67**, 168.

https://doi.org/10.18524/1810-4215.2025.38.343165

THE FEATURES OF FI SGE PHOTOMETRIC VARIABILITY ON TRANSITING EXOPLANET SURVEY SATELLITE OBSERVATIONS

L. E. Keir[1,2], E. A. Panko[2], M. Yu. Pyatnytskyy[3],

[1] Vihorlat Astronomical Observatory, Humenne, Slovakia,
partneroae@gmail.com
[2] Odesa I. I. Mechnikov National University, Odesa, Ukraine,
panko.elena@gmail.com
[3] Private Observatory "Osokorky", Kyiv, Ukraine,
mpyat2@gmail.com

ABSTRACT. We present the result of the analysis of the FI Sge individual light curves constructed on Transiting Exoplanet Survey Satellite (TESS) observations. FI Sge the RR Lyrae pulsating variable star with bicyclicity effects and possible Blazhko effect. In the present study, we analyzed 3603 photometric data obtained by the Transiting Exoplanet Survey Satellite (TESS) in the special TESS IR bandpass with a time resolution of about 10 minutes. The observations covered a 27-day interval (BJD 2459769.90 – 2459796.12) with a small gap of about a day. The full data set contains 52 minima and 51 maxima of the seasonal light curve. We suppose that for this data set, the analysis of the light curve shapes in minima provides more reliable results. We studied the variations of the minima' shapes of the individual light curves at common and for the separate affinity groups. The last one allowed us to detect not only classical bicyclicity, but also secondary bicyclicity for FI Sge. This result was obtained at first and it is atypical behavior of light curves for pulsating variable stars.

Keywords: pulsating stars: RR Lyr type: light curves; Blazhko effect; bicyclicity; data analysis

АНОТАЦІЯ. Ми представляємо результат аналізу індивідуальних кривих блиску FI Sge, побудованих на основі спостережень Transiting Exoplanet Survey Satellite (TESS). FI Sge – пульсуюча змінна зоря типу RR Ліри з виявленою біциклічністю та ймовірним ефектом Блажка. У цьому дослідженні ми проаналізували 3603 фотометричних точок, отриманих супутником TESS в інфрачервоній фотометричній смузі TESS з часовою роздільною здатністю близько 10 хвилин. Спостереження охоплювали 27-денний інтервал (BJD 2459769.90 – 2459796.12) з перервою у спостереженнях близько доби. Повний набір даних містить 52 мінімуми та 51 максимум сезонної кривої блиску. Ми вважаємо, що для цього набору даних аналіз форми кривої блиску в мінімумах дає більш надійні та значущі результати. Ми проаналізували варіації форм мінімумів окремих кривих блиску для повного набору даних та для окремих груп спорідненості. Останній підхід дозволив нам виявити для FI Sge не тільки класичну біциклічність, але й вторинну біциклічність. Цей результат був отриманий вперше, і він є нетиповою поведінкою кривих блиску для пульсуючих змінних зір.

Ключові слова: пульсуючі зорі: RR Lyr тип: криві блиску; ефект Блажка; біциклічність; аналіз даних.

1. Introduction

The poorly studied pulsating variable of the RR Lyrae type FI Sge ($RA_{2000.0} = 20^h13^m16.2^s$, $Dec_{2000.0} = +17°30'37''$, RRab, magnitude in the limits of $13.2 - 14.3^m(p)$, Sp = A2) in a long dense series of observations shows atypical brightness variations for this type of star. The variability of the star was discovered in 1936 by Hoffmeister (1936) from photographic plates of the Sonnenberg Observatory. According to GCVS 5 (and GCVS 4), the initial pulsation epoch and period of the star are: $E = 2428333.441^d$ and $P = 0.5047545^d$ (Samus et al., 2017). Nevertheless, some other values of the pulsating period were published. Mainz (2017), based on her own observations, which were carried out over 5 nights in April 2017, determined the period value to be 0.50477d. She also analyzed the $(O-C)$ variations of the times of maxima using available literature sources (Richter, 1961, Wils et

al., 2006, and Agerer & Hubscher, 2002), and suggested that the period changed after the epoch of 2452000 J.D. As a result, the phase light curves with the new period value, constructed using the NSVS and ASAS data, differ from each other in amplitude and phase. The phase shift from the initial epoch of the phase light curve according to the NSVS data was 0.15 of the variability period. Skarka and Cagas observed FI Sge without a filter over 14 nights in August, September, and October of 2017 (Skarka & Cagas, 2017). Based on these observations, they found evidence of the Blazhko effect for FI Sge with a period of 22.4 days, in contrast to Mainz, who did not detect this effect (Mainz, 2017). More, in the list of 242 known Galactic field stars exhibiting the Blazhko effect FI Sge does not present (Skarka, 2013).

In the Gaia DR2 (Gaia Collaboration, 2018) the period for FI Sge, corresponding to the fundamental pulsation mode, is noted as 0.50479709^d. Keir (2023) determined pulsation period as 0.50500^d, based on the long-term dense series of observations, which contained total data of 55 nights of the observation seasons of 2013, 2014, and 2018. These data also allowed detection of the bicyclicity effect for FI Sge(Keir, 2023, Keir & Udovichenko, 2024). So, FI Sge is a star RRab type with bicyclicity and possible Blazhko effect.

The bicyclicity phenomenon in RR Lyr stars with the Blazhko effect was discovered in 2010 from Kepler observations and described by Smolec (2016). For the stars showing the bicyclicity effect, two consecutive pulsation cycles have different amplitudes of the light-curve maxima and different modulations of these maxima. Nevertheless, the difference in the amplitude of successive maxima alone cannot be a determining feature of this phenomenon. With different modulation dynamics in adjacent cycles, a situation may arise in which the observation period coincides with the moment when the amplitudes of consecutive maxima will differ slightly. In this case, the effect of bicyclicity will be smoothed out. We believe that the phenomenon of bicyclicity is determined precisely by the difference between two adjacent pulsation cycles. Namely, bicyclicity manifests itself in differences in the amplitude and shape of both minima and maxima, as well as in the dynamics of these differences. Taking into consideration all these differences, the phenomenon of bicyclicity cannot be explained by oscillations with two different periods or two different pulsation modes.

2. Observational data

Our observational data set contains 3603 individual photometric data obtained by the Transiting Exoplanet Survey Satellite (TESS) in the $600 - 1000\,nm$ photometric bandpass. The red end of the bandpass represents the red limit of TESS detector sensitivity, and the width of $400\,nm$ was the largest practical choice for the cosmic IR observations. This bandpass is centered on the traditional I_C band but is much wider. It is comparable to the union of the R_C, I_C, and z bands (Ricker et al., 2015). The observations span a 27-day interval (BJD 2459769.90 − 2459796.12) with a small gap over a day. The full data set contains 52 minima and 51 maxima of the seasonal light curve. The brightness of the star varied from 12.829^m to 13.616^m.

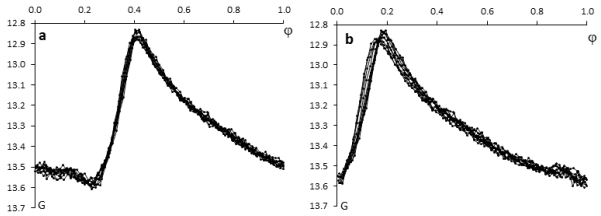

Figure 1: TESS observation data for FI Sge. They are shown: *a*) 10 phase light curves of FI Sge, constructed with a variability period of 0.504748^d, and *b*) the same data constructed with a period of 0.50500^d

If we represent the observation data in a dot plot, we can't detect the relationships between individual light curves (Fig. 1*a*, for example). In the classical dots' representation, we lose the opportunity to trace the dynamics of the light curve changes from cycle to cycle. We assume all points are important and reflect the individual characteristics of individual pulsation cycles. In a dot plot, we perceive the scatter of observational data points as variations in the light curves due to observational errors. Using the line-dot plots, we can trace to a change in the shape of light curves in the individual cycles. The result we obtained by applying the $O - C$ minimum method to determine the variability period is shown in Fig. 1*a*. We see scattered data defining some mean curve.

However, for pulsating stars, modulation of the brightness amplitude without modulation of the period contradicts the theory of these stars' pulsations. Using $O - C$ technique to determine the variability period of FI Sge, we obtain a false value for the variability period. Using the period determined for this star by another method (Keir, 2023), we obtain phase curves in which modulation of the brightness amplitude is accompanied by modulation of the pulsation period. Lower brightness maxima correspond to shorter pulsation periods. Maxima with a larger brightness amplitude correspond to longer pulsation periods (Fig. 1*b*).

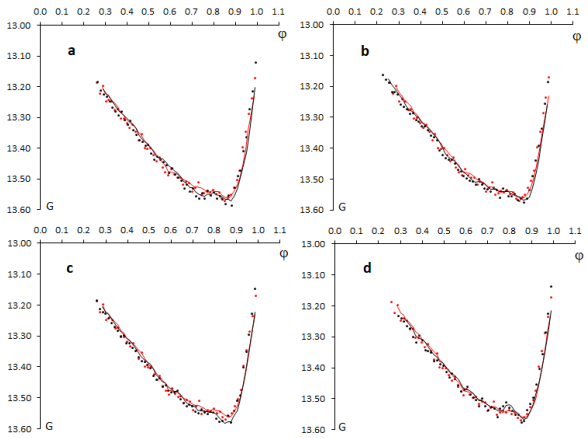

Figure 2: Difference in shapes of 5 sequential light curves' minima. Cycle number 1 is shown as red and others are shown as black: *a*) cycles 1 and 2, *b*) cycles 1 and 3, *c*) cycles 1 and 4, *d*) cycles 1 and 5

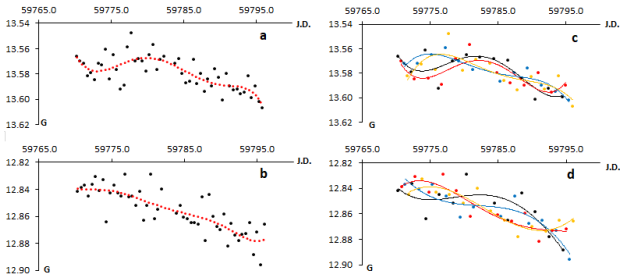

Figure 3: The BJD moments are shown: *a*) for minima for all cycles, *b*) for maxima for all cycles. The same diagrams: *c*) for the minima in the affinity groups, *d*) the maxima in the affinity groups, and the approximation for different affinity groups, are present as color lines

3. Light curves analysis and discussion

We approximated the light curves' maxima and minima by sixth-degree polynomials and determined phases and amplitudes of the maxima and minima (Fig. 2*a*,*b*). The amplitude of adjacent maxima changes only slightly over this time ($0.01 - 0.02^m$). The TESS telescope's time resolution is 10 minutes, so the maxima are recorded by 3 or 4 points only. Given that the shape of this star's light curve changes during pulsations, we suppose that maxima approximating do not provide a very reliable result in this case. Therefore, we investigated the dynamics of changes in the light curve shapes at minima in all pulsation cycles.

We smoothed the observational data with a three-point moving average and constructed 2D affinity diagrams. In these diagrams, we horizontally plotted two light curves with two minima in the each diagram, namely: 1+2, 1+3, 1+4, 1+5. Vertically, we took all the minima in order: 1, 2, 3, ...52. We obtained an affinity matrix consisting of 208 diagrams. The first row of this matrix is shown in Fig. 2. The figure shows that the plots with adjacent minima (1+2, 2+3...) and minima separated by 2 (1+4, 2+5...) coincide with each other much worse than the plots with minima separated by 1 (1+3, 2+4...) and by 3 (1+5, 2+6...). Other rows of the affinity matrix show a similar coincidence. Therefore, we divided all the graphs with minima into two groups: odd (1, 3, 5,... 51) and even (2, 4, 6, ... 52). This division reflects that the shapes of the minima of adjacent pulsation cycles are different. Thus, the pulsation cycles are different. This behavior of pulsation cycles is characteristic of the phenomenon of bicyclicity.

We also compared similar affinity diagrams with minima at intervals of 1 and 3 cycles, that is, 1+3, 2+4..., and 1+5, 2+6... The similarity of the diagrams at intervals of 3 cycles was better. Therefore, we further divided the odd and even minima into two groups. All odd ones at intervals of 1, 5, 9, 13,... 49 and 3, 7, 11, 15,... 51. All even ones at intervals of 2, 6, 10, ... 50 and 4, 8, 12, 16, ... 52. Thus, we obtained four groups of the most similar light curve minimum plots. This repeated division of minima characterizes a phenomenon that we conventionally call secondary bicyclicity. Next, we divided all the minima and corresponding maxima into four groups, accordingly to the above. In Fig. 3, we compare the BJD times of minima and maxima for all cycles (Fig. 3 *a*,*b*) and separately for affinity groups, approximating their points with fourth-degree polynomials (Fig. 3*c*,*d*).

From (Fig. 3*c*,*d*), it is clearly seen that graphs are divided according to the times of the minima and maxima. The times of the maxima are grouped according to the cycles' affinity: $1 - 3$ and $2 - 4$. The times of the maxima are grouped according to the cycles' affinity: $1 - 2$ and $3 - 4$. This division of the graphs of the moments of minima suggests that several processes overlap at the moments of minimum, and pulsations and minima for stars of this type are not an unambiguous criterion of their pulsation activity. The best marker for sorting a light curve by affinity group and secondary bicyclicity is its shape at the minimum. We suggest that this phenomenon still requires further study and analysis.

4. Conclusion

1. Our analysis of the FI Sge light curves' shape in minima indicated that, despite low pulsation activity at the dates of observations, bicyclicity and secondary bicyclicity were detected.

2. Dividing minima into affinity groups allows for

analysis of changes in stellar activity dynamics within each minima group separately.

3. Dividing minima into affinity groups allows tracing the bicyclicity and secondary bicyclicity effects.

4. In the star FI Sge, at certain time intervals, a decrease in the amplitude of maximum brightness is observed, accompanied by a decrease in the amplitude of minimum brightness, which is atypical for pulsating variable stars.

5. For pulsating stars with amplitude modulation, it is not recommended to determine the variability period using the $O - C$ minimum method. This can lead to a false determination of the variability period.

Acknowledgements. The authors express their sincere gratitude to Ivan Andonov for fruitful discussions during the preparation of the paper.

This research has made use of NASA's Astrophysics Data System.

References

Agerer F., Hubscher J.: 2002, *IBVS*, 5296.
Hoffmeister C.: 1936, *AN*, **259**, 37.
Gaia Collaboration: 2018. VizieR Online Data Catalog: Gaia DR2. https://vizier.cds.unistra.fr/viz-bin/VizieR?-source=I/345
Keir L.E.: 2023, *OAP*, **36**, 59
Keir L., Udovichenko S.: 2024, *OAP*, **37**, 35.
Maintz G.: 2017, *BAVSR*, **66**, 128.
Richter G.: 1961, *VeSon*, **4**, 434.
Ricker G.R., Winn J.N., Vanderspek R., et al.: 2015, *Journal of Astronomical Telescopes, Instruments, and Systems*, **1**, id. 014003.
Samus N. N., Kazarovets E. V., Durlevich O. V., et al.: 2017, *Astron. Zh*, **94**, 87.
Skarka M., Cagas P.: 2017, *IBVS*, 6229.
Skarka M.: 2013, *A&A*, **549**, A101.
Smolec R.: 2016, *PASP.conf*, **3**, 22.
Wils P., Lloyd C., Bernhard K.: 2006, *MNRAS*, **368**, 1757.

https://doi.org/10.18524/1810-4215.2025.38.341537

SPECTRAL STUDY OF THE HERBIG Ae STAR HD 31648. THE Hα AND Hβ EMISSION LINES

S. O. Mammadova[1],V. I. Aliyeva[1], B. N. Rustamov[2,1]

[1] Shamakhi Astrophysical Observatory named after Nasraddin Tusi, Azerbaijan
[2] Baku State University, Baku, Azerbaijan
bayram_rustam@yahoo.com

ABSTRACT. We present the results of observations of the Hα and Hβ lines in spectrum of Herbig Ae star HD 31648. Seven spectra from the Be Stars Spectra Database, with a spectral resolution of R $\approx$ 11,000, were used, along with three spectra obtained using the 2-m telescope at the Shamakhi Astrophysical Observatory with the Shamakhi Fiber Echelle Spectrograph (R $\approx$ 28,000). In the spectra at our disposal, the Hα line is predominantly observed as a P Cyg III type profile, characterized by a line intensity ratio of Ib/Ir $\ll$1 and in two cases it was observed as a classical P Cyg type profile – a red-shifted emission peak with blue-shifted absorption. There is no correlation in the changes in the intensity of the blue (Ib) and red (Ir) components. The blue component undergoes the greatest changes, and variability is also present in the intensity of the red emission peak. The Hβ line profile in the central part shows a P Cyg – type structure with wide photospheric wings. The red emission component of the Hβ line shows strong variability, which correlated with the red emission component of the Hα line. In general, variability in the profiles of the Hα and Hβ lines occur synchronously. In the work, a comparative analysis of the behavior of the Hα and Hβ lines is carried out using similar data from published data.

Keywords: pre-main sequence – stars: variables: Herbig Ae/Be: individual: HD31648.

АНОТАЦІЯ. Ми представляємо результати спостережень ліній Hα та Hβ у спектрі зорі типу Ae Хербіга — HD 31648. Для дослідження було використано сім спектрів із бази даних Be Stars Spectra Database зі спектральною роздільною здатністю R $\approx$ 11 000, а також три спектри, отримані на 2-метровому телескопі Шамахинської астрофізичної обсерваторії з використанням Шамахинського волоконного ешель-спектрографа (R $\approx$ 28 000). У наявних спектрах лінія Hα переважно спостерігається як профіль типу P Cyg III, що характеризується співвідношенням інтенсивностей синього та червоного компонентів Ib/Ir $\ll$1, а в двох випадках зафіксовано класичний профіль типу P Cyg — червонозміщений емісійний пік із синьозміщеним поглинанням. Кореляції між змінами інтенсивностей синього (Ib) і червоного (Ir) компонентів не спостерігається. Найбільших змін зазнає синій компонент, проте варіації також присутні в інтенсивності червоного емісійного піку. Профіль лінії Hβ у центральній частині показує структуру типу P Cyg із широкими фотосферними крилами. Червоний емісійний компонент лінії Hβ демонструє значну змінність, що корелює зі змінами червоного емісійного компонента лінії Hα. Загалом змінність профілів ліній Hα і Hβ проявляється синхронно. У роботі проведено порівняльний аналіз поведінки ліній Hα і Hβ із використанням аналогічних опублікованих даних.

Ключові слова: зорі до головної послідовності – змінні зорі до головної послідовності – Herbig Ae/Be — окрема зоря: HD 31648.

1. Introduction

The formation of stars and planetary systems is one of the primary research topics in modern astrophysics. Studies of young stars with small (stars T Tauri type) and intermediate (stars Ae/Be Herbig type) masses connected with early stages of stellar evolution are among the priority areas of astrophysics. At the beginning of the 21st century, considerable progress took place in the study of the physical processes of the interaction of a star and an accretion disk, also in the numerical simulation of various variants of the formation of a stellar wind and star accretion of matter.

Comparison of the observed characteristics of young stars with model calculations requires sufficiently long-term spectral observations, which make it possible to estimate the characteristic time of accretion and wind variability.

According to modern astrophysical concepts, the physics of the observed particularities of young stars type Ae/Be Herbig, in general, is determined by the

results of the interaction between the young star and the surrounding circumstellar medium.

The goal of this message: based on the spectral data of the young star type Herbig Ae HD31648, to study the observed peculiarities of the star's emission in the regimes of accretion and stellar wind.

HD 31648 (MWC480) is an isolated Herbig Ae star in the Taurus-Auriga star-forming region, spectral class of the star is A2-A3e, one of the brightest (V $\sim$ $7^m.6$) stars of this type in the northern sky. The star HD31648 belongs to the group of photometrically quiet young stars with signs of matter outflow in the spectrum. Its age is estimated 2,5–7 million years, star mass $M_* = (1.65 - 2.2)\ M_\odot$, luminosity $L_* = (11.2 - 32.4)\ L_\odot$, $R_* = 1.67\ R_\odot$, $T_{eff} = 8250 - 8710$ K (Augereau et al., 2001; Montesinos et al., 2009).

The star HD31648 has been studied in detail spectroscopically in the optical range mainly in the following works: Beskrovnaya and Pogodin, 2004; Kozlova, Grinin and Chuntonov, 2003; Kozlova, Alekseev and Shakhovskoi, 2007; Mendigutia, Eiroa, Montesinos et al., 2011; Mendigutia, Brittain, Eiroa et al., 2013; Tambovtseva et al., 2016.

2. Observations and data reduction

Seven spectra from the Be Stars Spectra Database, with a spectral resolution of R $\approx$ 11,000, were used, along with four spectra were carried out at the Cassegrain focus of the 2-m telescope of the Shamakhi Astrophysical Observatory, on fiber echelle spectrograph (ShAFES) with the spectral resolution of R = 28,000. During the period December 2019 – January 2020 on every four nights, 2 spectra of the studied star, also 2 spectra of a hot, rapidly rotating a standard star A2 θ And as a standard for remove telluric lines in the spectrum of HD31648 (Mikailov, Musaev, Alekberov et al., 2020).

The reduction of echelle spectra was carried out according to the standard technique using the recent version of the DECH 30 program developed by Galazutdinov (1992).

3. Results of observations

Emission Hα and Hβ lines in the spectrum of the star HD31648 are formed in the sufficiently extended circumstellar shell and show profiles of type P Cyg, which are direct indicators of mass ejection.

In the spectrums at our disposal, the radial velocities of the Hα and Hβ line components were measured, and their profiles were constructed (Fig. 1).

As it is known, the results of the interaction of a star with its circumstellar matter show itself in the form of an outflow (stellar wind) or star accretion of matter (accretion).

It should be noted that in terms of observational astrophysics, spectral signs of stellar wind and star accretion of matter are shown in the so-called P Cyg and inverse P Cyg profiles, respectively, in certain diagnostic lines.

As can be seen from Fig. 1 the Hα line is predominantly observed as a P Cyg III type profile, characterized by a line intensity ratio of Ib/Ir $\ll$ 1 and in two cases it was observed as a classical P Cyg type profile – a red-shifted emission peak with blue-shifted absorption.

There is no correlation in the changes in the intensity of the blue (Ib) and red (Ir) components. The blue component undergoes the greatest changes, and variability is also present in the intensity of the red emission peak.

The Hβ line profile in the central part shows a P Cyg type structure with wide photospheric wings. The red emission component of the Hβ line shows strong variability, which correlated with the red emission component of the Hα line. In general, variability in the profiles of the Hα and Hβ lines occur synchronously. In the work, a comparative analysis of the behavior of the Hα and Hβ lines is carried out using similar data from published data([Beskrovnaya and Pogodin, 2004, Tambovtseva et al., 2016).

When processing echelle spectra of early spectral type stars, in particular Herbig Ae/Be stars, one of the main difficulties is the determination of the continuum level, due to the broad wings of the hydrogen lines. We constructed a continuum for orders containing the Hα and Hβ lines by interpolating the continua of two adjacent orders. After this procedure, the continuum shape was refined using the spectrum of the standard star obtained under the same conditions. Fig. 2 shows the profiles of the Hα and Hβ lines in the spectrum of HD 31648 and the standard star θ And (sp. A2). As a result, we obtained a close match of the outer part of the wings of the photospheric profiles of Hα and Hβ in the spectra of HD 31648 and the standard star θ And.

The profiles of the Hα and Hβ lines in the spectrum of the star HD 31648 presented in Fig. 1 according to our data in appearance are generally consistent with similar data published in the works (Beskrovnaya and Pogodin, 2004, Tambovtseva et al., 2016).

4. Conclusions

We present preliminary results of observations of the Hα and Hβ lines in the spectrum of the Herbig Ae star HD 31648.

- In the spectra at our disposal, the Hα line is predominantly observed as a P Cyg III type profile, characterized by a line intensity ratio of Ib/Ir $\ll$ 1 and in two cases it was observed as a classical P Cyg type

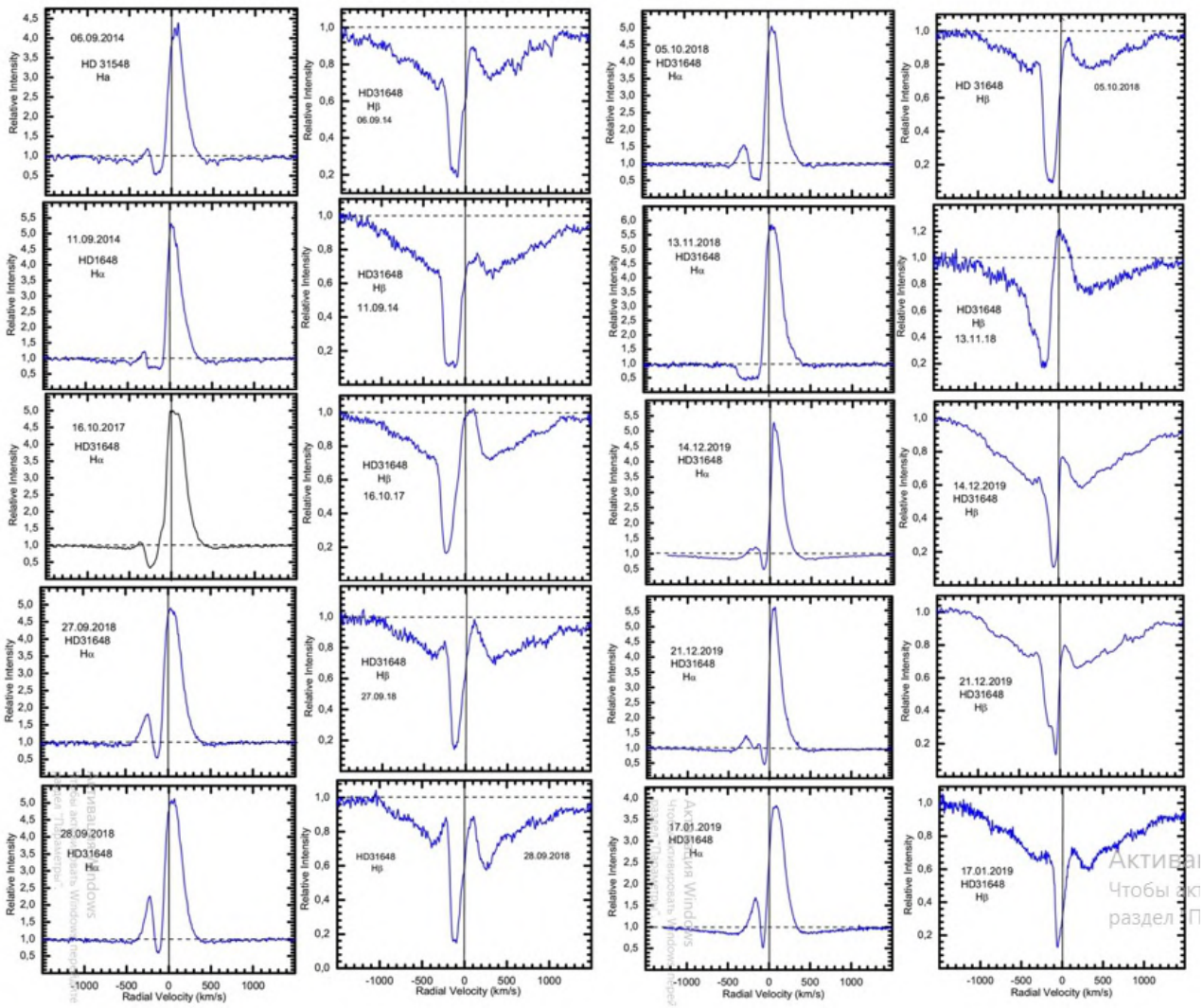

Figure 1: Profiles of the Hα and Hβ lines in the spectrum of HD 31648

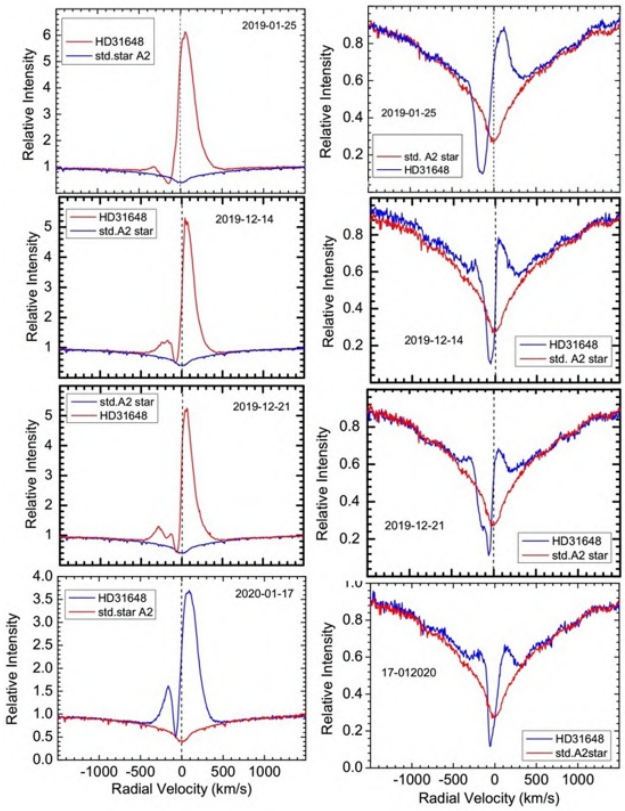

Figure 2: Profiles of the Hα and Hβ lines in the spectrum of HD 31648 and the standard star θAnd (sp. A2)

profile – a red-shifted emission peak with blue-shifted absorption.

• There is no correlation in the changes in intensity of the blue (Ib) and red (Ir) components.
• The blue component undergoes the greatest changes, and variability is also present in the intensity of the red emission peak.
• The Hβ line profile in the central part shows a P Cyg-type structure with wide photospheric wings.
• The red emission component of the Hβ line shows strong variability, which correlated with the red emission component of the Hα line.
• In general, variability in the profiles of the Hα and Hβ lines occur synchronously. In the work, a comparative analysis of the behavior of the Hα and Hβ lines is carried out using similar data from published data.

References

Augereau J.C. et al.: 2001, *A&A*, **365**, 78.
Beskrovnaya N.G. and Pogodin M.A.: 2004, *A&A*, **414**, 2.
Galazutdinov G.A.: 1992, Preprint SAO, 92.
Kozlova O.V., Grinin V.P., and Chuntonov G.A.: 2003, *Ap*, **46**, 265.
Kozlova O.V., Alekseev I.Yu., and Shakhovskoi D.N.: 2007, *Ap*, **50**, 467.
Mendigutia I., Eiroa C., Montesinos B. et al.: 2011, *A&A*, **529**, A34.
Mendigutia I., Brittain S., Eiroa C. et al.: 2013, *ApJ*, **776**, 44.
Mikailov Kh.M, Musaev F.A., Alekberov I.A. et al.: 2020, *KPCB*, **36**, 22.
Montesinos B. et al.: 2009, *A&A*, **495**, 901.
Tambovtseva L.V. et al.: 2016, *AstL*, **42**, 583.

https://doi.org/10.18524/1810-4215.2025.38.340398

A PERSPECTIVE ON ECLIPSING BINARY STAR STUDIES IN THE POST-GAIA ERA

E. F. Milone

University of Calgary, Canada

ABSTRACT. Eclipsing binary stars have intrigued astronomers for centuries. To study them is to journey through discoveries and innovations. One of the earliest significant insights came in 1783 when 18-year-old John Goodricke boldly proposed that the periodic dimming of the star Algol, which he and his friend and mentor Edward Pigott had carefully studied, was due to an eclipse by a large dark body revolving about Algol. The communication so impressed the Royal Society of London that Goodricke was awarded the prestigious Copley medal that same year. As observational techniques evolved and photographic photometry developed, the quality as well as the quantity of data increased and by the early 20th century, gravitational physics had matured sufficiently that Henry Norris Russell and Harlow Shapley could provide quantitative procedures for finding the properties of stars in eclipsing systems to capitalize on them, an example of a path characterized by Russell (1948) as the Royal Road of Eclipses. Over the following decades, deeper understanding of the physics governing systems of short-period binary stars led to more sophisticated treatments. Zdenêc Kopal and other researchers expanded the analytical framework and initiated more rigorous studies of the internal and orbital dynamics of these systems. The advent of high-speed computing in the 1970s revolutionized the field by enabling simulations of increasing complexity. Continued computational and analytical improvements, coupled with the explosive growth in observational data from wide-field surveys culminating in the Gaia mission, are propelling eclipsing binary research into a new era. We have now both the computational power and the observational depth to probe stellar structure and evolution with unprecedented precision. This presentation highlights key milestones in the study of eclipsing binaries, innovative capabilities in data acquisition and modeling, and the promising role of high-precision infrared photometry. Particular attention will be paid to the enhanced precision attainable through the use of improved passbands for ground-based infrared photometry at local observatories, and to the extended functionalities of the Wilson-Devinney modeling framework, and complementary analytical tools and programs.

Keywords: binary stars, eclipsing binaries, photometry, Wilson-Devinney models and program, Gaia, TESS, IRWG passbands.

АНОТАЦІЯ. Затемнювані подвійні зорі інтригували астрономів упродовж століть. Їх вивчення – це подорож шляхом відкриттів та інновацій. Одне з перших значних прозрінь сталося в 1783 році, коли 18-річний Джон Гудрайк сміливо припустив, що періодичне ослаблення блиску зорі Алголь, яку він і його друг і наставник Едвард Піготт ретельно вивчали, викликано затемненням темним великим тілом, що обертається навколо Алголю. Це повідомлення настільки вразило Лондонське королівське товариство, що того ж року Гудрайк був нагороджений престижною медаллю Каплі. У міру розвитку методів спостережень та розвитку фотографічної фотометрії якість і кількість даних зростали, і до початку XX століття гравітаційна фізика досягла достатньої зрілості, щоб Генрі Норріс Рассел і Харлоу Шеплі змогли запропонувати кількісні процедури для визначення властивостей зір у затемнених системах і отримати з них вигоду, – приклад шляху, який Рассел (1948) охарактеризував як Королівську дорогу затемнень. У наступні десятиліття глибше розуміння фізичних процесів, управляючих системами короткоперіодичних подвійних зір, призвело до появи складніших методів дослідження. Зденек Копал та інші дослідники розширили аналітичні рамки та ініціювали суворіші дослідження внутрішньої та орбітальної динаміки цих систем. Поява високошвидкісних обчислень у 1970-х роках справила революцію у цій галузі, дозволивши проводити моделювання дедалі більшої складності. Удосконалення обчислювальних та аналітичних технологій, що триває, у поєднанні зі стрімким зростанням обсягу спостережних даних, отриманих у ході широкосмугових оглядів, кульмінацією яких стала місія Gaia, виводять дослідження затемнюваних подвійних зір на новий рівень. Тепер у нас є як обчислювальна потужність, так і глибина спостережень, що дозволяють досліджувати структуру та еволюцію зір із безпрецедентною точністю. У цій презентації висвітлюються ключові віхи у вивченні затемнюваних подвійних зір, інноваційні можливості збору даних та моделювання, а також перспективна роль високоточної інфрачервоної фотометрії. Особливу увагу приділено підвищенню точності, яка досягається за рахунок використання покращених смуг пропускання для наземної інфрачервоної фотометрії в місцевих обсерваторіях, а також розширеним функціональним можливостям моделі Вілсона-Девінні

та додатковим аналітичним інструментам та програмам.

Ключові слова: подвійні зорі, затемнювані подвійні зорі, фотометрія, моделі та програма Вілсона-Девінні, Gaia, TESS, смуги пропускання IRWG.

1. Introduction

One may ask why, after centuries of study, we should continue to observe and analyze binary stars. One may answer: there are many of them! More than half of all stars are in binary or multiple orbital systems. And there are many other reasons! The Earth and every living thing on it depends fundamentally on our local star and the conditions around it, so we should find out a lot about stars. That means getting fundamental data such as the sizes, masses, luminosities (involving sizes and temperatures), distances, and ages of the stars to find how they change over time and why. Such changes result in different positions on color-magnitude diagrams, on isochrone plots, and on evolutionary tracks. Additionally, we would like to observe and to explore the evolution of interacting components. These include stellar wind buffeted or magnetically coupled components as in hot, massive binaries, or cooler RS CVn systems, respectively, or stars undergoing common envelope evolution, or those undergoing mass exchange at varying rates from semi-detached binaries to over-contact W UMa systems to cataclysmic variables and various types of nova-like variables to type Ia supernovae. And then there are the merger products such as blue stragglers (stars in clusters that are too bright and blue, for their positions on plots of luminosity vs. temperature or color), and which, when found in eclipsing systems in globular clusters, may provide clues of ancient hierarchical systems. Finally there are binary systems involving brown dwarfs, white dwarfs, neutron stars, and black holes in various combinations. Milone (2003) provides more details of the contributions to astrophysics of observations of binary stars, anticipated especially from the Gaia mission; that mission did not disappoint; El-Badry (2024) describes the resulting "binary star renaissance."

A unique contribution of *eclipsing* binary stars is the information gotten by monitoring one star scanning the surface of the other, yielding not only the radii from the precise timings of the four contacts of a total eclipse, but also the limb-darkening resulting from the star's opacity and temperature profiles, gravity brightening related to the tidal elongation, and active region phenomena such as spots, faculae, and prominences. Additionally, information about other components may be seen in changes in the timing of the eclipses and in measurements of 3rd light. These key contributions require highly precise photometric observations. A bonus is their usefulness as potential standard candles (once fully characterized) or, rather, non-standard distance indicators, as each binary system is unique so a derived distance for it does not depend on statistical correlations such as the period-luminosity relations for Cepheids. It does depend on accurate standardization and flux calibration, and distances from eclipsing binaries can be compared with direct parallax measurements, available now from the Gaia mission in unprecedented numbers. Finally, eclipsing variables self-advertise and are not hard to find: Gaia DR3 lists 2,184,447 eclipsing binaries (Mowlavi et al., 2023), about 20% of all variable objects found thus far in the mission.

The study of eclipsing binary stars is divisible into observational and analytical components, both historically and functionally. A model to be used in the analyses must be physically accurate in order to extract the most precise and accurate elements of the system. The historical trend is toward more exacting data acquisition and reduction techniques, models ever more faithful to the actual physical circumstances of the stars and their systems, and comprehensive analyses that make use of all, while prioritizing the most precise and reliable, information through careful weighting of each datum. Consequently, the growth of understanding of binaries, and stars generally, is inextricably linked to the development of observational equipment and techniques to achieve higher observational precision and accuracy, and to the development of models that incorporate accurate physics and analytical techniques. We begin by reviewing the history of binary star studies and that of eclipsing systems in particular, in the course of which we will examine test cases from two different epochs that illustrate these points.

2. Discoveries, Hypotheses, and Observations

By 1750 dozens of pairs of visual double stars had been discovered. From the frequency distribution of angular separations across the sky, J. Michell (1767) argued that "…it is highly probable, and next to a certainty in general, that such double stars … do really consist of stars placed nearly together, and under the instance of some general law…". Initially skeptical, William Herschel (1803, p. 340) undertook a thorough investigation of the claim:

> "We have already shewn the possibility that two stars, whatsoever be their relative magnitudes, may revolve, either in circles or ellipses, round their common centre of gravity; and that, among the multitude of the stars of the heavens, there should be many sufficiently near each other to occasion this mutual revolution, must also appear highly probable. But neither of these considerations can be admitted in proof of the actual existence of such binary combinations. I shall therefore now proceed to give an account of a series of observations on double stars, comprehending a period of about 25 years, which, if I am not mistaken, will go to prove, that many of them are not merely double in appearance, but must be allowed to be real binary combinations of two stars, intimately held together by the bond of mutual attraction."

And he did so.

We have already noted the 18th century origin of the eclipsing hypothesis for Algol but names given to it in antiquity (*al ghul*, *Rosha ha Satan*, *Caput Gorgonis*) suggest that its variability had been noticed for millennia. The first attempt to measure radial velocities of stars based on Doppler's (1842) discovery of the effect on perceived frequency in relative motion was by W. Huggins (1868) who discussed in detail his estimation of the difference between a strong hydrogen line in the spectrum of Sirius and a superimposed bright line from a lamp. He attempted a challenging experiment and provided complete details of how he did it, enabling others to improve on it. The orbital motion of Algol's stars, confirming the eclipse hypothesis, was established first by H. C. Vogel (1890), who thus inaugurated the study of spectroscopic binary stars.

2.1. Early observations

Observationally, stellar brightness assessment began with visual estimates by eye with or without telescopic aid. Thus did Goodricke and Piggott determine the period of Algol's variation. This and their subsequent study of β Lyrae effectively marked the onset of eclipsing binary photometry. We leave for another discussion the discoveries of variation of δ Cephei and η Aquilae; but altogether the discoveries effectively initiated variable star photometry.

Visual estimates of the relative brightness of stars had been made since ancient times, as in Ptolemy's Almagest star catalog, where "magnitudes" (literally, "sizes") were assigned to stars within constellations and asterisms alongside a description of where the stars lay among the depictions on a celestial sphere. Thus, Algol is described as the "bright one," #12, of stars 12-15 in the Gorgon head. The brightest star in a constellation could be assigned a brightness different than 1, suggesting a roughly uniform scale across the sky. Thus Sirius = α Canis Majoris is of magnitude "<1" whereas both α and β Persei (present day designations) are of magnitude 2, and α and β Lyrae are of magnitude 1 and 3, respectively. Estimates of fractions of visual magnitudes were carried out within brightness sequences of stars by observers such as William Herschel and his son John in the late 17th-mid 18th centuries. Following attempts by other astronomers to establish a magnitude scale, Norman Pogson (1856) proposed a logarithmic scale in which stars differing by a factor of 100 in brightness were defined to have a magnitude difference of exactly 5 magnitudes. This scale became widely adopted, and later was applied to the light limited to specific regions of the spectrum by the use of spectral filters and detector sensitivities, among other factors, defining the spectral passbands. Examples are the photographic and photo-visual passbands, and the V and B Johnson passbands. The magnitudes in every passband have a zero point which needs to be determined, in order to establish a standard photometric system, to which all observations should be reduced to provide common understanding of the results. Drilling and Landolt (2000) cite the flux calibrations for a star of zero magnitude and spectral class A0 V (i.e., a white color, and where "V" stands for the luminosity class of a main sequence star) in five Johnson passbands; for example, that for the Johnson *B* is $6.40 \cdot 10^{-9}$ erg cm^{-2} s^{-1} Å^{-1}.

Relative brightness measurements systematically began in the 18th century. Working with Anders Celsius, Andreas Tulenius (1740) moved a wedge of increasing optical density in an eyepiece to dim a star's light systematically until it disappeared; the distance moved correlated with the brightness of the star. This was the first of a series of extinction-photometry techniques, to be followed by brightness measurements relative to artificial light sources, dimmed by measured amounts of increasing optical density within a movable wedge, or by use of a polarizing prism and rotated analyzer. Procedures like these were carried out widely, but usually yielded precision no better than ~5%. A turning point came with the use of another star as the comparison source. The history of these devices is reviewed by multiple authors writing in Milone & Sterken (2011), starting with Sterken et al. (2011).

2.2. Advancing differential photometry: visual vs. photographic photometry

Beginning at the Harvard College and later at the Princeton University Observatory visual comparative devices permitted the observer to vary the brightness of a selected comparison star to visually match the brightness of the target variable star. Working with the Princeton Polarizing Photometer, Russell and associates achieved relatively high precision. John Merrill, for example, achieved a best precision of ~2% observing eclipsing variables RT Lac and RW Com. This exceeded the typical 4-5% best precision obtained from most photographic plate estimates, and a bit better than those obtained from plate measuring engines such as those designed and constructed by H. T. Stetson (1916), and independently by J. Schilt (1922). See Sterken et al. (2011) for a history of these engines. Some photographic techniques made use of jiggle plates (producing square images of stars) or extra-focal images, to spread out the light so as to involve more grains on the plate surfaces and improve measurement precision. These could be accommodated by varying the iris aperture of the measuring engines.

2.2.1. A Case Study of SZ Camelopardalis. One of the better results from photographic photometry stemmed from a project suggested by Ejnar Herzsprung to A. J. Wesselink, (1941), to compare the brightness of the eclipsing variable SZ Cam (HR 1260, ADS 2984B) with its equally bright visual binary companion (ADS 2984A), 18 arc-sec to the south. A further idea was to use an objective grating to provide multiple images of known brightness ratios of both stars on each exposed plate. He and colleagues obtained 367 plates containing 12,479 useful exposures of the two stars and measured the images with the Schilt photometer. In the systematic determination of the errors at each step,

Wesselink was meticulous in every detail. The study yielded an internal mean precision of ~2% in the star image measures, the dominant source of internal errors. We discuss the analysis of this work in Section 3.1.1.

2.3. Light curve acquisition in the photoelectric and CCD eras

With the advent of the photoelectric cell, photoelectric photometry (PEP) became an alternative method to photography for recording the light of single objects or for scanning small areas of the sky sequentially. Butler and Elliott (1993) describe the pioneering work in the 19th century. With a photoconductive selenium cell, Stebbins (1910) achieved 2% precision in recording the light curve of Algol, sufficient to reveal the very shallow secondary minimum in blue light. Whitford (1932) designed and built a DC amplifier to boost the weak current from those devices, increasing the number of observable targets, and proceeded to obtain a light curve of the prototypical short-period eclipsing binary W UMa. John Hall (1934) obtained the earliest near-infrared stellar observations with the aid of a dry ice cooling chamber around the detector housing. With the appearance of the photomultiplier tube (Whitford & Kron, 1937), sensitivity and precision improved again. The original techniques involved measurement of minute currents and voltages; photon counting was a further development that facilitated data collection and provided excellent measurement precision (cf. Armbruster et al., 2011).

Differential photometry with a single detection element involving alternate observation of variable star and comparison and check stars became the normal procedure through the middle of the 20th century. However, strict photometric conditions were required for such work and this made observing in many observing sites challenging. Although dry, clear, high-elevation sites are always preferred, they are not always available when or as long as needed. For this purpose, two- or more channel photometers were devised.

2.3.1. Differential Photometry with single pixel and array detectors. The development of pulse-counting photoelectric differential photometry is discussed at length in Milone, Sterken, & Young (2011). The Rapid Alternate Detection System (RADS) developed at the Rothney Astrophysical Observatory was inspired by the previous work of Walraven (1953) described to the present writer by his advisor, Adriaan Wesselink, who had seen the two-star photometer in action in South Africa. Like the most advanced version of Walraven's instrument, RADS operated in a 4-channel mode with two channels set on the variable and comparison star and two channels set on the sky nearby. The RADS function generator attached to the photometer head allowed setting of the duty cycle and positioning of each of the four channels, usually used for variable and comparison stars and empty sky areas near them. Although the system was devised and used to obtain data even in skies impaired by light cirrus, when conditions permitted the precision in the differential photometry could exceed 1%.

Differential photometry is currently carried out with CCD and CMOS arrays which are generally favored over single-pixel detectors, and means of self-calibration have been devised to meet the challenge of calibrating many pixels. Howell (2011) discusses the history of array devices. With appropriate techniques, milli-magnitude precision is now obtainable. Software such as *IRAF* and *ESO-Midas* have been used for image processing and, with *DAOPHOT*, for the extraction of magnitudes and precise positions on the sky of each star in the field.

2.3.2. Photometric calibration. Typically PEP data of variable stars and one or more selected comparison stars are measured simultaneously, ideally, or alternately, to provide a differential light curve. Usually one or more comparison stars will be observed as a check on the constancy of the comparison star. The comparison and check stars must at some point be linked to a standard system by observation of standard stars in the same run. Landolt (1983) provided a list of standard stars that were spread around the equator for the benefit of astronomers in both northern and southern hemispheres. Procedures and the equations of condition for least squares determination s of extinction and transformation coefficients, can be obtained from various sources, the most classic being that of Hardie (1962). The subsequent modeling analysis of the data at some point must be converted into physical units, or at least solar values for the radii and masses, and astronomical units for distances within the binary system. Standardization is typically done by transforming local system magnitudes into standard system magnitudes; this requires observation of stars whose intrinsic magnitudes are known for the passbands of interest, such as m_{pg} and m_{pv}, the Johnson *UBV*, or the Strömgren *uvby* passbands, for example. Establishing those standards ultimately requires calibration. Calibration efforts for absolute photometry are critical for tying observational data into physical units. This effort similarly has evolved over time.

Photographic standard stars were established after ~1870 when emulsions sensitive enough to record star images became available. A commission of the International Astronomical Union (IAU) was established in part to refine and coordinate efforts to do so. The North Polar Sequence of stars which could be widely observed from observatories in the northern hemisphere established such standards. Leavitt & Pickering (1917) present and discuss an early version of this important sequence for photographic and photo-visual magnitudes. This was subsequently replaced by other standards and in other areas of the sky for more modern passbands. Landolt (2011) and Sterken et al, (2011) discuss how procedures have changed over time and affected photometric precision and accuracy. Cohen (2011) discusses the history of photometric calibration efforts in the ultraviolet through the far infrared spectral regions, with relative and absolute methods, respectively, and Adelman (2011) does this for spectrophotometry. Considering that filter

photometry can be considered low-resolution spectroscopy, it may not be inappropriate to discuss in this section the calibration of other observables that can contribute to eclipsing binary analyses.

Stefanik, Latham, & Torres (1999) discuss the establishment of an absolute zero point for radial velocity measures for the standards established by the IAU Radial-Velocity Standard Stars group. The development of high resolution spectrographs with calibration lamps led to the detection of the relatively small orbital motions of stars due the presence of massive planets (Mayor & Queloz, 1995), as well as to the improvement of precision and accuracy of spectroscopic binaries. The development of CORAVEL to provide radial velocity data for stars observed with the Hipparcos mission instruments and the subsequent development of Elodie are important examples. One of the more recent developments for precise calibrations is the laser comb for superimposing precise wavelength lines along with the spectrum of interest on the same array detector.

The bounteous data from Gaia and other scanning space missions as well as ground-based survey instruments can be inspected with rapid machine methods for classification purposes and perhaps orbital information and indications of the presence of other stars in the system (see, for example, Kostov et al., 2025; Li et al., 2024; Mowlavi et al., 2023; Prša et al., 2022). As these preliminary results will require detailed follow-up studies involving ground-based instruments and telescopes, we now demonstrate with an example why follow-up observations may be needed to provide still higher accuracy and precision of the observable curves. In illustration, we now discuss the system HP Dra, an eclipsing binary discovered in data obtained by the Hipparcos mission, although the derived orbital period that was reported (6.6930^{d}) was incorrect.

2.3.3. A Case Study of the Eclipsing Variable HP Draconis

In the fourth paper in a series to evaluate how well Gaia would perform in furnishing fundamental data from eclipsing binaries, Milone et al. (2005) presented their analysis of replicative data, the Hipparcos and Tycho photometry and Asiago radial velocities, for three eclipsing binaries. One of the systems selected was HP Dra, with an EA-type light curve. For this system, a more correct orbital period and an eccentricity were found. The masses were determined to a precision of 2% and the radius of star 1 to 3%; however the radius of star 2 was determined to a precision of only 10%. Each of the minima is $\sim 0.02^{p}$ wide, and in a 10.76^{d} period, the data acquisition in these phase segments was so sparse it degraded the determinations of the stellar radii and the temperature differences between the components. Thus, the Gaia proxy photometric data from the Hipparcos mission proved insufficient within the eclipses to provide as fully precise and accurate stellar radii as one could expect. Because the Gaia test case required data comparable only with that expected of the mission's instrumentation as specified at that time, all available data were not used in the Milone et al. (2005) analysis. The situation was remedied in a follow-up study with the inclusion of 869 ground-based *BV* observations from Cracow Observatory and RV data from Haute-Province Observatory (Kurpinska-Winiarska et al., 2000) in addition to the Asiago RV data used in the previous study. As noted in Milone et al. (2010), the photometry was carried out carefully and meticulously. We discuss the analyses in Section 3.2.2.

3. Light Curve Modeling and Analysis

3.1. Basic Modeling

By 1880, there were six known eclipsing variables and, according to Russell (1948), E. C. Pickering (1880) made the first precise theoretical calculation of the light variation from a stellar eclipse. As noted, Vogel's confirmation of the eclipse hypothesis defined the first discovery of a spectroscopic binary; his was also the first attempt to determine system elements, thus the first RV analysis of an eclipsing spectroscopic binary --- on the basis of six photographic plate observations. The classification of systems by light curve appearance will be shown to require improved models to describe them adequately. The early 20^{th} century Russell binary star model assumed spherical stars for systems with Algol-like light curves [EA], and tri-axial ellipsoids for those that displayed β Lyrae [EB] or W UMa [EW] type light curves. Neither shape correctly matches the true shapes of stars in a close binary system, but were considered adequate for most of the observations of the time. The means to derive the elements of a system (the "inverse problem") and then to calculate the light curve from the derived elements (the "direct problem") were and are critical stages in light curve modeling. Subsequently, more comprehensive models became available to analyze and model systems which had been systematically excluded from the longer-period, far-apart systems traditionally studied for fundamental properties such as radii, masses, and luminosities.

3.1.1. A Case Study Analysis of SZ Cam. For one of the better determinations of fundamental data prior to modern light curve acquisition and analysis methods we consider the Wesselink (1941) analysis of the EB type light curve of SZ Cam, the acquisition of which was described in Section 2.2.

The data were averaged in groups and once the period was determined [$P = 2.6984166(33)^{d}$], and the data phased, averages of ~10 contiguous averaged points were taken to produce normal points, an essential step in an age of hand computation. In the analysis of the light and radial velocity curves that he obtained, Wesselink used a spherical star model, presenting a uniform disk, considered appropriate for stars of early spectral type at the time. The eclipses are partial only (although Wesselink found them nearly total, and the analyses were made of the light curves rectified of ellipticity and reflection

effects. He had rectified the light curve to remove the curvature outside of the minima, and applied corrections for limb-darkening and gravity brightening effects. Wesselink found the ellipticity, the tidal distortion expected from what he regarded as the Roche model hypothesis, to be 0.04 and 0.02 for the two components. He sought but found no evidence of the reflection effect in the cosine term of the light curve. These procedures were similar to those devised by Russell (1912a; 1912b) and Russell & Shapley (1912a; 1912b). The ratio of surface brightness (1.24 ± 0.13) was determined from depths of the minima of the rectified light curve, but the RV curve of only the more luminous component could be measured so that only the mass function was known for the secondary star. Given the period and semi-amplitude of the RV curve, $v_1 \sin \iota = 100$ km/s,

$$F^{1/3} = (M_1 + M_2)^{1/3} \cdot [M_2 / (M_1 + M_2)] \sin \iota = v_1 \sin \iota \cdot P^{1/3} = 0.65 \pm 0.08, \quad (1)$$

which provides a method of determining M_2 by iteration even if it is not small, if the inclination is known or is close to 90° and M_1 is known accurately; see, for example, Milone & Wilson (2014, p. 746). That was not quite the case here. As only two of the four contact points can be seen in primary minimum (although the secondary provides suggestions of slope change near deep minimum in the m_{pg} light curve) neither the ratio of radii, *k*, nor the difference in brightness, Δm_{pg}, could be determined from the light curve alone. Therefore Wesselink computed least squares solutions for each of five values of *k* over the range 0.45 to 1, all of which fitted the primary minimum well enough, but the secondary minimum was best fit with his solution 5, $k = R_2/R_1 = 0.45$. Wesselink's solution yielded radii $r_1 = 0.412a$ and $r_2 = 0.185a$ where *a* is the semi-major axis. For this solution the inclination, $i = 76.1°$, and the difference in the component magnitudes, $\Delta m_{pg} = 2.00$. With the best assumed values of the day for the distance, interstellar reddening and extinction, and other astrophysical information, Wesselink obtained radii of 7.5 and 3.3 $R_\odot$ and masses of 20.0 and 8.7 $M_\odot$ for stars 1 and 2, respectively, for a mass ratio q = 0.44, with the primary minimum a transit eclipse.

The photographic light curve was held to be unusually accurate by Kopal, who included the solution in his catalogue (Kopal & Shapley, 1956, pp. 168-169); in rediscussing it, Kopal obtained a mass ratio, q = 0.29, derived from the ellipticity. Wesselink's value for the fraction of the area of the eclipsed disk at mid-eclipse, $\alpha = 0.96$ for his favored solution and his drawing of the system shows a near-total eclipse; Kopal considered it to be total. Kopal's reworking yielded radii of 10.9 ± 0.9 and 4.5 ± 0.5 $R_\odot$ and masses of 21 ± 4 and 6 ± 1 $M_\odot$, respectively; these are the data entered in his catalogue.

Results from modern solutions are quite different although the overall system configuration is confirmed. Techniques such as rectification produce light curves that would be produced by uniform non-interacting stellar spheres. Although capable of yielding reasonable parameters for some elements and parameters, a far better course is to model the tide- and reflection-related causes for the classical "oblateness" and "reflection" effects, as in WD models. See Milone, Wilson, & Hrivnak (1987) for a comparison of results from both types of methods in the analysis of the overcontact system RW Com. The SZ Cam system is in an open cluster (NGC 1502) and the close proximity of ADS 2984A and fainter stars makes photometry and spectroscopy challenging because of light contamination, but in this case these challenges were met. Nevertheless progress with instrumentation and modeling techniques have enabled even more exacting results to be obtained from this interesting system. A modern solution is discussed in section in Section 3.2.1.

3.2. *The Development of More Rigorous Binary Star Models*

Recognizing the increasing availability of photoelectric light curves, and with the least squares element determination method of Piotrowski (1948), Kopal (1950), provided a more physically appropriate model for eclipsing binaries. In doing so, he and others built on the idea of gravitational equipotentials to describe the shapes of the component stars in close binary systems. This work ultimately stemmed from the treatment of the restricted three body problem by Lagrange (1772) and the subsequent fluid dynamic treatment of three body systems by Roche (1849, 1850). Kopal's (1959) equation (1-3) for the modified Roche potential of the binary may be written more generally as in Equation 2.

$$\Omega(\mathbf{r}; q, d) = \frac{1}{r} + q\left[\frac{1}{\sqrt{d^2 - 2\lambda d r + r^2}} - \frac{\lambda r}{d^2}\right] + \frac{1}{2}F^2(q+1)r^2(1-\nu^2) \quad (2)$$

where *r* is the distance to the center of gravity of star 1, *q* is the mass ratio, M_2/M_1, *d* is the separation of centers of the two stars (taken as unity by Kopal and Wilson & Devinney), λ and ν are direction cosines, and *F* is the ratio of the angular rotational to the synchronous velocity, and is used to generalize the expression for non-zero eccentricity cases (Wilson, 1979). In the following decades, the basic model was turned into programming code. The potential expression has been divided by the factor GM_1, as per the expression used in publications by Wilson & Devinney (1971) and others who discuss his models. Among those who developed analysis programs to solve the inverse problem by deriving the elements of the systems and parameters relating to the component stars and produce synthetic light curves was Lucy (1968). Many other modelers were similarly developing models and methods as well, and their contributions are discussed in detail in Kalrath & Milone (2009). Except for the detached systems where neither star fills its inner lobe, the basic morphological configurations can be seen displayed in Figure 1: over-contact, semi-detached, and double-contact models.

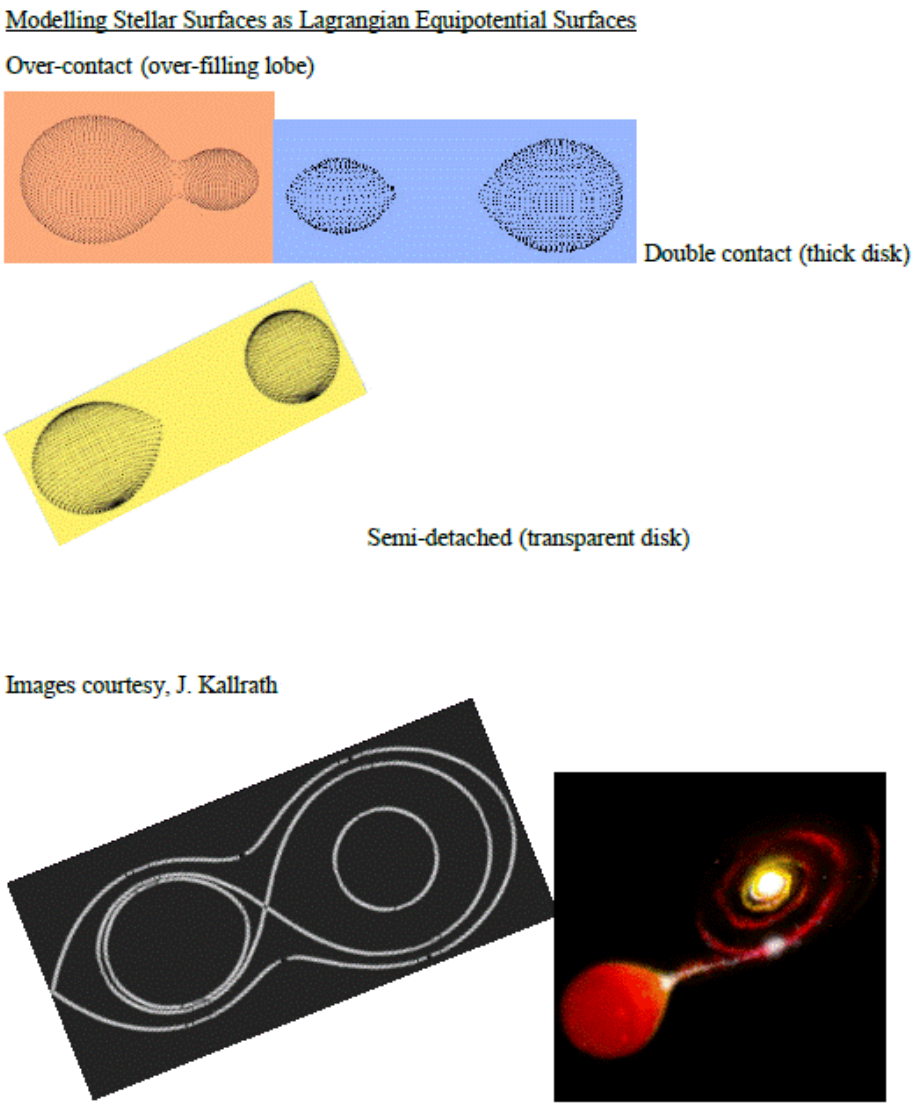

Figure 1: A pastiche of shapes of stellar surfaces as equipotential surfaces, defining the types of morphological models and informing their designations. From the top: left, an over-contact system (V728 Herculis, from Nelson et al., 1995) shown over-filling its inner Lagrangian surface; top right, a double contact binary with semi-transparent or opaque disk occupying one of the lobes and a lobe-filled donor star filling the other lobe; below them, on a tilt, a semi-detached system with the donor star filling its lobe but with a thin transparent disk around the other component star. That model is shown in a cross-sectional profile tilted to match the artful rendition of the system on the right. Individual figures, courtesy of Josef Kallrath.

Here we have focused on the models, methods, and programs of Wilson and his collaborators because the Wilson-Devinney program (hereafter, WD) is the most popular program and in more than fifty years of development it has continued to incorporate the best available physical models in order to determine optimum solutions for simultaneous analysis of multiple observable curves. Its many successive versions of accumulating features are described by Kallrath (2022) in detail. An on-line earlier WD program version called PHOEBE was developed by Prša (2018) who has now extended the program to incorporate AI in order to evaluate and analyze large numbers of newly discovered Gaia and TESS eclipsing binaries as well as those from ground-based surveys.

The current code site and source for recent versions of the WD program are:

https://faculty.fiu.edu/~vanhamme/binary-stars/
ftp://ftp.astro.ufl.edu/pub/wilson/lcdc2015/

It should be noted that Walter Van Hamme should be given credit for providing much of the updating over the last 30 years. The latest 2017 WD program version

includes 95 passbands (the 95th is for the TESS passband), the Kurucz and Phoenix model atmospheres for high and low temperature models, respectively, and all the other features of previous versions. The various modes available for use within WD constitute the WD models. The downloadable document *Binary Star Observables* is effectively the manual for the program and also contains details about the WD models. It contains sample input files for both the Differential Corrections (DC) and the Light Curve (LC) program routines. The *Observables* documents are updated for each new version and each contains a list of the changes applied since the previous version.

3.2.1. SZ Camelopardalis Revisited. Tamajo et al. (2012) used an enhanced 1998 WD version with Kurucz stellar models to analyze 40 high resolution RV data of both components, and 1517 BVI_C CCD observations [with median total budget errors of 0.006, 0.001, and 0.007 for V, and B-V & V-I_C color indices, respectively, where I_C refers to Cousin's passband (bluer and narrower than Johnson's *I* passband)]. They obtained an equivalent determination of k = 0.75; and q = 0.747 ± 0.006; ι = 75.16°; R_1 = 8.91 ± 0.05, R_2 = 6.70 ± 0.12 $R_\odot$; and M_1 = 14.31 ± 0.54, and M_2 = 10.69 ± 0.38 $M_\odot$. With updated values of reddening and bolometric corrections, they determined the distance to be 870 ± 30 pc, in agreement with the Gaia parallax value equivalent, 849 (+69, -61) pc. From this we conclude that Wesselink's work, having an abundance of relatively precise observations and using powerful differential techniques, and uncovering the general nature of the system -- a transit eclipse at primary minimum – nevertheless did not succeed in determining accurate values of the fundamental data partly because of incomplete data suites. In addition to being limited to one RV curve, and one photometric passband (m_{pg}), and having to reply on a mass-luminosity relation for a value for M_1, the analysis could not include a major 3rd light contribution to the light curve --- that of a third component, discovered by Mayer et al. (1994; 2010) and confirmed through speckle interferometry by Mason et al. (1998). Tamajo et al. (2012) used a spectral disentangling technique to see the effects of the third star in the spectral line profiles of the H_α, H_β, and H_γ, which were also fitted with NLTE (non-thermal equilibrium) line profile models. The relative contributions of the three components agrees with the WD analysis that included the 3rd light parameter (26% in I_C), to within 0.5%. This case study thus highlights the effects of light curve precision and instrumentation as well as innovative techniques and modeling tools on absolute parameter determinations. In Section 3.5 we describe other discoveries in this system.

Next we discuss analyses of data of the relatively wide EA type eclipsing variable HP Dra with data suite surrogates of that expected of the Gaia mission and subsequent analyses with a much enhanced and complete data suite.

3.2.2. A Case Study Analysis of HP Draconis. As noted in section 2.4, the reported analysis by Milone et al. (2005) was followed up by another, reported in Milone et al. (2010). Figure 2 illustrates the model fittings to the RV and Hipparchus data and illustrates why a follow up study was required. The latter study made use of additional 869 photoelectric BV observations and Asiago RVs augmented by CORAVEL and Elodie spectrometer data totaling 51 observations of each component. The Tycho data (with m.s.e. of single observation of σ_{BT} = 0.11, σ_{VT} = 0.09) were excluded from the analysis.

Even though later WD programs are even more efficient, have more features, and allow a wider range of parameters to be determined, it is instructive to relate selected capabilities of this version and how they were used for this particular analysis. The analysis made use of the 2007 WD version (Wilson & Devinney, 2007; Wilson, 2008), hereafter, WD07. WD makes use of a damped least-squares engine with damping coefficient, λ usually set to 10^{-7}, but solutions were not significantly affected by other values. Runs were made in mode 2, appropriate for detached binaries. We adjusted simultaneously 13 non-curve dependent and two curve-dependent parameters for a total of 19 of parameters. The weighting of the data, the subsets that were run, and the modeling procedures are recounted in detail in Milone et al. (2010). Because WD07 was not self-iterating, thousands of individual runs across several series of models were carried out in order to explore the parameter space adequately. After each run, the main set and all ten subsets were run, and the parameters of the subset that promised the most improvement in the sums of squares of the curve fitting residuals (SSR) was adjusted; if the overall fitting error did not improve, then the next most promising was chosen, and so on until convergence was achieved in all ten subsets. The final errors were taken from the full 19 parameter set. At the end of one of the last series of runs, every parameter was altered, one by one, by positive and negative increments of 1σ; 2σ; and by much larger increments (10–100 σ). No significant changes were found in this series of checks. The fittings for this analysis can be seen in Figure 3.

The results: The radii, R_1 = 1.371 ± 0.012 and R_2 = 1.052 ± 0.010 $R_\odot$, were determined to precisions of 0.88% and 0.95%; the masses, M_1 = 1.133 ± 0.005, M_2 = 1.094 ± 0.007 $M_\odot$, to precisions of 0.44% and 0.64%, respectively. From these, the mean densities of the components are 620 ± 20 and 1325 ± 47 kg/m^3, and the gravitational accelerations are log g_1 = 4.218 ± 0.010 and log g_2 = 4.433 ± 0.011 (cg s) for stars 1 and 2, respectively.

No spectral analysis was carried out for this investigation, but the properties of the components are known well enough to place them on log plots of luminosity vs. temperature and radius vs. mass. M.K.W. examined the range of models of different ages and chemical composition on the Padova interactive Web site http://stev.oapd.inaf.it/cgi-bin/cmd based on Marigo et al. (2008). A grid of models was explored in steps of 0.05 in log(τ), where τ is the age in Gy, over the compositional range 0.008 < *Z* < 0.030. A model with *Z* = 0.019 and age 4.47 Gy (i.e., an isochrone of chemical composition and age similar to the sun) fit the components' properties best as revealed on two plots. See Figure 4 (Fig. 4 of Milone et al., 2010).

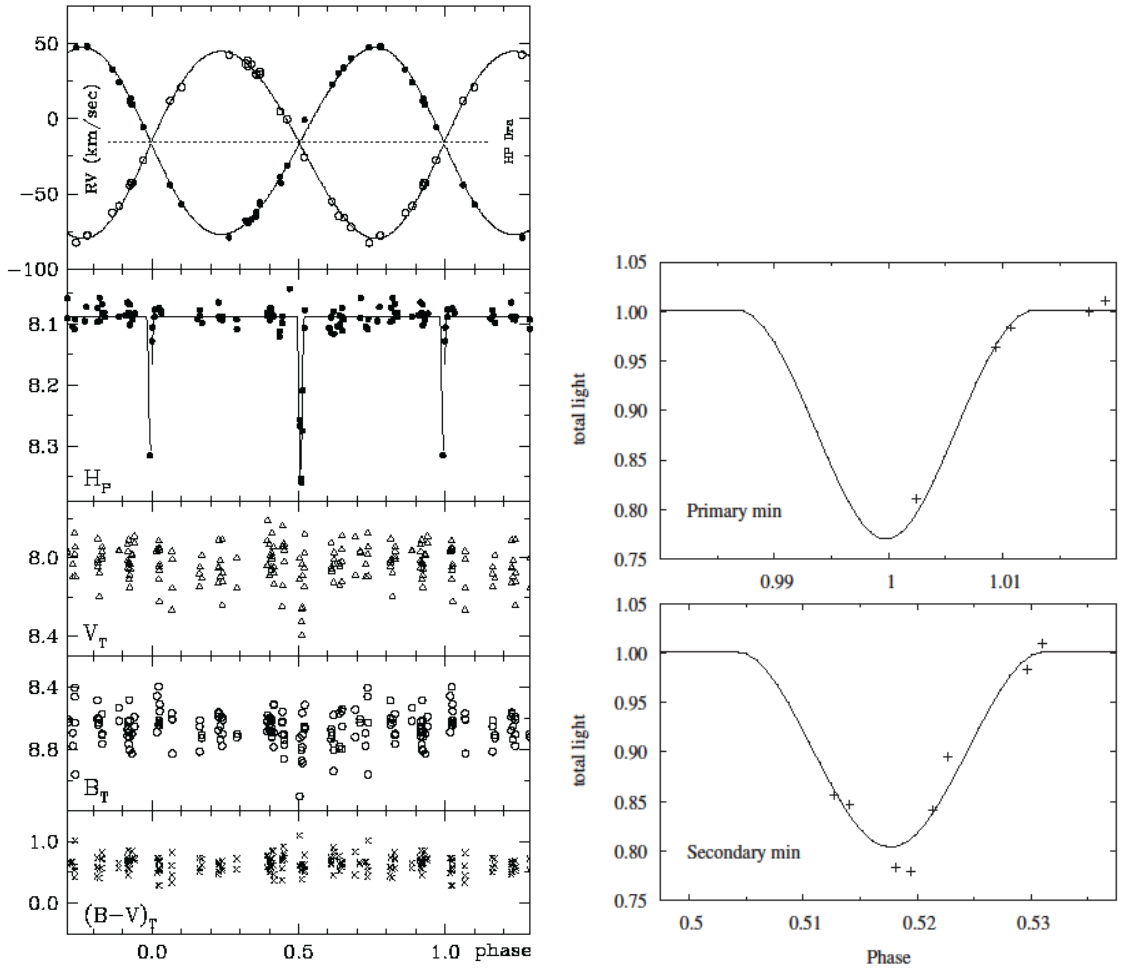

Figure 2: Phase-folded surrogate Gaia RV and light curves of HP Draconis from Milone et al. (2005). Left, from the top: Asiago RV curves, Hipparcos (H_P), and Tycho light and color curves (V_T, B_T, and $(B-V)_T$. Right: blow-up of the H_P light curve primary and secondary minima and model curve. Note the sparse coverage in the minima of the H_P curve (and the large scatter in the Tycho curves) that whan used alone limit the accuracy as well as the precision of the radii and luminosities.

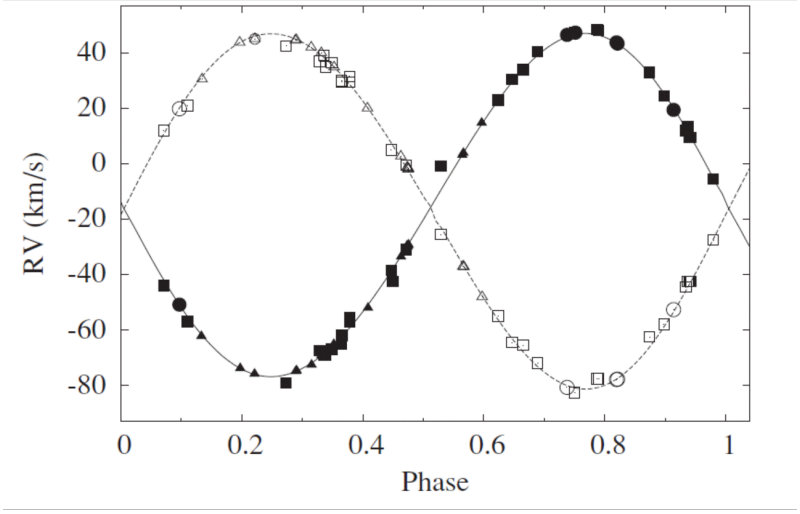

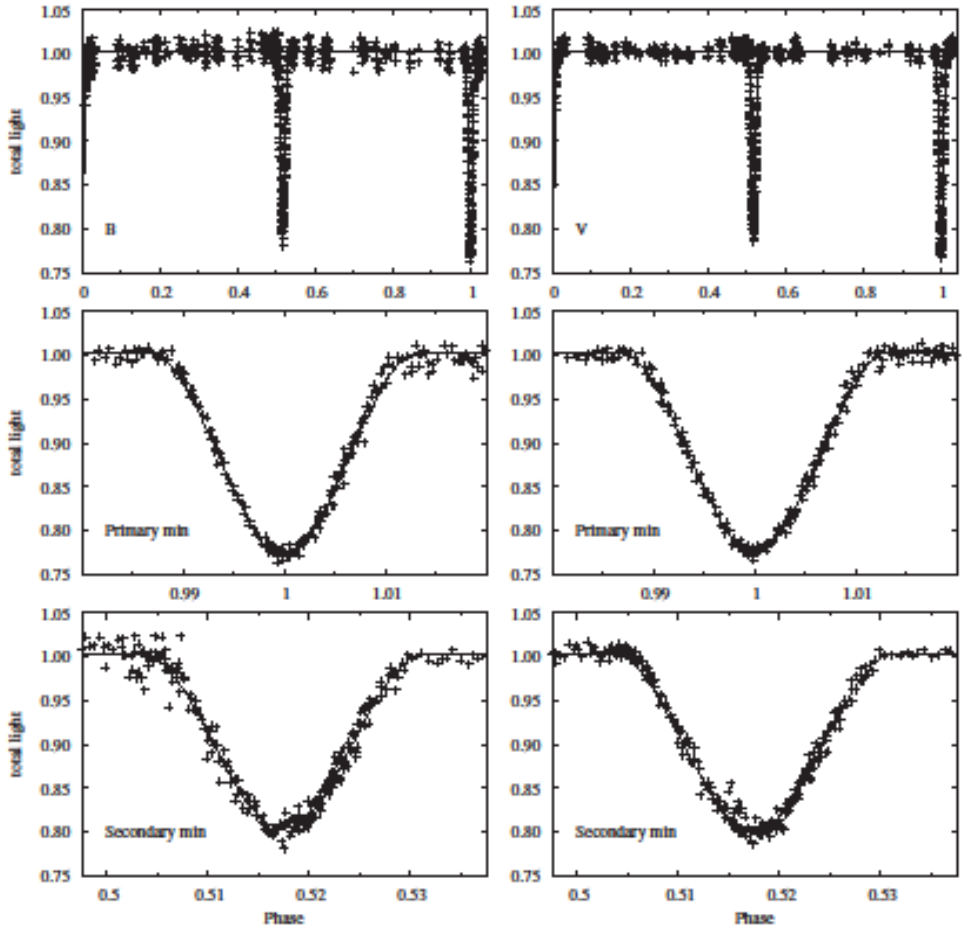

Figure 3: Phase-folded RV and light curves of HP Dra from Milone et al. (2010). Top: Asiago RV data represented by squares, CORAVEL data by triangles, and Elodie data by circles. Star 1 data have filled symbols; star 2 data have open symbols. Star 1 is the hotter and slightly more massive component. The discrepant point on the Star 1 RV curve just after secondary minimum received zero weight in the analysis. The curves of the final fitting are shown. Bottom: *B* (left) and *V* (right) full, primary minima, and secondary minima light curves of HP Dra and the fitted curves of the adopted model. Note the completeness of coverage. See Figure 2 for the H_P minima fittings.

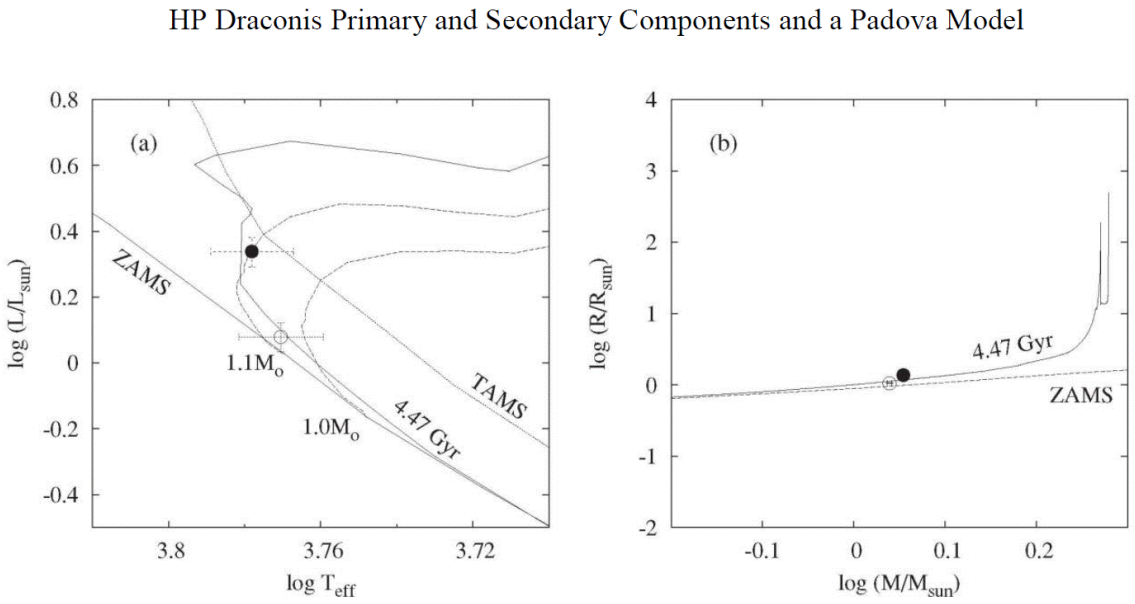

Figure 4: HP Dra components compared with the ZAMS on (a) a plot of log ($L/L_\odot$) vs. log ($T_{\rm eff}$) with evolutionary tracks for 1.0 and 1.1 $M_\odot$ stars, showing also the TAMS; and (b) a plot of log ($R/R_\odot$) vs. log($M/M_\odot$). The properties of the components seem to fit best (among the Padova family of models inspected) with the 4.47 Gy isochrones. With this model, component 2 is seen to lie within $\sim 1\sigma$ of the ZAMS. Component 1, with only 3.4% more mass than its companion, has evolved off the ZAMS but not as far as the TAMS. From Milone et al. (2010), Fig. 7.

Finally, Cracow Observatory CCD observations at primary minimum, were obtained following the conclusion of the analyses and thus not used in them, are shown in Figure 5 along with the synthetic light curve from the model, computed for that interval of observation. Nevertheless it is curious that the secondary lies within 1σ of the zero-age main sequence (ZAMS), whereas the primary that has less than 4% greater mass than the secondary is approaching the terminal age main sequence (ZAMS). Similarly odd is the condition that the primary has half the mean density of the secondary component. Perhaps there is more to be learned from the solar-analogue stars in this system. A spanking new study may help to provide some of it.

In August, 2025, Southworth (2025), hereafter *S25*, posted a preprint linked to the DEBCat website claiming a greater precision in the mass and even more in the radii determinations in this partial eclipse system. S25 made use of 14 sectors of TESS data, which are abundant, used the flux level in a narrow range on either side of the eclipses, and used a spherical model code, JKTEBOP, to analyze the minima. Of course use of a code that assumes stars to be spherical is usually safe enough if the stars are far enough apart and well within their inner Lagrangian surfaces. The WD program computed the sizes of the polar, inward-pointing, side, and back radii for the final model and demonstrates that they agreed with each other well within errors for each component, so an assumption of sphericity itself is not inappropriate in this case.

For components 1 and 2, S25 obtained for the masses: 1.1354 ± 0.0023 and 1.0984 ± 0.0022 $M_\odot$ and for the radii, 1.2474 ± 0.0046 and 1.1498 ± 0.0049 $R_\odot$, respectively, noting that these are among the most precise absolute parameters for binary star components currently available.

S25 finds a much smaller third light: 0.5% vs. ~10%, "and this changes the measured radii significantly." S25 analyzed the light and radial velocity curves separately, unlike the Wilson-Devinney approach (where all data are solved simultaneously and where all weights, including curve weights, are carefully determined). The S25 approach provides the amplitudes of the radial velocity curves: K_1 = 61.971 ± 0.056 km/s, K_2 = 64.067 ± 0.060 km/s where the error bars are determined not by least-squares but by 1000 Monte Carlo simulations; this yields q = 0.9673. S25 "determined the distance to HP Dra using the BV magnitudes from Tycho, JHK$_S$ magnitudes from 2MASS and surface brightness correlations…" from another source. S25 "allowed an uncertainty of 0.02 mag, for the interstellar reddening" and states "Our most precise distance estimate is the K$_S$ band and is 77.9 ± 1.2 pc," which agrees with the Gaia DR3 parallax result of 79.27 ± 0.32 pc. S25 found a solar composition model with 3.5 Gy age that adequately matches his results. Finally, S25 finds evidence for magnetic cycle activity in TESS light curve variations suggesting possible non-synchronous rotation by one of the components and by emission in-filling of Ca H & K line profile centers.

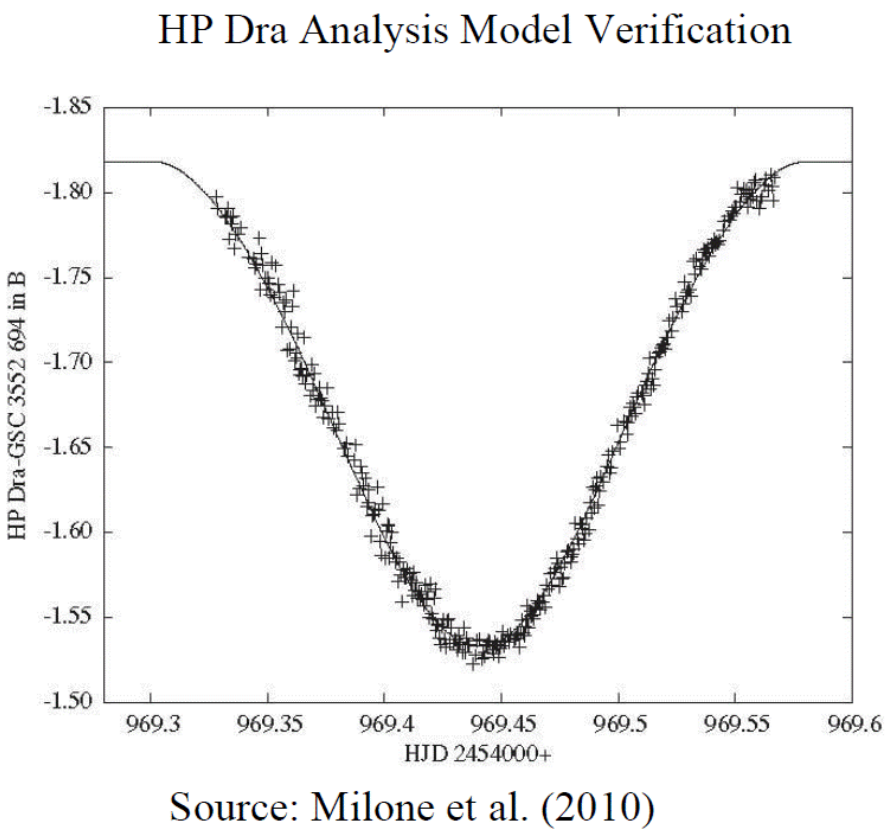

Figure 5: From Milone et al. (2010, Fig. 4), CCD differential *B* passband observations of HP Dra, obtained at Cracow Observatory on 2009 May 17 near phase zero, and plotted along with the light curve predicted from our adopted model. These data were not included in the analysis and thus represented an independent check on the results, including apsidal motion.

3.2.3. Comparisons of HP Draconis Models and Results. As the system is an important one to understand how stars like the sun evolve over time, it is important to understand any differences in determinations.

Milone et al. (2010), hereafter, *MK-WO* or *we*, found a distance also in agreement with the DR3 results, but with a stated error that reflects the uncertainties in the temperature scale (±150 K), in the absolute luminosities relative to the sun, in the interstellar extinction A_λ, and in the bolometric correction. S25 assumes the same T_1 = 6000 effective temperature that we did, and that value is hardly without large uncertainty. The derived distance, 77 pc, agrees within errors with the distance previously derived from the *hip* and Asiago RV data alone, 73 ± 4 pc. If we adopt, E_{B-V} = 0.00, as did S25, then the distance increases slightly, to 80 ± 3 pc, in close agreement with the Gaia DR3 parallax result of 79.27 ± 0.32 pc

Although the S25 mass ratio is in agreement with the MK-WO adjusted parameter, q = 0.9658 ± 0.0037, and the MK-WO and S25 masses similarly are in agreement, the radii are not; S25 finds the primary star to be 7% smaller and the secondary 5% larger than did we, a difference he ascribes to a larger amount of 3rd light. The claimed effect of third light on radii determination is unclear. It would be of interest to see the full details of how the S25 results and uncertainties were obtained. Regarding the reality of 3rd light in this system, MK-WO comment: "As part of the exploration of the reality of the l_3 quantities, runs were made with these values set to zero, and the results followed up through more than a dozen runs of successive changes. In each case, the preferred adjustment was to restore the value to the ~10% level." The source is yet to be determined, however. It would be of interest to see how S25 was able to improve on the radius determination and precision and to make a determination of third light in the system with the procedures described.

If improved precision arises from differences from averages in a large number of trials we note that such a determination of errors does not necessarily provide an accurate assessment of the true uncertainty. The question needs to be asked: are the individual run determinations truly independent? If not, one must be wary of claims of extraordinary precision. Additionally, systematic error, arising from sources outside the averaging process, must be considered.

To resolve discrepancies and explore this partially eclipsing system further, a number of systematic adjustment of the potentials to produce a grid of sizes for each component as suggested by D. Terrell (2025, private correspondence), and use of features of later WD versions

(>2013) to analyze the now further enhanced data suite, with the eclipses timings, the Ca line profiles, and, as S25 suggests, further spectral analysis to determine more precisely the chemical composition of the system. More recently adjustable parameters are *log d* (via the direct distance estimation), interstellar extinction, A_λ, as well as star spot property and aging parameters, and third body dynamical parameters; with updated solar values and other constants, analysis then may yield tighter fittings and more accurate results, and provide information about the dynamics of any other components in the system. Given strong confidence in the Gaia distance, the IDE (inverse distance estimation) can be used to strengthen the determinations of other parameters. The differences between the Asiago assessment of approximately solar composition, the previous lower metallicity estimates based on Strömgren system photometry, and the suggestion of a slight improvement in the residuals with a higher metallicity, all point to a need for further spectral analysis. Given the question of third light and the apparently relevant $d\omega/dt$ and dP/dt parameters despite large internal errors, in addition to adjusting WD third body parameters, speckle interferometry, as we note below, could be revealing.

It is clear that the results from analysis of the initial Gaia-simulation using Hipparcos +Tycho +Asiago proxy data are superseded by those from larger, improved data sets. Later results are among the most precise determinations of fundamental stellar data that have been made. With the discoveries of S25, even further characterization appears possible.

And this leads us back to further opportunities for high precision photometry and to a broader range of spectral coverage, to uncover the spectral distribution of any third light sources.

3.3. Disk Models and Double Contact Sytems

Beginning in 1979, Wilson turned his attention to proposed disks surrounding an unseen companion in systems such as β Lyrae. The basic idea was to approximate the self-gravitation of a circumstellar disk by that of a massive but infinitesimally thin wire-like ring concentric with the star at the center of the disk, analogous to conceiving of the stars in the Roche model as represented by central massive points. This led to the expansion of Equation 2 to include the gravitational potentials of stars 1 and 2, the centrifugal potential, and the gravitational potential of the massive wire ring lying in the orbital plane, resulting in the total modified potential for such a binary star system (Wilson 1979, 1981, Eqn. 1) in Equation 3.

$$\Omega = \frac{1}{r} + q\left[(D^2 + r^2 - 2r\lambda D)^{-1/2} - \frac{r\lambda}{D^2}\right] + \frac{(1+q+q')F^2 u_1{}^2}{2(n+1)}\left[\left(\frac{u}{u_1}\right)^{2(n+1)} + n\right] + \frac{q'}{\pi(2R)^{1/2}}\int_0^{\pi}\frac{d\phi}{[(R^2+r^2)/2R - u\cos\phi\,]^{1/2}}. \quad (3)$$

where the quantities r and ϕ are polar coordinates with r measured from the center of star 1, D is the instantaneous separation of star centers, R is the radius of the wire ring in the disk's equatorial plane, λ is the direction cosine of the line of centers, n is a constant so that the angular velocity is proportional to u^n where u is the distance of a point from the rotation axis of star 1, and u_1 is the null point of effective gravity for the (uniformly) rotating primary star. It defines the outer limit of the disk; another null point defines the inner limit. Given n, F, and u_1 the angular rotation speed, the centrifugal potential and the centrifugal force are everywhere determined.

Wilson (2018, Fig. 12) applied the accretion-decretion (A-D) self-gravitating disk model to a differential V light curve of β Lyrae, the prototypic EB eclipsing variable, with a hot less-luminous supergiant (B8 Ib) component, and a component long considered to be completely enshrouded within a disk. β Lyrae was among the five eclipsing binaries that Plavec & Koch (1978) reported to have strong far ultraviolet emission lines and continua and were later (Plavec, 1980) referred to as W Serpentis stars, after the system with the strongest emission and a clear view of the disk component that is far more luminous than the donor (unlike the case with the brightest member of the group, β Lyrae). They noted that

> "The high level of ionization indicated by strong emission lines of Si IV, C IV, and N V is remarkable. It is not yet clear from which region or regions of the systems these emissions come. One possibility is a high temperature, low density plasma surrounding the hotter component. It should be noted that the hot component may well be the spectrographically invisible one if it is surrounded by an optically thick disk of gas."

The disk in the β Lyrae system has the lower surface brightness, enshrouding an unseen, star. β Lyrae is an SB1 system; only the donor star's spectral lines have been observed. Wilson's (2018) preliminary trial-and-error fitting (Fig. 12) is reproduced and annotated in Figure 6. The data are from the Villanova APT instrument; original observations are in Abt (1995). In the deeper eclipse, the disk is eclipsing the B8 Ib lobe-filling donor star; other eclipse is of the disk by the donor. The light variation between eclipses is attributed to tides in the disk and donor. In Wilson's basic disk model there is natural closure of level surfaces without arbitrary disk truncation. Tidal stretching of the disk by the donor star enhances overall tidal brightness variation. The light curve has been relatively stable over centuries, so the high accretion rate, characteristic of a binary in the rapid stage of mass transfer, requires the accreted material to be either absorbed by the non-compact star at the disk center or, as Wilson (2018) suggests, decreted back into the disk. In either case it is a DbC and a strong candidate for an A-D disk system. In some Algol systems, the emission line features may be seen only in the deep minimum implying that the disk is consequently thin and not massive enough to be self-gravitating. In such systems the recipient component readily absorbs the accreted material and can drain the disk on short time scales.

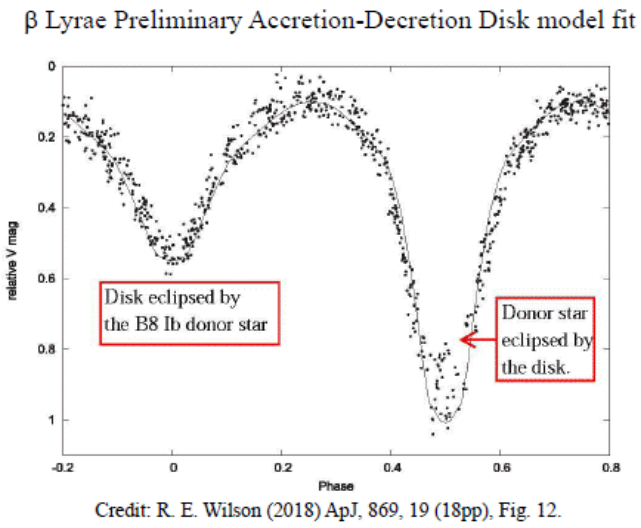

Figure 6: From Wilson (2018, Fig. 12), a preliminary trial-and-error fitting of the A-D disk model to a differential V light curve of β Lyrae. The data are from the Villanova APT instrument; original observations are in Abt (1995). In the deeper eclipse, the disk is eclipsing the B8 Ib lobe-filling donor star; other eclipse is of the disk by the donor, so the B8 Ib component has a higher surface brightness than the disk.

Whereas the β Lyrae light curve is relatively stable, that of CI Aquilae is not; it is a recurrent nova. Figure 7 (from Fig. 6 of Wilson, 2018) shows a fitting for the eclipsing cataclysmic variable (CV), CI Aql, in quiescent state after its eruption in 2000. The photometry data are from Schaefer (2011, 2014) and Wilson & Honeycutt (2014) and the RVs are from Sahman et al. (2013), who made ingenious use of Doppler tomography to secure velocities from the line profile wings of the disk as proxy values for those of the white dwarf. Wilson (2018) provides evidence that if they are massive enough A-D disks around the nova may survive moderate outbursts. That a similar light curve is seen before and after the last outburst of CI Aql proves that its disk has done so. In the present instance, the model allows the disk to be semi-transparent so that when it eclipses the donor star, some light is able to diffuse through the disk and the "oblateness effect" in the maxima is due not so much to the lobe-filling donor, but mainly due to the lobe-filling tidally distorted disk. In this case the hidden star is a white dwarf, spun up by the angular momentum of the disk material to the point of decreting it back into the disk. Consequently in this DbC case, the disk is massively self-gravitating and undoubtedly an A-D disk system. Wilson & Hunnicutt (2014) treat the dynamics of the stream and disk.

The modeling of disks in double contact (DbC) systems uncovers some interesting and even surprising results. Aspects of the equipotential disk include its semi-transparency to allow both attenuation and re-emission and the irradiance of the companion star, and the reflection functions defined in Wilson (1990) provide the efficiency to allow multiple reflections. An inner null point defines the inner edge of the disk; both null points are computed at each iteration. As a consequence, there is no arbitrariness in defining the confines of the disk; they are determinable in the model. In their recent work, Wilson & Van Hamme (2025) emphasize a number of details about the cases of CI Aquilae and U Scorpii where the disks contain 3% and 6% of the white dwarf mass, respectively:

1. The white dwarf's rotation is coupled analytically to disk properties such as size and shape that affect the photometric variation via the A-D condition;
2. The parameter F (the ratio of the white dwarf angular rotation to the orbital angular rate) is a parameter that can be adjusted and so is determinable;
3. The orbital rate is known from the orbital period and size, hence the rotation rate and Period;
4. The outer disk edge parameter, x_{outer} is found to be close to x_{null} where the effective gravity is zero, within errors. This constitutes a check on the model.

It is possible and may even be likely that many if not most post-novae are double contact binaries. The DbC model should lead to more precise determinations of the properties of these objects. More observations are needed of CVs and novae in quiescent states. Two eclipses are needed for modeling and because the disks are typically hotter than the donor stars, IR photometry will be useful.

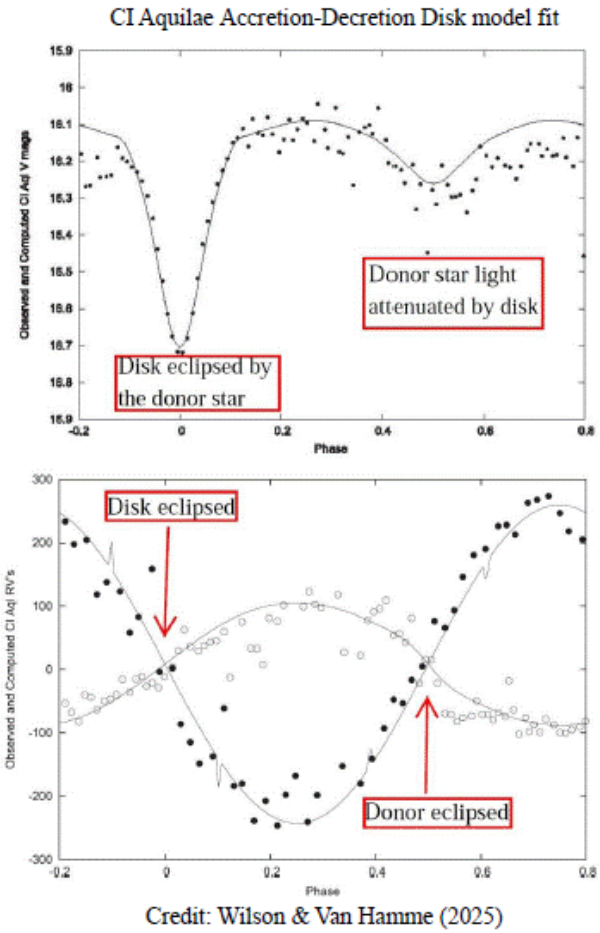

Figure 7: From Wilson (2018, Fig. 6), the *V* passband binned light curve (top) and radial velocity curves (bottom) of the recurrent nova CI Aql in quiescent stage together with the preliminary fitting to them of an A-D disk model. The light curve data are from Schaefer (2011, 2014) and Honeycutt & Wilson (2014), the RV data from Sahman et al. (2013). The open circles are donor RVs and the closed circles are disk RVs; the latter are based on emission line wings, considered proxies for the white dwarf itself. The deeper eclipse at phase 0 is of the disk by the donor star. The shallower, broader eclipse is of the donor star by the semi-transparent disk.

3.4. Ancillary Software

Over the decades that this astronomer has been working much ancillary software has appeared which have proven very useful in light curve analysis. These include algorithms to seek out the deepest minimum in parameter space with efficiency, such as Simplex, and robustness, such as Simulated Annealing (SA). Both are fully referenced and discussed in Kallrath & Milone (2009). A version of SA was implemented by Kallrath within a package coupled directly to WD07 (described above). Tests of this SA version, discussed in Milone & Kallrath (2008) was used in the analyses of newly discovered eclipsing binaries in a field of the RAO's Baker-Nunn patrol camera by Williams & Milone (2013). Currently D. Terrell is using the algorithm in addition to the 2013 WD version in his study of V372 Draconis.

Doppler tomography as used in *Shellspec* (Budaj & Richards, 2004) is a very promising way to check the dynamical layout of close binary systems; Janos Budaj (2025, private communication) relates that the latest public release is Shellspec49 but that such advanced features as dust reddening and extinction, definition and treatment of shadows by opaque objects, and the introduction of ellipsoidal disk like structures is being incorporated into the program. See Budaj, Maliuk, & Hubeny (2022) for its use in modeling an exotic white dwarf system.

Spectrophotometry has not been mentioned thus far, but if it can be done to avoid stray light issues, it can produce a boon to ground-based acquisition of a large number of light curves across the spectrum simultaneously. Such as instrument in fact has been designed and built for absolute calibration purposes. Adelman (2011) discusses the history of spectrophotometers and scanners and a specially made optical telescope telescope.to avoid light loss and scattering.

Polarization measurements, although challenging to make, are also worth pursuing, given the importance of magnetic fields in systems with compact components. Bastien (2011) discusses the history of polarimetry and its usefulness in discerning electron scattering envelopes in binary components and even in the determination of orbital elements. It may be especially useful in studying DbC systems. One important instrument for this purpose is *ESPaDOnS*, a bench-mounted high resolution echelle spectrograph/spectropolarimeter, available at the Canada France Hawaii Telescope (CFHT). Bailey et al. (2023) report on recent high-precision polarimetry and new results with PICSARR (Polarimeter using Imaging CMOS Sensor And Rotating Retarder).

Finally, speckle interferometry can confirm the presence of additional objects within a binary star system, as we note below.

3.5. The Study of Hierarchical Systems

With improved models, attention returns to improving the precision and accuracy of the observables. One area that is emerging is the extent to which binary stars are parts of greater systems, hierarchies. This impacts the analyses of eclipsing systems in such configurations.

Improved light curve coverage is providing accumulated evidence of hierarchical stellar systems with binaries and a third component having the simplest such configuration. Pribulla & Rucinski (2006) found that a significant number of W UMa systems had wider companions. Similarly, Nelson et al. (2023) in searching for solid evidence for mass exchange in W UMa systems, found many examples of other components in time-of-minimum analyses. Although sixty systems were investigated, in the end only seventeen presented sufficiently strong evidence for mass exchange. This was due, in large part, to insufficient coverage of the orbits of additional companions to the eclipsing binary systems to satisfy the light time effect (LiTE) analyses of the period variation.

Hierarchical components have been studied spectroscopically and astrometrically by Tokovinen (2025), who notes that the Gaia mission detection of such systems is quite incomplete. Therefore, like systems discovered through minimum timing in eclipsing systems, extensive ground-based follow-up observations are needed to provide the full picture. Starting with visual binaries, he probes the inner components. Some of his studies are of historical interest as well; in one case, a visual binary separated by 3 arc-sec when discovered by John Herschel in 1837 (HJ 4310, HIP 49442), is found to be a multiple star system. The brighter component, A, has a companion only 0.18 arc-sec apart as revealed by Speckle interferometry: components Aa and Ab. But the spectrum of A reveals three set of lines; component Ab is itself a binary system (Ab1, Ab2) separated by 0.0098 arc-sec, making them part of a quadruple system of 3+1 hierarchy. The masses of the A components need to be refined, requiring more observations.

According to Tamajo et al. (2012), SZ Cam, in addition to being the northern component of the visual binary ADS 2984, has another component, discovered through speckle interferometry, and it is a single-lined spectroscopic binary system (SB1). One of the four stars is a β Cephei pulsating variable. More recently, the southern component of the visual binary with SZ Cam, ADS 2984A, has been found to be an SB1 system (Gorda, 2016). If all these reports are correct, SZ Cam is in a system of six stars, all of which would be members of the young open cluster NGC 1502.

From an entirely different area of study, evidence for a systemic acceleration during a black hole merger led S.-C Yang et al. (2025) to propose that the merger occurred in the vicinity of another, possibly supermassive, black hole. Disks around SMBHs have been suggested as a site where smaller black holes could merge, creating the unexpectedly large masses found for increasing numbers of them from LIGO event studies.

4. The Promise of Precise Infrared Photometry for Future Light Curve Analyses

Almost all the photometry discussed above was done in the visible part of the spectrum, but the Earth's atmosphere also has windows in the infrared part of the

spectrum (≥1μm; hereafter IR, but not to be confused with Johnson's "red" *R*, and "Infrared" *I*, passbands). Analyses now are able to make use of the milli-magnitude-precision achievable from ground-based optical photometry. Up to the present, that has not yet been achieved to the same extent in the infrared.

In systems with greatly contrasting components, the IR will help to define the secondary minima so that temperature differences, modified Kopalian potentials, limb-darkening, albedos, and gravity-darkening coefficients may be determinable with unprecedented precision. The smaller contrast of cool spot temperatures in the IR, combined with other passband data, will permit better separation from the overall morphology to produce improved spot temperature, longitude, size, and, for central eclipses, perhaps also latitude.

Algol's B and V light curves defined its EA light curve character but its infrared light curve resembles an EB type. A posting at the American Association of Variable Star Observers (AAVSO) website notes the importance of continually observing 12.9^{d}-period β Lyrae in the infrared as that system evolves (Terrell, 2025). A DbC system in which the disk is radiatively cooler than the donor is a good target for IR work. Wilson (2025) notes that a *B* light curve does not show a secondary eclipse in the recurrent nova U Sco whereas an *I* light curve does. This system may be a good target for photometry in the even redder passbands discussed below. The system DS And is a 1-day period, double-lined eclipsing binary in an open cluster (NGC 752), and both recent major analyses of the system (Milone et al., 2019; Sandquist et al., 2022) although arriving at different absolute parameters (at least some of which may be due to the re-reduction of RV data), find anomalies in one or both components. In such a case, additional types of data and perhaps new stellar models need to be considered and explored.

Now we describe the status of infrared passbands, the challenges in carrying out photometry with them, and how those challenges can be met.

IR Photometry can produce high photometric precision in principle because:

1) there is little atmospheric Rayleigh scattering ($\propto \lambda^{-4}$) in these wavelengths; and

2) there are now passbands that minimize the parts of the windows with absorption bands of water vapor and other atmospheric molecules.

The Earth's atmosphere is not as transparent to radiation beyond 1 μm as is visible light, because of molecular absorption bands, mainly from water vapor, which is variable on all time scales. There are however spectral regions where the absorption is minimal, referred to as atmospheric windows. As part of a multi-color, wide-band set of passbands that included *UBVRI*, Harold Johnson (1964; 1966) defined for the region between 1 and 4 μm the passbands *JKL* (*H*, between *J* and *K*, was added later), and for the >4 to 22 μm region *M* and *N* (*Q* was added later). With relatively insensitive detectors and limited options, the filters selected to sample these regions were so broad they overlapped atmospheric windows, so the passbands are partly defined by the varying water vapor absorption. Several attempts were made by astronomers to narrow the passbands somewhat to improve the resulting problem with precision and repeatability of the IR photometry at their sites, resulting in many versions of the Johnson passbands, and yet all bearing the same Johnson designations. The problem with contemporary IR astronomy, how astronomers dealt with it, and how it could be improved, was discussed at length at a joint meeting of IAU commissions 9 and 25, at the IAU General Assembly in Baltimore in 1988 (Milone, 1989). The problem was identified and resulted in the creation of a Working Group to fix it. The work was described and preliminary results were reported in Young et al. (1992). The history is summarized in Milone & Young (2011).

Young et al. (1994) noted that the *J* passband included a strong water-vapor band at 1.14 μm and proposed replacing that *J* passband with two passbands on either side of the water vapor band: a new passband we called *z*, after the Kodak Z sensitization class which was useful for this spectral region, and an improved *J* on the long-ward side of the absorption band. Later we referred to the improved *J* passband as "*iJ*" and the *z* passband "*iZ*" for consistency. The 1 μm window we refer to as the Z window, and that beyond it as the J window. Similarly, we referred to the other windows with the designations formerly accorded to the Johnson passbands in which each of them was most centered and we placed a lower case letter I in front to designate the new passbands, hence *iH*, *iK*, etc. The recommended change in usage for the ZJHKLMNQ designations was formally approved by the International Astronomical Union: IAU Resolution B1, *on guidelines for the designations and specifications of optical and infrared astronomical photometric passbands*, that was put forward on behalf of Commission 25 and its Infrared Working Group (IRWG) and passed at the 2012 Bejing General Assembly. The resolution states in part that "the designations ZJHKLMNQ should be used henceforth to refer exclusively to the terrestrial atmospheric windows in the near and intermediate infrared (see Young et al. A&AS, 105, 259-279; Milone & Young (2005), PASP, 117, 485-502)."

As a consequence, while primes and subscripts on the old passband names have proliferated, amid a continuing use of the old names by some astronomers, newer passbands have rarely been optimized for use at all elevations and atmospheric models. Even those designated as "short" passbands, such as K_S, though trimmed to be less affected by water vapor absorption at high-elevation observatories such as Mauna Kea (4.2 km), fail to perform as well at lower sites in varying atmospheric conditions. The IRWG-designed passbands central wavelength placement and bandwidth were optimized to avoid the obscuration within the windows by minimizing the diminution of each of two Kurucz model stellar flux bundles traversing the atmosphere. The full methodology is presented in Young et al. (1994), and the realization of the near-IR suite of the recommended

passbands, through testing *iZ*, *iJ*, *iH*, and *iK* filters manufactured within specifications by Custom Scientific of Tucson, Arizona, is described in Milone & Young (2005, 2007), among other references. It is necessary to add, however, that photometry with unoptimized passbands carried out at a high and dry site under photometric conditions can be precise and accurate, and astrophysical relations among color indices valid. Wing (2011) notes that because basic information content of three-color photometry in the JHK windows is governed by the effects of stellar H- opacity the information content is not expected to change with the use of the IRWG passbands in these windows.

The upper portion of Figure 8 demonstrates the obscuration in atmospheric Z and J windows mainly due to molecular absorption by water vapor. The atmospheric transmission was computed with the MODTRAN program (Berk et al., 1989) for a standard atmosphere and a site at 1 km elevation above sea level. Superimposed are the passband profiles for *iJ* and *iZ* and their Custom Scientific equivalent filters, *cyJ* and *ciz*; *rJ*, is a Johnson *J*-like passband. The lower plots show simulated Bouguer extinction curves for the *J*, *iJ* and *iZ* passbands, all with the same stellar flux sources for a mid-latitude summer atmosphere at elevation of 1.3 km, the elevation of the RAO. Note the strong Forbes effect, the curvature of the extinction curve upward between 1 and 0 airmass for the *J* passband due to molecular absorption high up in the atmosphere. Actual extinction curves for Vega with *cyJ* and *ciz* passbands, on a particular night are shown in the lower right. In these passbands the extinction coefficients are low and the extrapolations to zero airmass give sufficiently close approximate to the outside the atmosphere magnitudes that differential photometry with well-chosen comparison stars, promises accurate and precise results.

A drawback in carrying out long-wavelength photometry has been that specialized telescopes and equipment have been needed. In the thermal IR, beyond ~3μm, liquid nitrogen or liquid helium cryogens are needed to reduce noise, and for single pixel detectors the sky background must be measured alongside the target stars, by rapidly chopping (oscillating) the telescope's secondary mirror, nodding the telescope to sample the opposite sky area, and using a lock-in amplifier and integrator to remove the sky signal and measure the flux. Consequently, IR work has usually been carried out only at observing sites at high elevations to minimize water vapor absorption and justify the expense of the operation. The latter constraint has been eased. The former constraint now also has a remedy.

Figure 9 shows the simulated spectral transmission of a mid-latitude, summer atmosphere at a site elevation of 300 m. Superimposed on this are the profiles for near-IR IRWG passbands, iZ, iJ, iH, and iK. Note that they are not defined by the opaque edges of the windows, whereas wider passbands would be. It can be appreciated therefore that under such conditions the IRWG set cannot be called "narrow-band" in any real sense, and once signal to noise ratios, efficiency, and quality of the photometry is considered, they can be called "improved."

Recent work by Mishra & Kamath (2022) has confirmed this work and demonstrated the feasibility of using the three shortest IRWG passbands at observatories at both high and low elevations to obtain infrared light curves of improved precision and accuracy. Planning is underway at one site to realize that, in order to study population II pulsating stars among other targets (Mishra et al, 2024). Indeed in pulsating stars the IR is more sensitive to radius variation. Mishra & Kamath (2022) note the suitability and commercial availability of InGaAs single-pixel and array detectors and of additional filters that approximate the specifications for the iZ, iJ, and iH profiles. They provide a table of integration times to achieve S/N = 100 per observation of stars with J/H magnitudes between 7.5 and 12.5 with four different detectors on a 1-m telescope, with dark current and read noise specified for the array detectors and NEP for the single-pixel devices.

The Mishra and Klamath work involves the non-thermal IR, but the full suite of IRWG passband recommendation extends much further into the IR. Just as the RAO, located at 1.3 km elevation above sea level, found it worthwhile to invest in thermal IR instrumentation in the 1980s into the early part of the current century, other observatories may find it equally worthwhile to do so. Figure 10 demonstrates the case for observing in the N (10 μm) window by comparing the obscuration and simulated extinction curves for old (*N*) and newer (*coN*) versions of Johnson's passbands in this window, and two IRWG passbands optimized for the main part and a smaller part of the N window, *iN* and *in*, designated here by *yN* and *yn*, temporary designations in Young et al. (1994). The lower four plots are simulated extinction curves for the *N* and *yN* passbands. Plots on the left, are computed for a tropical atmosphere and a site of 4.2 km; plots on the right, are computed for a mid-latitude, summer atmosphere at ~1 km altitude. Note the decreased Forbes effect with the *yN* passband even for both elevations.

Future IR discoveries made with the James Webb (JWST) and Nancy Roman Space Telescopes likely will require follow-up data from ground-based observatories. Experience teaches that observing proposals seeking to monitor individual variable stars are rarely allocated observing time at premier observatories. Observatories at lower elevation sites able to invest in IR infrastructure and instrumentation can provide the opportunities to fill that need.

Z and J atmospheric windows, J, iJ & iZ Passband profiles and extinction curves

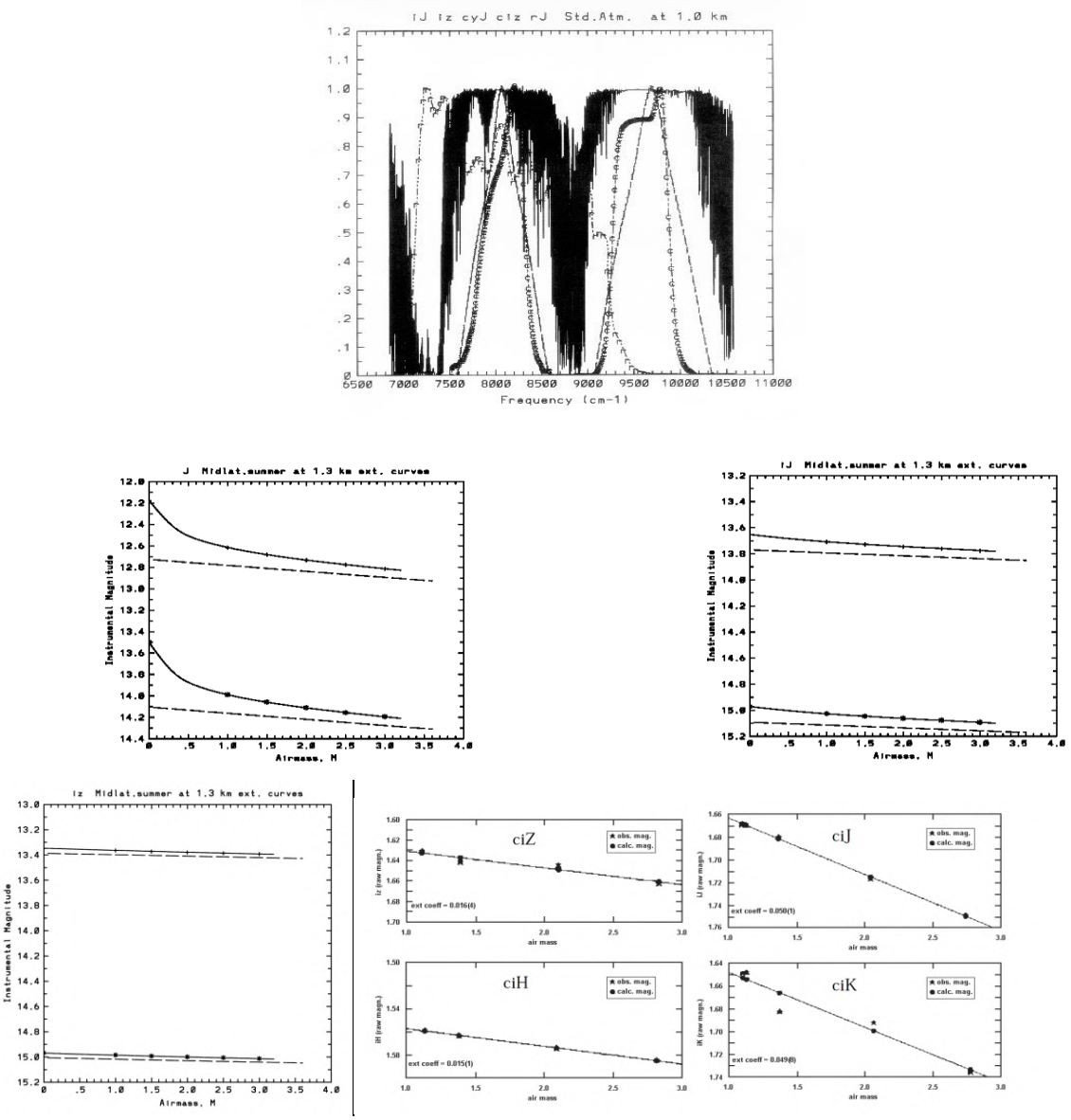

Figure 8: The top plot shows the spectral transmission between 0.9 and 1.5 μm of a standard atmosphere computed with the MODTRAN program (Berk et al., 1989). It is plotted in wavenumber units of frequency. A value divided into 10,000 gives the wavelength in μm. The Z (~1μm) window is thus to the right and the J (~1.25μm) window to the left. Also plotted are the *iz* = *iZ*, *iJ* and Custom Scientific filter profiles *ciz*, *ciJ*, and an older Johnson *J* passband previously used at the RAO, *rJ*, designated by first letter in the plots. Three of the lower plots, show simulated Bouguer extinction curves for *J*, *iJ* and *iZ*, all with the same stellar flux sources for a mid-latitude summer atmosphere at elevation of 1.3 km, the elevation of the RAO. Note the strong Forbes effect, the curvature of the extinction curve upward between 1 and 0 airmass, for *J*. Actual extinction curves for Vega with the Custom Scientific filters approximating *iZ* and *iJ* on top and *iH* and *iK* (prefixed with "c") on the bottom, on Sept. 26, 2000 at the RAO, are shown in the bottom right set of four plots.

Near-infrared Atmospheric Windows and IRWG Passband Profiles

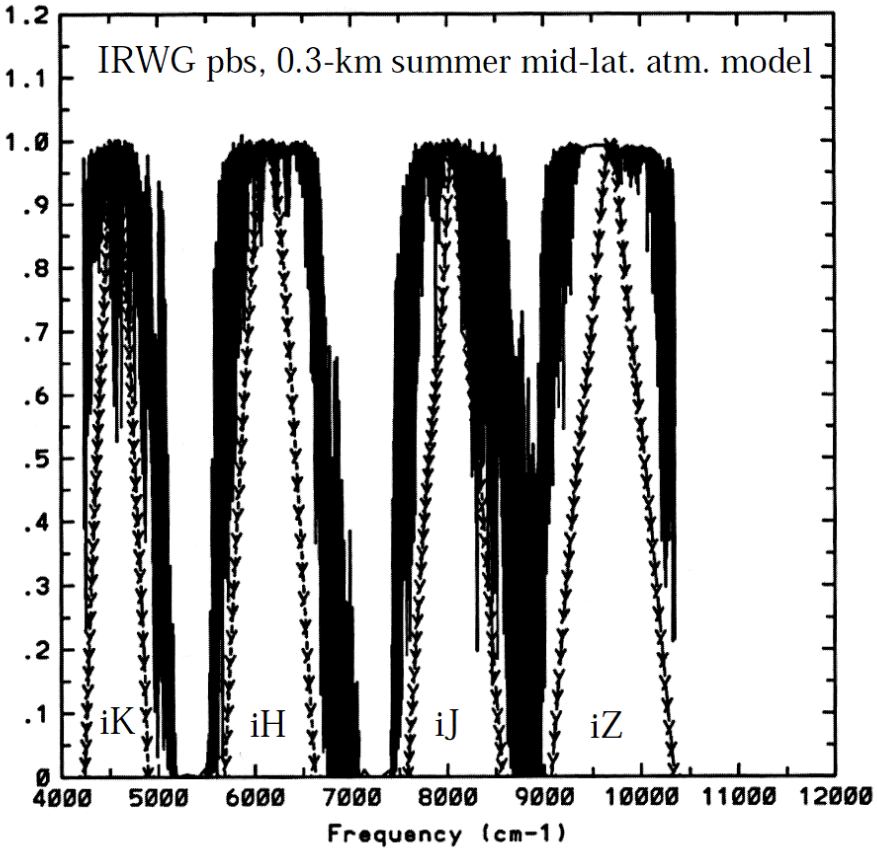

Figure 9: The simulated spectral transmission of a mid-latitude, summer atmosphere at a site elevation of 300 m, computed with MODTRAN software. Superimposed on this are the profiles for the near-infrared IRWG passbands *iZ*, *iJ*, *iH*, and *iK*. Note that the passbands fit comfortably into the atmospheric windows but are not defined by their opaque edges even at this low elevation site.

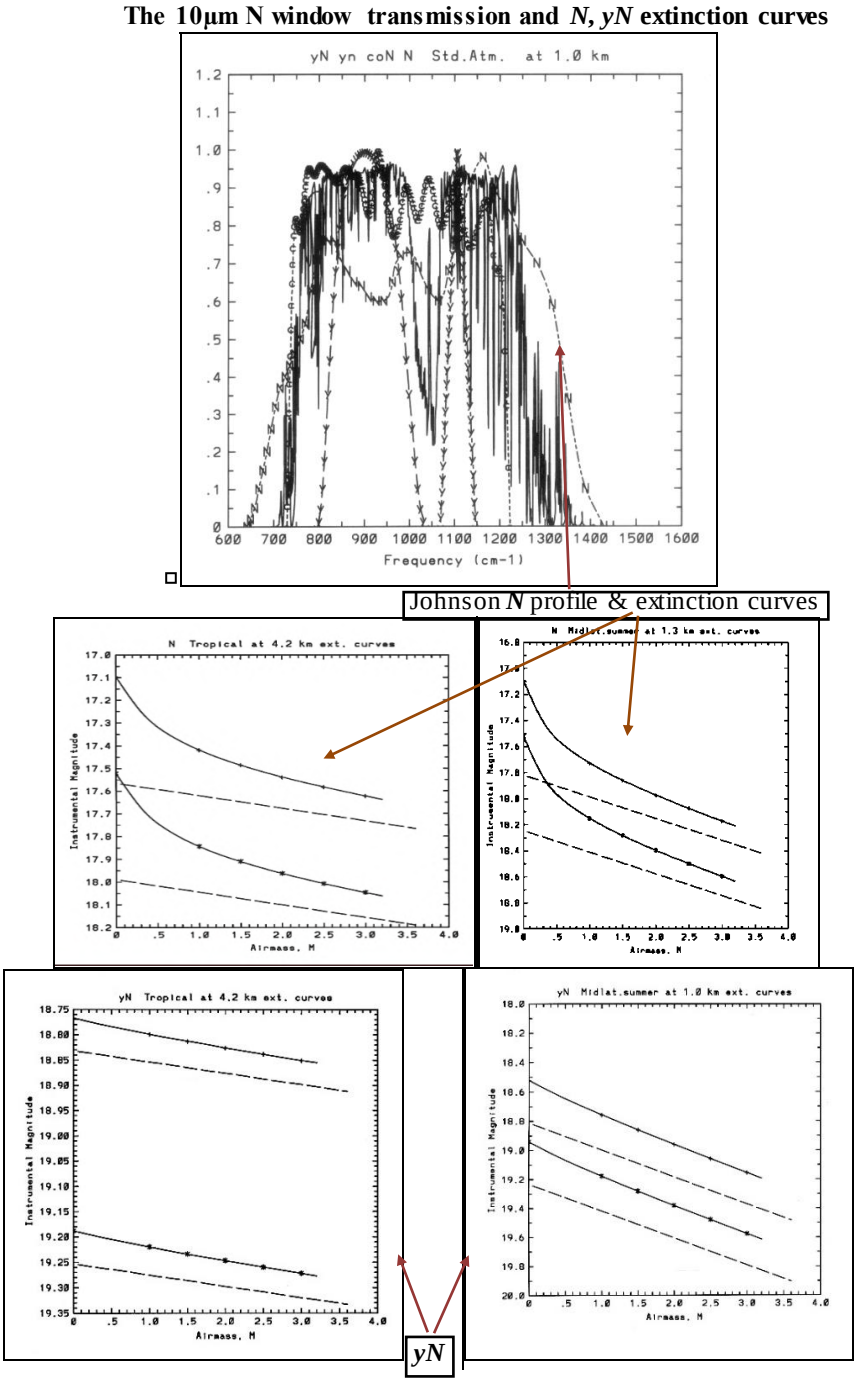

Figure 10: The top plot shows the spectral transmission computed with MODTRAN for a standard atmosphere and a site at 1 km elevation above sea level for the N window spectral region. Superimposed on it are the profiles of two IRWG passbands, here designated *yN* and *yn* (temporary designations for the profiles presented in Young et al. (1994), and now referred to as *iN* and *in*, respectively. The original Johnson *N* passband, and a newer, somewhat improved one, designated *coN*. The lower four plots are simulated extinction curves for the *N* (top two), and the *yN* (bottom two) passbands. Plots on the left are computed for a tropical atmosphere and a site of 4.2 km; those on the right are computed for a mid-latitude, summer atmosphere at ~1 km altitude. Note the decreased Forbes effect with the *yN* passband for both elevations, allowing thermal infrared photometry to be carried at many photometric sites.

5. Conclusion

We have followed parallel themes of the origins and development of the observation, modeling, and analysis of eclipsing variable star studies, and of the analytical tools and techniques to study them. We have explored the progress in the field over the past century and with case studies highlighted the effects of improvements in data acquisition and quality as well as methods of analysis. Hopefully the exposition has shown that to study eclipsing binary stars is to undergo a journey of adventure and discovery. With space-scanning missions, we now have an

enormous collection of data, most of which will need to be followed up at ground-based observatories. For that work, we have the observing tools to produce the precise light & radial velocity curves and other observables needed for the analyses. With present modeling programs that incorporate physically realistic stellar and system models, the determination of ever more precise and accurate fundamental parameters of the component stars and the direction of their evolution seems secure. Henry Norris Russell's royal road even after more than a century of progress wide-open and inviting.

Acknowledgements. The author was honored and privileged to have been asked by Prof. I. Andronov to present a plenary paper on eclipsing binary stars at this important conference. I acknowledge with thanks the assistance of colleagues for some material in this presentation, particularly, R. E. Wilson, J. Kallrath, D. Terrell, and W. Van Hamme, and A. T. Young for insightful comments and corrections, but note that the views expressed are fully mine, and I alone bear responsibility for omissions or misrepresentations. Apologies to other colleagues, past and present, whose extensive and seminal works are not included in this personal and necessarily limited perspective. Most of my research drawn on here was funded by grants from the National Research Council and by the Natural Sciences and Engineering Research Council of Canada, the Research Grants Committee and the Department of Physics and Astronomy of the University of Calgary; specialized grants from agencies of the provincial government of Alberta, and the Cross Educational Foundation, all of which were received with gratitude.

Appendix: Objectives of Two IAU Commissions:

This work has undertaken a broad view of the subject through the perspective of a techniques astronomer, but the spirit of the undertaking is also in accord with that of at least two IAU Commissions. The scientific objectives and interests of Commission G1 – Binary and Multiple Stars (https://iauarchive.eso.org/science/scientific_bodies/commissions/G1/) are:

- "the full range of observational tools that reveal binary and multiple systems (astrometry, photometry, spectroscopy, polarimetry, structure of cluster HR diagrams, products of space missions including Kepler, Gaia and LSST), and the interface of these with concerns of other Divisions and Commissions;
- kinematics, and ultimately dynamics, of binary and multiple systems;
- improved codes for binary and multiple systems, stellar atmospheres, structure and evolution, yielding surface compositions, tracks in the HR diagram, temporal changes in system masses and separations, etc;
- improvements of existing binary and multiple star system databases, regular production of publications (online and perhaps in print on paper), sharing databases, new codes, exciting discoveries, and opportunities for interaction with other parts of the astronomical community; and
- accurate knowledge of the history of the subject and its continuing impact on astronomy in general."

The statement of the scientific objectives of IAU Commission B6, Astronomical Photometry and Polarimetry (https://iauarchive.eso.org/science/scientific_bodies/commissions/B6/) is:

"Commission B6 is concerned with photometric and polarimetric techniques and their standardization for the UV through far-IR/sub-mm spectral regions. These are essential tools in the exploration and investigation of astronomical objects and quantities.

Solutions to a wide range of scientific problems require calibrated photometry and polarimetry at better than the 1% level. Standardization is inescapable for exchanging data or merging data from different sources."

References

Adelman, S. J.: 2011, Optical Region Spectrophotometry: Past and Present, in Astronomical Photometry: Past, Present, and Future, eds. Milone, E. F. Sterken, C. (Springer, New York, Heidelberg, Dordrecht, London), 187-197.

Apt, H.: 1995, *The AAS CD-ROM Series*, Vol. **5** (Oldsmar, FL: Advanced Data Solutions).

Armbruster, C. W., Hull, A. B., Koch, R. H., Mitchell, R. J.: 2011, The Pierce-Blitzstein Photometer, in Astronomical Photometry: Past, Present, and Future, eds. Milone, E. F. Sterken, C. (Springer, New York, Heidelberg, Dordrecht, London), 83-105.

Bailey, J., Cotton, D. V., De Horta, A., Kedziora-Chudczer, L., Shastri, O.: 2023, PICSARR: high-precision polarimetry using CMOS image sensors, MNRAS, arXiv:2301.09782 [astro-ph.IM]

Bastien, P.: 2011, Measurement of Polarized Light in Astronomy, in Astronomical Photometry: Past, Present, and Future, eds. Milone, E. F. Sterken, C. (Springer, New York, Heidelberg, Dordrecht, London), 199-210.

Berk, A., Bernstein, L. S., Robertson, D. C.: 1989, MODTRAN: A moderate Resolution Model for LOWTRAN 7, GL-TR-89-0122 (Air Force Geophysics Laboratory, Bedford, Mass.).

Budaj, J., Richards, M. T.: 2004, A description of the shellspec code, Contrib. Astron. Obs. Skalnaté Pleso, 34, no. 3, 167-196.

Budaj, J., Maliuk, A., Hubeny, I.: 2022, WD 1145+017: Alternative models of the atmosphere, dust clouds, and gas rings, *A&A*, **660**, A72 [https://doi.org/10.1051/0004-6361/202141924]

Cohen, M.: 2011, Absolute Photometry: Past and Present, in Astronomical Photometry: Past, Present, and Future, eds. Milone, E. F. Sterken, C. (Springer, New York, Heidelberg, Dordrecht, London), 177-186.

Doppler, C.: 1842, Ueber das farbige Licht der Doppelsteme und einiger anderer Gestirne des Himmels, Abhandlungen der Königl. Böhemischen Gesell. der Wissenchaften zu Prag, V. Folge, Bund ii, Prag, 465.

Drilling, J. S., Landolt, A. U.: 2000, Normal Stars, Chapter 15, in A. N. Cox, Allen's Astrophysical Quantities, (AIP Press Springer-Verlag, New York), Table 15.6, p. 387.

El-Badry, K.: 2024, Gaia's binary star renaissance, New Astronomy Reviews, 98, 6.
Gorda, S. Yu.: 2016, Radial Velocity of the Spectroscopic Binary HD 25639 (ADS 2984A), *Astron, Lett*., **42**, 693-702.
Hall, J. S.: 1934, Photo-electric Photometry in the Infrared with the Loomis Telescope, ApJ, 79, 145-181.
Hardie, R. H.: 1962, Photoelectric Reductions, Chapter 8, in Astronomical Techniques, ed. W. A. Hiltner, (The University of Chicago Press, Chicago), 178-208.
Herschel, W.: 1803, XV. Account of the Changes that have happened, during the last Twenty-five Years, in the relative Situation of Double-Stars; with an Investigation of the Cause to which they are owing, *Phil. Trans. Roy. Soc*., **93**, 339-382 + Plates VII and VIII.
Huggins, W.: 1868, Further observations on the spectra of some of the stars and nebulae, with an attempt to determine therefrom whether these bodies are moving towards or from the Earth, also observations on the spectra of the Sun and of Comet II, *Phil. Trans. Roy. Soc*., **158**, 529–564.
Johnson, H. L.: 1964, *Bol. Tonantzintla Tacubaya*, **3**, 305-324.
Johnson, H. L.: 1966: Astronomical Measurements in the Infrared, in *Ann. Rev. A&Aph*, **4**, 193-206.
Kallrath, J.: 2022, Fifty Years of Eclipsing Binary Analysis with the Wilson-Devinney Model, *Galaxies*, **10**, 17-30.
Kallrath, J., Milone, E. F.: 2009, Eclipsing Binary Stars: Modeling & Analysis, 2nd ed. (Springer, New York, Dordrecht, Heidelberg, London).
Kallrath, J.; Milone, E.F.; Terrell, D.; Young, A.T.: 1998, Recent Improvements to a Version of the Wilson–Devinney Program. *Astrophys. J.*, **508**, 308–313
Kopal, Z.: 1950, The Computation of Elements of Eclipsing Binary Systems. Harvard Observatory Monograph No. 8.
Kopal, Z.:1959, Close Binary Systems. (John Wiley & Sons, New York), 127.
Kopal, Z., Shapley, M. B.: 1956, Catalogue of the Elements of Eclipsing Binary Systems, Reprint, Jodrell Bank Annals, 1, fascicle. 4, 168-169.
Kostov, V. B., Powell, B. P., Fornear, A. U. et al.: 2025, The TESS Ten Thousand Catalog: 10,001 Uniformly Vetted and Validated Eclipsing Binary Stars Detected in Full-frame Image Data by Machine Learning and Analyzed by Citizen Scientists, *ApJS*, **279**, 50 (32pp).
Kurpinska-Winiarska, M., Oblak, E., Winiarski, M., Kundera, T.: 2000, Observations of Two Hipparcos Eclipsing Variables IBVS, 49, No. 4823, 1 -3.
Lagrange, J.-L.: 1772, Essai d'une nouvelle méthode pour résoudre le problème des trois corps. Oevres complètes VI, Prix de l'Academie royale des sciences de Paris, tome IX, 229-331.
Landolt, A. U.: 1983, UBVRI Photometric Standard Stars around the Celestial Equator, *AJ*, **88**, 439-460.
Leavitt, H. S. & Pickering, E. C.: 1917, The North Polar Sequence, Harvard Annals, 71, No. 3, 47-232.
Li, X.-Z., Zhu, Q.-F., Ding, X. et al.: 2024, Physical Parameters of 11,100 Short-period ASAS-SN Eclipsing Contact Binaries, *ApJS*, **271**, 32 (9pp).
Lucy, L B.: 1968, The Light Curves of W Ursae Majoris, *ApJ*, **153**, 877-884.
Marigo, P., Girardi, L., Bressan, A., Groenewegen, M. A. T., Silva, L.,& Granto, G. L.: 2008, Evolution of asymptotic giant branch stars. II. Optical to far-infrared isochrones with improved TP-AGB models, *A&A*, **482**, 883-905.
Mayor, M., Queloz, D.: 1995, A Jupiter-mass Companion to a Solar-type Star, *Nature*, **378**, 355-359.
Michell, J.: 1767, An Inquiry into the Probable Parallax, and Magnitude of the Fixed Stars, from the Quantity of Light Which They Afford us, and the Particular Circumstances of Their Situation, *Phil. Trans. Roy. Soc*., **57**, 234-264.
Milone, E. F., ed.: 1989, Infrared Extinction and Standardization, *Lect. Not. in Phys.*, **341** (Springer-Verlag, Berlin, Heidelberg).
Milone, E. F.: 2003, Fundamental stellar parameters from eclipsing binaries, in *GAIA, Spectroscopy, Science and Technology*, ed. U. Munari, ASP Conf. No. 298, 303-312.
Milone, E. F., Kallrath, J.: 2008, The Tools of the Trade and the Products they Produce: Modeling of Eclipsing Binary Observables, in Short-Period Binary Stars: Observations, Analysis, and Results, eds. Milone, E.F., Leahy, D.A., Hobill, D.W. (Springer Science+Business Media B.V.), 191-214.
Milone, E.F., Pel, J. W.: 2011, High Road to Astronomical Photometric Precision: Differential Photometry in Astronomical Photometry: Past, Present, and Future, eds. Milone, E. F., Sterken, C. (Springer, New York, Dordrecht, Heidelberg, London), pp 33-68.
Milone, E. F., Sterken, C., eds.: 2011, Astronomical Photometry: Past, Present, and Future, (Springer, New York, Dordrecht, Heidelberg, London).
Milone, E. F., Young, A. T.: 2005, An Improved IR Passband System for Ground-Based Photometry: Realization, *PASP*, 117, 485-502.
Milone, E. F., Young, A. T.: 2007, Standarization and the Enhancement of Infrared Precision, in The Future of Photometric, Spectrophotometric, and Polarimetric Standardization, ed. C, Sterken, ASP Conf. Series 999, 387-407.
Milone, E.F., Young, A.T.: 2011, The Rise and Improvement of Infrared Photometry, in Astronomical Photometry: Past, Present, and Future, eds. Milone, E.F., Sterken, C. (Springer, New York, Dordrecht, Heidelberg, London), pp 125-141.
Milone, E. F., Kurpinska-Winiarska, M., Oblak, E.: 2010, Observations and Analysis of the Eccentric Orbit Eclipsing Binary HP Draconis, *AJ*, **140**, 129-137.
Milone, E. F., Wilson, R. E., and Hrivnak, B. J.: 1987, RW Comae Berenices III. Light Curve Solution and Absolute Parameters, *ApJ*., **318**, 325-338.
Mishra, A. K., Kamath, U. S.: 2022, Filters for NIR astronomical photometry: comparison of commercial IRWG filters and design using OpenFilters, *Journal of Astrophysics and Astronomy*, **43**, 13 (16pp).
Mishra, A. K., Sarkar, D. R., Prajapati, P., Singh, A., Kasarla, P. K., Ganesh, S.: 2024, A summary of instruments proposed for observing pulsating variables from the Mt. Abu Observatory, *Journal of Astrophysics and Astronomy*, **45(2)**, 34 (15pp).
Mowlavi, N. et al.:2023, Gaia Data Release 3: The First Gaia catalogue of eclipsing-binary candidates, *A&A*, **674**, A16 (45pp).
Nelson, R. H., Terrell, D., Milone, E. F.: 2023, A Critical Review of Period Analyses and Implications for Mass Exchange in W UMa Eclipsing Binaries: Paper 4, New Astronomy Reviews, 97.
[https://doi.org/10.1016/j.newar.2023.101684]
Nelson, R. H., Milone, E. F., Van Leeuwen, J., Terrell, D., Penfield, J. E., Kallrath, J.: 1995, *AJ*, **110**, 2400-2407.
Pickering, E. C.: 1880, Dimensions of the Fixed Stars with especial Reference to Binaries and Variables of the Algol Type, Proceedings of the American Academy of Arts and Sciences, 16, 1.
Piotrowski, S. L.: 1948, Some Remarks on the Weights of Unknowns as Determined by the Methods of Differential Corrections, Procs., *Nat. Acad. Scis*., **34**, No. 2, 23-26.

Plavec, M. J.: 1980, IUE Observations of Long Period Eclipsing Binaries: A Study of Accretion onto Non-degenerate Stars, in Close Binary Stars: Observations and Interpretation, eds. M. J. Plavec, D. M. Popper, R. K. Ulrich. IAU Synposium 88, 251-261.

Plavec, M., Koch, R. H.: 1978, Detection of Emission Lines of Hot Plasma in Five Peculiar Eclipsing Binary Systems, IBVS, Vol. 15, No. 1482, 1-3.

Pogson, N.: 1856, Magnitudes of Thirty-six of the Minor Planets for the First Day of Each Month of the Year 1857, *MNRAS*, **17**, 12-16.

Prša, A.: 2018, Modeling and Analysis of Eclipsing Binary Stars; IOP Publishing: Bristol, UK, pp. 2514–3433.

Prša, A., Kochoska, A., Conroy, K. E. et. Al.: 2022, TESS Eclipsing Binary Stars. I. Short-cadence Observations of 4584 Eclipsing Binaries in Sectors 1-26., *ApJS*, **258**, 16 (22pp).

Roche, E. A.: 1849, La Figure d'une Masse Fluide Soumise à l'Attraction d'un Point Éloigné (I), Acad, des Sciences et Lettres de Montpellier, Mém., de la Section des Sciences, Tome Premier (1847-1850), 243-262.

Roche, E. A.: 1850, La Figure d'une Masse Fluide Soumise à l'Attraction d'un Point Éloigné (II), Acad, des Sciences et Lettres de Montpellier, Mém., de la Section des Sciences, Tome Premier (1847-1850), 333-348.

Russell, H.N.: 1912a, On the Determination of the Elements of Eclipsing Variable Stars I, *ApJ*, **35**, 315-340.

Russell, H.N.: 1912b, On the Determination of the Elements of Eclipsing Variable Stars II, *ApJ*, **36**, 54-74.

Russell, H. N.: 1948, The Royal Road of Eclipses (First Henry Norris Russell Lecture), in Centennial Symposia, Contributions on Interstellar Matter, Electronic and Computational Devices, Eclipsing Binaries, The Gaseous Envelope of the Earth. Cambridge, MA, Harvard Observatory Monograph, 7, 181-209.

Russell, H. N. & Merrill, J. E.:1952, The Determination of the Elements of Eclipsing Binaries. Contr. Princeton Univ. Obs, No. 26, (The Observatory, Princeton, N.J.)

Russell, H. N. & Shapley, H.: 1912a, On the Darkening of the Limb in Eclipsing Variable Stars I, *ApJ*, **36**, 239-254.

Russell, H. N. & Shapley, H.: 1912b, On the Darkening of the Limb in Eclipsing Variable Stars II, *ApJ*, **36**, 385-408.

Sahman, D. I., Dhillon, V. S., Marsh, T. R., et al.: 2013, CI Aql: a Type Ia supernova progenitor? *MNRAS*, **433**, 1588-1598.

Schaefer, B. E.: 2011, The Change of Orbital Periods across Eruptions and the Ejected Mass for Recurrent Novae CI Aquilae and U Scorpii, *ApJ*, **742**, 112 (28pp).

Schaefer, B. E.: 2014, Erratum: "The Change of Orbital Periods across Eruptions and the Ejected Mass for Recurrent Novae CI Aquilae and U Scorpii" (2011, ApJ. 742, 112), *ApJ*, **781**, 127.

Schilt, J.: 1922, A Thermo-electric Method of Measuring Photographic Magnitudes, Bulletin of the Astronomical Institutes of the Netherlands, 1, No. 10, 51-52.

Southworth, J.: 2025, Rediscussion of Eclipsing Binaries. Paper XXVI. The F-Type Long-Period System HP Draconis. {arXiv:2508.04218v1 [astro-ph.SR] 6 Aug 2025}

Stefanik, R. P., Latham, D. W., & Torres, G.: 1999, Radial-Velocity Standard Stars, in Hearnshaw, J. B. & Scarfe, C. D., eds., Precise Stellar Radial Velocities, IAU Colloquium 170, *ASP Conf. Ser.*, **185**, 354-366.

Sterken, C., Milone, E. F., and Young, A. T.: 2011, Photometric Precision and Accuracy, in Astronomical Photometry: Past, Present, and Future, eds. Milone, E. F. Sterken, C. (Springer, New York, Heidelberg, Dordrecht, London), ASSL, 373, 1-32.

Stetson, H. T.: 1916, On an Apparatus and Method for Thermo-Electric Measurements in Photographic Photometry. I. *Astron. J.*, **43**, 253-285.

Stetson, H. T.: 1916, On an Apparatus and Method for Thermo-Electric Measurements in Photographic Photometry. II. Application to Variable Stars. *Astron. J.*, **43**, 325-340.

Tamajo, E., Munari, U., Siviero, A., Tomasella, L., Dallaporta, S.: 2012, *A&A*, **539**, A139.

Terrell, D.: 2025, This summer's Variable Star of the Season. Available at: (https://www.aavso.org/vsots_betalyr).

Tokovinin, A.: 2025, Spectroscopic Orbits of Subsystems in Multiple Stars, XI, *AJ*, **170**, 143. [doi.org/10.3847/1538-3881/adee23].

Tulenius, A.: 1740, Dissertatio astronomica de constellatione Arietis (Homiae, Stockholm)Vogel, H. C.: 1890, Spectrographische Beobachtungen an Algol, *AN*, **123**, 289-292.

Walraven, T.: 1953, On the Use of Servomechanisms in the Photometry of Stars, in Astronomical Photoelectric Photometry, ed. Wood, F. B. Publications, AAAS, 114.

Wesselink, A. J.: 1941, A Study of SZ Camelopardalis. Leiden Annalen, 17, Part 3.

Whitford, A. E.: 1932, The Application of a Thermionic Amplifier to the Photometry of Stars, *ApJ*, **76**, 213-223.

Whitford, A. E., Kron, G. E.: 1937, Photoelectric Guiding of Astronomical Telescopes, The Review of Scientific Instruments, 8, 78-82.

Williams, M. D., and Milone, E. F.: 2013). Results from the Rothney Astrophysical Observatory Variable Star Search Program: Background, Procedure, and Results from RAO Field 1, Journal of Astronomical Data, 19 (2), 1-86. [arxiv.org/abs/1101.5650]

Wilson, R. E.: 1971, A Model of Epsilon Aurigae, *ApJ*, **170**, 529-539.

Wilson, R. E.: 1979, Eccentric Orbit Generalization and Simultaneous Solution of Binary Star Light and Velocity Curves, *ApJ*, **234**, 1054-1066.

Wilson, R. E.: 1981, Equilibrium Figures for beta Lyrae Type Disks, *ApJ*, **251**, 246-258.

Wilson, R. E.: 1990, Accuracy and Efficiency in the Binary Star Reflection Effect, *ApJ*, **356**, 613-622.

Wilson, R. E.: 2018, Self-gravitating Semi-transparent Circumstellar Disks: An Analytic Model, *ApJ*, **869**, 19-37.

Wilson, R. E. & Devinney, E. J.: 1971, Realization of Accurate Close-Binary Light Curves: Application to MR Cygni, *ApJ*, **166**, 605-619.

Wilson, R. E., Honeycutt, R. K.: 2014, Outburst-related Period Changes of Recurrent Nova CI Aquilae, *ApJ*, **795**, 8 (6pp).

Wilson, R. E., Van Hamme, W.: 2025, An Equipotential Disk Model with Irradiation for Nova-Like Variables, ApJ, in press.

Wing, R. F.: 2011, On the Use of Photometry in Spectral Classification, in Astronomical Photometry: Past, Present, and Future, eds. Milone, E. F., Sterken, C. (Springer, New York, Dordrecht, Heidelberg, London), pp 143-176.

Yang, S,-C., Han, W.-B., Tagawa, H., Li, S., Zhang, C.: 2025, Indication for a Compact Object Next to a LIGO–Virgo Binary Black Hole Merger, *ApJL*, **988**, No. 2, L41(9pp).

Young, A. T., Milone, E. F., Stagg, C. R.: 1993, On Improving IR Photometric Passbands, in Stellar Photometry – Current Techniques and Future Developments, eds, C. J. Butler, I. Elliott (University Press, Cambridge), 235-241.

Young, A. T., Milone, E. F., Stagg, C. R.: 1994, On Improving IR Photometric Passbands, *A&AS*, **105**, 259-279.

https://doi.org/10.18524/1810-4215.2025.38.340394

ENRICHMENT WITH THE FIRST- AND SECOND-PEAK S-PROCESS ELEMENTS IN GALACTIC DISC GIANTS

T. Mishenina [1], T. Gorbaneva [1], M. Pignatari [2,3,4], T. Kurtukian-Nieto [5]

[1] Astronomical Observatory, Odesa I. I. Mechnikov National University, 1v Marazliivska St, Odesa, 65014, Ukraine, *tmishenina@ukr.net*

[2] Konkoly Observatory, HUN-REN, Konkoly-Thege Miklós út 15-17, Budapest 1121, Hungary

[3] MTA Centre of Excellence, Konkoly-Thege Miklós út 15-17, Budapest 1121, Hungary

[4] E. A. Milne Centre for Astrophysics, University of Hull, Cottingham Rd, Hull HU6 7RX, UK

[5] Instituto de Estructura de la Materia, C. de Serrano, 113 bis-119-121-123, Madrid E-28006, Spain

ABSTRACT. The distribution patterns of chemical elements in the Galactic disc remain insufficiently described. In particular, despite considerable attention to the enrichment of disc stars with neutron-capture elements, several questions remain unresolved and warrant further investigation.

In this study, we examine the enrichment of disc stars with first- and second-peak slow neutron-capture (s-process) elements using a sample of 150 Galactic disc giants. Their spectra were obtained with the 1.93-m telescope at the Observatoire de Haute-Provence (France), using the ELODIE echelle spectrograph.

Elemental abundances of the first-peak (Sr, Y, Zr) and second-peak (Ba, La, Ce) s-process elements were determined using synthetic spectrum fitting under the assumption of Local Thermodynamic Equilibrium (LTE). The results were compared with predictions from Galactic Chemical Evolution (GCE) models.

Our findings confirm that the enrichment in both first- and second-peak s-process elements is driven by contributions from both the s-process and r-process, with a possible additional input from other nucleosynthesis sources.

Keywords: stars: abundances – stars: atmospheres – stars: stellar evolution.

АНОТАЦІЯ. Моделі хімічної еволюції Галактики, що враховують внесок кількох поколінь зір та різних подій нуклеосинтезу, зазвичай використовуються для визначення збагачення та походження хімічних елементів у Галактичному диску. Однак ми все ще маємо недостатнє відтворення спостережуваних проявів збагачення та розподілу елементів у диску. Зокрема, незважаючи на значну увагу до питань, пов'язаних зі збагаченням зір диска елементами, утвореними в процесах захоплення нейтронами, питання все ще залишаються, і це потребує подальшого розгляду. У цій роботі ми досліджуємо збагачення зір диска елементами 1-го та 2-го піків повільного захоплення нейтронів, так званого s-процесу, спираючись на вибірку з 150 гігантів Галактичного диска. Використовувалися спектри зір-гігантів, отримані за допомогою 1,93-метрового телескопа Обсерваторії Верхнього Провансу (Франція) і ешельного спектрографа ELODIE, що охоплюють діапазон довжин хвиль 4400–6800 Å з роздільною здатністю R = 42 000 та співвідношенням сигнал/шум від 130 до 230 при 5500 Å. Вміст елементів першого (Sr, Y, Zr) та другого (Ba, La, Ce) піків s-процесу було отримано методом синтетичного спектру в припущенні Локальної Термодинамічної Рівноваги (ЛТР). Отримані дані порівнюються з моделями Галактичної хімічної еволюції (ГХЕ). Наші результати підтверджують, що збагачення елементів 1-го та 2-го піків s-процесу зумовлене як s-процесом, так і r-процесом (швидким захопленням нейтронів), не виключаючи також додаткового внеску інших джерел нуклеосинтезу.

Ключові слова: зорі: вміст – зорі: атмосфера – зорі: еволюція зір.

1. Introduction

Modern models of the chemical evolution of the Galaxy at disc metallicities account for contributions from multiple generations of stars and incorporate various enrichment sources. However, they still fall short of fully reproducing observational data, leaving several key aspects of elemental enrichment insufficiently explained. It is generally accepted that first-peak slow neutron-capture (s-process) elements – such as strontium (Sr), yttrium (Y), and zirconium (Zr) – are primarily produced in the ejecta of massive asymptotic giant branch (AGB) stars, whereas second-peak elements – such as barium (Ba), lanthanum (La), and cerium (Ce) – are mainly contri buted by low-mass AGB stars. This leads to a relative enhancement of first-peak elements around [Fe/H] ≈ –2 and of second-peak elements around [Fe/H] ≈ –1.5.

Despite significant progress in modeling and observations, the enrichment of Galactic disc stars with

Table 1: Comparison of obtained stellar parameters with those reported by other authors for the N stars common to our sample.

Reference	ΔT_{eff} (K)	Δlogg (dex)	ΔV_t (km/s)	Δ[Fe/H] (dex)	**N**
Tautvaišienė et al. 2021	–32 ±86.70	–0.30 ± 0.29	–	–0.02 ± 0.09	88
Forsberg et al. 2019	–10.56 ±57.03	–0.32 ± 0.08	0.00 ± 0.12	0.03 ± 0.05	89

neutron-capture elements (particularly those formed via the s-process) still presents unresolved questions. In this study, we address these issues by analyzing the abundances of first- and second-peak s-process elements in a sample of 150 disc giant stars.

2. Observations and atmospheric parameters

The spectra were observed with the 1.93-m telescope at Observatoire de Haute-Provence (France) using the ELODIE echelle spectrograph covering 4400–6800 Å at a resolving power of R = 42,000, with signal-to-noise ratios of 130 to 230 at 5500 Å. The initial data reduction followed Katz et al. (1998), and further analysis (continuum normalisation, equivalent width measurement, etc.) was conducted with the DECH30 software developed by G. Galazutdinov (http://gazinur.com/DECH-software.html).

To determine the effective temperature Teff, we used the calibrations of the dependence of line intensities on Teff obtained in the work of Kovtyukh et al. (2006), with the mean random error of a single calibration being 65–70 K (45–50 K in most cases and 90–95 K in the least accurate cases). The use of about 70–100 calibrations per spectrum reduces the uncertainty to 5–7 K. Spectroscopic determinations of the gravity log g by two methods were used: 1) a method of iron ionization equilibrium, where the average iron abundance determined from Fe I lines and Fe II lines must be identical, and 2) a method that relies on the detailed wing fitting of the Ca I 6162 Å line. Turbulent velocity V_t is determined by the independence of the iron content determined for a given line from its equivalent width. The metallicity [Fe/H] is adopted as the iron abundance determined from the Fe I lines. The more details and comparisons with results of other authors, see Mishenina et al. (2006).

In this work, we compared the parameter values with those obtained in recent works by Tautvaishiene et al. (2021) and Forsberg et al. (2019), as shown in Table 1. For more details and comparisons with results of other authors, see Mishenina et al. (2006).

The errors of the log g determination for giants are about 0.2-0.3 dex as indicated in Mishenina et al. (2006). The comparison of our atmospheric parameters with the results of Tautvaishiene et al. (2021) and Forsberg et al. (2019) estimated that the accuracy of our parameter determinations is as follows: ΔT_{eff} =±100 K, surface gravities Δlogg =±0.3 dex and microturbulent velocity ΔV_t =±0.1 km/s.

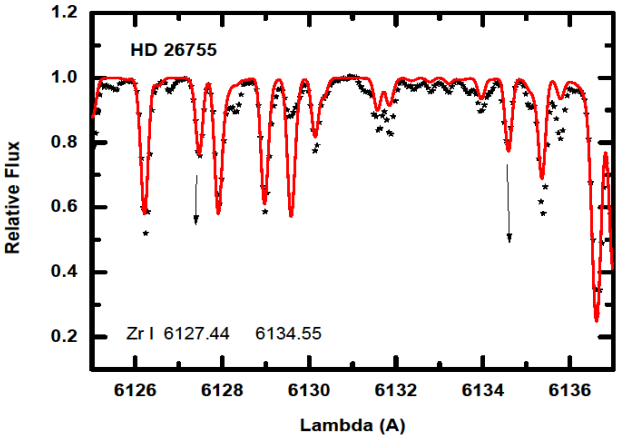

Figure 1: Spectrum synthesis fitting of the Zr lines to the observed profiles.

3. Abundance and age determinations

The Sr, Zr, Ba, La, Ce abundances were derived using the Local Thermodynamical Equilibrium (LTE) approach applying the models of Castelli & Kurucz (2004) and the modified STARSP LTE spectral synthesis code (Tsymbal, 1996). The oscillator strengths log gf were adopted from the last version of the VALD data base (Kupka et al., 1999). Hyperfine structure and isotopic composition were considered for Ba and La. Yttrium abundances were taken from Mishenina et al. (2007). Adopted solar abundances follow Asplund et al. (2009). Typical abundance uncertainties from atmospheric parameters are ~0.15 dex for all elements.

Stellar ages were estimated using the [Y/Mg] vs. age calibration (see, e.g. Tucci Maia et al. 2016), based on Mg and Y abundances taken from Mishenina et al. (2006; 2007).

4. Results and discussions

We investigated the abundances of six elements formed via neutron-capture processes: strontium (Sr), yttrium (Y), and zirconium (Zr), classified as first-peak s-process elements, and barium (Ba), lanthanum (La), and cerium (Ce), associated with the second peak. To facilitate comparative analysis, we calculated the mean abundances for each group: $\langle[El/Fe]\rangle_{1\text{-st}}$ = ([Sr/Fe] +

[Y/Fe] + [Zr/Fe]) / 3 (first peak) and $\langle[El/Fe]\rangle_{2\text{-nd}}$ = ([Ba/Fe] + [La/Fe] + [Ce/Fe]) / 3 (second peak).

We then plotted the average abundance of the first-peak elements against that of the second-peak elements.

Figure 2 displays a correlation between these two datasets, with a Pearson correlation coefficient of r = 0.656, indicating a moderate linear relationship, underlining that AGB star contributions dominate the sample. But not a direct proportionality suggests that the two groups of elements may originate from distinct nucleosynthetic processes.

This result may support the prevailing hypothesis that first-peak elements are predominantly synthesized in moderately massive AGB stars (4–7 $M_{\odot}$), while second-peak elements are mainly produced in low-mass AGB stars (1–3 $M_{\odot}$), indicating different sources of enrichment. However, the absence of a strict linear proportionality implies the possible involvement of other production mechanisms associated with massive stars, e.g. such as core-collapse supernovae (CCSNe), the weak s–process (Pignatari et al., 2010), or such as the νp-process contributions by Fröhlich et al. (2006) as well as the neutrino wind contributions by Arcones & Thilemann (2013) etc.

Figure 3 presents the difference between the average abundances of the second- and first-peak elements, normalized to the first-peak mean. The plot reveals a weak correlation and a broad scatter of data points. If AGB stars dominate, their difference between second peak and first peak contributions should be close to constant, independent of the abscissa coordinate. This is what was found in Fig.3, combined with a large scatter.

In contrast, Figure 4, which shows the difference between the first- and second-peak average abundances relative to the second-peak mean, exhibits a clearer correlation with a Pearson coefficient of r = 0.85. This can be interpreted as the contribution of massive stars minus AGB stars vs. the contribution of AGB stars. If AGB stars dominate, then as their contribution increases, this difference should obviously decrease, leading to a moderately strong negative linear relationship between both quantities, as we can be seen in Fig. 4 (with a Pearson correlation coefficient of -0.85).

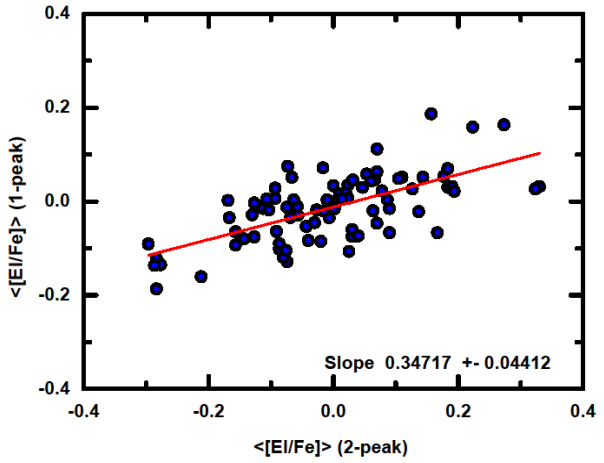

Figure 2: Dependences of the average abundance of the 1-st s-process peak relative to the 2-nd-peak average.

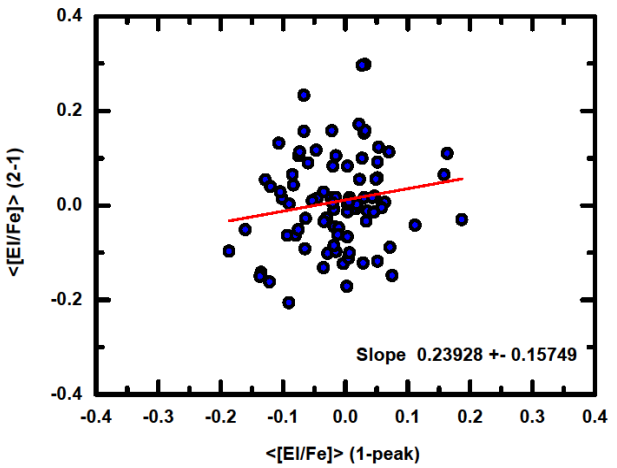

Figure 3: Difference between the average abundances of the 2-nd and 1-st s-process peaks relative to the 1-st-peak average.

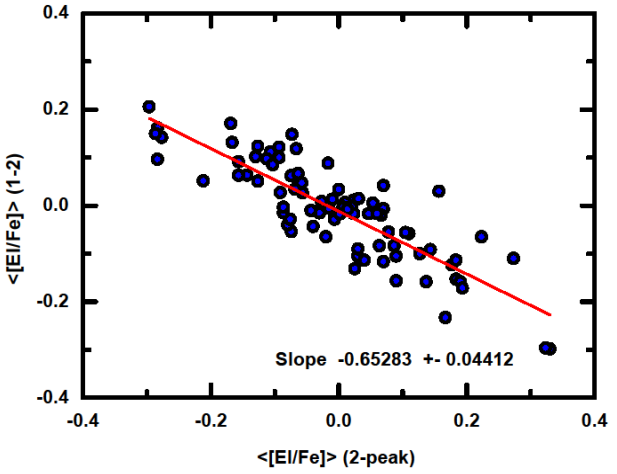

Figure 4: Difference between the average abundances of the 1-rst and the 2-nd peaks relative to the 2-nd peak average.

Both figures (3 and 4) further support the view that these two groups of elements originate from different stellar sources, and suggest a non-negligible role of additional enrichment processes.

Figure 5 illustrates the relationship between the average abundances of first- and second-peak elements and stellar age. Although no strong trends are apparent, the second-peak elements show a notably larger scatter. This may reflect differences in production sources or inherent uncertainties in abundance determinations. However, the uncertainties are comparable across all studied elements, which implies that the observed scatter is likely of astrophysical origin. If the larger scatter in second peak elements is not due to uncertainties in abundance determinations, it might reflect the metallicity dependence of a secondary s-process behaviour in AGB stars combined with the fact that lower metallicities lead to a larger neutron/Fe seed ratio and consequently to an abundance pattern shifted towards heavy elements.

For stars with near-solar metallicity, direct comparison with individual nucleosynthesis models becomes

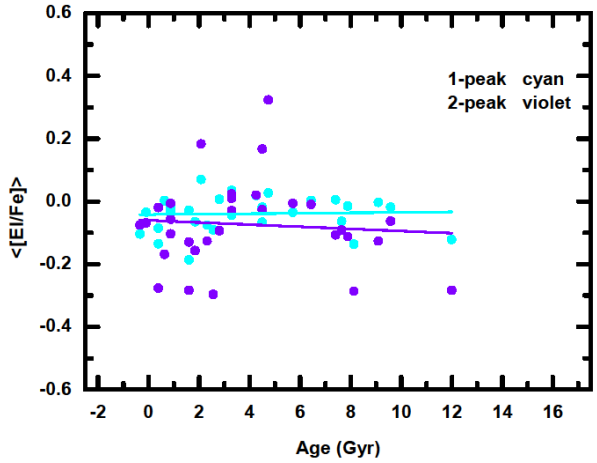

Figure 5: Dependence of the average abundances of the first- and second-peak s-process elements on stellar age.

challenging due to cumulative enrichment from multiple stellar generations. In such cases, Galactic Chemical Evolution (GCE) models are used to trace enrichment sources. These models incorporate parameters such as the initial mass function (IMF), stellar yields from different mass ranges, star formation rates, and timescales of chemical enrichment.

Our preliminary analysis suggests that GCE models must account for the relative contributions of low- and intermediate-mass AGB stars, as well as potential input from other nucleosynthetic sources, to adequately reproduce the observed abundance patterns of s-process elements.

To interpret our results, we compared the observed abundances with GCE model predictions developed by Kobayashi et al. (2020). These models incorporate multiple nucleosynthesis sources: The s-process from AGB stars based on yields from Karakas & Lugaro (2016) for metallicities Z = 0.007, 0.014, and 0.03). Additional contribution besides iron: ECSNe (high-mass super-AGB stars that explode as electron-capture supernovae) using yields from Wanajo et al. (2013).

The r-process (rapid neutron capture) from various sources: ν-driven winds (Arcones et al. 2007; Wanajo 2013, and their calculations of SN II), NS-NS/NS-BH (neutron stars, black hole) mergers (the nucleosynthesis yields from the 3D-GR calculation of a NS-NS merger ($1.3M_{\odot}$+$1.3M_{\odot}$) from Wanajo et al. (2013) both for NS-NS and NS-BH mergers, and MRSNe – supernovae with strong magnetic field (e.g. Nishimura et al., 2015).

Figures 6–8 show the comparison between observed and model-predicted abundances of the first-peak elements Sr, Y, and Zr. The dashed lines represent models with the s-process from AGB stars only, while the solid lines include additional contributions from ECSNe, NS–NS/NS–BH mergers, and MRSNe. As noted by the model authors: "The first peak elements, Sr, Y, and Zr, are sufficiently produced by ECSNe together with AGB stars." We would note, however, that at these metallicities we expect rather the weak s-process is produced by massive supernovae CCSNe (Pignatari et al. 2010) than by ECSNe.

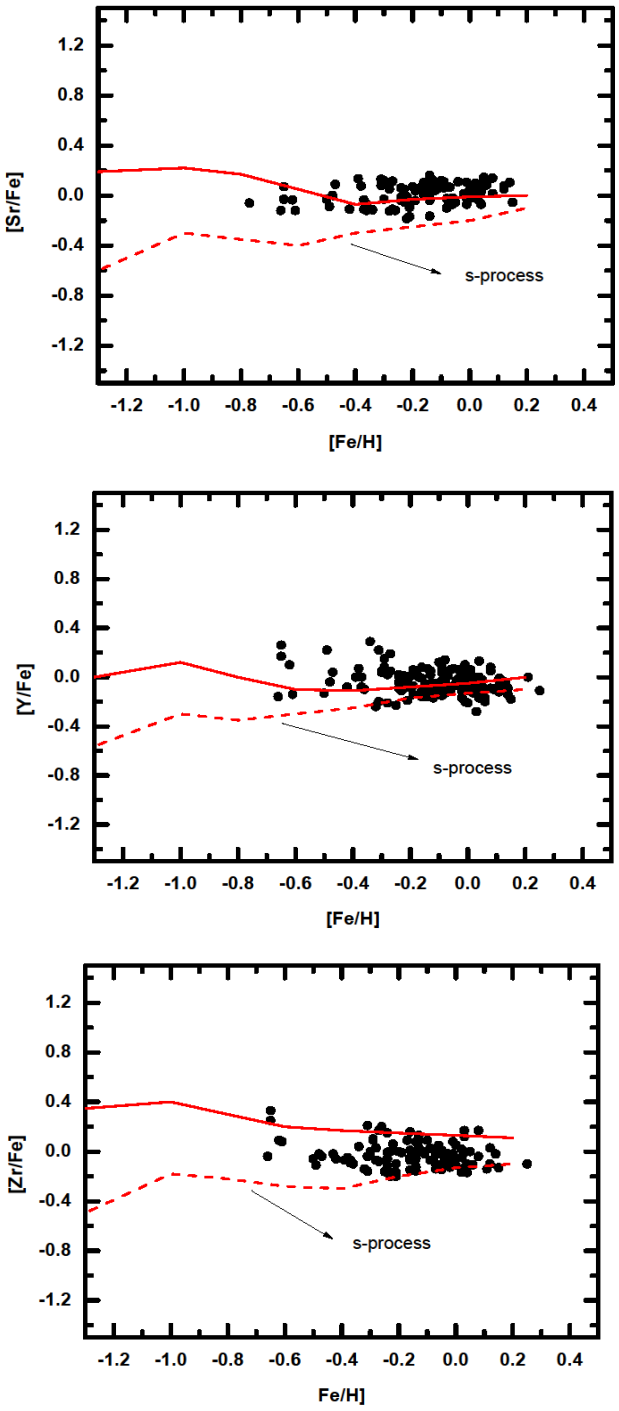

Figures 6, 7, 8: [Sr/Fe], [Y/Fe], [Zr/Fe] vs. [Fe/H] and model tracks from Kobayashi et al. (2020).

Figures 9–11 show model comparisons for the second-peak elements Ba, La, and Ce. For Ba, the s-process from AGB stars alone matches the observed data well. For La and Ce, however, the model predictions slightly overestimate the observed abundances. This discrepancy may indicate that the adopted yields require refinement–either in the stellar source parameters or in the modeling of neutron-producing reactions.

These comparisons reinforce our earlier observational findings, particularly the differences in behavior between first- and second-peak elements, and support the conclusion that multiple nucleosynthesis processes–

beyond the classical s-process–contribute to the chemical enrichment of the Galactic disc.

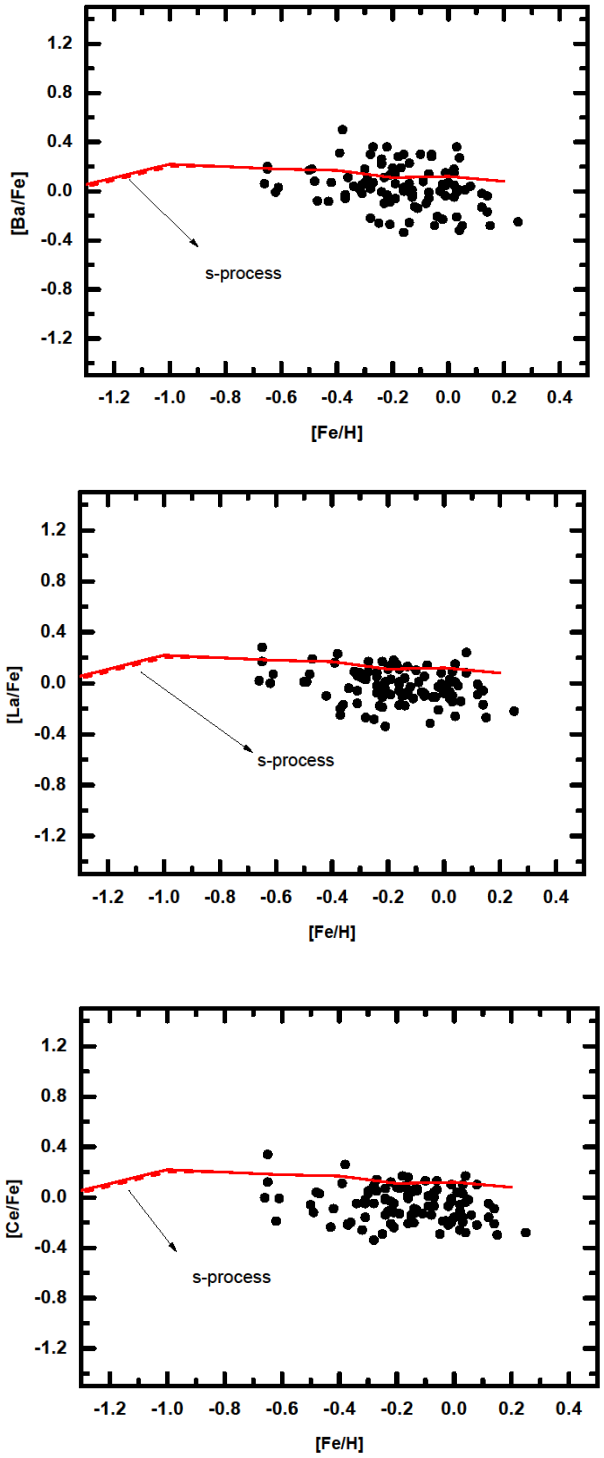

Figures 9, 10, 11: [Ba/Fe], [La/Fe], [Ce/Fe] vs. [Fe/H] and model tracks from Kobayashi et al. (2020).

5. Conclusions

1. We studied abundances of Sr, Y, Zr, Ba, La, and Ce for a sample of 150 giant stars in the Galactic disc.
2. A moderate linear correlation (Pearson's coefficient r = 0.656) was found between the average abundances of first- and second-peak s-process elements. However, the lack of direct proportionality indicates contributions from distinct nucleosynthesis processes, and possibly additional production channels.
3. Comparisons with Galactic Chemical Evolution (GCE) models support our observational results. While the models can explain some trends (especially for Ba), they also highlight the need to refine yield predictions and better understand the contributions of different nucleosynthetic sources.
4. Our findings underscore the complexity of neutron-capture element production in the Galactic disc and emphasize the need for further theoretical modeling and high-precision observational data to better constrain the origins of both first- and second-peak s-process elements.

Acknowledgements. We express our deepest gratitude to the referee for their careful reading of the manuscript and a number of valuable comments that significantly improved the work. We kindly acknowledge the support of the project "Stellar Nucleosynthesis in Advanced Burning Phases and Explosive Scenarios, 2024-2027" of the Institute of the Structure of Matter (Instituto de Estructura de la Materia), Madrid, Spain.

References

Arcones A., Janka H.-Th., Scheck L.: 2007, *A&A*, **467**, 1227.
Arcones A., Thielemann F.-K.:2013, *JPhysG*, **40**, id. 013201
Asplund M., Grevesse N., Sauval A. J., Scott P.: 2009, *ARA&A*, **47**, 481.
Castelli F., Kurucz R.: 2004, *ArXiv Astrophysics e-prints astro-ph/0405087*
Galazutdinov G.: http://www.gazinur.com/DECH-software.html
Forsberg R., Jonsson R., Ryde N., Matteucci F.: 2019, *A&A*, **631**, 113.
Fröhlich C., Martínez-Pinedo, G, . Liebendörfer, M. et al.: 2006, *PRL*, **96,** id. 142502
Karakas A. I., Lugaro M.: 2016, *ApJ*, **825**, 26.
Katz D., Soubiran, C., Cayrel R. et al.: 1998, *A&A*, **338**, 151.
Kobayashi C., Karakas A.I., Lugaro M.: 2020, *ApJ*, **900**, 179.
Kovtyukh V., Soubiran C., Bienaymé O. et al.: 2006, *MNRAS*, **371**, 879.
Kupka F., Piskunov N., Ryabchikova T. et al.: 1999, *A&AS*, **138**, 119.
Mishenina T., Bienaymé O., Gorbaneva T. et al.: 2006, *A&A*, **456**, 1109.
Mishenina T., Gorbaneva T., Bienaymé O. et al.: 2007, *ARep*, **51**, 382.
Nishimura N., Takiwakai T., Thielemann F.-K.: 2015, *ApJ*, **810**, 109.
Pignatari M., Galino R., Heil M. et al.: 2010, *ApJ*, **710**, 1557.
Tautvaišienė G., Viscasillas Vázquez C., Mikolaitis Š. et al.: 2021, *A&A*, **649**, A126.
Tsymbal V.: 1996, *ASPC*, **108**, 198.
Tucci Maia M., Ramírez I., Meléndez J. et al.: 2016, *A&A*, **590**, A32.
Wanajo S.: 2013, *ApJ*, **770**, L22.
Wanajo S., Janka H.-T., Müller B.: 2013, *ApJ*, **767**, L26.

https://doi.org/10.18524/1810-4215.2025.38.343164

SPECTROSCOPIC STUDY OF THE POST-AGB BINARY HR 4049

Sh. T. Nurmakhametova[1], N. L. Vaidman[1,2], A. S. Miroshnichenko[1,2,3], A. T. Agishev[1], A. A. Khokhlov[1]

[1] Al-Farabi Kazakh National University, Al-Farabi Ave, 71, 050040, Almaty, Kazakhstan, *shahidanurmahametova@gmail.com; aldiyar.agishev@gmail.com; kh.azamat92@gmail.com*

[2] Fesenkov Astrophysical Institute, Observatory 23, 050020, Almaty, Kazakhstan, *nva1dmann@gmail.com*

[3] Department of Physics and Astronomy, University of North Carolina at Greensboro, Greensboro, USA, *a_mirosh@uncg.edu*

ABSTRACT. We present a new spectroscopic study of HR 4049, a post-AGB star in a binary system, based on échelle spectra obtained between 2019/03/19 and 2025/04/08 with the 0.81 m telescope of the Three College Observatory (North Carolina, USA) at a resolution of $R \approx 12{,}000$. A cross-correlation analysis of 83 spectra in the 4760–4780 Å range yielded the following orbital parameters: period $P = 428.47 \pm 0.01$ days, eccentricity $e = 0.29 \pm 0.01$, argument of periastron $\omega = 242.3° \pm 0.3°$, epoch of periastron $T_0 = 2{,}458{,}383.2 \pm 0.6$, systemic radial velocity $\gamma = -30.12 \pm 0.09$ km s^{-1}, and semi-amplitude $K_1 = 15.52 \pm 0.13$ km s^{-1}. Using the Gaia DR3 parallax ($d = 1397^{+176}_{-168}$ pc) and the average maximum brightness ($m_v = 5.35$ mag), the luminosity was estimated as $\log(L/L_\odot) = 4.22 \pm 0.12$, consistent with an initial mass of 3-4 $M_\odot$. The mass function combined with likely orbital inclinations implies current masses of ~ 0.75 $M_\odot$ for the primary and 0.70–0.82 $M_\odot$ for the secondary. These results confirm the long-term orbital stability of HR 4049 and provide new constraints on the properties of post-AGB binaries.

Keywords: spectroscopy; binary stars; emission-line stars; post-AGB stars; circumstellar matter.

АНОТАЦІЯ. Ми представляємо нове спектроскопічне дослідження HR 4049, зорі після AGB у подвійній системі, на основі échelle-спектрів, отриманих у 2019/03/19 – 2025/04/08 рр. за допомогою телескопа діаметром 0.81 м Обсерваторії Трьох Коледжів (Північна Кароліна, США) з роздільною здатністю $R \approx 12\ 000$. Кроскореляційний аналіз 83 спектрів у діапазоні 4760–4780 Å дозволив визначити орбітальні параметри: період $P = 428{,}47 \pm 0{,}01$ доби, ексцентриситет $e = 0{,}29 \pm 0{,}01$, аргумент періастра $\omega = 242.3° \pm 0.3°$, епоха періастра $T_0 = 2{,}458{,}383.2 \pm 0.6$, системна швидкість $\gamma = -30.12 \pm 0.09$ км с$^{-1}$ та напівамплітуда $K_1 = 15.52 \pm 0.13$ км с$^{-1}$. Використовуючи паралакс Gaia DR3 ($d = 1397^{+176}_{-168}$) та середню максимальну зоряну величину ($m_v = 5{,}35$ mag), світність оцінено як $\log(L/L_\odot) = 4{,}22 \pm 0{,}12$, що відповідає початковій масі 3–4 $M_\odot$. Масова функція у поєднанні з вірогідними нахилами орбіти вказує на сучасні маси ~ 0.75 $M_\odot$ для первинної компоненти та 0,70–0,82 $M_\odot$ для вторинної. Отримані результати підтверджують довготривалу орбітальну стабільність HR 4049 та встановлюють нові обмеження на властивості пост-AGB подвійних систем.

Ключові слова: спектроскопія; подвійні зорі; зорі з емісійними лініями; зорі після AGB ; навколозоряна речовина.

1. Introduction

Post-AGB stars are an intermediate evolutionary stage of low– and intermediate–mass stars ($\sim$ 0.8–8 $M_\odot$) after the Asymptotic Giant Branch (AGB) phase and before becoming Planetary Nebulae (PN). At this stage, the star has lost most of its outer envelope due to strong stellar winds, leaving behind a hot core surrounded by an expanding circumstellar shell of gas and dust.

This phase is very short in astrophysical terms (10^3–10^5 years) which makes post-AGB stars rare. Their luminosities are typically around 10^3–10^4 $L_\odot$, with effective temperatures ($T_{\rm eff}$) ranging from about 3000 K to over 100,000 K as they evolve towards higher temperatures (Miller Bertolami 2016).

One of the most remarkable post-AGB objects is HR 4049 (HD 89353, AG Ant), a spectroscopic binary in Antlia. Its high $T_{\rm eff} \approx 7500$ K (Bakker et al. 1998), complicates abundance work because metal lines are weak. HR 4049 shows an extreme iron underabundance, [Fe/H]= -4.8 dex (Van Winckel et al. 1995), together with a strong infrared excess and a UV deficit attributable to dust from past mass loss (Andrews, Lépine 2013). Selective depletion is common among post-AGB binaries with circumbinary disks; HR 4049 is among the most extreme cases. As a result, its optical spectrum contains very few measurable metal lines.

Spectroscopic monitoring revealed radial velocity (RV) variations with a 429–430 day period (Bakker et al. 1998), confirming its binarity with a faint companion (Andrews, Lépine 2013). The companion is likely an M–type main-sequence star with $T_{\rm eff} \approx 3500$ K, $R \approx 0.6 R_{\odot}$ and the compact orbit has $a \sin i \approx 0.6$ AU (Bakker et al. 1998).

The system also hosts a stable circumbinary disk with a bright ring (Andrych et al. 2023). The double-peaked Hα profile follows the orbital phase, suggesting accretion activity (Gorlova et al. 2012), while star–disk interactions may cause severe photospheric depletion of volatile elements (Oomen et al. 2019).

The aim of this study was to refine the orbital parameters of HR 4049 using new RV data and test for possible long-term changes. We recalculated P, γ, ω, e, K, and T_0, thereby improving constraints on the orbital architecture and fundamental properties of this post-AGB binary.

2. Observations, Data Reduction and Analysis

We obtained 83 spectra of HR 4049 between 2019/03/19 and 2025/04/08 with the 0.81 m telescope at the Three College Observatory (North Carolina, USA), equipped with an échelle spectrograph manufactured by Shelyak Instruments [1] and an ATIK-460EX detector. The setup provides $R \sim 12{,}000$ over 3800-7900 Å, with S/N ratios in the continuum up to ∼300 for typical combined exposure times of ∼1 hour in the 4500-5500 Å range. Wavelength calibration using 800-1000 ThAr lines yields an RV precision of ∼300 m s^{-1}. Spectra were reduced with standard IRAF échelle routines (bias subtraction, flat-fielding, optimal extraction, and continuum normalization).

To achieve the main objectives of this study, we applied several complementary methods. To measure RV values, we applied the cross-correlation method implemented in the IRAF/RVSAO 2.0 package, using one high-S/N spectrum as a template and focusing on the C I multiplet in the 4760–4780 Å region.

[1] `https://shelyak.com`

Periodogram analysis of the RV data was then performed with the Lomb–Scargle (LS) algorithm (Scargle 1982), which is well suited for unevenly sampled observations and allowed us to identify the dominant periodicity of the system.

Subsequently, we modeled the RV curve with our Python pipeline (NumPy, Pandas, Matplotlib, SciPy) and performed Bayesian inference using the affine-invariant ensemble sampler `emcee` (Foreman-Mackey et al. 2013). The RV+MCMC code is documented in Vaidman et al. (2025) and has already been applied in Nurmakhametova et al. (2025) and in Vaidman et al. (2025); we follow the same workflow here to obtain the most probable orbital elements—period, systemic velocity, semi-amplitude, eccentricity, and argument of periastron—with robust uncertainties.

3. Results

In the 4760–4780 Å region, the spectra of HR 4049 clearly show the neutral–carbon multiplet (top panel of Fig. 1). HR 4049 is strongly depleted in refractory elements, so its optical spectrum contains comparatively few clean metal lines; many wavelength ranges are either line–poor or affected by blends and circumstellar features. The chosen window, however, contains several relatively strong, well–isolated C I lines with stable, symmetric profiles and minimal telluric contamination. The phase–resolved cross–correlation map (bottom panel of Fig. 1) demonstrates coherent Doppler shifts of these lines with orbital phase, confirming that this set is well suited to precise RV measurements and a subsequent orbital analysis.

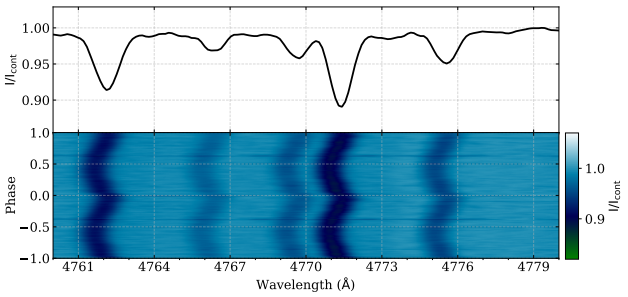

Figure 1: Top panel: Spectrum of HR 4049 in the 4760–4780Å region. Bottom panel: Phase-resolved cross-correlation map.

Table 1 compares the orbital parameters of HR 4049 obtained in this work with previous studies. Our analysis confirms the overall consistency of the system's orbital characteristics with earlier results, while providing an improved precision. Small differences in systemic velocity are most likely related to the choice of template spectrum and reference frame. The refined

parameters strengthen the evidence for the long-term stability of the binary system.

Table 1: Comparison of orbital parameters.

	Bakker et al. (1998)	**Oomen et al. (2019)**	**This work**
P	430.7 ± 0.3	430.6 ± 0.1	428.47 ± 0.01
T_0	$46\,746.6 \pm 2.4$	$47\,176.6 \pm 3.8$	$58\,383.2 \pm 0.6$
e	0.30 ± 0.01	0.30 ± 0.01	0.29 ± 0.01
ω	237.2 ± 2.3	236.5 ± 3.5	242.3 ± 0.3
γ	-32.1 ± 0.1	-31.9 ± 0.2	-30.1 ± 0.1*
K_1	15.96 ± 0.19	16.6 ± 0.2	15.52 ± 0.13
$f(m)$	0.16 ± 0.01	0.18 ± 0.01	0.15 ± 0.01
N	60	86	83

Notes. (1) Orbital period (days); (2) periastron epoch for the elliptical orbit and time of superior conjunction (at γ RV) for the circular orbit (HJD -2,400,000); (3) eccentricity; (4) argument of periastron (degrees); (5) systemic RV (km s^{-1}); (6) semi-amplitude of the RV variations of the visible component ($km\,s^{-1}$); (7) mass function ($M_\odot$); (8) number of spectra used in the orbit calculation.

* The value is obtained from the RV template, with the systemic velocity determined relative to the template spectrum and reported in the heliocentric frame.

To determine the orbital period from our irregularly sampled velocities, we computed LS periodogram as a first-order approach. For improved accuracy, we also included archival spectra from Bakker et al. (1998), which complement our recent observations and help to extend the temporal baseline of RV measurements. As shown in Fig. 2, the resulting LS spectrum displays a dominant peak at $P = 428.47$ d. We therefore adopt this period as the starting point for the orbital analysis. With P fixed at this value, we then fit a Keplerian model with free parameters K, e, ω, T_0, and the systemic velocity γ, ensuring a consistent solution across all available datasets.

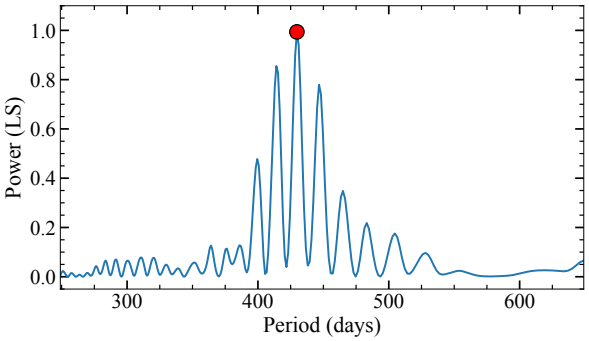

Figure 2: Lomb–Scargle periodogram. The red dot marks the global maximum at $P = 428.47 \pm 0.01$ d.

Fig. 3 compares this model to the RV time series. The fit reproduces both the amplitudes and the evident asymmetry of the RV curve, indicating a non-zero eccentricity. In this workflow, the LS periodogram serves to identify the fundamental timescale under uneven sampling, while the subsequent Keplerian fit accounts for the non-sinusoidal shape of eccentric orbits and yields physically interpretable parameters.

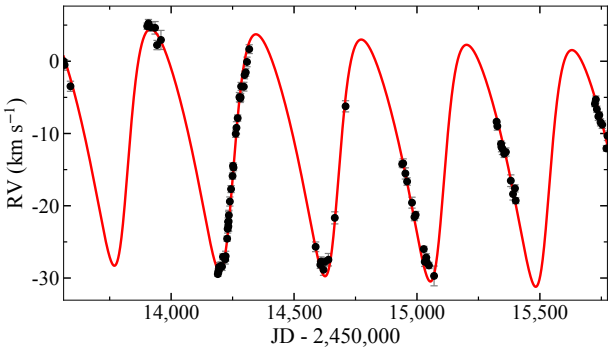

Figure 3: Radial velocities as a function of time, plotted as JD$-2{,}450{,}000$ (black points with 1σ error bars), together with the best-fitting Keplerian model (red curve).

To illustrate the coherence of the solution, Fig. 4 shows the phase-folded velocities at the same period together with the best-fitting Keplerian model. The residuals, normalized by their formal uncertainties, scatter symmetrically about zero with no visible structure, supporting the adequacy of the single-orbit description and the robustness of the adopted period.

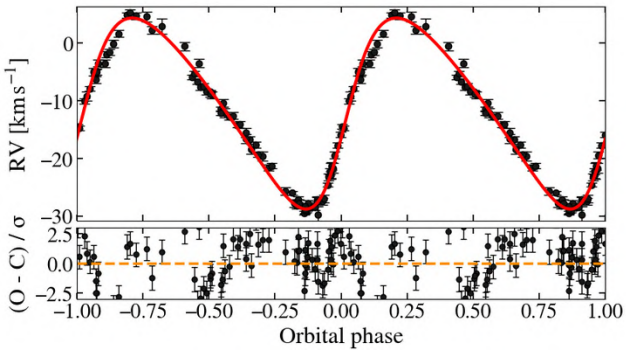

Figure 4: Radial velocity variations of HR 4049 as a function of orbital phase. Top panel: Black points show the observed heliocentric RVs; the red curve represents the best-fitting Keplerian model. Bottom panel: Normalised residuals $(O-C)/\sigma$; the orange dashed line marks zero. The plot shows all $N = 83$ measurements; the eccentric Keplerian fit yields a reduced $\chi^2_\nu = 1.69$.

We estimated the luminosity of HR 4049 at its maximum optical brightness using the observed visual magnitude $m_V = 5.35$ mag (Waelkens et al. 1991; Rufener

& Bartholdi 1982; Lake 1965). For the distance, we adopted the *Gaia* DR3 value $d = 1397^{+176}_{-168}$ pc as determined by Bailer-Jones et al. (2021, Vizier catalogue I/352), providing a reliable geometric basis for our estimates. To convert the apparent magnitude to bolometric luminosity, we applied a bolometric correction of $BC_V = 0.02$, appropriate for an effective temperature of $T_{\rm eff} = 7500$ K according to the calibration of Pecaut & Mamajek (2013).

Assuming a modest interstellar reddening of $E(B-V) < 0.07$, we obtained $\log(L/L_\odot) = 4.13$, whereas adopting a slightly higher color excess of $E(B-V) = 0.20$ yields $\log(L/L_\odot) = 4.30$ (Green et al. 2019). These values define the plausible luminosity range, and for the subsequent discussion we adopt the mean estimate $\log(L/L_\odot) = 4.22 \pm 0.12$, which agrees, within the quoted uncertainties, with previous determinations reported by Oudmaijer et al. (2022).

When placed on the Hertzsprung–Russell (HR) diagram (Fig. 5), HR 4049 occupies a position along the post–AGB evolutionary tracks corresponding to progenitors of approximately 3–4 $M_\odot$. This location is consistent with the phase of nearly constant luminosity and gradually increasing effective temperature that characterizes the final stages of post–AGB evolution, supporting the classification of HR 4049 as a well–advanced post–AGB object.

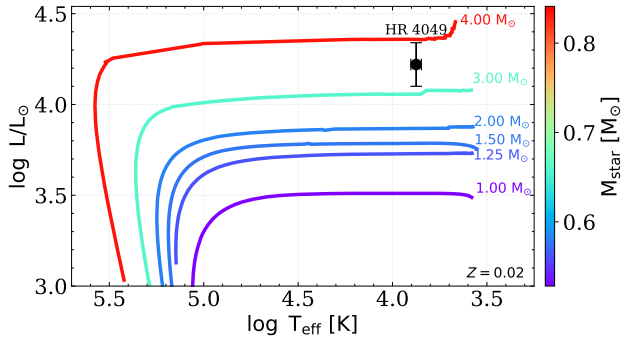

Figure 5: HR diagram of post-AGB tracks for initial masses 1–4 $M_\odot$ at $Z = 0.02$ (Miller Bertolami 2016). The color bar shows the present stellar (core) mass. The black symbol marks HR 4049.

The mass function derived from our orbital solution (Table 1) provides a valuable quantitative constraint on the possible masses of both stellar components and thus serves as an important diagnostic of the system's nature. For representative orbital inclinations in the range $i = 60°$–$75°$ (Dominik et al. 2003; Oomen et al. 2018), the resulting mass of the primary component is estimated as $M_1 \approx 0.75\,M_\odot$, a value that agrees very well with theoretical expectations for evolved post–AGB remnants. In particular, according to the post–AGB evolutionary calculations of Blöcker (1995), stars with initial main–sequence masses between $3-5\,M_\odot$ are expected to leave the AGB phase with core masses in the range $0.605-0.889\,M_\odot$. The mass we infer for the primary thus falls comfortably within this theoretical interval, further strengthening the internal consistency and physical plausibility of our orbital solution. The inferred $M_2 \approx 0.70$–$0.82\,M_\odot$ is difficult to reconcile with a late-M dwarf; this range is more consistent with either an early-K main-sequence star or a compact white dwarf. The corresponding mass of the unseen secondary component therefore remains compatible with both possibilities. It should be emphasized that this range is still strongly dependent on the adopted inclination, and the steep sensitivity of M_2 to i clearly illustrates how delicate and model–dependent mass determinations can be for single–lined spectroscopic binaries with unresolved companions (Fig. 6).

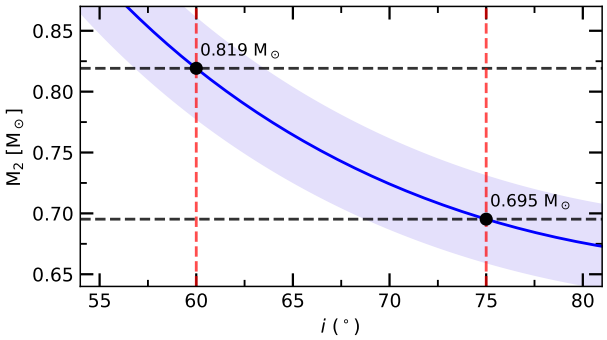

Figure 6: Mass of the secondary component M_2 as a function of the orbital inclination i. The solid blue line shows the best-fit solution for the mass function $f(M) = 0.15$, with the shaded region representing the uncertainty (± 0.01). The dashed horizontal line marks the assumed primary mass $M_1 = 0.75 \pm 0.05\,M_\odot$. Red dashed vertical lines highlight the solutions at $i = 60°$ and $i = 75°$.

4. Conclusions

We carried out a spectroscopic analysis of the post-AGB binary HR 4049 using 83 échelle spectra obtained between 2019 and 2025. The RV measurements of the C I multiplet lines allowed us to refine the orbital parameters, which are consistent with previous determinations but now have improved precision. Placing HR 4049 on the HR diagram confirms that it follows post-AGB evolutionary tracks for progenitors of 3-4 M⊙, while the derived mass function constrains the present-day component masses to ∼0.75 M⊙ for the primary and 0.70–0.82 $M_\odot$ for the secondary. These results confirm the system's long-term orbital stability and provide important constraints for understanding post-AGB binaries with circumbinary disks.

Despite this progress, several open problems remain.

The origin of the extreme iron deficiency in HR 4049 is still unclear and likely linked to complex depletion and re-accretion processes in the circumbinary environment. Moreover, as HR 4049 is in a rare and short-lived evolutionary phase, a follow-up spectroscopic and photometric monitoring will be essential to trace its variability, chemical composition, and dynamical evolution. Future monitoring of HR 4049 will be crucial for tracing possible secular variations in orbital and spectral properties.

Funding. This research has was funded by the Science Committee of the Ministry of Science and Higher Education of the Republic of Kazakhstan (Grant No. AP19175392).

Acknowledgements. This research has made use of the SIMBAD database, operated at CDS, Strasbourg, France; SAO/NASA ADS, ASAS, and Gaia data products. This paper is partly based on observations obtained at the 0.81 m of the Three College Observatory (North Carolina, USA). A.M. acknowledges technical support from Dan Gray (Sidereal Technology Company), Joshua Haislip (University of North Carolina Chapel Hill), and Mike Shelton (University of North Carolina Greensboro), as well as funding from the UNCG College of Arts and Sciences and Department of Physics and Astronomy.

References

Andrews J., Lépine S.: 2013, *Astron. Astrophys.,* **551**, A76.

Andrych K., Kamath D., Kluska J., Van Winckel H., Ertel S., Corporaal A.: 2023, *Mon. Not. R. Astron. Soc.,* **524**, 4168.

Bakker E.J., Lambert D.L., Van Winckel H., McCarthy J.K., Waelkens C., Gonzalez G.: 1998, *Astron.Astrophys.,* **336**, 263.

Bailer-Jones C.A.L., Rybizki J., Fouesneau M., Demleitner M., Andrae R.: 2021, *Astron. J.,* **161**, 147.

Blöcker T.: 1995, *Astron. Astrophys.,* **299**, 755.

Dominik C., Dullemond C.P., Cami J., van Winckel H.: 2003, *Astron. Astrophys.,* **397**, 595–609.

Foreman-Mackey D., Hogg D.W., Lang D., Goodman J.: 2013, *Publ. Astron. Soc. Pac.,* **125**, 306.

Gorlova N., Van Winckel H., Gielen C., Raskin G., Prins S., Pessemier W., Waelkens C., Frémat Y., Hensberge H., Dumortier L., et al.: 2012, *Astron. Astrophys.,* **542**, A27.

Green G.M., Schlafly E.F., Zucker C., Speagle J.S., Finkbeiner D.P.: 2019, *Astrophys. J.,* **887**, 93.

Lake R.: 1965, *Mon. Not. Astron. Soc. S. Afr.,* **24**, 41.

Miller Bertolami M.M.: 2016, *Astron. Astrophys.,* **588**, A25.

Nurmakhametova S.T., Vaidman N.L., Miroshnichenko A.S., Khokhlov A.A., Agishev A.T., Yermekbayev B.S., Danford S., Aarnio A.N.: 2025, *Galaxies,* **13**(2), 26.

Oomen G.-M., Van Winckel H., Pols O., Nelemans G.: 2019, *Astron. Astrophys.,* **629**, A49.

Oomen G.-M., Van Winckel H., Pols O., Nelemans G., Escorza A., Manick R., Kamath D., Waelkens C.: 2018, *Astron. Astrophys.,* **620**, A85.

Oudmaijer R.D., Jones E.R.M., Vioque M.: 2022, *Mon. Not. R. Astron. Soc.: Lett.,* **516**, L61.

Pecaut M.J., Mamajek E.E.: 2013, *Astrophys. J. Suppl. Ser.,* **208**, 9.

Rufener F., Bartholdi P.: 1982, *Astron. Astrophys. Suppl. Ser.,* **48**, 503.

Scargle J.D.: 1982, *Astrophys. J.,* **263**, 835.

Van Winckel H., Waelkens C., Waters L.B.F.M.: 1995, *Astron. Astrophys. Lett.,* **293**, L25.

Vaidman N.L., Nurmakhametova S.T., Miroshnichenko A.S., Khokhlov S.A., Agishev A.T., Khokhlov A.A., Ashimov Y.K., Yermekbayev B.S.: 2025, *Galaxies,* **13**(5), 101.

Vaidman N.L., Miroshnichenko A.S., Zharikov S.V., Khokhlov S.A., Agishev A.T., Yermekbayev B.S.: 2025, *Galaxies,* **13**(3), 47.

Waelkens C., Lamers H.J.G.L.M., Waters L.B.F.M., Rufener F., Trams N.R., Le Bertre T., Ferlet R., Vidal-Madjar A.: 1991, *Astron. Astrophys.,* **242**, 433.

https://doi.org/10.18524/1810-4215.2025.38.341543

ORBITAL SPECTRAL VARIABILITIES IN SYMBIOTIC STAR AG PEGASI

A. B. Rustamova[1], Kh. M. Mikailov[2], B. N. Rustamov[2,1]

[1] Shamakhi Astrophysical Observatory named after Nasraddin Tusi, Azerbaijan
[2] Baku State University, Baku, Azerbaijan, *mikailov.kh@gmail.com*

ABSTRACT. The results of the study of orbital spectral variability due to binary nature of the symbiotic star AG Peqasi are presented. We used high-resolution spectra (R = 28,000) taken by 2-m telescope of the Shamakhi Astrophysical Observatory during 2016–2019, and medium-resolution amateurs' spectra (R = 9,000–11,000) taken from the Astronomical Ring for Access to Spectroscopy (ARAS) database obtained during 2020–2024. The system's orbital period is approximately 815 days, and its spectral changes are correlated with this period. In this paper we present the radial velocity curve of the cold component (M3III), as well as the emission lines Hα, Hβ, and the HeII lines λ4686 Å and λ5412 Å formed around the hot component of the AG Peg system, constructed according to our measurements. We determined the mass function of the cool component, $f_1 \approx 0.023$ $M_\odot$.

Keywords: symbiotic star, binary star, spectroscopy, radial velocity.

АНОТАЦІЯ. Представлено результати дослідження орбітальної спектральної змінності, зумовленої подвійною природою симбіотичної зорі AG Pegasi. Внаслідок взаємодії гарячого білого карлика та холодного гіганта спостерігаються періодичні зміни променевих швидкостей як абсорбційних ліній холодного гіганта, так і емісійних ліній, що формуються поблизу гарячого компонента.

У даному дослідженні використано два набори спектральних спостережень. Перший набір – 16 спектрів, отриманих у фокусі Кассегрена 2-метрового телескопа Шамахинської астрофізичної обсерваторії імені Н. Тусі на волоконному ешельспектрографі (ShAFES) з роздільною здатністю R = 28 000 у 2016–2019 роках. Другий набір – 25 спектрів, запозичених із бази даних ARAS Spectral Database, отриманих у 2020–2024 роках із роздільною здатністю 9 000–11 000.

Орбітальний період системи становить приблизно 814 діб, і спектральні зміни системи AG Peg корелюють із цим періодом. У роботі представлено криву променевих швидкостей холодного компонента (зорі спектрального класу M3III), а також лінії випромінювання Hα, Hβ і HeII λ4686 Å та λ5412 Å, що формуються навколо гарячого компонента системи AG Peg, побудовані за результатами наших вимірювань. Масова функція холодного компонента симбіотичної системи AG Pegasi була оцінена за кривою швидкостей червоного гіганта: $f_1 \approx 0{,}023$ $M_\odot$.

Побудовано криву променевих швидкостей і визначено орбітальні елементи для зорі класу M у системі AG Peg: максимальні та мінімальні значення орбітальних швидкостей зорі M3III — υ(max) = -10,72 км/с, υ(min) = -23,65 км/с; швидкість центра мас системи (γ-швидкість): $V_\gamma \approx$ -17 км/с; швидкості в перицентрі та апоцентрі: υp = 6,65 км/с, υa = 6,28 км/с. Ексцентриситет орбіти: $e \approx 0{,}027$. $a_1 \sin i = 7{,}2 \cdot 10^7$ km $\approx 0{,}48$ a.u. $\approx 103 R_\odot$.

Ключові слова: симбіотична зоря, подвійна система, спектроскопія, променева швидкість.

1. Introduction

Symbiotic stars are the most interesting, because they host the white dwarf (WD), which may be progenitors to Type Ia supernova explosions (Munari U. 1994; Boffi F.R et al. 1994). The symbiotic system consists of two completely different types of stars that interact: A cold red giant (RG in some cases yellow) and hot compact star, most frequently a WD. By studying symbiotic stars, we simultaneously study 3 different types of space objects:

1. Red giant
2. White dwarf and accretion disk
3. Star environment gas and dust nebula.

In systems of this type, a powerful flow of matter occurs through the stellar wind from a cold star, and an accretion disk is formed around a hot compact star. Symbiotic stars can reflect a transitional stage in the evolution of several types of double systems with a powerful flow of matter from a large-mass star to a small-mass star (Munari, 1994; Boffi et al., 1994).

The system AG Peg (HD 207757) is the oldest known

symbiotic nova (Boyarchuk, 1967). The symbiotic star AG Peg is a binary system that consists of a more massive M3 III RG and a less massive hot WD surrounded by nebulous gas.

a) massive RG star: spectral type MIII, mass – 2.6 $M_\odot$, radius – 85$R_\odot$, luminosity – 1100 $L_\odot$, eff. temperature – 3650 K.

b) dwarf (WD) star: mass – 0.65 $M_\odot$, radius – 0.06 $R_\odot$, luminosity – (1180-2400) $L_\odot$, eff. temperature – (95000-168000) K. (Kenyon et al., 1993; Fekel et al., 1985; Skopal, 2005; Sion et al., 2019; Skopal et al., 2017; Murset & Schmid, 1999).

The orbital period of AG Peg, according to published data, is (812-818) days (Kenyon et al., 1993; Fekel et al., 2000; Fernie, 1985).

Based on the AAVSO data for the period 1954-2022, a periodicity in the star's bright changes was identified, with a period of about 815 days. (Mikailov et al., 2023).

The recent major outburst occurred in 2015, which is the second major one since the first major nova outburst in 1850 (see: Kenyon et al., 2001; Ramsay et al., 2016; Tomov et al., 2016; Skopal et al., 2017). The analysis of the observations carried out in different spectral regions during the past years, model of this system – a stage of colliding winds. For the first time this model was proposed by Penston & Allen (1985) on the basis of three IUE high resolution spectra. Since the cool giant also loses mass through a stellar wind, it was concluded that the two winds probably interact. A model of winds in collision was proposed also by Tomov N.A. (1993b) on the basis of profiles, fluxes and radial velocities, derived from homogeneous high dispersion spectral observations in the visual during two consecutive orbital cycles (Tomov & Tomov, 1992; Tomov, 1993a).

The star AG Peg belongs to the subclass of symbiotic novae. Only eight nova-like symbiotic stars are currently known. During an outburst, the visible brightness of these stars reaches a very high value, and they maintain their brightness at such an elevated state for tens, sometimes hundreds of years. Powerful shock waves generated during flares heat the surrounding plasma to temperatures of (10^7-10^8) K and these regions become sources of emission lines with different degrees of ionization. In the spectrum of the star AG Peg, along with coronal lines FeX, FeXI, [NiXV], forbidden lines [NII], [OII] and Balmer lines of hydrogen are observed.

2. Observations and data reduction

Two sets of spectroscopic observations were used in the present study. The first set 16 spectrum were carried out at the Cassegrain focus of the 2-m telescope of the Shamakhi Astrophysical Observatory named after N.Tusi, on fiber echelle spectrograph (ShAFES) with the spectral resolution of R = 28000, in 2016-2019 years (Mikailov et. al., 2020), the second set 25 spectrum borrowed from the ARAS Spectral Database, obtained in 2020–2024 with spectral resolutions of 9000–11000 (https://aras-database.github.io/database/). The reduction of echelle spectra was carried out according to the standard technique using the new version of the DECH 30 program developed by Galazutdinov (Galazutdinov, 1992).

3. Results of observations

Due to the orbital motion of the hot WD and the RG, periodic variations in the radial velocities of the absorption lines of the RG and the emission lines formed around the WD are observed. The system's orbital period is approximately 815 days (Mikailov et al., 2023), and its spectral changes are correlated with this period. In this paper we present the radial velocity curve of the cold component (M3III), as well as the emission lines Hα, Hβ, and the HeII lines λ4686 Å and λ5412 Å formed around the hot component of the AG Peg system, constructed according to our measurements. The mass function of the cold component of the symbiotic AG Pegasi system was estimated from the velocity curve of the red giant.

Fig. 2 shows the radial velocity curve of the cool component of the star AG Peg constructed on the basis of the average values of the measured absorption lines of the star M3III.

The measured heliocentric radial velocities of more than thirty pure (unblended) absorption lines of metals (FeI, CaI, CrI, TiI) in the length range of $\lambda\lambda$5000-8000 Å were used.

The results of determining the spectral parameters of RG are presented in Table 1. This table also contains similar data from other authors. Since the spectral lines of only one component of the star AG Peg are observed, we cannot determine the masses of both components but can only estimate the mass function and $a_1 \sin i$.

Figures 3-5 shows the radial-velocity curves for emission lines: HeII λ4686 Å, λ5412 Å; HI Hα and Hβ as well as forbidden lines 4363[OIII], 5721 [FeVII] in spectrum of the star AG Pegasi compared to the M star.

In Fig. 5, when constructing the radial velocity curves of forbidden lines, the radial velocity values were used: at half maximum intensity - FWHM (Full Width at Half Maximum) and at the level of maximum intensity and were designated as, for example, [OIII]1/2 and [OIII]peak.

The change in the radial velocities of the HeII emission lines occurs in antiphase with the changes in the radial velocities of the absorption lines of the cold giant (Fig. 3). Apparently, the He II emission lines are formed in the close vicinity of the hot component.

Table 1: Spectral orbital parameters for RG star

maximum of orbital velocity	-10.72 km/s
minimum of orbital velocity	-23.65 km/s
velocity at periastron	6.65 km/s
velocity at apastron	6.28 km/s
orbital eccentricity	≈ 0.027
semi amplituda of the velocity change (K)	6.46 km/s
$a_1 \sin i = 1.376 \cdot 10^4 K_1 P \cdot (1 - e^2)^{1/2}$	$\approx 7.2 \cdot 10^7$ km
mass function: $f_1 = 1.038 \cdot 10^{-7}\ K_1{}^3 \cdot P(1 - e^2)^{3/2}$	0.023 $M_\odot$

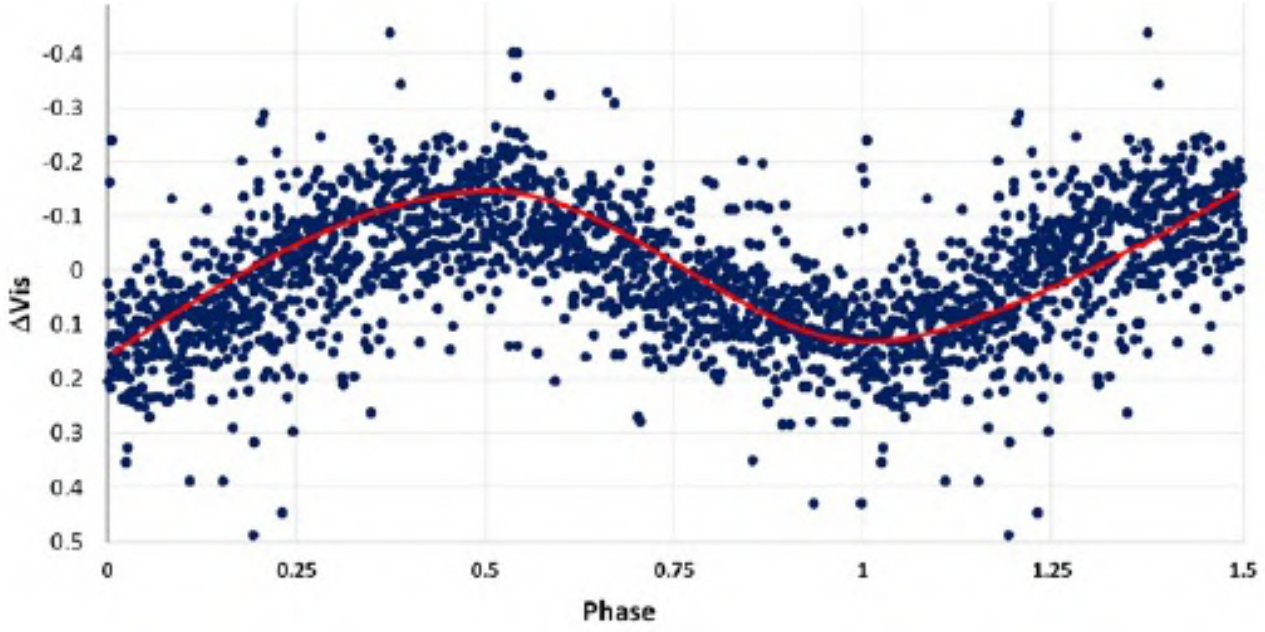

Figure 1: Based on the AAVSO data for the period 1954-2022, periodicity in the star's brightness changes was identified, with a period of about 815 days (Mikailov et al., 2023).

The behavior of the HI Hα, Hβ and 5721 [FeVII] lines is similar to the HeII lines (Fig. 4-5). The change in radial velocities of the forbidden lines 4363[OIII] differs from these lines (Fig. 5). Apparently, this line is formed by a gas flow from a hot component near a cold component.

Based on the radial velocities and intensities of the He II emission lines and the hydrogen Balmer lines in the spectrum of AG Pegasi, one can determine the regions where these lines are formed. The line half-widths allow us to estimate the distances of these regions from the hot component (the white dwarf). The width of a spectral line reflects the maximum velocity of the gas emitting it. Assuming that the gas is gravitationally bound to the white dwarf and moves in a Keplerian orbit, its velocity is given by

$$v = (GM/r)^{1/2}$$

where G is the gravitational constant, M is the mass of the white dwarf, and r is the distance of the line-formation region from the white dwarf.

Hence,

$$r = GM/v^2$$

The velocity v is inferred from the measured line width. Two width parameters are commonly used:

a) FWHM (Full Width at Half Maximum):
gives the characteristic velocity of the gas.

b) HWZI (Half Width at Zero Intensity):
the line wings trace the fastest (innermost) gas, so

$$v_{max} \approx \text{HWZI}$$
$$r \approx GM/v^2{}_{max}$$

Thus, comparing the widths of Hα, He II 4686, and [O III] lines makes it possible to reconstruct the structure of the circumstellar environment and estimate the distances to different emitting regions.

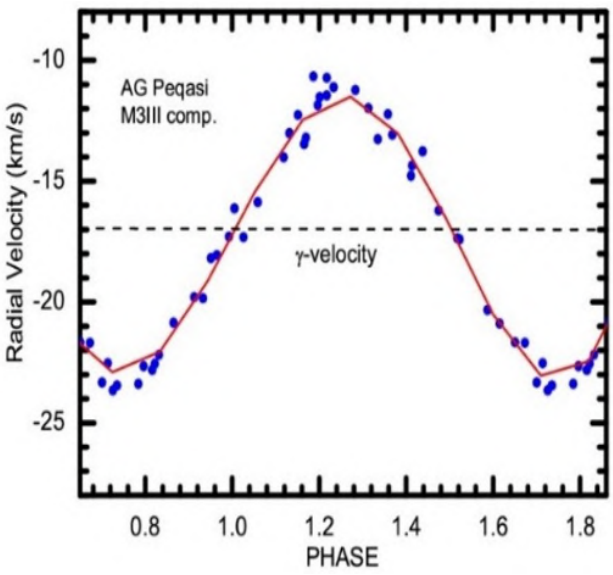

Figure 2: Radial velocity curve for the M3 III star in AG Peg (Mikailov et al., 2023). Orbital phases were calculated based on the ephemeris Min (Vis)=JD2439050 + 814.99E (Mikailov Kh.M. et al., 2023).

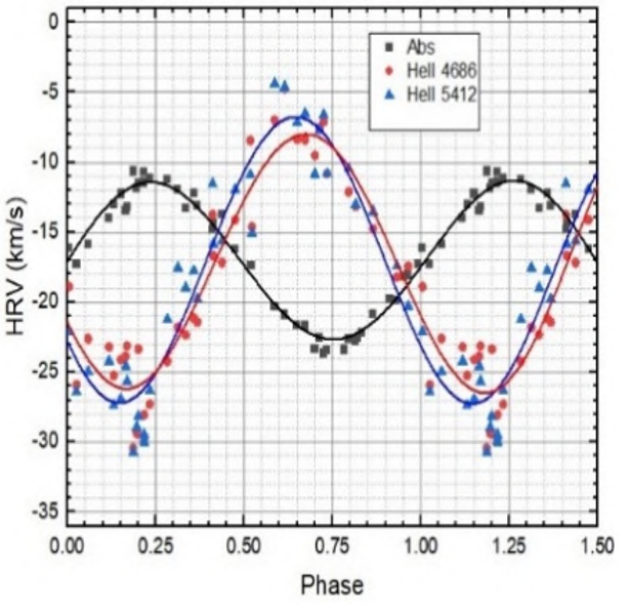

Figure 3: Radial-velocity curves for emission lines HeII λ4686 Å and λ5412 Å compared to the M star.

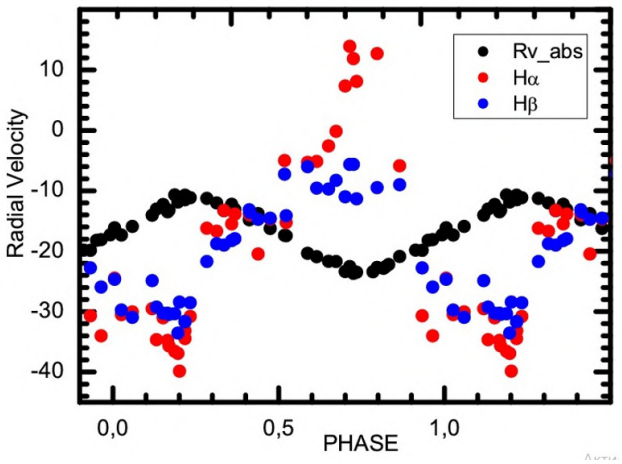

Figure 4: Radial-velocity curves for emission lines HI Hα and Hβ compared to the M star.

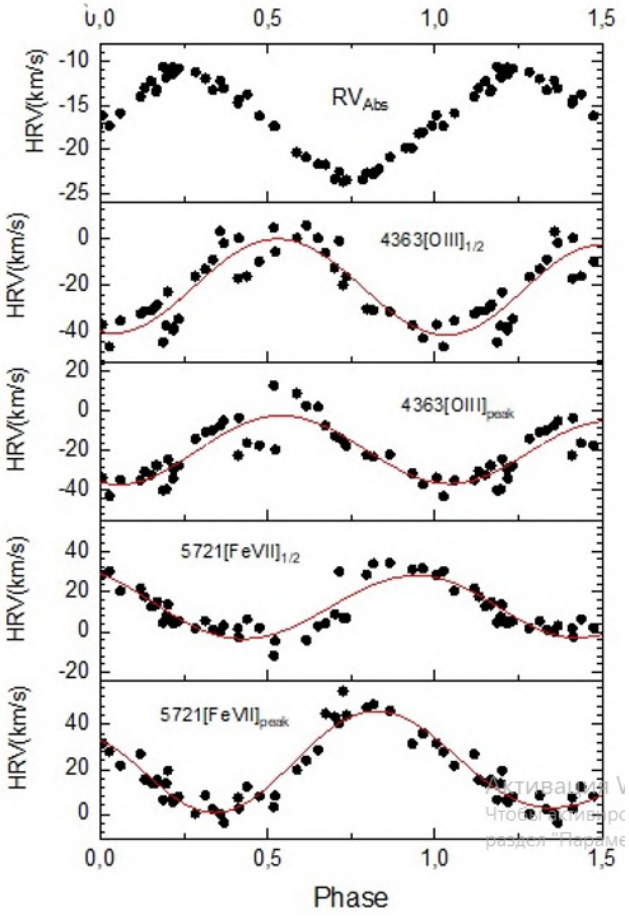

Figure 5: Radial-velocity curves for the M3 III star and the forbidden lines 4363[OIII] and 5721 [FeVII]

4. Conclusions

Radial velocity curve was constructed, and orbital elements were determined for the M Star in AG Pegasi:

• Maximum and minimum values of orbital velocities of the star M3III υ(max) = -10.72 km/s, υ(min) = -23.65 km/s

• Velocity of the center of mass of the system (γ-velocity) V$\gamma \approx$ -17 km/s

• Velocity at periastron and at apastron υa = 6.28 km/s, υp = 6.65 km/s

• Orbital eccentricity, e $\approx$ 0.027.; Period of the system: P $\approx$ 815 d.

• $a_1 \sin i = 7.2 \cdot 10^7$ km $\approx$ 0.48 a.u. $\approx 103 R_\odot$. Mass function: f_1=0.023 M$\odot$

• The results of comparative behavior of absorption and emission lines in the spectrum of the symbiotic system AG Pegasi are presented.

References

Boffi F.R. et al.: 1994, *A&A*, **184**, 5707.

Boyarchuk A.A.: 1967, *Soviet Astronomy*, **11**, 8.

Fekel F.C., Joyse R.R., Hinkle K.H.: 2000, *Astron.J.*, **119, 3**, 1375.

Fernie, J.D.: 1985, *PASP*, **97**, 653.

Galazutdinov G.A.: 1992, *Preprint SAO*, **92**.

Kenyon S.J., Mikolayewska J., Mikolayewska M. et al.: 1993, *Astron.J.*, **106**, 1573.

Kenyon S.J., et al.: 2001, *AJ*, **122**, 349.

Mikailov Kh.M, Musaev F.A., Alekberov I.A. et al.: 2020, *Kinem. and Phys. of Cel. Bod.*, **36**, 22.

Mikailov et al.: 2023, *Modern problems of physics, mathematics and astronomy. Conf. Nakhchivan State University*

Munari U.: 1994, *MnSAIm*, **65**, 157.

Murset U., Schmid H.M.: 1999, *A&Ap*, **137**, 473.

Penston M.V., Allen D.A.: 1985, *MNRAS*, **212**, 939.

Ramsay G., Sokoloski J.L., Luna G.J. M. et al.: 2016, *MNRAS*, **461,4**, 3599.

Sion E.M.m Godon P., Mikolayewska J. et al.: 2019, *Astrophys. J.*, **1**, 874.

Skopal A.: 2005, *A&Ap*, **440, 3**, 995.

Skopal A., Shugarov S.Y., Sekeras M. et al.: 2017, *A&Ap*, **604**, A48.

Tomov N.A., Tomova M.T.: 1992, *Izv. Krym. Astrophys. Obs.*, **86**, 19.

Tomov N.A.: 1993a, *Izv. Krym. Astrophys. Obs.*, **88**, 11.

Tomov N.A.: 1993b, *Izv. Krym. Astrophys. Obs.*, **88**, 22.

Tomov T., Stoyanov K.A., Zamanov R.K.: 2016, *MNRAS*, **462, 4**, 4435.

https://doi.org/10.18524/1810-4215.2025.38.341538

OPTICAL SPECTROSCOPY OF SYMBIOTIC STAR EG And. Hα ORBITAL VARIABILITIES

A. B. Rustamova[1], Kh. M. Mikailov[2], B. N. Rustamov[2,1]

[1] Shamakhi Astrophysical Observatory named after Nasraddin Tusi, Azerbaijan
[2] Baku State University, Baku, Azerbaijan
aysel.rustemova@yahoo.com

ABSTRACT. This paper includes the results of the studies of the orbital variability of the emission and absorption components of the Hα line of the eclipsing symbiotic system EG And. We used medium-resolution amateurs about 30 spectra (R = 9,000-11,000) taken from the Astronomical Ring for Access to Spectroscopy (ARAS) database obtained during 2020-2025. Radial velocity curves of the cool component were derived from the mean of the measured radial velocities of selected absorption lines forming in the atmosphere of a M-type red giant. The system's orbital period is approximately 483.3 days (Kenyon & Garcia, 2016). It is assumed that the emission lines, and in particular the Hα line, are formed in the vicinity of a hot white dwarf. We have established that the intensity of the emission component of the Hα line has the greatest value at an orbital phase of about 0.5 (corresponding to the eclipsing of the cold primary component by the white dwarf) and the lowest at about 0.1 (the red giant eclipses the hot secondary component and the region of formation of strong emission lines), and an average at about a phase of 0.8.

Keywords: symbiotic star, binary star, spectroscopy, line profile, radial velocity curve.

АНОТАЦІЯ. У даній роботі представлено результати досліджень орбітальної змінності емісійних та абсорбційних компонентів лінії Hα у затемненій симбіотичній системі EG And. Для дослідження було використано близько 30 спектрів із бази даних ARAS Spectral Database. Ці спектри, отримані в період з 2010 по 2025 роки, мають спектральну роздільну здатність 9 000–11 000. Криві променевих швидкостей холодного компонента побудовано на основі середніх значень виміряних променевих швидкостей окремих абсорбційних ліній, що формуються в атмосфері червоного гіганта спектрального типу M. Орбітальний період системи становить приблизно 483,3 доби. Передбачається, що емісійні лінії, зокрема лінія Hα, формуються поблизу гарячого білого карлика. Встановлено, що інтенсивність емісійного компонента лінії Hα досягає найбільшого значення при орбітальній фазі близько 0,5 (що відповідає затемненню холодного первинного компонента білим карликом), мінімального – при фазі близько 0,1 (коли червоний гігант затемнює гарячий вторинний компонент і область формування сильних емісійних ліній), та середнього – при фазі близько 0,8.

Ключові слова: симбіотична зоря, подвійна зоря, спектроскопія, профіль лінії, крива променевих швидкостей.

1. Introduction

A symbiotic star is a special type of binary star system in which two vastly different kinds of stars coexist and interact in a way that resembles biological symbiosis. The term was introduced in 1941 by Paul Merrill, who borrowed the word from biology, where "symbiosis" describes the living together of different organisms as a single unit. In astronomy, the analogy applies because the two stars, though extremely different in physical properties, are bound together gravitationally and share material and energy in a complex, interdependent relationship.

A typical symbiotic system consists of:

A cool red giant (RG) – a large, luminous star in the late stage of its evolution. In some cases, instead of a red giant, a yellow giant is present. These stars have exhausted hydrogen in their cores, expanded enormously, and have cool outer atmospheres. They lose mass through a slow but dense stellar wind driven by the RG radiation and/or pulsations, ejecting vast amounts of gas and dust into surrounding space.

A hot compact companion — a white dwarf – the dense, Earth-sized remnant of a Sun-like star. The white dwarf has an extremely high surface temperature, often exceeding 100,000 K, and strong ultraviolet radiation. It can pull in matter from the red giant

through an accretion disk, a rotating structure of captured gas spiraling toward the white dwarf.

The entire system is embedded in a cloud of ionized gas and dust, formed from the red giant's stellar wind. This nebula glows because the intense radiation from the hot white dwarf ionizes the gas.

The interaction is dynamic: the red giant continuously loses material, and part of this gas flows toward the white dwarf, either directly or via an accretion disk. The gravitational capture of this material can trigger bursts of activity, such as nova-like outbursts, when the accumulated matter on the white dwarf's surface undergoes thermonuclear burning.

Studying symbiotic stars is scientifically valuable because each system is essentially a natural laboratory containing:

A red giant, representing the late stage of stellar evolution for Sun-like stars.

A white dwarf and accretion processes, illustrating mass transfer and disk physics.

A circumstellar nebula, providing insights into gas dynamics, ionization, and dust formation in binary environments. Because of their complexity, symbiotic stars are important for understanding binary star evolution, stellar winds, nova eruptions, and the chemical enrichment of the interstellar medium. They also help astronomers study how matter behave under extreme temperatures, densities, and radiation fields – all within a single, gravitationally bound cosmic partnership (e.g., Kenyon,1986; Mikolajewska, 1997).

EG And (HD 4174) is a low excitation eclipsing symbiotic star with no recorded outbursts. The binary system consists of a white dwarf that ionizes part of the neutral wind from the red giant. The presence of both ionized and neutral regions in this binary, along with its high orbital inclination, is favorable for observing variations in the parameters of spectral line profiles depending on the orbital motion of the system. This facilitates determining, and – over time, as high-precision observational data accumulate – refining the orbital elements of the EG And binary system (Munari, 1993).

The optical spectrum of EG And exhibits optical emission lines of HI, [OIII], and [NeIII] superimposed on the absorption spectrum of an M-type star. Photometric and spectroscopic observations of EG And have revealed orbital periods of 481–483 days (Skopal et al., 1991; Munari, 1993; Fekel et al., 2000; Kenyon & Garcia, 2016). At optical minimum, the red giant eclipses the hot secondary component and the strong emission lines. Using optical and infrared absorption lines, the orbital parameters of the EG And binary have been reliably determined. Nevertheless, to this day, the question of whether the optical variability is caused by ellipsoidal changes, by illumination of the red giant's photosphere, by the stellar wind, or by colliding with winds from the primary and secondary components remains a subject of discussion (Shagatova, Skopal, Sekeras et.al., 2019).

Table 1: . Radial velocities [km/s] of absorption lines formed in the atmosphere of the red giant in the symbiotic EG And system, based on our 29 spectra. Phase calculated using the ephemeris data in Section 2.

Date	JD2450000+	Phase	Rv abs
01.09.2010	5440.5808	0.81538	-100.88233
12.02.2011	5605.2755	0.15615	-89.67833
09.08.2012	6148.5650	0.28028	-89.09367
22.08.2013	6529.5689	0.06241	-88.80767
21.08.2015	7256.434	0.57258	-99.29667
08.10.2015	7304.381	0.67178	-101.23733
27.09.2015	7293.392	0.64905	-100.47033
01.10.2015	7297.428	0.6574	-103.35867
23.07.2016	7592.501	0.26794	-88.15867
06.08.2016	7607.492	0.29895	-89.214
09.09.2016	7641.412	0.36914	-91.663
03.10.2016	7665.359	0.41869	-95.97233
02.09.2017	7999.441	0.10994	-88.96067
19.09.2017	8016.352	0.14493	-89.77867
25.10.2017	8052.413	0.21954	-88.11467
15.11.2018	8437.545	0.01642	-90.06667
22.01.2020	8871.263	0.91383	-94.82133
18.09.2020	9111.336	0.41057	-96.139
22.10.2020	9145.321	0.48089	-99.01733
03.11.2020	9157.343	0.50576	-96.92733
28.12.2022	9942.404	0.13014	-87.427
04.10.2023	10222.313	0.7093	-102.83333
13.11.2023	10262.3252	0.79209	-100.626
17.11.2023	10282.7	0.80046	-98.83167
14.12.2023	10293.3	0.85618	-96.81633
17.01.2024	10327.3328	0.9266	-93.772
28.02.2024	10369.392	0.01362	-92.774
04.12.2024	10649.262	0.5927	-100.44567
03.02.2025	10710.338	0.71908	-102.10133

2. Observations and data reduction

About 30 spectra from the ARAS Spectral Database were used in this research. These spectra were obtained between the year 2010 to 2025 have spectral resolutions of 9000 - 11000 (https://aras-database.github.io/database/).

The reduction of echelle spectra was carried out according to the standard technique using the new version of the DECH 30 program developed by Galazutdinov (http://www.gazinur.com/DECH-software.html).

3. Results of observations

The spectral observation data are presented in ta-

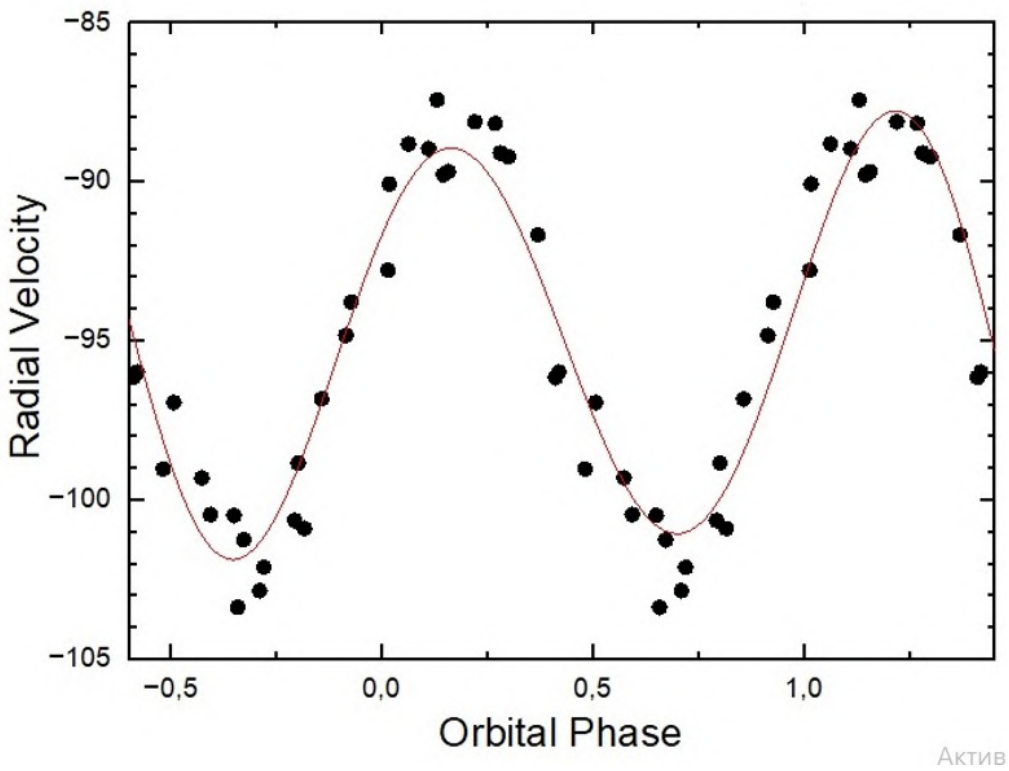

Figure 1: Radial velocity curve for the M star in EG And.

ble1. Radial velocity curves of the cool component were derived from the mean of the measured radial velocities of selected absorption lines forming in the atmosphere of a M-type red giant (table1, Fig.1). For calculation of the orbital phases of EG And we adopt an ephemeris of (Kenyon & Garcia, 2016):

JD spectros. conj.=2450213.508 +483.3×E

Moment of zero phase = moment of inferior conjunction of the giant (spectroscopic conjunction, i.e. when the giant is in front of the white dwarf)

Velocity of the center of mass of the system (γ-velocity): V$\gamma \approx$ -95 km/s.

Based on the available spectra, the profiles of the Hα line in the spectrum of the star EG And were constructed. In order to study the possible dependence of the Hα line emission intensity on the orbital phase of the EG And system, the profiles were grouped according to phase.

It is assumed that the emission lines, and in particular the Hα line, are formed in the vicinity of the hot white dwarf. It has been established that the intensity of the emission component of the Hα line reaches its maximum value at an orbital phase of about 0.5.

This phase corresponds to the moment when the white dwarf eclipses the cool primary component of the system, creating the most favorable conditions for observing the enhanced radiation.

The lowest intensity of the line is observed at a phase of about 0.1, when the red giant obscures the hot

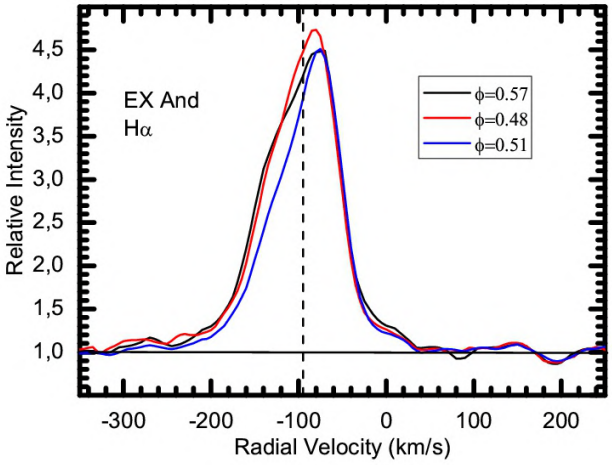

Figure 2: Profiles of the Hα line around the superior conjunction of the red giant in EG And (orbital phase 0.5).

secondary component together with the region where strong emission lines are formed. At this moment, a significant part of the radiation is blocked by the giant's envelope, and the lines weaken noticeably. The average intensity of the line is recorded at approximately phase 0.8, reflecting an intermediate state of the system, when neither of the components com-

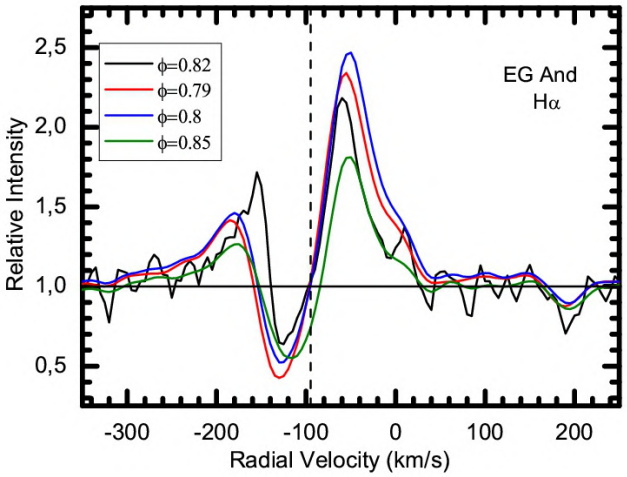

Figure 3: Profiles of the Hα line around the orbital phase 0.8 of the symbiotic system EG And.

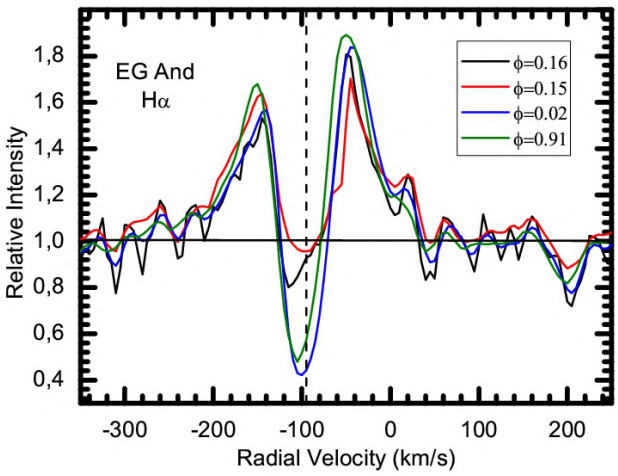

Figure 4: Profiles of the Hα line around the inferior conjunction of the red giant in symbiotic system EG And (orbital phase 0).

pletely covers the key emission-forming regions. Thus, variations in the intensity of the Hα line are closely related to the orbital geometry and the interaction processes of the components in the symbiotic system, confirming that its source is the hot white dwarf and the surrounding gaseous material. (Figs.2–4). In fig. 2-4, the vertical dotted line at the gamma velocity demonstrates the variation radial velocity of the absorption component in the Hα line profile. The solid horizontal line corresponds to the continuous spectrum level. The behavior of the Hα line in the spectrum of the symbiotic star EG And in different eclipse phases is in good qualitative agreement with similar profiles in the work (Shagatova et al., 2019).

4. Conclusions

This paper includes the results of the studies of the orbital variability of the emission and absorption components of the Hα line of the eclipsing symbiotic system EG And:

1. Radial velocity curves of the cool component were derived from the mean of the measured radial velocities of selected absorption lines forming in the atmosphere of an M-type red giant. The system's orbital period is approximately 483.3 days.

2. We have established that the intensity of the emission component of the Hα line has the greatest value at an orbital phase of about 0.5 (corresponding to the eclipsing of the cold primary component by the white dwarf) and the lowest at about 0.1 (the red giant eclipses the hot secondary component and the region of formation of strong emission lines), and an average at about a phase of 0.8.

References

Galazutdinov, G.A.: 1992, *Preprint SAO*, **92**.
Fekel H. et al.: 2000, *Astron. J.*, **119**, 1375 .
https://aras-database.github.io/database/
Kenyon, S. J.: 1986, *The Symbiotic Stars (Cambridge: Cambridge University Press).*
Kenyon S.J. & Garcia M.R.: 2016, *Astron. J.*, **152**, 1.
Mikolajewska, J.: 1997, *in Physical Processes in Symbiotic Binaries and Related Systems, ed. J. Mikolajewska (Warsaw: Copernicus Foundation for Polish Astronomy*, **3**.
Munari U.: 1993, *Astron.Astrophys*, **273**, 425.
Shagatova N., Skopal A., Sekeras M. et.al.: 2019, *Contrib. Astron. Obs. Skalnat'e Pleso*, **49**, 406.
Skopal A. et al.: 1991, *Astron. Astrophys.*, **245**, 531.

https://doi.org/10.18524/1810-4215.2025.38.340282

DETERMINATION OF THE EFFECTIVE TEMPERATURES AND SURFACE GRAVITIES OF SEVERAL A-TYPE STARS BASED ON PHOTOMETRIC PARAMETERS

Z. A. Samedov[1,2], Z. F. Aliyeva[2], G. M. Hajiyeva[1], N. H. Samedova[1]

[1] Shamakhi Astrophysical Observatory, Azerbaijan National Academy of Sciences, Shamakhi, Azerbaijan, *zahir.01@mail.ru*

[2] Department of Astrophysics, Baku State University, Baku, Azerbaijan, *zahir.01@mail.ru*

ABSTRACT. The fundamental parameters – effective temperatures (T_{eff}) and surface gravities (g) – have been determined for of A-type stars: HD 6364 (A5/7III), HD 6365 (A3III/IV), HD 6492 (A9V), HD 6723 (A8V), HD 25093 (A7II/III), HD 123798 (A8/9V), HD 129175 (A6V), HD 129433 (A0IV), HD 129660 (A7V), and HD 209124 (A0III-IV).

In order to determine the chemical composition of stars using the model or synthetic spectrum method, it is essential to know their fundamental parameters – effective temperatures (T_{eff}) and surface gravity (g). T_{eff} and log g are the basic parameters of stellar atmosphere models – determining these parameters is necessary to compute stellar atmosphere models. On the other hand, by knowing the effective temperature (T_{eff}) and surface gravity (g), it is possible to calculate the evolutionary parameters of stars – their masses (M), luminosities (L), radii (R), and ages (t). Thus, the accurate determination of the chemical composition of stars through the model or synthetic spectrum method depends on the precision of the T_{eff} and log g parameters.

The effective temperatures (T_{eff}) and surface gravities (log g) of stars were determined using photometric method. The method employed is based on comparing observed and theoretical values of the photometric indices $[c_1]$, Q, and β. This method is a simple and accurate method. The Q index in the UBV photometric system is defined as Q = (U – B) - 0.72(B – V), while the $[c_1]$ index in the uvby photometric system is defined as $[c_1] = c_1 - 0.2$ (b - y). These indices are free from the effects of absorption in the interstellar medium.

The following values of T_{eff} and log g were obtained for the studied stars: HD 6364: T_{eff} = 7,610 K, log g = 4.25; HD 6365: T_{eff} = 7,880 K, log g = 4.35; HD 6492: T_{eff} = 7,390 K, log g = 3.70; HD 6723: T_{eff} = 7,380 K, log g = 4.00; HD 25093: T_{eff} = 7,780 K, log g = 4.10; HD 123798: T_{eff} = 7,090 K, log g = 3.65; HD 129175: T_{eff} = 8,220 K, log g = 4.35; HD 129433: T_{eff} = 9,960 K, log g = 4.00; HD 129660: T_{eff} = 7,710 K, log g = 3.65; HD 209124: T_{eff} = 9,820 K, log g = 3.80.

Keywords: A-type stars, fundamental parameters.

АНОТАЦІЯ. Для зір типу А визначено фундаментальні параметри – ефективні температури (T_{eff}) та поверхневі гравітації (g): HD 6364 (A5/7III), HD 6365 (A3III/IV), HD 6492 (A9V), HD 6723 (A8V), HD 25093 (A7II/III), HD 123798 (A8/9V), HD 129175 (A6V), HD 129433 (A0IV), HD 129660 (A7V) та HD 209124 (A0III-IV). Для визначення хімічного складу зір за допомогою модельного методу або методу синтетичного спектру важливо знати їхні фундаментальні параметри – ефективні температури (T_{eff}) та поверхневу гравітацію (g). T_{eff} та log g є основними параметрами моделей зоряних атмосфер – визначення цих параметрів необхідне для обчислення моделей зоряних атмосфер. З іншого боку, знаючи ефективну температуру (T_{eff}) та поверхневу гравітацію (g), можна розрахувати еволюційні параметри зір – їхні маси (M), світності (L), радіуси (R) та вік (t). Таким чином, точне визначення хімічного складу зір за допомогою модельного або синтетичного спектрального методу залежить від точності параметрів T_{eff} та log g. Ефективні температури (T_{eff}) та поверхневі гравітації (log g) зір були визначені за допомогою фотометричного методу. Використаний метод базується на порівнянні спостережуваних та теоретичних значень фотометричних індексів $[c_1]$, Q та β. Цей метод є простим та точним. Індекс Q у фотометричній системі UBV визначається як Q = (U – B) - 0,72(B – V), тоді як індекс $[c_1]$ у фотометричній системі uvby визначається як $[c_1] = c_1 - 0{,}2$(b - y). Ці індекси не залежать від впливу погли-нання в міжзоряному середовищі. Для досліджуваних зір було отримано такі значення T_{eff} та log g: HD 6364: T_{eff} = 7 610 K, log g = 4,25; HD 6365: T_{eff} = 7 880 K, log g = 4,35; HD 6492: T_{eff} = 7 390 K, log g = 3,70; HD 6723: T_{eff} = 7 380 K, log g = 4,00; HD 25093: T_{eff} = 7 780 K, log g = 4,10; HD 123798: T_{eff} = 7 090 K, log g = 3,65; HD 129175: T_{eff} = 8 220 K, log g = 4,35; HD 129433: T_{eff} = 9 960 K, log g = 4,00; HD 129660: T_{eff} = 7 710 K, log g = 3,65; HD 209124: T_{eff} = 9 820 K, log g = 3,80.

Ключові слова: зорі типу А, фундаментальні параметри.

1. Introduction

The determination of the chemical composition of stellar atmospheres is one of the key issues in astrophysics. Recently, the chemical composition of supergiant star atmospheres has attracted the attention of astrophysicists.

Table 1: Observational values of photometric quantities of stars

№	Names of stars	Spectral class	b-y	c_1	$[c_1]$	β	U-B	B-V	Q
1	HD 6364	A5/7III	0.169	0.730	0.696	2.772	0.047	0.291	-0.1625
2	HD 6365	A3III/IV	0.150	0.826	0.796	2.804	0.046	0.256	-0.1383
3	HD 6492	A9V	0.165	0.855	0.822	2.751	0.096	0.283	-0.1078
4	HD 6723	A8V	0.184	0.766	0.729	2.746	0.023	0.294	-0.1887
5	HD 25093	A7II/III	0.290	0.822	0.764	2.795	0.270	0.450	-0.054
6	HD 123798	A8/9V	0.205	0.661	0.620	2.712	0.020	0.300	-0.196
7	HD 129175	A6V	0.170	0.910	0.876	2.842	0.100	0.245	-0.0764
8	HD 129433	A0IV	0.011	1.054	1.052	2.833	-0.05	-0.002	-0.0506
9	HD 129660	A7V	0.172	0.983	0.949	2.790	0.160	0.272	-0.0358
10	HD 209124	A0III/IV	0.025	1.141	1.136	2.820	-0.020	0.030	-0.0416

This is because, during the evolutionary process, variations occur in the abundances of certain elements in the atmospheres of A-, F-, G-, and K-type supergiant stars. In particular, an excess of the nitrogen element and a deficiency of the carbon element are observed.

In giant and supergiant stars of spectral classes A, F, G, and K, a deep convective mixing process takes place. As a result, the products of thermonuclear reactions from the cores of such stars are transferred to their atmospheres. Therefore, the observational determination of the chemical composition of stellar atmospheres is crucial for verifying the predictions of modern theories of stellar chemical evolution.

We have studied the atmospheres of many A, F, and G spectral class stars, including supergiant stars (Lyubimkov & Samedov, 1985, 1987, 1990; Samedov, 2019; Samedov et al., 2023, 2024). The first step in studying the chemical composition of stars is determining the effective temperature (T_{eff}) and surface gravity (g). T_{eff} and g are the basic parameters of stellar atmosphere models. The accuracy of determining the chemical composition depends on the computational precision of the star's atmospheric model. Furthermore, by knowing the effective temperature (T_{eff}) and surface gravity (g) parameters, the evolutionary characteristics of stars – such as their masses, luminosities, radii, and ages can be determined. Accurate determination of the effective temperature (T_{eff}) and surface gravity (g) is one of the important problems in astrophysics.

2. Determination of effective temperatures (T_{eff}) and surface gravity (g)

In this work, the main atmospheric parameters – effective temperatures (T_{eff}) and surface gravity (g) of the A-type stars HD 6364 (A5/7III), HD 6365 (A3III/IV), HD 6492 (A9V), HD 6723 (A8V), HD 25093 (A7II/III), HD 123798 (A8/9V), HD 129175 (A6V), HD 129433 (A0IV), HD 129660 (A7V), and HD 209124 (A0III-IV) have been determined. The effective temperatures (T_{eff}) and surface gravity (g) of the examined stars were determined based on the comparison of observed and theoretically calculated values of $[c_1]$, Q, and β quantities. This method is a simple and accurate method. The application of this method allows for the determination of the effective temperatures (T_{eff}) and surface gravity (g) of a large number of stars. The method was proposed by L.S. Lyubimkov (Lyubimkov et al., 2010).

The Q index in the UBV photometric system is defined as Q = (U – B) – 0.72(B – V), while the $[c_1]$ index in the uvby photometric system is defined as $[c_1] = c_1 – 0.2(b – y)$. The β index is related to absorption in the Hβ line, it measures the intensity of this line relative to the surrounding continuum in the spectrum. These indices are free from the effects of absorption in the interstellar medium. The observed values of c_1, b – y, U – B, B – V, and β quantities were taken from the Hauck, B. & Mermilliod catalog (Hauck and Mermilliod 1998). Theoretical values for c_1, b – y, U – B, and B – V were calculated by (Castelli et al., 2003), while the theoretical value of the β quantity was calculated by Castelli F. and Kurucz R.L. (Castelli & Kurucz, 2006). The observed values of the photometric quantities for the studied stars are shown in Table 1.

The theoretical calculated values of the $[c_1]$, Q, and β quantities are overlaid with the observed measured values, and based on each quantity, pairs of T_{eff} and log g are determined. The determined T_{eff} and log g pairs are plotted on the log g ─ T_{eff} diagram, and lines are drawn in the log g ─ T_{eff} plane based on the [c], Q, and β indices. The intersection point of these lines determines T_{eff} and log g (Figure 1).

The effective temperature (T_{eff}) and surface gravity (log g) we determined are given in Table 2.

For the star HD 6364, other authors have determined T_{eff} = 7433 K, log g = 3.9 (Steinmetz et al., 2020), and T_{eff} = 7400 K (Paunzen, 2024); for HD 6365, T_{eff} = 7861 K (Paunzen, 2015); for HD 6492, T_{eff} = 7183 K (Masana, Jordi & Ribas, 2006); for HD 25093, T_{eff} = 7800 K (Paunzen, 2024); for HD 123798, T_{eff} = 6908 K (Deacon, Henning & Kossakowski, 2019), T_{eff} = 7047 K (Nascimbeni et al., 2016), and T_{eff} = 7112 K (Bai et al., 2020); for HD 129175, T_{eff} = 8200 K (Kharchenko et al., 2007) and T_{eff} = 8040 K (Brown et al., 2021); for HD 129433, T_{eff} = 9709 K, lo gg = 3.64 (Shokry et al., 2018) and T_{eff} = 9817 K (Zorec and Royer, 2012); and for HD 129660, T_{eff} = 7800 K Tkachenko, Johnston & Aerts, 2024).

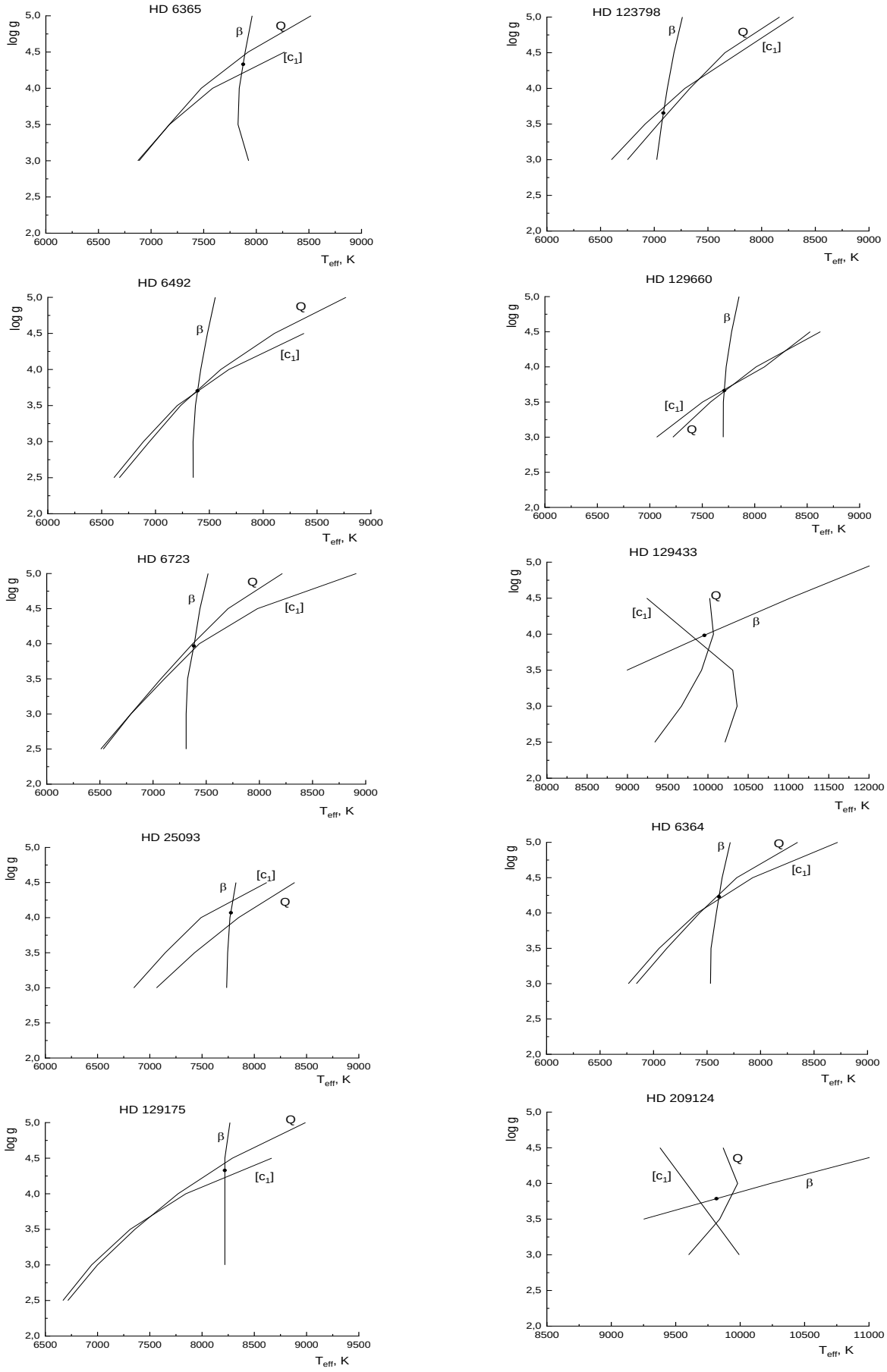

Figure 1: log g ─ T_{eff} diagrams

Table 2: Atmospheric parameters of stars (T_{eff}, log g)

№	Names of stars	Spectral class	T_{eff}, K	log g
1	HD 6364	A5/7III	7610 K	4.25
2	HD 6365	A3III/IV	7880 K	4.35
3	HD 6492	A9V	7390 K	3.70
4	HD 6723	A8V	7380 K	4.00
5	HD 25093	A7II/III	7780 K	4.10
6	HD 123798	A8/9V	7090 K	3.65
7	HD 129175	A6V	8220 K	4.35
8	HD 129433	A0IV	9960 K	4.00
9	HD 129660	A7V	7710 K	3.65
10	HD 209124	A0III/IV	9820 K	3.80

The differences between the effective temperatures (T_{eff}) and surface gravities (log g) determined in this study and those reported by other authors are as follows: for the star HD 6364, ΔT_{eff} = 193 K (mean value) and Δlog g = 0.35; for HD 6365, ΔT_{eff} = 19 K; for HD 6492, ΔT_{eff} = 207 K; for HD 25093, ΔT_{eff} = 20 K, for HD 25093, ΔT_{eff} = 68 K (mean value); for HD 129175, ΔT_{eff} = 100 K (mean value); for HD 129433, ΔT_{eff} = 197 K (mean value) and Δlog g = 0.36; and for HD 129660, ΔT_{eff} = 90 K.

The fundamental parameters of the stars were determined by various methods: spectral analysis and infrared photometry in Steinmetz et al. (2020); comparison of observed and theoretical values of the b photometric index in Paunzen (2015); spectral energy distribution fitting and infrared photometry in Masana, Jordi & Ribas (2006); Balmer jump in Shokry et al. (2018); broadband photometry in Nascimbeni et al. (2016); empirical or theoretical color–temperature relations in Deacon, Henning & Kossakowski (2019); photometric indices in Bai et al. (2020) and Tkachenko, Johnston & Aerts (2024); photometric and spectral indices in Kharchenko et al. (2007) and Brown et al. (2021); and hydrogen Balmer line profiles in Zorec and Royer (2012).

3. Conclusion

Based on the comparison of the observed and theoretically calculated values of the [c_1], Q, and β quantities, the main atmospheric parameters–effective temperatures (T_{eff}) and surface gravity (log g) – of the A spectral class stars HD 6364 (A5/7III), HD 6365 (A3III/IV), HD 6492 (A9V), HD 6723 (A8V), HD 25093 (A7II/III), HD 123798 (A8/9V), HD 129175 (A6V), HD 129433 (A0IV), HD 129660 (A7V), and HD 209124 (A0III-IV) have been determined.

The following values of T_{eff} and log g were obtained for the studied stars: HD 6364: T_{eff} = 7610 K, log g = 4.25; HD 6365: T_{eff} = 7880 K, log g = 4.35; HD 6492**:** T_{eff} = 7390 K, log g = 3.70; HD 6723: T_{eff} = 7380 K, log g = 4.00; HD 25093: T_{eff} = 7780 K, log g = 4.10; HD 123798: T_{eff} = 7090 K, log g = 3.65; HD 129175: T_{eff} = 8220 K, log g = 4.35; HD 129433: T_{eff} = 9960 K, log g = 4.00; HD 129660: T_{eff} = 7710 K, log g = 3.65; HD 209124: T_{eff} = 9820 K, log g = 3.80.

References

Bai Y., Liu J.F., Wang Y.L., Wang S.: 2020, *AJ*, **159**, 84. [https://doi.org/10.3847/1538-3881/ab63d5]

Castelli F., Kurucz R.L.: 2003, *IAUS*, **210**, A20. https://doi.org/10.48550/arXiv.astro-ph/0405087

Castelli F., Kurucz R.L.: 2006, *A&A*, **454**, 333.

Deacon N., Henning T., Kossakowski D.: 2019, *MNRAS*, **486**, 251.

Gaia Collaboration, Brown A.G.A., Vallenari A., Prusti T., et al.: 2021, *A&A*, **649**, A1.

Hauck B., Mermilliod M.: 1998, *A&AS*, **129**, 431.

IJspeert L.W., Tkachenko A., Johnston C., Aerts C.: 2024, *A&A*, **691**, A242.

Kharchenko N.V., Scholz R.-D., Piskunov A.E., et al.: 2007, *AN*, **328**, 889.

Lyubimkov L.S., Lambert D.L., Rostopchin S.I., et al.: 2010, *MNRAS*, **402**, 1369.

Lyubimkov L.S., Samedov Z.A.: 1985, *IzCrAO*, **72**, 99.

Lyubimk.ov L.S., Samedov Z.A.: 1987, *BCrAO*, **77**, 109.

Lyubimkov L.S., Samedov Z.A.: 1990, *Ap*, **32**, 30.

Masana E., Jordi C., Ribas I.: 2006, *A&A*, **450**, 735.

Nascimbeni V., Piotto G., Ortolani S. et al.: 2016, *MNRAS*, **463**, 4210.

Paunzen E., Netopil M., Prišegen M., Faltová N.: 2024, *A&A*, **689**, A270.

Paunzen E.: 2015, *A&A*, **580**, A23.

Paunzen E.: 2024, *A&A*, in press.

Samedov Z.A., Aliyeva Z.A., Hajiyeva G.M., et al.: 2024, *AzAJ*, **19**, 61.

Samedov Z.A., Rustem U.R., Hajiyeva G.M., Aliyeva Z.F.: 2023, *OAP*, **36**, 86.

Samedov Z.A.: 2019, *ARep*, **63**, 944.

Shokry A., Rivinius T., Mehner A., et al.: 2018, *A&A*, **609**, A108.

Steinmetz M., Guiglion G., McMillan P.J. et al.: 2020, *AJ*, **160**, 83.

Zorec J., Royer F.: 2012, *A&A*, **537**, A120.

https://doi.org/10.18524/1810-4215.2025.38.343167

3D IMAGE OF POLARIS FIELD STARS

I. A. Usenko[1,2], M. P. Kaliuzhnyi[2], A. S. Miroshnichenko[3,4], S. Danford[3], D. G. Turner[5], D. J. Majaess[6], D. D. Balam[7]

[1] Astronomical Observatory, Odesa I. I. Mechnikov National University, Shevchenko Park, Odesa, 65014, Ukraine, *igus99@ukr.net*
[2] Main Astronomical Observatory of the National Academy of Sciences of Ukraine, Mykolaiv Branch, 1 Observatorna St, Mykolaiv 54030, Ukraine, *nikalyuzhny@ukr.net*
[3] Dept. of Physics and Astronomy, University of North Carolina at Greensboro, P.O. Box 26170, Greensboro, NC 27402, USA, *a_mirosh@uncg.edu; danford@uncg.edu*
[4] Fesenkov Astrophysical Institute, Observatory, 23, Almaty, 050020, Kazakhstan
[5] Dept. of Astronomy and Physics, Saint Mary's University, 923 Robie St, Halifax B3H3C3, Nova Scotia, Canada *David.Turner1@smu.ca.*
[6] Mount Saint Vincent University, 166 Bedford Hwy, Halifax NS B3M 2J6, Canada *daniel.majaess@gmail.com*
[7] Dominion Astrophysical Observatory, 5071 W Saanich Rd, Victoria, BC V9E 2E7, Canada *cosmos@uvic.ca*

ABSTRACT. We present a three-dimensional model of the positions of 20 stars in the field of the Cepheid α UMi (Polaris) – 18 main sequence stars (spectral types A0–G0 V), the K-giant HD 6319 (K2 III) and Polaris itself (F8 Ib) – which was created using the 3D calculator Desmos 3D, based on the calculated U, V and W components of the full velocity vector of the stars in the Galactic coordinate system. In this paper, stellar radial velocity estimates from Usenko et al. (2023) were used. Two versions of the U, V, and W components were calculated based on Gaia DR3 parallaxes and photometric parallaxes. The resulting 3D image showed that, in both scenarios, 15 main-sequence stars, a K-giant, and Polaris form a noticeable clamp, while three stars (HD 14718, HD 90162, and HD 11696) are located outside of it. HD 14718 and HD 90162 belong to the thick disk, while HD 11696 is a remnant of a possible open cluster in Polaris's field. The K-giant HD 6319 is located inside the clamp and quite close to the Cepheid, and it is quite possible that this clamp is part of the main component of the probable open cluster Polaris, dissolved in the field of the Cepheid. Using a 3D calculator to construct a spatial image of stars may serve as a good tool for studying the structure and dynamics of open clusters in the future.

Key words: open clusters: stars: U, V, W components; GAIA parallaxes; photometric parallaxes; Cepheids, K-giants, main-sequence stars; Cepheids: α UMi; individual stars: HD 6319, HD 14718, HD 90162, HD11696.

АНОТАЦІЯ. Ми представляємо тривимірну модель положень 20 зір у полі цефеїди α UMi (Полярна зоря) – 18 зір головної послідовності (спектральні типи A0–G0 V), K-гіганта HD 6319 (K2 III) та самої Полярної зорі (F8 Ib) – яка була створена за допомогою 3D-калькулятора Desmos 3D, на основі розрахованих U-, V- та W-компонент повного вектора швидкості зір у Галактичній системі координат. У цій статті були використані оцінки радіальної швидкості зірок з Усенка та ін. (2023). Було розраховано дві версії компонентів U, V та W — на основі паралаксу Gaia DR3 та фотометричного паралаксу. Отримане 3D-зображення показало, що в обох сценаріях 15 зір головної послідовності, K-гігант і Полярна зоря утворюють помітний кламп, тоді як три зірки (HD 14718, HD 90162 та HD 11696) розташовані поза ним. HD 14718 та HD 90162 належать до товстого диска, тоді як HD 11696 є залишком можливого розсіяного скупчення в полі Полярної зорі. K-гігант HD 6319 розташований всередині клампу та досить близько до цефеїди, і цілком можливо, що цей кламп є частиною основного компонента ймовірного розсіяного скупчення навколо Полярної зорі, розчиненого в полі цефеїди. Використання 3D-калькулятора для побудови просторового зображення зір може служити гарним інструментом для вивчення структури та динаміки розсіяних скупчень у майбутньому.

Ключові слова: зорі розсіяних скупчень, U-, V- та W-компоненти, GAIA паралакси, фотометричні паралакси, цефеїди, K-гіганти, зорі головної послідовності, цефеїди α UMi, окремі зірки: HD 6319, HD 14718, HD 90162, HD11696.

1. Introduction

In our previous study (Usenko et al. 2023), we examined 18 main-sequence stars (spectral types from A0 V to G0 V located in the field of the Polaris Cepheid to confirm that these objects could be members of an open star cluster. Based on the analysis of their proper motions, radial velocities and parallaxes, it was shown that 15 stars belong to the same moving group, one star belongs to another group, and two more stars belong to the thick disk. For greater clarity, we decided to calculate the U, V, and W components of the total velocity vector for each of the 18 +1 stars (data for HD 6319, K2 III, were added), as well as Polaris (F8 Ib). These calculated components allow us to construct a 3D image and examine the positions of these stars in space relative to the Polaris Cepheid.

2. Objects and U, V, W calculations

Table 1 summarizes the U, V, W data for the 20 targets - Cepheid α UMi (Polaris), K–giant HD 6319 and 18 main-sequence objects taken from Usenko et al. (2023). U, V, W are the components of the full velocity vector of a celestial object in the Galactic coordinate system. U is the velocity component directed along the X-axis, V is along the Y-axis, and W is along the Z-axis, where they represent the radial and tangential velocities of the star relative to the local coordinate system. Strictly speaking, U (radial velocity) is the projection of velocity directed along the line of sight. The sign of "U" depends on the direction of the star's motion: positive if it is moving away from us, and negative if it is approaching. V (local velocity): the component of the star's velocity directed in the galactic coordinate system along the "Y" axis or along the galactic plane axis. W (vertical velocity): the velocity component of the star is directed perpendicular to the galactic plane, along the "Z" axis.

The Galactic components U, V, W were calculated according to the technique described in Johnson & Soderblom (1987) which uses a right-handed coordinate system for them so that they are positive in the directions of the Galactic center, the Galactic rotation and the North Galactic Pole. Using a right-handed system allows the same matrix to be used to transform both coordinates and velocities. Matrix systems allow for the calculation of these components and their uncertainties. Calculating these components requires such parameters as the star's equatorial and galactic coordinates, its proper motion, parallax, and radial velocity. Radial velocities were determined from spectra obtained at TCO (Usenko et al. 2023), and two types of parallaxes were used: from the Gaia DR3 catalog or photometric ones from Turner (see the spreadsheet Turner's ZAMS.xls at https://ap.smu.ca/~turner/A5500.html). The remaining parameters were selected from the SIMBAD database. Calculations were performed using a program written in Python. The calculated values of U, V and W in Table 1 are given in two versions because of the noticeable difference in the parallax estimates between Gaia DR3 (2022) and Turner's photometric data (see Usenko et al. 2023).

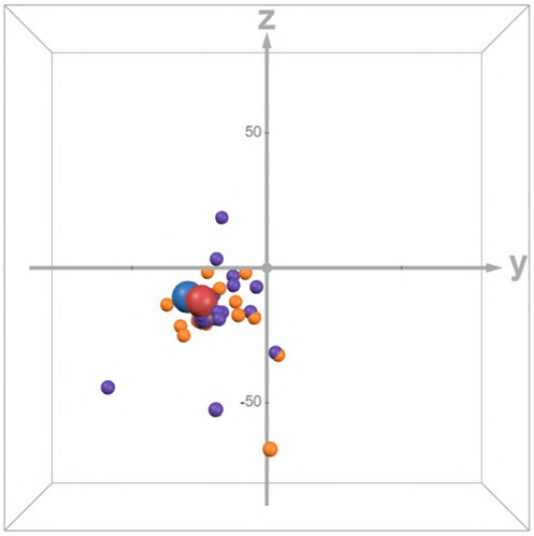

Figure 1: Polaris field stars. View along the X (U) axis, directed away from the observer. Symbols are described in Chapter 3.

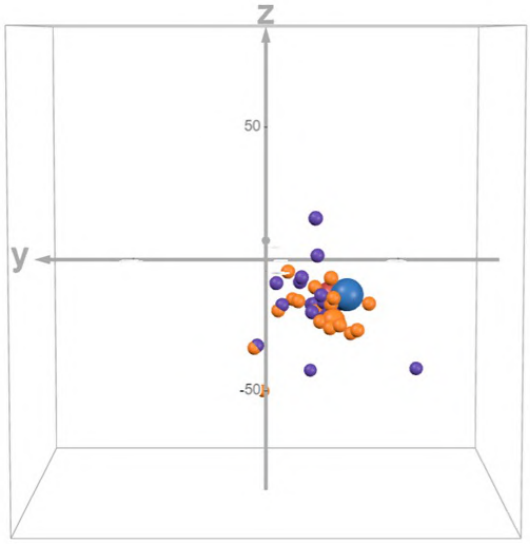

Figure 2: Polaris field stars. View along the X (U) axis, directed toward the observer.

Table 1: UVW data for Polaris field stars

Star	GAIA DR3 PARALLAXES						PHOTOMETRIC PARALLAXES					
	U km s^{-1}	σ km s^{-1}	V km s^{-1}	σ km s^{-1}	W km s^{-1}	σ km s^{-1}	U km s^{-1}	σ km s^{-1}	V km s^{-1}	σ km s^{-1}	W km s^{-1}	σ km s^{-1}
Polaris	-13.38	138.81	-24.76	165.12	-12.48	54.87	-20.07	9.48	-30.02	11.15	-11.06	3.70
HD 6319	-31.02	0.01	-24.61	0.01	-19.36	0.00	-27.29	1.92	-23.82	2.76	-18.80	0.92
HD 5914	-36.77	0.97	-26.80	2.24	-20.35	0.79	-29.32	1.95	-23.02	4.56	-18.16	1.60
HD 10772	-49.83	1.04	-23.26	2.28	-1.78	0.69	-33.95	0.75	-13.02	1.64	-3.19	0.50
HD 11696	-61.90	0.02	-23.78	0.03	-18.42	0.01	-51.40	0.72	-17.69	1 .61	19.72	0.56
HD 14369	-7.71	0.01	4.33	0.03	-32.56	0.01	-7.45	1.03	3.26	2.29	-31.70	0.85
HD 14718	74.46	1.01	1.14	2.10	-61.53	0.92	51.00	0.72	-17.86	1.60	-49.52	0.57
HD 16335	19.22	0.07	-10.33	0.13	-17.15	0.05	14.01	2.32	-17.46	4.79	-18.66	1.53
HD 66368	-6.12	4.77	-4.64	10.26	-18.60	4.35	-6.46	1.92	-6.13	4.12	-16.45	1.75
HD 90162	-18.28	0.01	-31.49	0.01	-25.63	0.00	14.94	4.07	-58.00	8.79	-43.60	4.03
HD 163988	-24.43	0.09	-11.91	0.23	-12.94	0.09	-15.70	1.77	-3.91	4.84	-7.21	1.92
HD 203317	-31.94	0.70	-19.83	2.00	-19.60	0.66	-25.00	0.89	-16.99	2.53	-16.98	0.83
HD 209556	-23.32	0.21	-18.03	0.56	-7.88	0.19	-19.05	1.23	-19.07	3.36	3.36	1.08
HD 224687	-34.17	0.98	-33.30	2.39	-22.48	0.67	-17.44	0.69	-24.65	1.74	-17.97	0.49
HD 224991	-24.80	0.04	-8.15	0.09	-1.99	0.03	-17.10	4.38	-12.65	10.93	-6.63	3.18
Polaris B	-23.04	0.03	-38.02	0.06	-14.04	0.02	-18.51	2.17	-31.27	5.01	-13.54	1.82
BD +86 44	-5.04	0.03	-18.52	0.06	-18.96	0.02	-2.66	1.87	-18.28	3.86	-16.46	1.29
BD +87 16	-29.13	0.10	-23.88	0.24	-13.73	0.08	-25.06	0.43	-21.33	0.96	-13.17	0.34
BD +87 26	-35.07	0.07	-24.55	0.15	-10.60	0.05	-27.92	1.24	-20.27	2.60	-10.36	0.91
BD +88 75	-35.11	0.11	-23.36	0.25	-21.54	0.12	-28.54	0.41	-20.64	0.96	-19.36	0.43

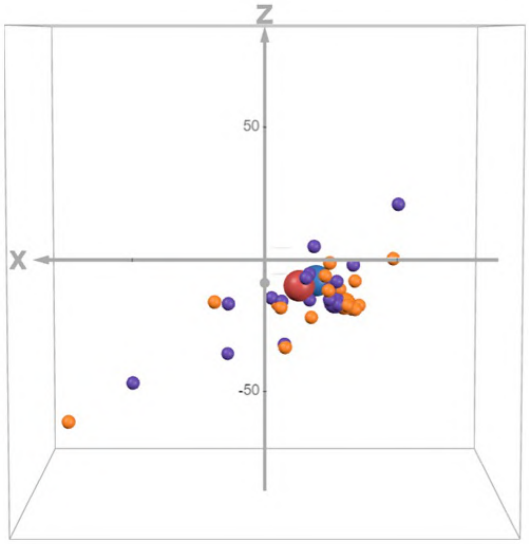

Figure 3: Polaris field stars. View along the Y (V) axis, directed away from the observer.

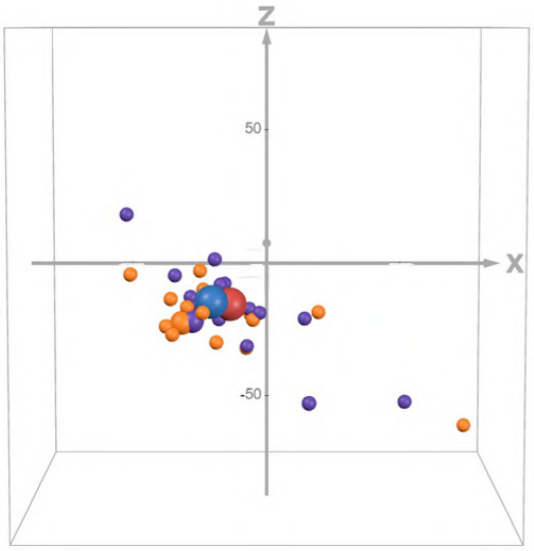

Figure 4: Polaris field stars. View along the Y (V) axis, directed toward the observer.

3. 3D image of Polaris field stars using U, V, W coordinates

To create a 3D image of 20 stars from the Polaris field, we used a 3D calculator from Desmos Studio[1]. This calculator not only allows you to position the objects along three coordinates but also view them from different angles by rotating the resulting graph along the three coordinate axes. As mentioned earlier, the U, V, and W data were positioned along the calculator's X, Y, and Z axes, respectively. The resulting 3D images of the stars from Table 1 are presented here as 2D graphics (Figures 1-8), showing how our stars appear from different viewing angles. The large red and blue symbols correspond to the coordinates of Polaris for the Hipparcos - Gaia DR3 parallax and photometric parallax, respectively. Similarly, the medium-sized symbols in orange and dark blue represent the giant HD 6319, while the small symbols of the same colors represent the remaining 18 main sequence stars.

As can be seen from the figures, the overwhelming majority of stars from both groups, despite the differences in coordinates associated with parallax estimates, form a kind of clamp together with Polaris. The exception, as already mentioned by Usenko et

[1]https://www.desmos.com/3d

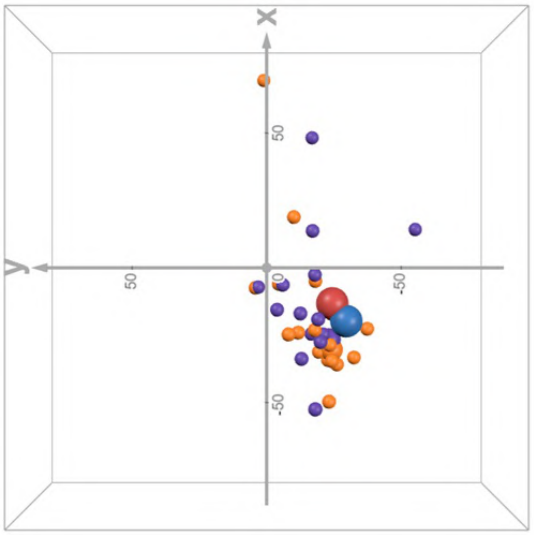

Figure 5: Polaris field stars. View along the Z (W) axis, directed away from the observer.

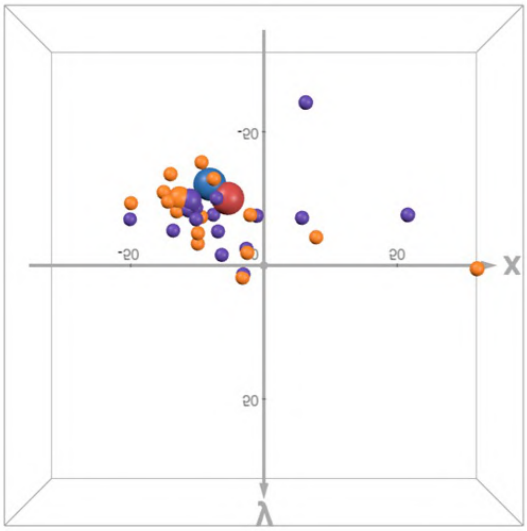

Figure 6: Polaris field stars. View along the Z (W) axis, directed toward the observer.

al. (2023), are three stars: HD 14718 and HD 90162, which belong to the thick disk, as well as HD 11696, which probably belongs to another group of stars in the Polaris' field. However, it is obvious that these three objects are located far from the clamp. It should be noted that the K-giant HD 6319 is located quite close to Polaris, and this fact may serve as evidence that the Cepheid is surrounded by the remains of an open cluster (Turner 2009).

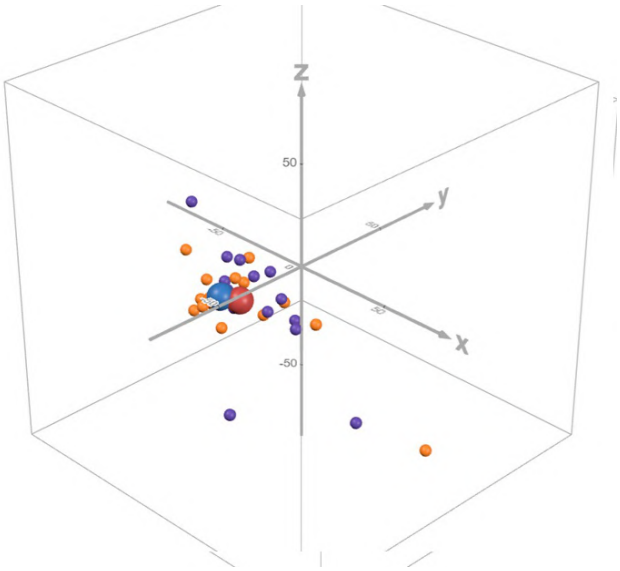

Figure 7: Polaris field stars. View at 45 degrees to the Z (W) axis from above.

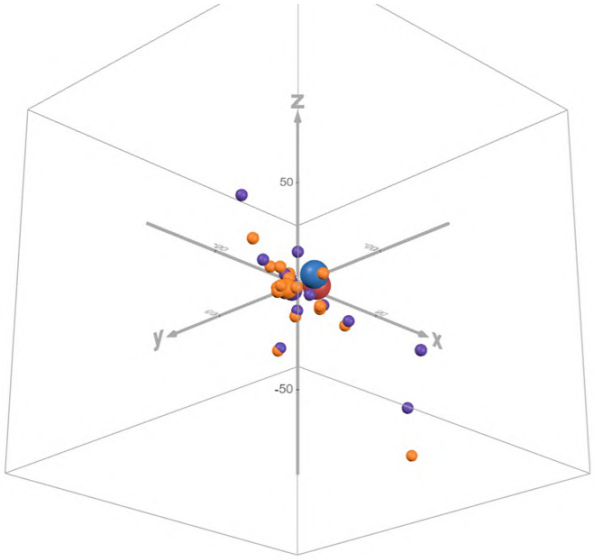

Figure 8: Polaris field stars. View at 45 degrees to the Z (W) axis from below.

4. Summary

1. For the first time, we applied a 3D calculator to the three-dimensional U, V and Z coordinates of 20 stars in the Polaris field to clearly show their locations in space.

2. Despite the differences in the parallax estimates for these stars, 17 objects form a noticeable clamp with Polaris, while three objects fall outside it. Two outlier objects belong to the thick disk, and one is a possible remnant of another cluster within

Polaris's field.

3. The close proximity of the K-giant HD 6319 to Polaris and its location within the clamp may be evidence of the existence of the remains of one of the open clusters in the Cepheid field.

4. Use of 3D calculators to produce spatial plots may serve as a new tool to study the structure and dynamics of open clusters in the future.

References

GAIA DR3 2022, *CDS/ADS Collection of Electronic Catalogues,* **1345**, 0.

Johnson, D.R.H, & Soderblom, D.R., 1987, *AJ,* **93**, 864.

Turner, D.G.: 2009, *AIPC,* **1170**, 59.

Usenko, I.A., Miroshnichenko, A.S., Danford, S., Turner, D.G., Majaess, D.J., Balam, D.D.: 2023, *Odessa Astron. Publ.,* **36**, 88.

SOLAR SYSTEM AND SPACE ENVIRONMENT

https://doi.org/10.18524/1810-4215.2025.38.343169

DETERMINING THE ORBIT OF THE TEMPORARY EARTH SATELLITE OF ASTEROID 2024 PT5

M. Karastan[1], O. Bazyey[2]

[1] Department of Physics and Astronomy, FMPIT of Odesa I. I. Mechnikov National University, 42 Pastera St, Odesa, Ukraine, *e-mail: karastan.mykyta@stud.onu.edu.ua*

[2] Department of Mathematical Analysis, FMPIT of Odesa I. I. Mechnikov National University, 2 Zmiienka Vsevoloda St, Odesa, Ukraine, *o.bazyey@onu.edu.ua*

ABSTRACT. This study investigates the gravitational influence of the major planets and the Moon on the orbital dynamics and mechanical energy of near-Earth asteroid 2024 PT5 during its temporary capture by Earth. Discovered on 7 August 2024 by the ATLAS Sutherland survey, the asteroid transitioned onto an elliptical geocentric orbit in late September 2024 and returned to a heliocentric trajectory in mid-November 2024.

The primary objective is to determine which massive bodies of the Solar System specifically the Moon and the nearest planets facilitated the capture process, induced changes in the asteroid's total mechanical energy during the capture phase, and provided the key perturbations leading to its escape from Earth's gravitational field. High-precision geocentric ephemerides and osculating orbital elements were obtained from the JPL Horizons service. Numerical analyses of the time series for kinetic, potential, and total mechanical energy, as well as eccentricity, were performed to characterize both the capture and release phases.

Particular attention was given to the temporal correlations between the asteroid's close approaches to the Moon and to the major planets, and the corresponding variations in its orbital elements. This approach isolates the intervals during which 2024 PT5 experienced the most pronounced dynamical changes, thereby informing targeted numerical simulations. The methodology includes a detailed statement of the problem and computational procedure, including the criteria used to define the start and end of the temporary satellite phase and efforts to identify the bodies exerting the strongest gravitational influence. The results lay the groundwork for developing a general algorithm to assess the probability of capture for any near-Earth object, and to evaluate its potential hazard or scientific value for future sample-return missions. Application of these techniques promises to enhance the precision of asteroid trajectory forecasts and to support ongoing planetary defense initiatives.

Keywords: temporarily captured objects; orbital dynamics; N-body integration; IAS15; REBOUND.

АНОТАЦІЯ. Виконано дослідження гравітаційного впливу великих планет та Місяця на орбітальну динаміку та механічну енергію астероїда 2024 PT5 під час його тимчасового захоплення Землею. Виявлений 7 серпня 2024 року за допомогою огляду ATLAS Sutherland, астероїд перейшов на еліптичну геоцентричну орбіту наприкінці вересня 2024 року та повернувся на геліоцентричну траєкторію в середині листопада 2024 року. Основна мета полягає у визначенні того, які тіла Сонячної системи, зокрема Місяць та найближчі планети, сприяли процесу захоплення, викликали зміни у повній механічній енергії астероїда під час фази захоплення та створили ключові збурення, що призвели до його виходу з гравітаційного поля Землі. Високоточні геоцентричні ефемериди та оскулюючі орбітальні елементи були отримані з сервісу JPL Horizons. Чисельний аналіз часових рядів для кінетичної, потенційної та повної механічної енергії, а також ексцентриситету, був проведений для характеристики як фаз захоплення, так і фаз вивільнення.

Особливу увагу було приділено часовим кореляціям між близькими зближеннями астероїда з Місяцем та великими планетами, а також відповідним змінам його орбітальних елементів. Цей підхід виокремлює інтервали часу, протягом яких 2024 PT5 зазнавав найбільш виражених динамічних змін, тим самим надаючи інформацію для цілеспрямованих числових моделювань.

Методологія включає детальне формулювання проблеми та обчислювальної процедури, зокрема критерії, що використовуються для визначення початку та кінця тимчасового захоплення супутника, та зусилля щодо ідентифікації тіл, що чинять найсильніший гравітаційний вплив.

Результати закладають основу для розробки загального алгоритму оцінки ймовірності захоплення будь-якого навколоземного об'єкта, а також для оцінки його потенційної небезпеки або наукової цінності для майбутніх місій з повернення зразків. Застосування цих методів обіцяє підвищити точність прогнозів траєкторії астероїдів та підтримати поточні ініціативи планетарної оборони.

Ключові слова: тимчасово захоплені об'єкти, орбітальна динаміка, інтеграція N-тіл, IAS15, REBOUND.

1. Introduction

Small bodies temporarily captured by Earth (so-called temporary satellites, TCOs — temporarily captured objects) are of scientific interest both in planetary dynamics and in applied problems — ranging from developing detection methods to assessing potential risks and mission planning. The analysis of temporary capture phases provides unique data on the interaction of a low-mass body with the multi-body Earth–Moon–planet system and allows for evaluating the contribution of individual bodies to changes in orbit and energy. In this work, we reconstruct the geocentric trajectory of asteroid 2024 PT5 and analyze its energetic characteristics during the period when the object behaved as a temporary satellite of Earth. The main objectives of the study are: (I) to determine the onset and termination of the capture phase, (II) to investigate changes in orbital elements and specific mechanical energy, and (III) to evaluate the contribution of the Moon and other bodies to the dynamics and energetics of the object.

2. Methodology

2.1. Data sources

Initial state vectors and orbital elements were obtained from the JPL Horizons service (JPL/NASA).

2.2.Construction of the dynamical model

For numerical integration we used the open-source N-body code REBOUND with the adaptive, high-accuracy integrator IAS15 (the integrator tolerance in this work was set to 10^{-9}). The model includes the Sun, the major planets, the Moon, and the asteroid itself. All initial vectors (positions and velocities) were brought to a common epoch (the start of the integration interval) and used as heliocentric input conditions.

2.3.Integration period and output grid

Integration was performed over the interval 25 September 2024 — 30 November 2024 with an output cadence of 1 day; all data were obtained at 00:00 UTC for each date (resolution can be increased for local events if required).

2.4.Energy calculations and capture criteria

Specific kinetic energy: T (km^2/s^2);
Specific potential energy relative to Earth: U (km^2/s^2);
Specific total mechanical energy (geocentric): E=T-U;
Criteria for temporary capture:
Geocentric eccentricity $e < 1$.
Specific energy $E < 0$.
Both criteria were used in parallel to check for consistency.

2.5.Sensitivity — assessment of the Moon's contribution

To evaluate the contribution of individual bodies, a series of control integrations was performed: in each experiment the mass of one body was set to zero while the initial positions and velocities of all bodies were preserved. Comparison of time series of orbital elements and E(t) between the base model and the variations allows isolating the influence of a specific body. For further statistical analysis we computed the difference series dE(t) and the correlation coefficients between distances r(t) and E(t).

2.6.Data processing and numerical details

All calculations were implemented in Python using the numpy, pandas, matplotlib and scipy libraries. Central-difference methods were applied for smoothing and differentiating the energy time series.

3. Results

3.1.Main time boundaries and capture duration

Based on the analysis of E(t) and geocentric eccentricity, it was determined that the transition into the captured state occurred on 29 September 2024 (the moment when E crossed zero), and the end of the capture phase took place on 25 November 2024. The duration of the temporary satellite phase was approximately 57 days.

Table 1: E(t) e(t)

Date (UTC)	**E, $km^2/s^2(\pm 2 \times 10^{-9})$**	**e ($\pm 10^{-9}$)**
2024-09-28	0.01023	1.0361500465
2024-09-29	0.00456	1.0160313087
2024-09-30	-0.00092	0.9967642306
2024-10-01	-0.00619	0.9782629997
...	...	...
2024-11-24	-0.00903	0.9581747075
2024-11-25	-0.00365	0.9830847857
2024-11-26	0.00197	1.0091820203
2024-11-27	0.00782	1.0369552086

3.2.Orbital elements and trajectory

The time series of geocentric orbital elements shows a decrease in eccentricity at the end of September,

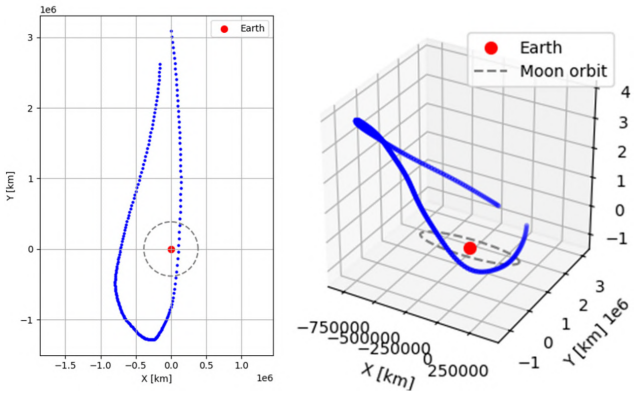

Figure 1: Complete geocentric orbit of asteroid 2024 PT5 for the interval 27 June 2024 – 31 January 2025. (Left): projection of the orbit onto the X–Y plane with the geocentric orbit of the Moon (dashed line) and the position of the Earth (red dot) indicated. (Right): three-dimensional view of the trajectory.

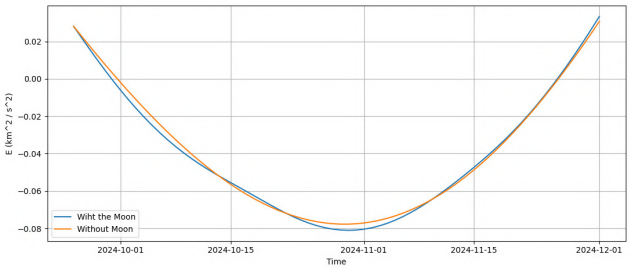

Figure 2: The specific energy of the asteroid and the specific energy of the asteroid without accounting for the influence of the Moon during the period from 2024-09-25 to 2024-11-30.

followed by a return to higher absolute values toward the end of November. The period during which $e < 1$ correlated with the interval $E < 0$. The trajectory in geocentric coordinates has a horseshoe-like shape during the capture phase.

3.3.Role of the Moon and other bodies

The analysis of the "without Moon" integration series showed local deviations of $dE(t) = 4.729 \times 10^{-3}$ km^{2}s^2 compared to the base model. Correlation analysis revealed a strong correlation between the asteroid–Moon distance and energy variations; the absolute value of the correlation coefficient was approximately 0.95, while for other bodies it was less than 0.1.

4. Discussion

The results indicate that short-term fluctuations in the total mechanical energy of the asteroid relative to Earth are mainly determined by local gravitational in-

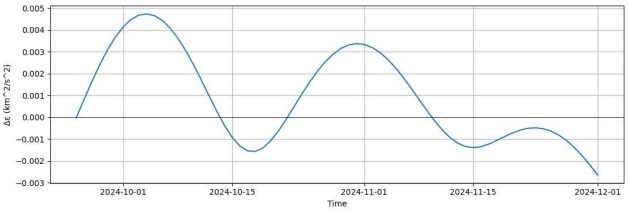

Figure 3: The difference in energy (model without the Moon minus model with the Moon).

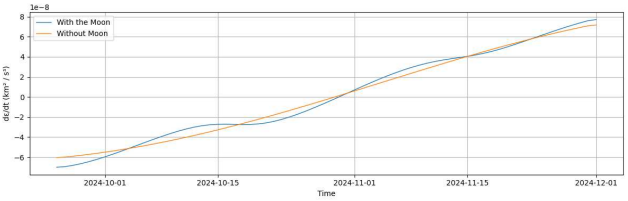

Figure 4: Energy variation over time (with the Moon and without the Moon).

fluences, among which the Moon plays the dominant role. The weak contribution of other planets within the considered interval is explained by their large distances and less favorable configurations for momentum transfer to the asteroid. The results of the "mass=0" test series confirm that the local asymmetry of the E(t) curve is caused by gravitational "impulses" from the Moon during close approaches.

It is important to note the sources of error and limitations:

Uncertainty in the asteroid's initial mass and internal parameters (in this work it was treated as a test particle).

Errors in initial vectors (influence of observational and interpolation errors from Horizons).

Neglect of minor non-gravitational effects (e.g., Yarkovsky), which are insignificant for short-term evolution but may affect long-term behavior.

Proposed improvements for future studies include refining GM values based on SPICE/NAIF data, performing ensemble integrations to assess sensitivity to initial condition uncertainties, and, if necessary, accounting for non-gravitational forces for longer integrations.

5. Conclusion

It was established that asteroid 2024 PT5 entered a temporary capture state on 29 September 2024 and remained in it for about 57 days, until 25 November 2024.

Analysis of the orbital elements and energy confirms

the phase transition: entry into the state with $e < 1$ and $E < 0$ at the end of September and exit from it at the end of November.

The series of control integrations showed that the Moon provides the most significant contribution to local deviations of the energy curve; the correlation between the asteroid–Moon distance and E was approximately 0.95.

The applied methodology (JPL Horizons → REBOUND (IAS15) → series of mass-zero runs) is effective for assessing the influence of individual bodies on the orbit of a low-mass object and can be used for further studies of other temporary satellites.

References

Acton C.H.: 1996, *Planet. Space Sci.,* **44**, 65.

Ginsburg A. et al.: 2019, *Astron. J.,* **157**, 98 (Astroquery package).

JPL Horizons: 2024, *NASA Jet Propulsion Laboratory, Solar System Dynamics, JPL Horizons On-Line Ephemeris System,* available at *https://ssd.jpl.nasa.gov/horizons/.*

NAIF, NASA: 2024, *SPICE Toolkit Documentation,* available at *https://naif.jpl.nasa.gov/naif/toolkit.html.*

Rein H., Liu S.F.: 2012, *Astron. Astrophys.,* **537**, A128.

Rein H., Spiegel D.S.: 2015, *Mon. Not. R. Astron. Soc.,* **446**, 1424.

Tonry J., Denneau L., et al.: 2018, *Publ. Astron. Soc. Pacific,* **130**, 064505 (ATLAS Project).

https://doi.org/10.18524/1810-4215.2025.38.343170

EVOLUTION OF THE ROTATION PARAMETERS OF THE ROCKET′S UPPER STAGE (SPACE OBJECT 1987-074G)

N. Koshkin [1], O. Kozhukhov [2], L. Shakun [1], O. Bryukhovetskyi [2], E. Korobeynikova [1], S. Melikyants [1], S. Strakhova [1], V. Dragomiretsky [1], A. Ryabov [1]

[1] Astronomical Observatory of Odesa I. I. Mechnikov National University, Odesa, Ukraine

[2] National Space Facilities Control and Test Center, Kyiv, Ukraine

ABSTRACT. Active space debris removal operations require a priori knowledge of the target objects' rotation parameters, i.e., information on their rotation speed and current orientation in space. This can be achieved through appropriate observations designed to determine these parameters. Recording and subsequent analysis of light curves is the most common method for monitoring space objects' rotation using optical means. This paper examines the results of long-term photometric observations of a large space debris object — the third stage of the SL-14 rocket (international COSPAR number 1987-074G, USSTRATCOM ID 18340). It shows how this resident space object's (RSO) rotation speed around its center of mass repeatedly changed between 2006 and 2025. To understand the cause of this behavior of RSO 18340, it is necessary to study the relationship between its different rotation speed states and the corresponding orientation of its rotation axis in inertial space. In paper, we consider the observed light curves of RSO 18340, recorded in 2024 at different observatories, analyze their structure and identify similar photometric patterns in different light curves. These photometric patterns are used to determine the spatial direction of the object's rotation axis in two short (1–3 days) time intervals in late February – early March 2024. As a result of this analysis of the light curves, four estimates of the average direction of the rotation axis and its evolution over a two-week interval were obtained. Using two light curves obtained during flybys over different observing points on February 27, 2024, we obtained the current direction of the rotation axis in the inertial coordinate system: RA = 10°, Decl. = -66°. And based on six light curves obtained on March 9, 10 and 11, 2024, the following average coordinates were determined: RA = 06°, Decl. = -39°. We estimate the internal error of these results to be ±(5–10)°. Based on these results, we hypothesize that there are no rapid shifts in the rotation axis of RSO 18340.

Keywords: space object; photometric observation; light curve; apparent period; photometric pattern; spin axis orientation.

АНОТАЦІЯ. Для операцій з активного видалення космічного брухту необхідне апріорне знання параметрів обертання цільових тіл, тобто інформація про швидкість їхнього обертання та поточну орієнтацію у просторі. Це може бути забезпечено відповідними спостереженнями, призначеними для визначення цих параметрів. Реєстрація та подальший аналіз кривих блиску є найпоширенішим методом моніторингу обертання космічних об'єктів оптичними засобами. У роботі розглянуті результати багаторічних фотометричних спостережень великого об'єкта космічного брухту – 3-го ступеня ракети SL-14 (міжнародний номер COSPAR 1987-074G, USSTRATCOM ID 18340). Показано, як протягом 2006–2025 рр. неодноразово змінювалася швидкість обертання навколо центру маси цього резидентного космічного об'єкта (КО). Для розуміння причини такої поведінки КО 18340 необхідно вивчити взаємозв'язок між різним станом швидкості його обертання та відповідною орієнтацією в інерційному просторі його осі обертання. У роботі для цього розглянуто спостережні криві блиску КО 18340, які отримані та зареєстровані в 2024 році на різних обсерваторіях, проаналізовано їх структуру та ідентифіковано схожі фотометричні патерни на різних кривих блиску. Ці фотометричні патерни потім були використані для визначення напрямку у просторі осі обертання даного об'єкта у двох коротких часових інтервалах (1–3 доби) наприкінці лютого – на початку березня 2024 року. В результаті цього аналізу кривих блиску отримано чотири оцінки середнього напряму осі обертання та її еволюцію на двотижневому інтервалі. Використання двох кривих блиску, отриманих у прольотах над різними пунктами спостереження 27 лютого 2024 року дозволило визначити поточний напрямок осі обертання в інерційній системі координат: RA = 10°, Decl. = -66°. А на основі шести кривих блиску, що отримано 9, 10 і 11 березня 2024 року визначені наступні середні координати: RA = 06°, Decl. = -39°. При цьому внутрішню помилку цих результатів ми оцінюємо як ±(5–10)°. На основі цих результатів зроблено припущення про відсутність швидких коливань осі обертання КО 18340.

Ключові слова: космічний об'єкт; фотометричні спостереження; крива блиску; видимий період; фотометричний патерн; орієнтація осі обертання.

1. Introduction

Orbital spacecraft play a vital role for modern civilization. However, as the number of objects in near-Earth space grows, so too do the undesirable consequences associated with possible and even inevitable collisions. The growing number of space debris is of exclusive concern. Space debris is artificial objects in orbit that perform no useful function (inoperative spacecraft, spent rockets, fragments of destroyed spacecraft, etc.). To protect operational spacecraft and the space environment as a whole, several measures have been proposed to reduce the risk of collisions—primarily, active debris removal (ADR).

Such operations require a priori knowledge of the rotational parameters of the target bodies, that is, their rotational speed and current orientation in space. This can be ensured by appropriate observations designed to determine these parameters. In general, both for the mass removal of space debris from orbit and for accurately predicting its orbital motion, it is important to understand and consider the causes and mechanisms that cause changes in the rotation of space objects.

Light curve recording is the most common method for analyzing the rotation of space objects using optical means. They can be used to determine the rotation states of space debris, including the rotation period (Silha, 2018; Hall, 2014; Rachman, 2025) and the orientation of the rotation axis (Santoni, 2018; Zhao, 2020; Vananti, 2023; Kudak, 2024). Of interest is the study of the evolutionary of both the rotation period and the spatial orientation of the rotation axis of a space debris objects. Many authors have noted the cyclic nature of the rotation period variations in different studied space debris objects (See, for example, Earl, 2017; Rachman, 2025). The main goal of these studies was to extract apparent periods and explain the observed rotation accelerations and decelerations by modeling the torques acting on the space debris. For example, tilted solar panels with different orientations and different reflectivities for the front and back sides experience torques caused by the pressure of solar rays. For example, Ojakangas & Hill (2011), Albuja (2015), Benson & Scheeres (2017), it was shown that solar radiation pressure and the YORP effect can lead to complex, tumbling rotations of asymmetric satellites.

However, the causes of the acceleration and deceleration of the rotation of various inactive spacecraft and rocket bodies require further study. A better understanding of the relationship between different rotational speed states and the corresponding orientation of the satellite's spin axis is also needed.

2. Variations in the rotation period of RSO 18340

In this paper, we present the results of photometric observations and their analysis for a large space debris object, namely the 3rd stage of the SL-14 rocket body (R/B). This space debris object moves in a circular orbit at an altitude of approximately 1450 km above Earth with an inclination of 82.5°. The Astronomical Observatory of the Odesa I. I. Mechnikov National University has been take photometric monitoring of large space debris bodies in low orbits for many years (Koshkin, 2021). The first observations of RSO 18340 were obtained in September 2006. At the same time, the first estimates of the apparent rotation period of this space debris were made, which was approximately 135 seconds. However, observations obtained in May 2007 revealed that the period of its light curve decreased to approximately 68 seconds. This value was almost exactly half the duration of the period in the previous observation, and this gave some reason to consider it a harmonic of the main rotation period. It should be noted that the light curves of the RSO 18340 exhibits two significant oscillations with similar amplitudes per rotation, between which secondary maxima are sometimes observed, either as a separate increase in brightness or as a hump on the descending or ascending branch of the main oscillation. This fact provides a strong argument in favor of an acceleration of the rotation of RSO 18340 over the expired eight months. Observations in July 2008 showed that the brightness oscillation period of this RSO was approximately 58 seconds. Subsequent observations yielded the following estimates of its rotation period: on October 8, 2009 and September 10, 2010, it was approximately 50 seconds, while on April 26, 2010, it was approximately 72 seconds. Figure 1 shows the light curves of RSO 18340 that we recorded on these dates.

Subsequent, unfortunately also not always regular, photometric observations have shown that this object continues to experience significant variations in its rotation velocity around its center of mass. Figure 2 shows our obtained rotation period values for the period 2006–2022. We see mostly slow, possibly cyclical, variations in the apparent rotation period of RSO 18340, ranging from 30 to 158 seconds. The cycle length was likely approximately 2.5 years or more.

In 2020, an international campaign of photometric observations of rocket bodies (R/B) was launched, announced by the Inter-Agency Space Debris Coordination Committee (IADC). Its goal was to evaluate the potential of photometry to determine all possible rotation parameters of rocket bodies, given the availability of extensive data from various observatories. The observation program included eight R/Bs with orbital altitudes below 1000 km, i.e., located in the region of highest spatial density of space bodies. This region of altitude above Earth is primarily in need of active debris removal from orbit. However, RSO 18340 was also included in the observational program of this campaign, as it has an interesting history of rotational speed variations around its center of mass. The campaign lasted until mid-2022. Approximately 80 light curves of RSO 18340 were obtained, which were very unevenly distributed over time. Figure 3 shows the distribution of these observations, obtained at four observatories. As can be seen, there are intervals when a group of observations were obtained on close dates. However, overall, there are significant gaps between the observations, which significantly reduces their value for some types of analysis.

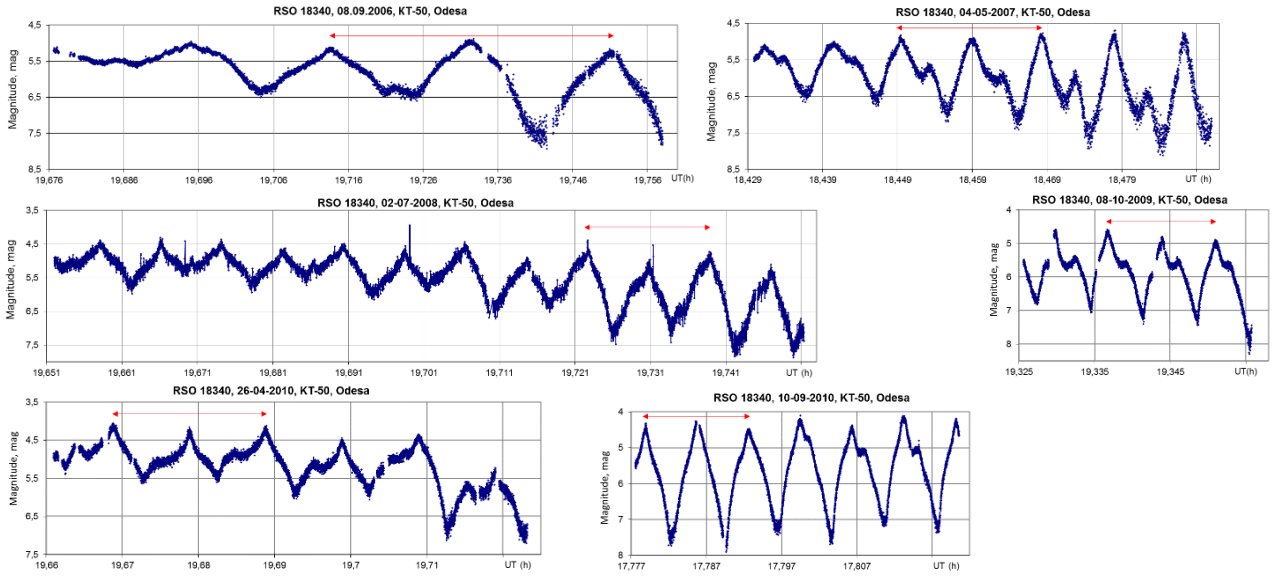

Figure 1: Examples of light curves for RSO 18340. The x-axis represents time in hours (the x-axis scale is maintained). The red line with arrows indicates the light curve period corresponding to the apparent rotation period of the RSO.

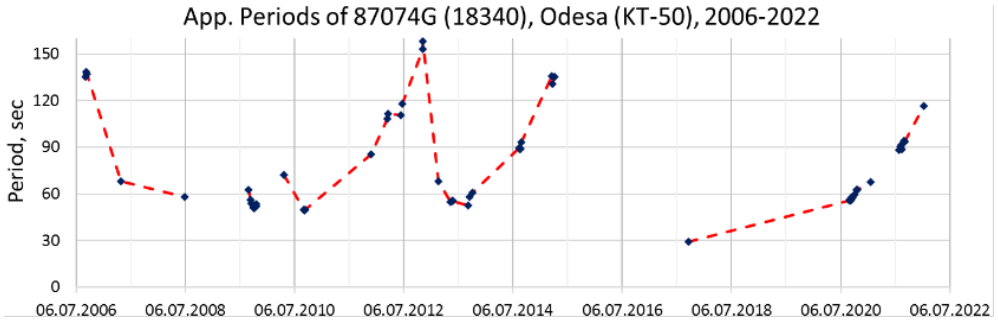

Figure 2: Variation in the apparent rotation period of RSO 18340 between 2006 and 2022. Odesa, KT-50 (Koshkin, 2021).

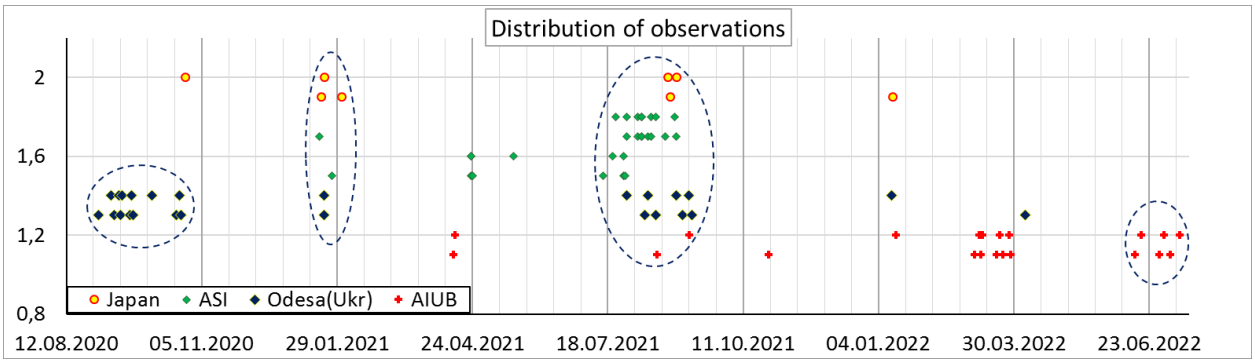

Figure 3: Time distribution of photometric observations of RSO 18340 obtained at four observatories during the IADC campaign in 2020–2022. The horizontal axis represents the observation date, and the vertical axis represents the arbitrary value (for clarity, to evenly distribute all points along the Y coordinate).

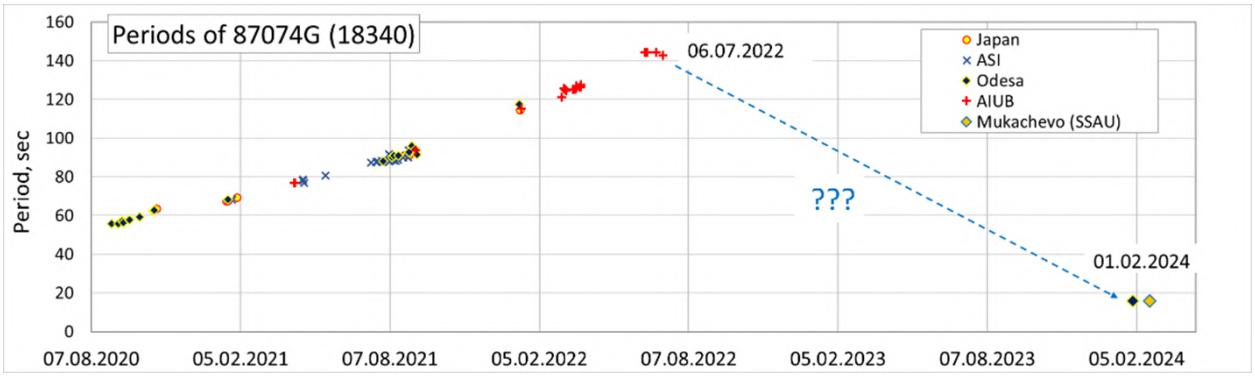

Figure 4: Trend in the apparent rotation period of RSO 18340. The data were obtained as a result of an international campaign organized by the IADC in 2020-2022.

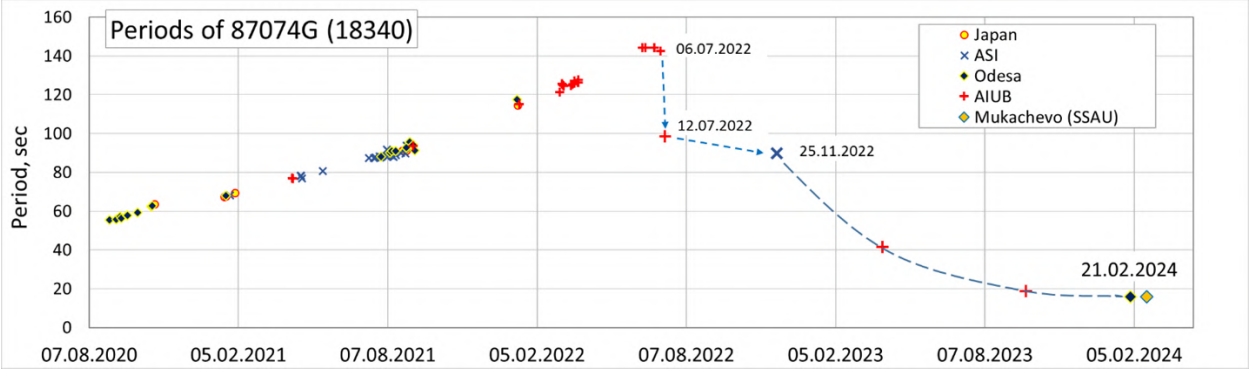

Figure 5: Variation in the apparent rotation period of RSO 18340. Data for the period 2020-2022 were obtained from the IADC. Period values after July 6, 2022, were provided by ASI and AIUB (see Kumar, 2025)

Nevertheless, these observations were analyzed for the possibility of estimating the apparent rotation period of RSO 18340. As a result, a nearly linear trend of increasing apparent rotation period of RSO 18340 from 55.6 seconds to 144.4 seconds was detected over the time period from September 2020 to early July 2022, with an average period increase rate of approximately 0.13 seconds/day. At this point, the campaign ended, and the operational exchange of observation data stopped. It seemed that RSO 18340's rotation had entered a state of stable, gradual deceleration, as is often observed in other space debris objects. However, on February 1, 2024, in Odesa, we obtained another light curve of this RSO, and unexpectedly found that the observed rotation period was 15.8 seconds. This represents a ninefold increase in the angular velocity (see Fig. 4).

At the same time, it was discovered that, after the end of the campaign, colleagues from Switzerland (AIUB) and Italy (ASI) also obtained sporadic observations of this RSO. Based on their data (Kumar, 2025), it was concluded that in the second week of July 2022, the rotation velocity of RSO 18340 rapidly increased (the period decreased to 98.6 sec) and possibly remained at almost the same level until the end of November 2022. After this, a period of slow rotational velocity increase was observed until the end of February 2024, as shown in Fig. 5. Let us pay attention to the fact that the acceleration of rotation of RSO 18340 (see Fig. 2) observed from 08.11.2012 to 20.02.2013 (the visible period decreased from 158 to 68 seconds) occurred in approximately 100 days, while the acceleration in 2022-2024 apparently continued for 1.5 years.

As a result, the cooperative observing campaign for photometry of RSO 18340 was restart from late February 2024. It involved primarily two observing stations of the National Space Facilities Control and Test Center of Ukraine in Novosilki and Mukachevo, as well as the Astronomical Observatories of Odesa, Uzhgorod, and Lviv Universities. Some observations were also provided by the UK Space Agency (UKSA, Herstmonceux) and the Italian Space Agency (ASI, Scudo), and the Swiss company s2a systems subsequently joined the observations. Ultimately, it was established that, since the end of February 2024, the apparent rotation period of RSO 18340 has been increasing monotonically, initially slowly at a rate of approximately 0.02 sec/day, then more rapidly at a rate of approximately 0.05 sec/day (Fig. 6). However, the rate of period increase never reached the level observed in 2020–2022, remaining, on average, three times slower.

We observed another nonlinear change in the apparent rotation period of RSO 18340 beginning on June 22, 2025, when it decreased by 0.3 seconds over approximately three weeks and then continued to increase at a rate of approximately 0.072 seconds/day for several months (see Fig. 7).

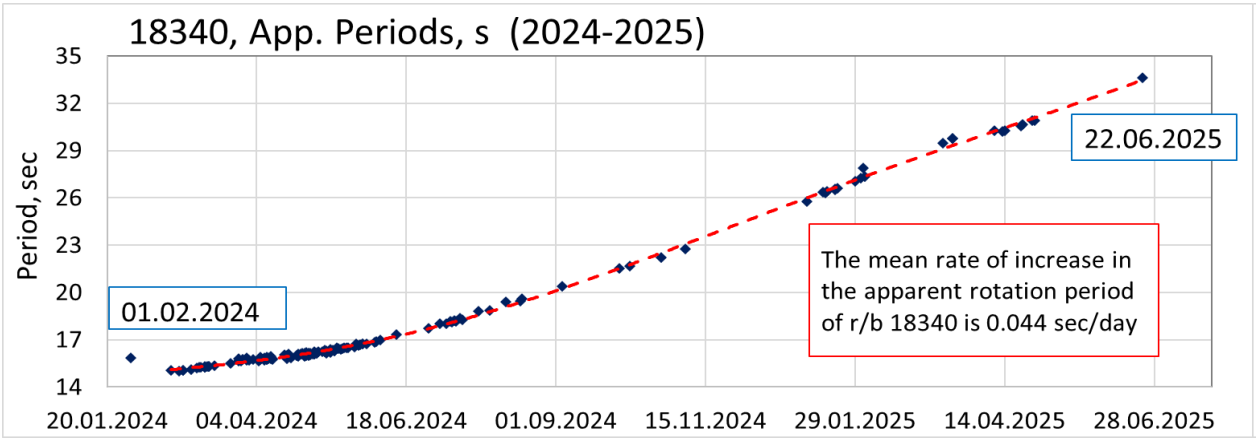

Figure 6: Change in the apparent rotation period of RSO 18340 from February 1, 2024 to Juny 22, 2025.

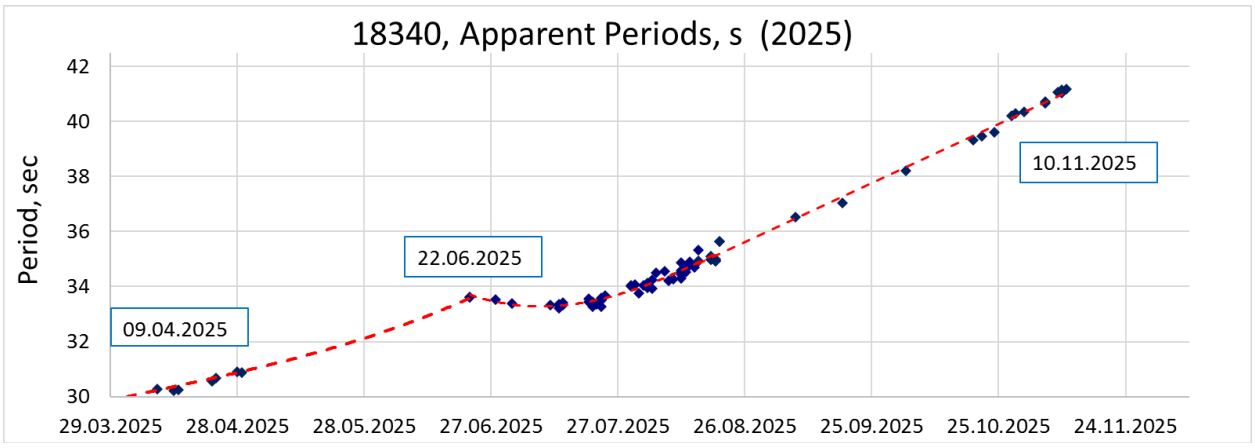

Figure 7: Variation in the apparent rotation period of RSO 18340 between April 9, 2025 and November 10, 2025.

This unstable change in the rotation speed of RSO 18340 raises questions about its possible cause. In (Kumar, 2025), the authors considered the possible cause to be the loss of residual fuel due to a mechanical failure of one of the R/B engine's nozzle valves during its spin-up period from July 2022 to February 2024. Such a cause cannot be ruled out, but given the entire history of its rotation period variations, its effect must be very complex and repetitive.

3. Orientation of the Rotation Axis of RSO 18340

A comprehensive study of the nature of its rotation around the center of mass could be the solution to the problem of the complex, possibly cyclical, variations in the rotation period of RSO 18340. On the one hand, the slow deceleration of its rotation observed in recent years occurs at varying rates. This could support a change in the nature of its rotation and the position of its rotation axis within the body. On the other hand, the shape of its light curves generally appears to be consistent across seasons over many years.

An attempt was made at the Sapienza University of Rome (Kumar, 2025) to determine the rotation parameters of RSO 18340 by comparing the observed and synthetic light curves, using a physical and digital model (physical simulation + "digital twin"). By fitting model light curves to the observed one, they obtained a complex motion, including rapid nutation and precession of the rotation axis of R/B 18340.

We attempted to test an alternative hypothesis, which assumes a planar rotation of the RSO around a single axis within the body and a slow precession of the rotation axis in space. We used our previously proposed method for determining the spatial orientation of the rotation axis of an arbitrary-shaped RSO (Koshkin, 2024a and Koshkin, 2024b). To do this, we examined 13 light curves of RSO 18340 obtained from several observatories between February 27 and March 11, 2024 (10 light curves from the National Space Center, 1 from Lviv University, and 2 from Herstmonceux). Through expert comparison, we identified 17 fragments (patterns) in these light curves that are similar to each other and distinct from the others. For the time of each pattern observation, the position of the phase angle bisector (PAB) vector was calculated. By grouping these data, the average position of the rotation axis in the inertial coordinate system was determined for each 1-2-day time interval (Fig. 8). We see a significant drift of the rotation axis in declination, while right ascension changed little. At the same time, the results based on observations over a single night show a scatter of approximately ±3° relative to the solution based on a two-day observation interval, i.e., the averaged solution. This allows us to estimate the internal error of the individual pole solution as no more than ±(5-10)°. In the orbital coordinate system, the rotation axis is offset from the ascending node by an average of 122-127 degrees in right ascension.

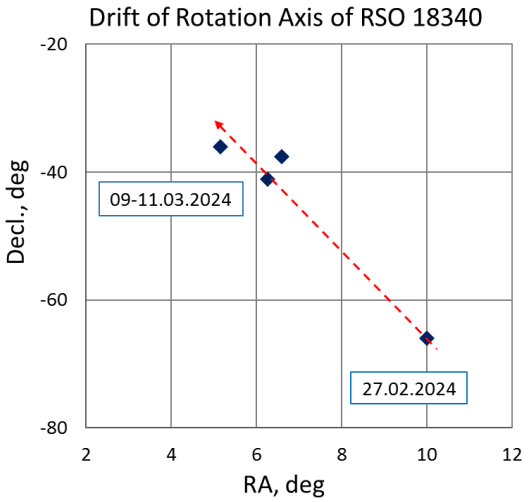

Figure 8: The position of the rotation axis of RSO 18340 in the inertial coordinate system for four dates, calculated by selecting similar photometric patterns in light curves obtained at different observatories over short time intervals (1-3 days).

In addition to searching for the optimal position of the rotation axis in space, this method allows us to simultaneously determine of the latitude of each photometric pattern in the coordinate system associated with rotation axis in the satellite body. This latitude is determined by the current latitude of the PAB vector in the inertial coordinate system. In this sense, we use the term "latitude of the photometric pattern." The determined correspondence between the photometric pattern and latitude should remain constant for all satellite passes as long as the rotation axis maintains its position within the body (although it shifts in space).

In Figure 9, fragments of the observed light curves (patterns) are superimposed on the PAB latitude plots for RSO 18340 at the exact times and latitudes calculated for the determined rotation axis position in space. We see the close equality of the latitudes of the similar patterns across different transits and for different observation sites, confirming the correctness of the determined rotation axis position in the corresponding time interval.

4. Discussion and future work

It appears that our estimates of the spatial position of RSO 18340's rotation axis may indicate a slow shift over an interval of approximately two weeks (February 27 – March 11, 2024), i.e., the absence of rapid, significant oscillations. However, this conclusion remains insufficiently substantiated. Although we (together with colleagues) obtained numerous light curves for RSO 18340 in 2024 and 2025, we have not yet been able to determine the rotation axis orientation and its evolution over significant timescales. This is because the technical challenge of creating a pipeline for comparing many light curves and identifying unique patterns across the entire dataset remains unresolved. The light curves of RSO 18340 often exhibit very similar patterns over several rotations, making clustering them difficult.

The successful solution to the problem of determining the rotation axis orientation of RSO 18340 using the pattern method in the two-week interval discussed above in February–March 2024 was facilitated by the fact that the PAB trajectory during these RSO transits apparently approached the direction of the current rotation axis. This was manifested in a significant change in the amplitude of brightness variations during the considered RSO transits—from 0.5 to 3 magnitudes on average (see Fig. 10). This resulted in an increased diversity of observed pattern types and a significant distribution by latitude in the coordinate system related with the current rotation axis.

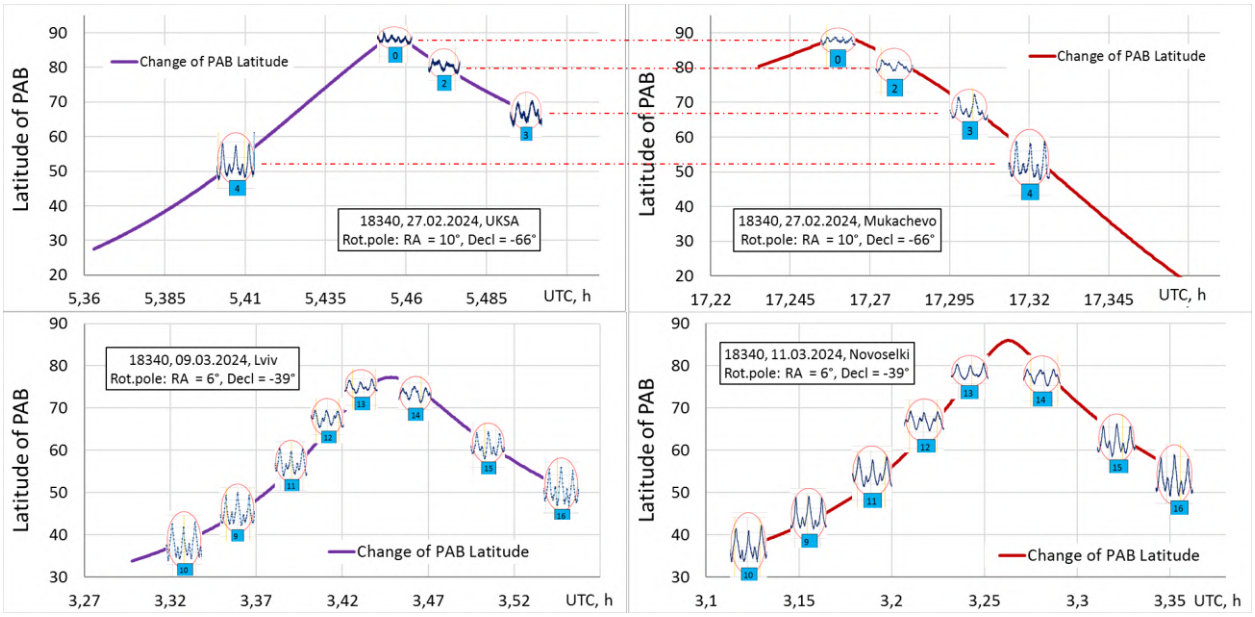

Figure 9: Graphs of the PAB latitude variation during different transits of RSO 18340 for different observing sites. The used by us patterns at the corresponding times and at the latitude calculated for the current rotation axis position are also shown. The top panel shows observations on February 27, 2024, obtained at Herstmonceux and Mukachevo. The bottom panel shows observations obtained on March 9 in Lviv and on March 11, 2024, at Novosilky.

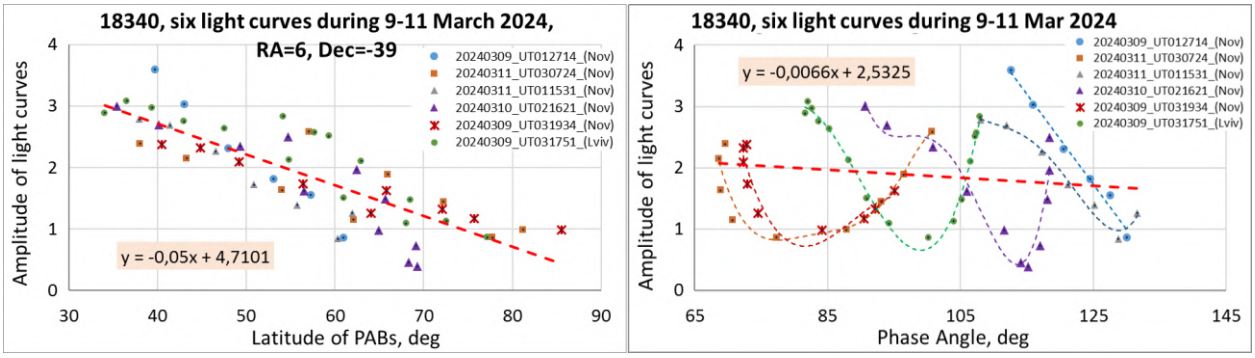

Figure 10: Dependence of the amplitude of the light curves of RSO 18340 on the latitude PAB for the adopted direction of the rotation axis RA = 6°, Decl = -39°, common for six passages in the interval of March 09 – 11, 2024 (left); Dependence of the same amplitude values of the light curves of RSO 18340 on the phase angle (right).

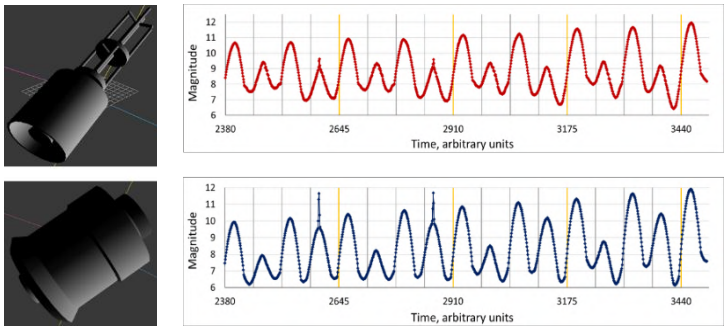

Figure 11: Computer model of RSO 18340 in two variants of its shape (left) and fragments of the corresponding synthetic light curves (right).

Figure 10 (left) shows the local amplitude of brightness variations in six different transits of RSO 18340 during the interval March 9–11, 2024. The X-axis plots the PAB latitude at the corresponding mean times. We see a good correlation between the amplitude and latitude of the PAB for the mean direction of the rotation axis (RA = 6°, Decl. = -39°). This confirms the expected dependence of the amplitude on the PAB latitude for an elongated body. This also indirectly confirms the agreement between the position obtained in our analysis and the actual position of the rotation axis of RSO 18340 during this time interval. The noticeable spread in the amplitude values can be partially explained by the influence of other observing conditions during different RSO transits — the phase angle and the orientation of the light scattering plane (relative to the rotation plane). The right panel of Figure 10 shows the dependence of the same amplitude values on the phase angle. This dependence, while expected, is generally almost an order of magnitude less significant than the amplitude dependence on PAB latitude (slopes of 0.0066 and 0.05 magnitudes per degree of phase angle and per degree of PAB latitude, respectively). Moreover, this graph significantly reveals a different amplitude dependence, distinct from the phase dependence, for each individual transit (highlighted by color and thin dashed lines).

Considering that for man-made space objects, even in the absence of specular flares, the amplitude of brightness variations is quite large (in this case, reaching 3m), and the phase dependence of the amplitude is significantly less significant than its dependence on the PAB latitude, this can in some cases serve as a rough method for finding the current position of the rotation axis in space. This requires several light curves obtained over a short time interval (e.g., over the course of a day and preferably from different observation sites), demonstrating significant amplitude variations. In this case, an attempt can be made to find the minimum scatter of observed local amplitude values for all light curves in each latitude interval of the PAB (in the coordinate system associated with the trial axis) by enumerating trial rotation axis directions. The spatial direction of the trial rotation axis in this case will likely be close to the actual direction.

To test the solution to the inverse problem of determining the satellite's rotation axis orientation based on photometric data, we also plan to use its digital optical-geometric model. The modeling was done in 3ds Max software. Figure 11 on the left shows a computer digital model of RSO 18340 in two variants of its shape (based on data from different sources), and the panel on the right shows the corresponding synthetic light curves. The model rotates around an axis almost perpendicular to its longitudinal axis, and in space, the rotation axis has coordinates: RA = 10°, Decl. = -66°. The calculation of the synthetic light curve was made for the passage of RSO 18340 over the observation point Mukachevo on 02/27/2024 at 17h15m UTC.

Comparison of the synthetic light curves of the RSO 18340 model with numerous observed curves should

provide additional support for a conclusion regarding the rotation pattern of this SL-14 rocket's third stage and the possible cause of its repeated spin accelerations. Furthermore, we propose an international observational campaign to photometry other similar space objects, as a cluster (approximately 20 RSOs) of identical SL-14 rocket stages orbits in very similar orbits.

5. Conclusion

In this paper, we consider the results of long-term photometric monitoring of a large space debris object—the 3rd stage of the SL-14 rocket (RSO 18340). It is shown how the rotation velocity around the center of mass of this object repeatedly changed during 2006–2025. To better understand the reason for this behavior of RSO 18340, the structure of its light curves is considered, and the identified similar photometric patterns are used to determine the direction of the rotation axis of this object in inertial frame. As a result of this analysis of the light curves of RSO 18340, estimates are made of the average direction of the rotation axis during two short (1–3 days) time intervals in late February – early March 2024. Based on two light curves obtained during the flybys of RSO 18340 over Mukachevo and Herstmonceux on February 27, 2024, the following coordinates of the rotation axis in the inertial coordinate system were found: RA = 10°, Decl. = -66°. Based on six light curves obtained on March 9, 10, and 11, 2024, at different observation locations, the average coordinates of the rotation axis were found to be RA = 06°, Decl. = -39°. We estimate the internal error of these results to be ±(5-10)°.

References

Albuja, A.A.; Scheeres, D.J.; McMahon, J.W.: 2015, *Adv. Space Res*., **56**, 237–251.

Benson, C.; Scheeres, D.J.; Ryan, W.H.; Ryan, E.V.; Moskovitz, N.: 2017, in *Proc. of the 18th AMOS Technical Conf*., Maui, HI, USA, 19–22 Sept. 2017.

Hall D., Kervin P.: 2014, in *Proc. of the 14th AMOS Technical Conf.*, Maui, HI, USA, 09–12 Sept. 2014.

Earl, M.A.: 2017, Photometric analysis and attitude estimation of inactive boxwing geosynchronous satellites. Ph.D. Thesis. Canada.

Koshkin N., Shakun L., Korobeynikova E., et al.: 2021, *Atlas of light curves of space objects*, vol. **6** (2019 – 2020). DOI: 10.18524/Atl_v.6(2019-2020).2021

Koshkin, N., Shakun, L., Korobeynikova, E., et al.: 2024a, *Adv. in Space Res.*, **74**, 11, 5725-5744. https://doi.org/10.1016/j.asr.2024.08.038.

Koshkin, N.I., Shakun, L.S., Korobeynikova, E.A., et al.: 2024b, *OAP*. **37**, 73–80. https://doi.org/10.18524/1810-4215.2024.37.315007.

Kozhukhov O., Koshkin N., et al.: 2024, *AMOS Conf. Proc.*, https://amostech.com/TechnicalPapers/2024/Poster/Kozhukhov.pdf

Kudak V., Perig V., Dzhumelya V., Kryoka O.: 2024, *Artificial Satellites*, Vol. **59**, 2, 42–54. https://doi.org/10.2478/arsa-2024-0003

Kumar S., Chiavari L., Cimino L., et al.: 2025, *Acta Astronautica*, **232**, 654-665. https://doi.org/10.1016/j.actaastro.2025.04.018

Ojakangas, G.W.; Hill, N.: 2011, *in Proc. of the 12th AMOS Technical Conf.*, Maui, HI, USA, 13–16 September 2011.

Rachman, A.; Vananti, A.; Schildknecht, T.: 2025, *Aerospace*, **12**, 283. https://doi.org/10.3390/aerospace12040283

Santoni, F.; Cordelli, E.; Piergentili, F.: 2013, *J. Spacecraft and Rocket*, **50**, 701–708. https://doi.org/10.2514/1.A32372

Silha, J.; Pittet, J.N.; Hamara, M.; Schildknecht, T.: 2018, *Adv. Space Res.*, **61**, 844–861.

Vananti, A.; Lu, Y.; Schildknecht, T.: 2023, *Int. J. Astrophys. Space Sci.*, **11**, 15–22.

Zhao, S.; Steindorfer, M.; Kirchner, G.; Zheng, Y.; Koidl, F.; Wang, P.; Shang, W.; Zhang, J.; Li, T.: 2020, *Adv. Space Res.*, **65**, 1518–1527.

https://doi.org/10.18524/1810-4215.2025.38.341473

REFLECTANCE SPECTRA OF DISTINCT SURFACE UNITS IN THE MARCIA CRATER REGION ON VESTA

V. V. Rychahova, I. G. Slyusarev

V. N. Karazin Kharkiv National University,
Kharkiv, Ukraine, *richagova_valeriya@ukr.net*

ABSTRACT. The pre-equatorial Marcia crater on asteroid (4) Vesta represents one of the youngest and best-preserved impact structures on the body, distinguished by its complex morphology and strong spectral variability. Within the Av-8 Marcia quadrangle, two spectrally and morphologically distinct surface units — pitted impact deposits (PIDs) and orange material patches (OMPs) — dominate the region and provide valuable insights into post-impact surface evolution. Using calibrated Framing Camera (FC) images from NASA's Dawn mission obtained during HAMO and LAMO phases, we analyzed the spectral characteristics of these units through color-ratio imaging (*C(438 nm/749 nm)* and *C(749 nm/917 nm)*) and reflectance spectra derived from Level 1b datasets. Results show that both PIDs and OMPs display higher albedo, redder spectral slopes, and deeper 0.9 μm pyroxene bands relative to surrounding materials, yet their spectral signatures differ markedly. PIDs generally exhibit deeper 0.9 μm absorption bands and broader reflectance variability, while OMPs display consistently redder slopes and lower reflectance at 438 nm. Spatially, OMPs and PIDs frequently co-occur in the southwestern vicinity of Marcia crater, where lobate, flow-like morphologies also appear. Our findings confirm that simultaneous examination of *C(438 nm/749 nm) and C(749 nm/917 nm)* color-ratio maps is an effective approach to discriminate between OMPs and PIDs.

Keywords: asteroid (4) Vesta, reflectance spectra, color-ratio imagery, pitted impact deposits (PIDs), orange material patches (OMPs), flow-like features.

АНОТАЦІЯ. Кратер Марсія розташований у приекваторіальній частині астероїду (4) Веста та є однією з наймолодших і найкраще збережених ударних структур з виразною складною морфологією та значними спектральними варіаціями. У межах квадранту Av-8 Marcia переважають два морфологічно та спектрально відмінні типи поверхневих утворень — поклади ямчастих ударних структур (PIDs) та ділянки «помаранчевої» речовини (OMPs), які надають цінну інформацію про еволюцію поверхні після удару. Використовуючи відкалібровані зображення бортової камери Framing Camera (FC) місії NASA *Dawn*, отримані під час орбітальних фаз HAMO та LAMO, було проаналізовано за допомогою методу колориметричних відношень (*C(438 нм/749 нм)* і *C(749 нм/917 нм)*) спектральні характеристики PIDs та OMPs. На основі відкаліброваних зображень Level 1b побудовано та проаналізовано спектри відбивної здатності відповідних поверхневих утворень.

Результати показують, що як PIDs, так і OMPs характеризуються вищим альбедо, червонішим спектральним нахилом та глибшою смугою поглинання піроксену на 0,9 мкм порівняно з навколишнім матеріалом, проте їх спектральні ознаки суттєво відрізняються порівняно одне з одним. PIDs, як правило, мають глибші смуги поглинання поблизу 0,9 мкм і більшу варіативність відбивної здатності, тоді як OMPs демонструють стабільно червоніший нахил спектра та нижчі значення відбиття на довжині хвилі 438 нм. Просторово обидва типи утворень часто спостерігаються разом у південно-західних околицях кратера Марсія, де також розташовані потокові структури.

Наші результати підтверджують, що одночасний аналіз карт колориметричних відношень *C(438 нм/749 нм)* і *C(749 нм/917 нм)* є ефективним методом для розрізнення OMPs та PIDs.

Ключові слова: астероїд (4) Веста, спектри відбивної здатності, метод колориметричних відношень, pitted impact deposits (PIDs), orange material patches (OMPs), потокові структури.

1. Introduction

Marcia crater located in equatorial part of asteroid (4) Vesta within Av-8 Marcia quadrangle and appears to be the youngest well-preserved crater on Vesta (Michalik et al., 2021). Crater's age is estimated by Williams et al. (2014) as 40 Ma (lunar-derived chronology model applied to the smooth part of elevated bench within southern crater floor) or 60 (asteroid flux-based chronology, smooth floor units) while ejecta blanket around Marcia is associated with older surface (120–150 Ma and 200–390 Ma as for lunar and asteroid flux-based chronologies, respectively). While majority of vestan craters is characterized by simple conical cavity, Marcia stands out by its complex morphology which manifests in presence of gully- and flow-like features, central peak, terraced rim and asymmetric shape of crater, being 58 km wide and 68 km long (Michalik et al., 2021). Along with morphological features, Marcia demonstrates non-uniform spectral (large variations of pyroxene band depths and reflectance) and thermal properties. Within the Av-8 quadrangle and Marcia Crater, two distinct surface units are of particular interest: pitted impact deposits (PIDs), notable for their characteristic morphology, and orange material patches (OMPs),

distinguished by their spectral properties. These units represent the primary focus of this study.

Pitted impact deposits (PIDs), previously known as *pitted terrains*, are (i) circular-shaped surface units with distinct pitted morphology and spectral behaviour as a rule demonstrating (ii) higher reflectance and (iii) deeper 0.9 μm pyroxene band depth comparing to their immediate surroundings. This feature was found on a number of planetary bodies (Mars, Vesta, Ceres Callisto, Europa, Mercury, Triton, Pluto) and related to the volatiles outgassing process (Michalik et al., 2021; Sizemore et al., 2017). The majority of PIDs population on Vesta (~96%) is located within Marcia crater and its vicinity, appearing as deposits within old altered craters' floors and/or depressions (Michalik et al., 2021). Within studied region PIDs are not homogenous in terms of spectral behavior and Michalik et al. (2021) outline two main types of PIDs based on differences in reflectance and mean *C(749nm/917nm)* color ratio values, having Type 1 as units with higher reflectance and deeper 0.9 μm band depths and Type 2 units exhibiting similar to background material values, although still preserving typical pitted morphology. Both types occur within and outside Marcia itself and belonging of each specific PID to one of two types is dependent on the hosting deposit's spectral properties (Michalik et al., 2021; Michalik et al., 2022). The additional feature of all PIDs is their redder slope comparing to immediate surrounding which makes these units distinct on the C(438nm/917nm) color ratio distribution maps.

Orange material patches were previously known as light mantle, orange material lobate patches or 'pumpkin patches' as one of three types of orange material deposits (along with diffuse dark mantle ejecta and ejecta rays from young fresh-looking craters). Orange material takes its name after its orange-to-red tones on the global false-colour mosaics in Clementine colours (R=*C(750nm/450nm)*, G= *C(750nm/920nm)*, B= *C(450nm/750nm)*) (LeCorre et al., 2013; Garry et al., 2014) and was interpreted as an impact melt with possible cumulative eucrite component (LeCorre et al., 2013). In this study we suggest to name such deposits as orange material patches (OMPs) regarding their irregular shapes and redder spectral slope. OMP is a widespread surface unit which covers almost whole asteroid's equatorial belt excluding relatively narrow range of longitudes (from 30°E to 90°E with several rare occurrences of separate OMPs). Shapes and sizes of OMPs strongly vary with their location along Vesta's surface – from single spots with diameter of around 0.7 km to 60-km long assemblage of patches, having roundish to fully irregular outlines. As mentioned above, the spectral behavior of OMPs is generally characterized by a redder spectral slope — presumably due to an absorption feature near 438 nm (Rychahova et al., 2024) — as well as by higher overall reflectance and, typically, deeper 0.9 μm pyroxene absorption bands compared to the surrounding material. Nevertheless, global population of OMPs appears to be quite non-homogeneous demonstrating a high level of diversity of edge sharpness, sizes, and variations of absorption at 438 nm within a single spot (Rychahova et al., 2024).

OMPs and PIDs have a number of common features (higher albedo, steeper slope of spectra, deeper 0.9 μm pyroxene band) while still demonstrating differences in morphology, size distribution and diversity of shapes. Their close location within Av-8 quadrangle makes this region an interception of two distinct surface units gives an opportunity to compare spectral characteristics of OMPs and PIDs in case of close disposition and identical surroundings. Additionally, vicinity of Marcia demonstrates presence of lobate and flow-like features related to the impact melt originated during Marcia (and possibly Calpurnia) formation (Williams et al., 2014). These flows occasionally demonstrate various pitted morphology and appear to be of high interest along with OMPs and PIDs population. In this study, we focus primarily on comparing the spectral properties of OMPs and PIDs, including several samples associated with a flow-like feature near the southern rim of Marcia crater.

2. Methods and data

We used Level 1b calibrated images obtained by NASA Dawn's spacecraft on-board imager Framing Camera (FC) during HAMO and LAMO orbital mapping phases (spatial resolution 62 m/pxl and 20 m/pxl, respectively). The Framing Camera (FC) instrument was equipped with one clear filter (F1) and seven narrow bandpass filters (F2–F8), covering the visible to near-infrared wavelength range (from 438 nm for F8 to 965 nm for F2) and make it possible to apply color-ratio imagery technique in order to analyze spectral characteristics of selected surface units.

The data used in this study are available in free access as a part of Planetary Data System archive (*https://sbn.psi.edu/pds/sbib/*). All coordinates provided in Claudia coordinate system, which is the main preferable coordinate system.

Color-ratio imagery was initially invented as an approach to examine and analyze spectral behavior of selected areas on lunar surface and required at least two to pixel-by-pixel coaligned images obtained at close phase angle values and different wavelengths λ_1 and λ_2 (Kaydash et al., 2010**)**. After spectral calibration and alignment procedure were preformed, images can be divided by each giving the output which represents a map of color ratio C(λ_1/ λ_2) distribution along the studied area. Obtained color-ratio distribution map gives an opportunity to identify spectrally distinct surface units such as young craters ejecta halo, taluses, indications of impact melt presence, etc. Simultaneous analysis of color-ratio distribution maps corresponding to different spectral characteristics (slope of spectra, band depth, spectral bend at specific wavelength, etc.) and reflectance images allows accurate classification of distinct spectral units and contributes to the interpretation of their formation processes. In this study we built color ratios *C(438nm/749nm)* and *C(749nm/917nm)* distribution maps of selected regions within Marcia crater and its vicinity. The color ratio *C(438nm/749 nm)* is used to discriminate areas with differing spectral slopes. Regions exhibiting lower ratio values (appearing as darker tones on the map) represent one of our key indicators used to identify OMP units. In contrast, the color ratio *C(749nm/917 nm)* is sensitive to the depth of the 0.9 μm pyroxene absorption band, and higher ratio values correspond to areas characterized by a deeper band.

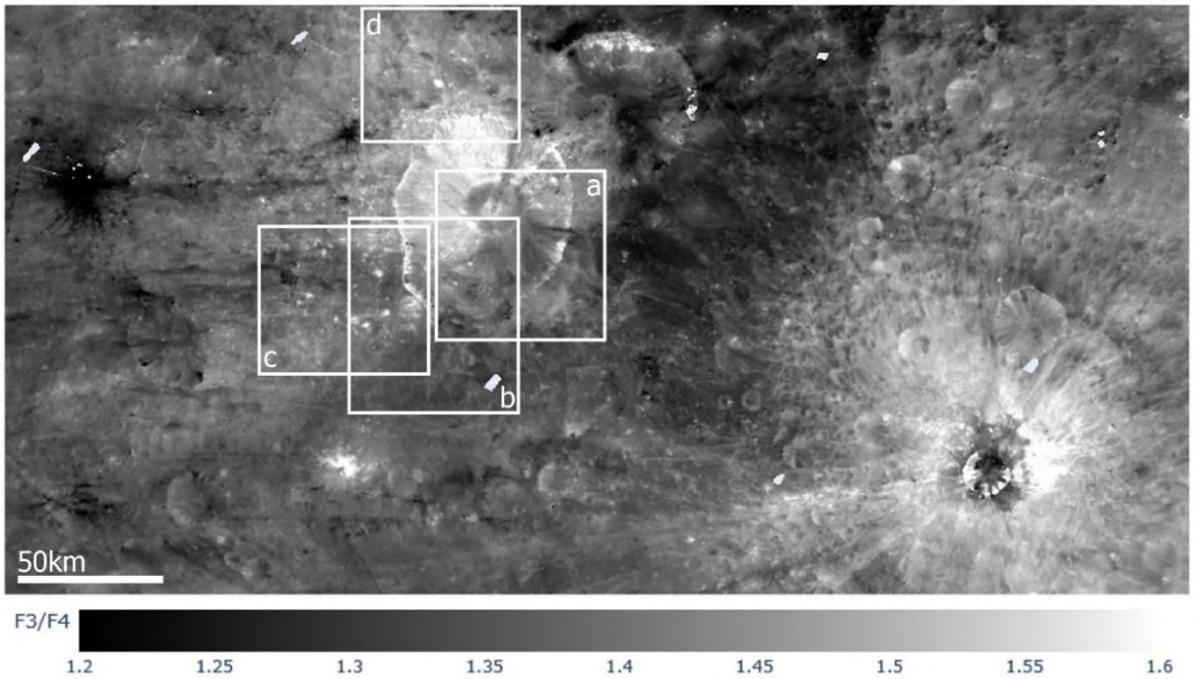

Figure 1: Color ratio C(438nm/749nm) distribution map of Marcia crater region. White boxes a—d define specific areas which were selected for detailed analysis.

3. Results

We selected 4 images series (regions a–d, Fig.1) within Marcia crater vicinity and crater's floor in order to build color ratio distribution maps *C(438nm/749nm)*, *C(749nm/917nm)* and normalized reflectance spectra for 15 PIDs (6 outside Marcia and 9 within crater's floor) and 10 OMPs.

3.1. Spatial distribution

As OMPs and PIDs are distributed unequally along the region, we focused our attention on the areas which contain mostly both PIDs and OMPs simultaneously. The highest concentration of co-occurring units is observed in the region between the southwestern rim of Marcia crater and Eumachia crater (Fig.1c). Seven of ten studied OMPs and four PIDs placed within the region, including cases of OMPs and PIDs close occurrences (Table 1, b and d). Region b (SW rim of Marcia crater and southern crater's vicinity) partially includes samples from the region c as well as PIDs within Marcia's terrace and flow-like features near the crater rim. Region d is not abundant with prominent occurrences of both units and counts just one remarkable PID and 3 relatively small OMPs. We do not observe OMPs within Marcia's terrace and floor which are covered by region a.
We do not include the full list of all units present within the region, but focus on the most prominent example which is available for morphologic and spectral analyses as representatives of each group. Along with typical PIDs there's a number of cases of pitted surface within flow-like lobate features within the southern and eastern vicinity of Marcia rim. Those PIDs vary in terms of shapes and sizes (from irregular roundish clusters of pits to elongated wide stripes that align with the lobate feature), as well as in spectral characteristics. Due to the ambiguity in defining the boundaries of individual PIDs and the limitations in obtaining reliable spectra for some of them, these cases were excluded from our analysis.

3.2. Sizes and shapes

Within our sample, the large part of units of both types exhibits roundish shapes with mean diameter around 2–3 km, while irregular-shaped deposits also occur within OMPs type more frequently. Presence of such complex shapes of OMPs clusters (e.g., OMP assemblages which bear OMP4-6) makes it more difficult to establish accurate upper bound for size. While in general OMPs' upper bound is much larger (up to 60 km), within Marcia crater region the maximal size of OMPs assemblage is around 5–6 km comparing to the largest PIDs cluster with size of 11.36 km (PID12). The mean value is slightly greater for PIDs due to presence of large cluster within crater floor (PIDs: 3.06 km; OMPs: 2.88 km). Minimum values are similar for both unit types – 0.68 km and 0.78 km (OMPs and PIDs, respectively).

3.3. Spectral behavior

For all selected PID and OMP samples, reflectance and normalized reflectance spectra were produced. The general spectral characteristics, including variations in spectral slope and the 0.9 μm pyroxene band depth, are summarized in Fig.2. Two reference spectra were selected to facilitate quantitative comparison between the spectra of distinct surface units: (a) background material sample within Marcia region which does not differ from the majority of surface by reflectance or values of *C(438nm/749nm)* and *C(749nm/917nm)*;

Table 1: Comparison of morphological settings and color ratio distribution maps

	Morphological settings	C(438nm/749nm)	C(749nm/917nm)
a	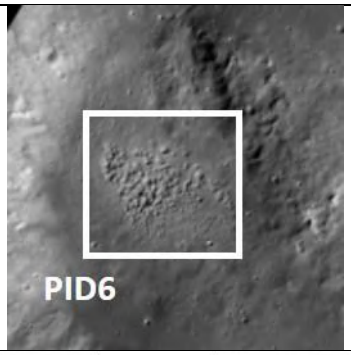	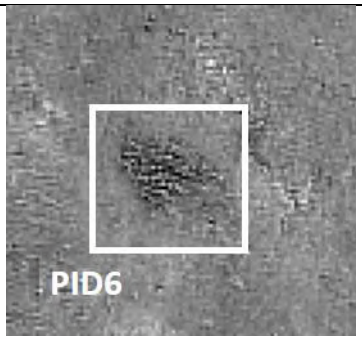	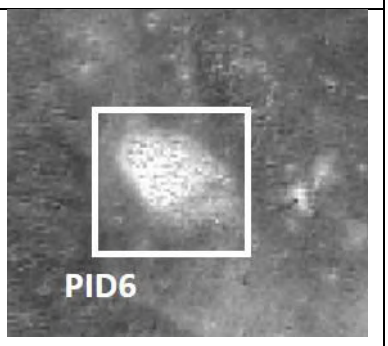
b	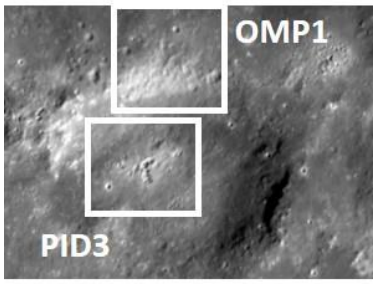	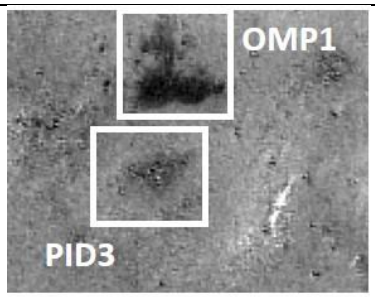	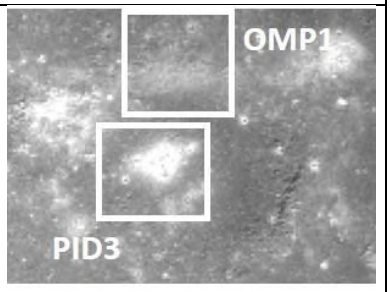
c	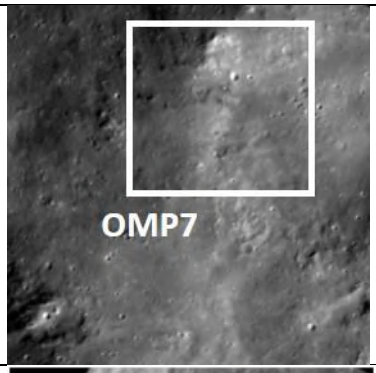	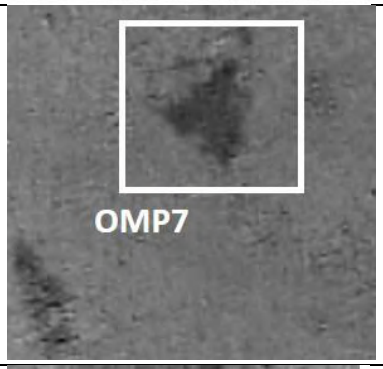	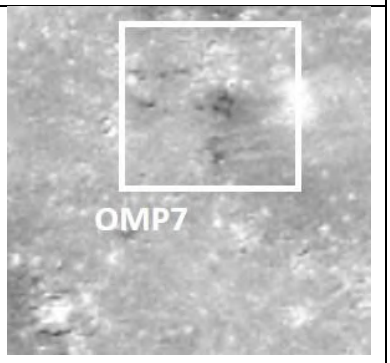
d	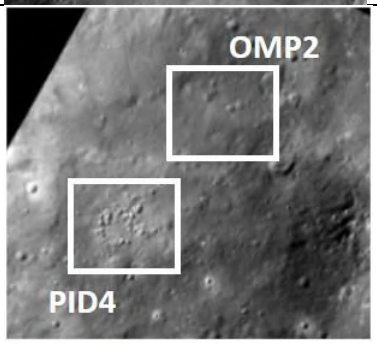	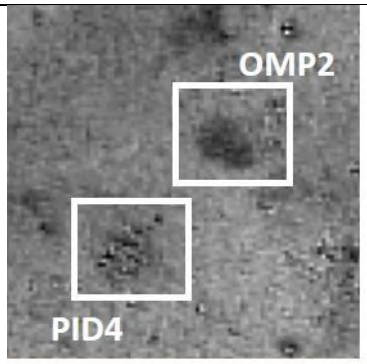	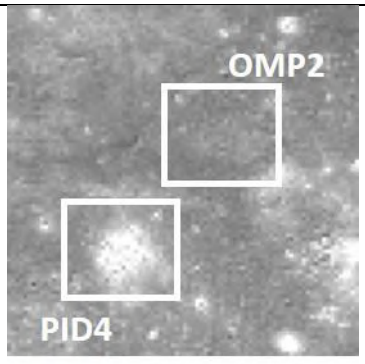
e	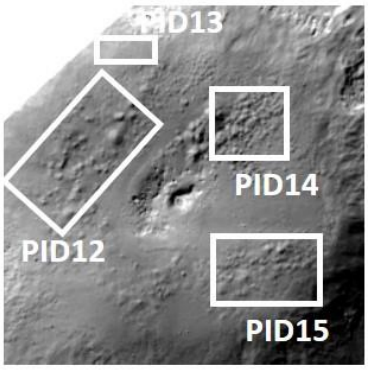	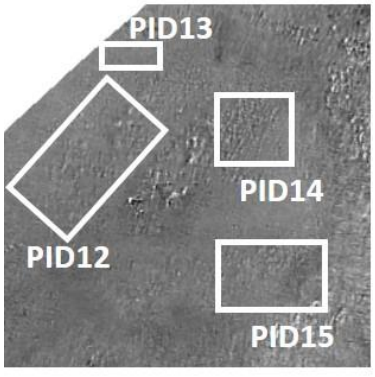	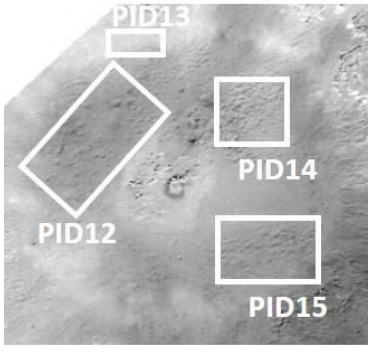

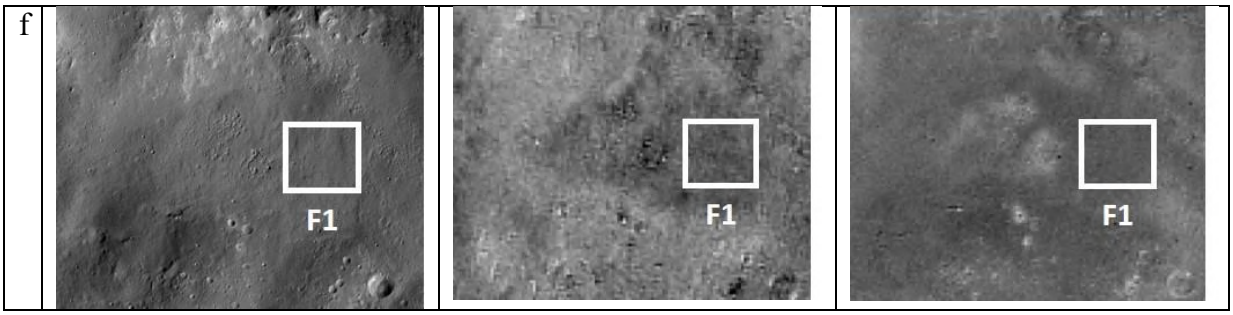

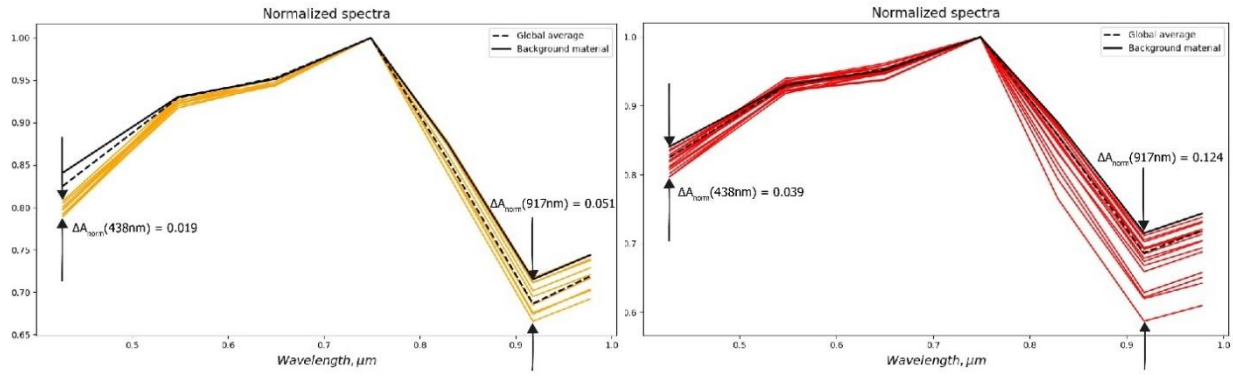

Figure 2: Normalized reflectance spectra for selected units with comparison of values variance at 438 nm and 917nm. Left panel – OMPs. Right panel – PIDs.

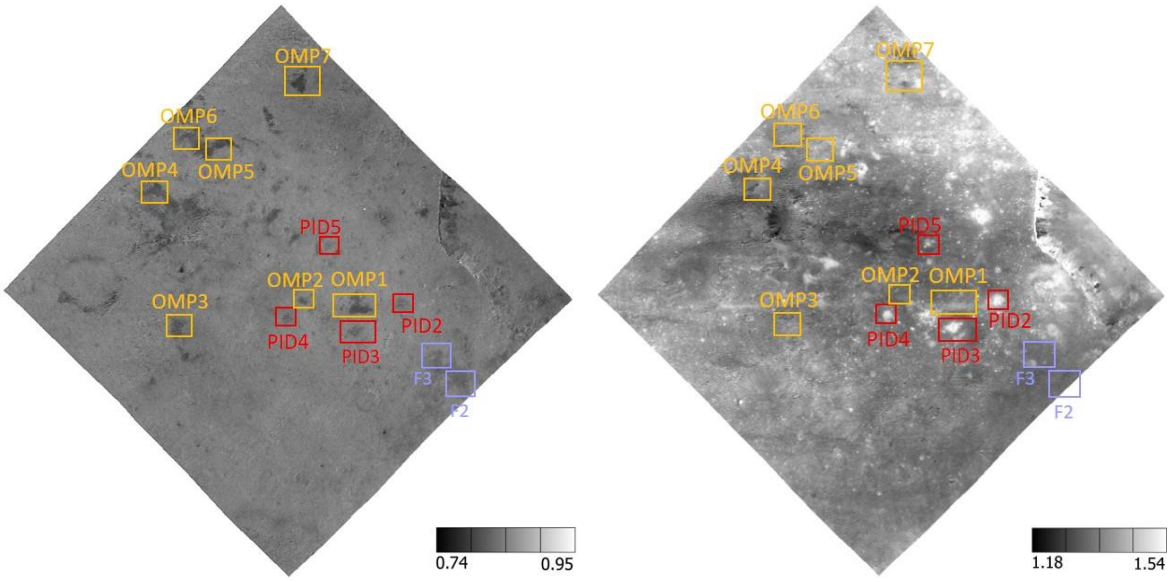

Figure 3: Color-ratio distribution maps of region c (Fig. 1). Left panel – *C(438nm/749nm)*, lower values correspond to redder spectral slopes. Right panel – *C(749nm/917nm)*, lower values correspond not shallower 0.9 μm pyroxene bands.

Table 2: Catalogue of selected surface units (PIDs, OMPs, flow-like features)

Name	Coordinates	Size, km	C(438nm/749nm)	C(749nm/917nm)	A(750 nm)
OMP1	181.24 °E, 2.05 °N	.33	0.81	1.40	0.19
OMP2	179.51 °E, 2.26 °N	1.74	0.82	1.35	0.17
OMP3	175.52 °E, 1.4 °N	3.26	0.82	1.37	0.17
OMP4	174.82 °E, 5.88 °N	3.10 (5.15 long x 4.47 wide)	0.81	1.36	0.17
OMP5	176.87 °E, 7.33 °N	4.62 (6.35 long)	0.81	1.43	0.19
OMP6	176.28 °E, 7.12 °N	3.78 (6.35 long)	0.82	1.41	0.18
OMP7	179.35 °E, 9.28 °N	2.88	0.79	1.43	0.18
OMP8	179.03 °E, 19.41 °N	0.68	0.80	1.55	0.19
OMP9	179.57 °E, 19.14 °N	1.36	0.79	1.56	0.19
OMP10	183.07 °E, 18.12 °N	4.09	0.81	1.49	0.18
PID1	181.24 °E, 2.05 °N	3.01	0.84	1.36	.15
PID2	180.0 °E, 2.21 °N	1.56	0.85	1.5	0.17
PID3	181.19 °E, 1.24 °N	1.45	0.84	1.52	0.20
PID4	178.98 °E, 1.73 °N	1.00	0.84	1.51	0.19
PID5	180.32 °E, 4.04 °N	0.78	0.85	1.44	0.18
PID6	186.31 °E, 18.66 °N	3.23	0.81	1.68	0.20
PID7	189.06 °E, 1.78 °N	2.23	0.81		0.16
PID8	187.55 °E, 1.56 °N	3.45	0.79	1.33	0.15
PID9	187.12 °E, 2.32 °N	1.23	0.81	1.30	0.15
PID10	186.52 °E, 2.43 °N	1.67	0.83	1.34	0.17
PID11	186.09 °E, 3.07 °N	1.23	0.83	1.37	0.17
PID12	190.84 °E, 10.57 °N	11.36	0.84	1.32	0.17
P I	189.22 °E, 11.43 °N	3.23 (the whole circle – 59.13)	0.84	1.49	0.20
P I	191.7 °E, 10.57 °N	4.90	0.84	1.37	0.18
PID15	191.49 °E, 8.74 °N	5.79	0.84	1.32	0.17
F1	186.52 °E, 0.16 °N	4.16	0.84	1.28	0.16
F2	184.37 °E, 0.0 °S	2.27	0.84	1.30	0.16
F3	183.83 °E, 0.49 °N	3.40	0.85	1.31	0.17

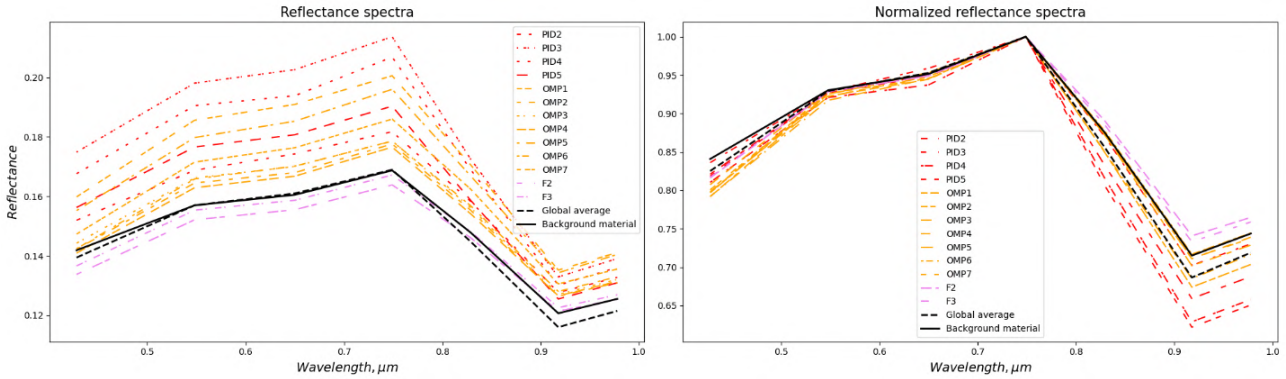

Figure 4: Reflectance (a) and normalized (b) reflectance spectra of units within region c (Fig. 1)

(b) global average spectra of the vestan surface. While PIDs and OMPs demonstrate similar characteristics comparing to background material – lower reflectance at 438 nm (redder spectral slope) and deeper pyroxene band at 0.9 μm, – the spectral behavior of units comparing to each other slightly differs. We can observe tendency to lower reflectance values at 438 nm and shallower band depths for OMPs comparing to PIDs. Additionally, OMPs demonstrate lower degree of variance of above the mentioned characteristics, especially for values of normalized reflectance at 917 nm which is associated with position of pyroxene band center (Fig. 2).

Average global vestan spectra show distinct behavior comparing to typical background material in Marcia region with redder slope between 438 nm and 555 nm and higher values of pyroxene band depth. According to this, OMP units still demonstrate redder slope in comparison to average spectra, while a number of PIDs doesn't follow this rule anymore. In terms of band depths, both unit types include several samples with shallower than average bands, but majority of PIDs still demonstrate higher band depths values.

Distributions of reflectance spectra at maximum wavelength (749 nm) point that PIDs in general tend to have slightly wider range of values than OMPs (Table 2, PIDs: 0.15–0.20; OMPs: 0.17–0.19). Color ratio *C(749nm/917nm)* and *C(438nm/749nm)* distribution maps provides a spatial context of how PIDs and OMPs behave along the region (Fig.3). Lower values (dark tones) on *C(438nm/749nm)* map characterize surface as such with a redder slope (lower reflectance at 438 nm) and the most prominent feature on these maps are OMPs, while PIDs differ from background material but at the much lower degree. The opposite situation is present on the *C(749nm/917nm)* map, where PIDs along with ejecta from small young craters demonstrate the highest values of color ratio and deeper pyroxene band, respectively. These facts confirm our results derived from comparison of normalized reflectance spectra of both unit types.

Additionally, comparison of the normalized reflectance spectra of both unit types with flow-like features indicates that this material exhibits an intermediate spectral slope between PIDs and OMPs, while the depth of the 0.9 μm band is significantly shallower than that of the background material and the global average spectrum of Vesta.

4. Conclusion

As known from previous studies, both OMPs and PIDs exhibit irregular shapes, however distinctive morphology features are only associated with PIDs. We found that PIDs have much smaller characteristic sizes than OMPs on a global scale, although they exhibit larger mean sizes within the studied region, particularly for PIDs on the Marcia crater floor. In terms of spatial distribution, PIDs are associated with a few craters (the Marcia region hosts ~96% of all PIDs on Vesta), while OMPs are widespread with gap on 30°E – 90°E.

Analysis of PIDs and OMPs spectra show that in comparison with typical surrounding material OMP and PID have slightly higher apparent albedo, deeper 0.9 μm pyroxene band and lower values of reflectance at 438 nm, however both surface units show prominent differences in spectral behavior comparing to each other. Namely: (a) OMPs always show lower reflectance at 438 nm in comparison with PIDs; (b) PIDs demonstrate significantly deeper pyroxene band depth in comparison with OMP. Additionally to the previously mentioned differences, we found out that the best way to distinguish OMPs and PIDs is simultaneous analysis of *C(438nm/749nm)* and *C(749nm/917nm)* color ratio distribution maps.

Flow-like features have lower reflectance at 438 nm in comparison with average vestan surface. Areas where flow-like features host PIDs material show deeper pyroxene band comparing to the rest of flow-like features.

References

Garry W.B. et al.: 2014, *Icar*, **244**, 104.
Kaydash V. et al.: 2010, *SoSyR*, **44**, 267.
Le Corre L. et al.: 2013, *Icar*, **226**, 1568.
Michalik T. et al.: 2021, *Icar*, **369**, 114633.
Michalik T. et al.: 2022, *PSJ*, **3,** 182.
Rychahova V. et al.: 2024, EPSC2024-577.
Sizemore H. G. et al.: 2017, *GeoRL*, **44**, 6570.
Williams D. A. et. al: 2014, *Icar*, **244**, 74.
Williams D. A. et. al: 2014, *P&SS*, **103**, 24.

https://doi.org/10.18524/1810-4215.2025.38.343168

ILLUMINATION OF ARTIFICIAL EARTH SATELLITES IN CIRCULAR ORBITS

A. Strautman[1], O. Bazyey[2]

[1] Department of Physics and Astronomy, FMPIT, Odesa I. I. Mechnikov National University 42 Pastera St, Odesa, Ukraine, *albinstrautman@gmail.com*

[2] Department of Mathematical Analysis, FMPIT, Odesa I. I. Mechnikov National University 2 Zmiienka Vsevoloda St, Odesa, Ukraine, *o.bazyey@onu.edu.ua*

ABSTRACT. The purpose of the work is to build an updated model of the illumination of artificial satellites in circular Earth orbits and to study the duration and nature of solar illumination in orbits with different inclinations and altitudes throughout the year.

The mathematical model uses the equation of the circular cone of the shadow, built taking into account the movement of the Sun relative to the Earth. The center of the cross section of the base of the cone coincides with the center of the Earth. The motion of the satellite is simulated by Kepler's orbit. The computer model makes it possible to determine with a given accuracy the duration of the satellite's stay in the Earth's shadow.

Simulation of the duration of illumination of satellites at two altitudes has been performed: 5,000 km and 35,786 km (geosynchronous orbit altitude) throughout the year. Curves of the duration of the satellites' stay in the shadow are given. The shape of the curves varies from a nearly straight line for inclined orbits 25°, then they become periodic, and then divide into two parts, resembling the shape of a parabola. Among all the possible inclinations of the orbits of satellites, extreme ones have been detected. These are orbits with an angle of inclination 23°26′, which defines a straight orbit. On them, an artificial satellite falls into the Earth's shadow throughout the year at each orbit. The second group of extreme orbits are orbits with inclinations, in which the satellite falls into the shadow only near the time of the equinoxes. Shortest duration of stay of satellites in the shadow moving in orbits with an angle of inclination 113°26′. Falling into the shadow lasts from 15.02 to 23.04 and from 19.08 to 27.10 for an altitude of 5,000 km, and from 12.03 to 28.03 and from 14.09 to 01.10 for an altitude of 35,786 km.

The results of the simulations will allow us to clarify the effect of sunlight and solar wind pressure on the motion of satellites over time. This will allow the use of additional satellite accelerations resulting from radiative impact to change the orbits of space debris and clean up near-Earth space.

Key words: Earth orbit, artificial satellite, shadow cone, duration of stay in the shadow.

АНОТАЦІЯ. Метою роботи є побудова уточненої моделі освітленості штучних супутників на колових навколоземних орбітах та дослідження тривалості та характеру сонячного освітлення на орбітах з різними нахиленнями та висотами протягом року.

У математичній моделі використане рівнянні колового конуса тіні, побудованого з урахуванням руху Сонця відносно Землі. Центр перерізу основи конуса збігається з центром Землі. Вплив атмосфери не враховується. Рух супутника моделюється Кеплеровою орбітою. Комп'ютерна модель дає змогу визначити з заданою точністю тривалість перебування супутника у тіні Землі.

Виконано моделювання тривалості освітленості супутників на двох висотах: 5 000 км та 35 786 км (висота геосинхронної орбіти) протягом року. Наведені криві тривалості перебування супутників у тіні. Форма кривих змінюється від практично прямої лінії для орбіт з нахиленням 25°, далі набувають періодичного характеру, а потім діляться на дві частини, що нагадують форму параболи. Серед усіх можливих нахилень орбіт супутників виявлені екстремальні. Це орбіти з кутом нахилення 23°26′, що визначає пряму орбіту. На них штучний супутник протягом усього року на кожному витку потрапляє у тінь Землі. Друга група екстремальних орбіт – це орбіти з нахилами, при яких супутник потрапляє у тінь лише поблизу часу рівнодень. Найменша тривалість перебування супутників у тіні, які рухаються по орбітах з кутом нахилу 113°26′. Потрапляння у тінь триває від 15.02 до 23.04 та від 19.08 до 27.10 для висоти 5000 км, та від 12.03 до 28.03 та від 14.09 до 01.10 для висоти 35786 км.

Результати моделювання дозволять уточнити вплив тиску сонячного світла та сонячного вітра на рух супутників протягом тривалого часу. Це дозволить використати додаткові прискорення

супутників, що виникають внаслідок радіативного впливу, для змін орбіт космічного сміття та очищення навколоземного простору.

Ключові слова: навколоземна орбіта, штучний супутник, конус тіні, тривалість перебування у тіні.

1. Introduction

Since the first launch of an artificial satellite in 1957, the number of spacecraft and the degree of contamination of near-Earth space has been constantly increasing. Space debris, consisting of broken satellites, spent rocket stages and debris from collisions, poses a serious threat to working vehicles in orbit. The main characteristic of this phenomenon is the concentration of space debris, which depends on altitude, type of orbit and time. Two approaches are used to predict the evolution of garbage - deterministic (modeling the orbits of individual objects) and stochastic (modeling the distribution of garbage concentration). However, both methods demonstrate a steady increase in the amount of debris, which over time can lead to a cascading effect - an avalanche-like increase in debris. The solution of this problem is possible through the development of new models of the motion and interaction of objects in near-Earth space, including taking into account radiation effects (sunlight pressure, solar wind, albedo, etc.), which can be used to change the orbits of "passive" objects. The purpose of the study is to build an updated model of the illumination of near-Earth satellites, determine the duration of stay in the Earth's shadow, as well as analyze the dependence of the duration of stay in the Earth's shadow on the inclination of the circular orbit at different altitudes throughout the year.

2. Mathematical model and software implementation

The Sun, illuminating the Earth, forms a cone of shadow in the opposite direction. For an observer at a satellite-centric point, the Sun is completely covered by the Earth's dark disk. To model the shadow, we use a simplified approximation of a circular cone, whose equation

$$\frac{x^2}{a^2} + \frac{y^2}{b^2} - \frac{z^2}{c^2} = 0$$

(Selezniova et al., 2016), and we describe the movement of the satellite in Kepler's orbit. The Earth is taken for a sphere without an atmosphere: polar compression and refraction of light in the atmosphere are not taken into account. The model uses the equation of the shadow cone, built taking into account the movement of the Sun relative to the Earth. The center of section of the base of the cone coincides with the center of the Earth.

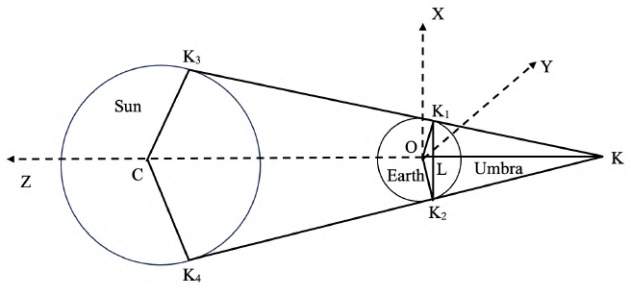

Figure 1: Shadow cone model.

As a result of the Earth's annual motion, the axis of the shadow cone, which is marked as the Z axis in Figure 1, also rotates. The center of the Sun remains on the Z axis, so the shadow cone equation

$$x^2 + y^2 = \frac{(z+217)^2}{47088},$$

where the unit of measurement of distances is the average radius of the Earth. Let's prove that the equation of the cone looks like this using Figure 1. The Sun is at a point with coordinates C(0, 0, 1 a.u.) Radius of the Sun $R_s \approx 109$ r. e. (1 a.u. $\approx$ 23 481 r. e. (r. e. – Radius of the Earth)). The Earth is at a point with coordinates O(0, 0, 0). Radius of the Earth R_e = 1 r. e. CO $\approx$ 23 481 r. e.; $OK_1 = OK_2 = 1$ r. e.; $CK_3 = CK_4 \approx 109$ r. e.; C(0, 0, 1 a.u.); O(0, 0, 0); KK_1K_2 – shadow cone; Let us recall the form of the cone equation for our case, given that the vertex of the cone is not at the center of the coordinate system at the point K(x_B, y_B, z_B):

$$\frac{(x-x_B)^2}{a^2} + \frac{(y-y_B)^2}{b^2} - \frac{(z-z_B)^2}{c^2} = 0$$

the equation of the shadow cone (we will find a, b, c, K(x_B, y_B, z_B).

Consider $\triangle KOK_1$ and $\triangle KCK_3$: OK_1 and CK_3 – these are the radii, $OK_1 \perp KK_3$ and $CK_3 \perp KK_3$ (with proper tangents and radii), $OK_1 \parallel CK_3$, $\triangle KOK_1 \sim \triangle KCK_3$ (according to the lemma about similar triangles),

$$\frac{CK_3}{OK_1} = \frac{CK}{KO} = \frac{109}{1},$$

[$\frac{KO+CO}{KO}$ = 109, 109 KO = KO + 23481, KO $\approx$ 217 r. e.; K(0; 0; -217); $cos < KOK_1 = \frac{OK_1}{KO} = \frac{1}{217} = \frac{OL}{OK_1}$, [$OL = \frac{1}{217} r.e.$, KL = KO - OL = 217 - $\frac{1}{217} = \frac{47088}{217} = c$, $sin < KOK_1 = \frac{LK_1}{OK_1} = LK_1$ (as $OK_1 = 1$ r.e.); $sin < KOK_1 = \sqrt{1 - cos < KOK_1^2} = \sqrt{1 - \frac{1}{217^2}} = \sqrt{\frac{47088}{47089}} = a = b$ (as the Earth is a ball); Shadow Cone Equation:

$$\frac{47089x^2}{47088} + \frac{47089y^2}{47088} - \frac{47089(z+217)^2}{47088^2} = 0,$$

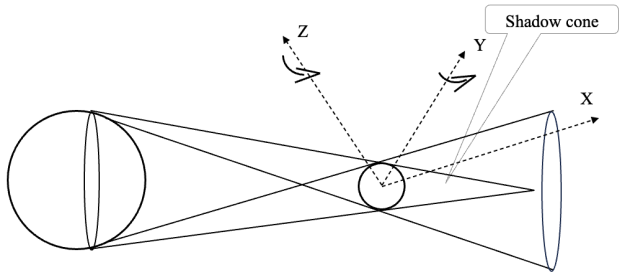

Figure 2: Rotation of axes to account for the movement of the Sun.

$$x^2 + y^2 = \frac{(z+217)^2}{47088}.$$

Since the Sun revolves around the Earth, you need to reduce the equation of the cone to the form that we gave above. To bring the shadow cone equation to the form we gave above, we, as shown in Figure 2, rotate the coordinate system around the Z axis and the Y axis counterclockwise so that the axes of the coordinate system are arranged in the same way as in Figure 1, so that the cone equation is the same as we gave above.

According to the specified Keplerian elements of the orbit, the coordinates of the satellite are calculated over the entire period of rotation with a given step. The resulting coordinates are compared with the equation of the shadow cone, which makes it possible to determine the illumination of the satellite: in the shadow or illuminated by the Sun. The developed software allows you to determine the duration of the satellite's stay in the shadow on one orbit with a given accuracy throughout the year. The distance from the Sun to Earth is modeled by Keplerian elements of the orbit of the mean Sun. We used the following values of the elements of the Sun's orbit:
e = 0,0167133
a = 1,00000261 a.u.
ω = 102,93768193°
Ω = 0
i = -0,00001531°
(https://ssd.jpl.nasa.gov/planets/approx_pos.html)

3. Conditions and results of modeling

The study was carried out for two values of the altitudes of circular orbits: 5000 km and 35786 km, the inclinations of which to the plane of the Earth's equator vary from 0 to 180° in increments of 5°, the longitude of the ascending node and the average anomaly are zero. The study was also carried out for the INTELSAT 10 (IS-10) satellite with the following orbital elements:
e = 0,0002520
a = 35786 km
ω = 186,593°
Ω = 253,512°
i = 0,018°
(https://celestrak.org/NORAD/elements/geo.txt)

We got the dependence of the duration of the satellite's stay in the shadow on the calendar date. Figures 3 and 5 show the duration of stay in the shadow of satellites with an inclination of the orbital planes from 20 to 120°, that is, these are mainly orbits with direct motion. Figures 4 and 6 show the duration of stay in the shadow of satellites with an inclination of the orbital planes from 120 to 20°, that is, these are mainly orbits with reverse motion. Figure 7 shows the duration of stay in the shadow on one branch each day for the INTELSAT 10 (IS-10) satellite. The inclination of the satellite's orbit is measured from the equatorial plane in increments of 5°, and the inclination of the Earth's (Sun's) orbit is not a multiple of this value. Because of this, we obtained asymmetric pairs of graphs in Figures 3 and 5, and 4 and 6. If the pitch of inclination of the satellite's orbits is chosen as a multiple of 23.44°, you can get completely similar pairs of graphs in the above figures.

The shape of the curves varies from an almost straight line for orbits with an inclination of 25°, become periodic, and then divide into two parts, resembling the shape of a parabola. Tilts of 0 and 180° obviously give the same curves, since both orbits lie in the plane of the Earth's equator. The difference between them lies solely in the direction of movement of the satellite.

In general, the graphs show the dependence of the duration of the stay of an artificial satellite in the shadow on one orbit on the calendar date at different altitudes above the Earth's surface and different inclinations of the orbital planes. The graphs are plotted in 5° pitch increments. The figures do not indicate slopes for curves that overlap each other. They are in the intervals: in Figure 3 – from 70° to 120°, in Figure 4 – from 120° to 160°, in Figure 5 – from 40° to 120°, in Figure 6 – from 120° to 80°.

The resulting shape of the graphs is determined by the inclination of the plane of the ecliptic to the plane of the celestial equator. Throughout the year, the declination of the Sun changes from +23°26′ to -23°26′ (Karttunen et al., 2007). On the days of the equinoxes, the declination of the Sun is 0, respectively, the axis of the cone of the shadow is parallel to the plane of the celestial equator, so the satellite stays in shadow at this time for the longest time. On the days of the solstices, the axis of the cone of the shadow is inclined at the greatest angle 23°26′, the artificial satellite for most orbital inclinations does not fall into the shadow at all. At this time, the duration of stay in the shade is the shortest.

For the INTELSAT 10 (IS-10) satellite, the same dependence of being in the shadow by analogy is

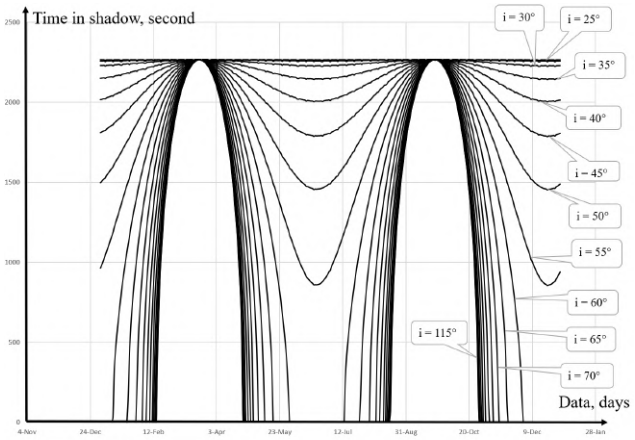

Figure 3: Time in the shadows, height above the Earth surface 5000 km, inclination 20-120°.

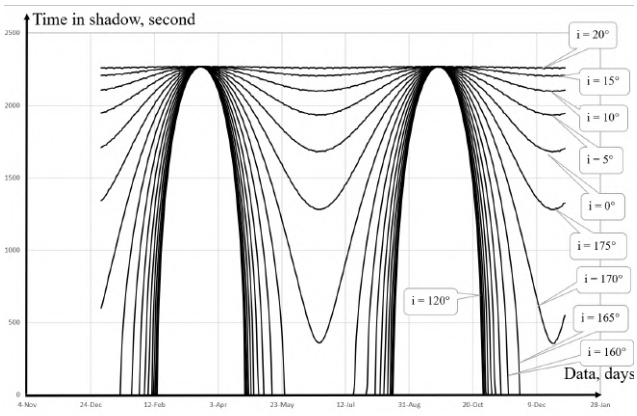

Figure 4: Time in the shadows, height above the Earth surface 5000 km, inclination 120-20°.

obtained as for satellites for geostationary orbit with zero inclination of the orbit relative to the Earth's equator, but the difference is only one thing: the maximum stay in the shadow for this satellite is greater (about 4,000 seconds).

4. Conclusion

In Figures 3 and 5, almost straight lines show that satellites in orbits with an inclination of 25° are in the Earth's shadow throughout the year for 2300 seconds at each revolution. This is because the planes of their orbits are very close to the plane of the ecliptic. As the inclination increases, the duration of stay in the shadow decreases as the date approaches the moments of the solstices. Starting from an inclination of 60° to an inclination of 165°, dates appear when the satellites are illuminated continuously. The longest duration of this period is in satellites moving in orbits with inclinations

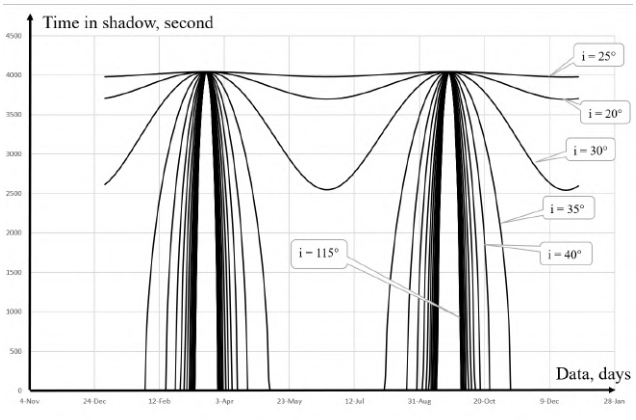

Figure 5: Time in the shadows, height above the Earth surface 35786 km, inclination 20-120°.

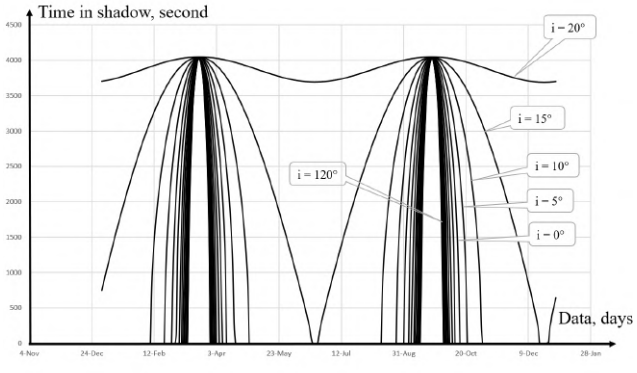

Figure 6: Time in the shadows, height above the Earth surface 35786 km, inclination 120-20°.

of 115-120°. Such orbits are almost perpendicular to the plane of the ecliptic. Thus, among all the possible inclinations of satellite orbits, there are extreme ones. This is the angle 23°26′, which defines the direct orbit in which an artificial satellite falls into the Earth's shadow throughout the year at each orbit. The second group of extreme orbits are orbits with inclinations, in which the satellite falls into the shadow only near the time of the equinoxes. The shortest duration of stay in the shadow is for satellites moving in orbits with an angle of inclination of 113°26′. Falling into the shadow lasts from 15.02 to 23.04 and from 19.08 to 27.10 for an altitude of 5000 km, and from 12.03 to 28.03 and from 14.09 to 01.10 for an altitude of 35786 km.

A practical example with the INTELSAT 10 (IS-10) satellite proves that our calculations of common cases that we have considered are correct and our example is one of our common cases.

The developed illumination model can be used for further studies of the effect of radiation effects on the orbital motion of objects. In particular, it is proposed to use the discontinuity of solar pressure (due to being

in the shadow) to control the movement of space debris.

If satellites or debris have variable reflectivity (albedo) or the ability to orient relative to the Sun, this opens up the prospect of changing orbits without additional fuel consumption – that is, cleaning up near-Earth space by natural forces.

References

CelesTrak: [online] Available at: https://celestrak.org/NORAD/elements/geo.txt [Accessed 5 Nov 2025].

Nasa.gov: [online] Available at: https://ssd.jpl.nasa.gov/planets/approx_pos.html [Accessed 5 Nov 2025].

Karttunen H., Kr*ö*ger P., Oja H., Poutanen M., Donner K. J. (eds.): 2007, Fundamental Astronomy, 5th ed., Springer, Berlin Heidelberg New York.

Selezniova N. P., Rudyk T. O., Lystopadova V. V., Sulima O. V.: 2016, Vyshcha Matematika. Rozdil "Teoriia poverkhon druhoho poriadku", Methodical guidelines, NTUU “KPI”, Kyiv.

RADIO ASTRONOMY

https://doi.org/10.18524/1810-4215.2025.38.340396

RESTORATION AND DEVELOPMENT OF THE GURT RADIO TELESCOPE NETWORK: OPPORTUNITIES FOR OBSERVATIONS UNDER WARTIME CONDITIONS

I. M. Bubnov[1], R. V. Vaschishyn[2], A. A. Stanislavsky[1], A. A. Konovalenko[1], A. S. Belov[1], V. Yu. Selin[1], A. V. Frantsuzenko[2], L. A. Stanislavskyi[1], M. V. Shevchuk[1], A. M. Reznichenko[1], O. M. Ulyanov[1], S. M. Yerin[1] and V. V. Shevchenko[1]

[1] Institute of Radio Astronomy, National Academy of Sciences of Ukraine, Kharkiv, Ukraine, *bubnov.igor.n@gmail.com*

[2] Poltava Gravimetric Observatory of S. Subbotin Institute of Geophysics of the NASU, Poltava, Ukraine, *vrv.uran2@gmail.com*

ABSTRACT. The restoration of three subarrays of the Ukrainian radio telescope GURT, damaged as a result of military hostilities, marked an important milestone in the continuation of astronomical research under challenging conditions. In 2023, two of them were successfully restored and equipped with autonomous power supplies at the site of S. Braude Radio Astronomical Observatory. This enabled the resumption of systematic solar observations and the implementation of a two-element interferometer for studying cosmic radio sources.

The third subarray was relocated and restored at the site of Poltava Gravimetric Observatory, where the primary challenge for its operation was strong radio-frequency interference (RFI) caused by the uninterruptible power supply system of the observatory. This issue was effectively resolved through the development and installation of a custom external mains filter.

The restoration efforts of these instruments demonstrate that scientific work can continue even under war time adverse conditions, thanks to innovative engineering solutions and the perseverance of the research team.

Keywords: radio astronomy, radio telescope, antenna arrays, space research

АНОТАЦІЯ. Відновлення трьох секцій низькочастотного українського радіотелескопа ГУРТ, пошкоджених унаслідок воєнних дій, стало важливим етапом у продовженні астрономічних досліджень в умовах значних викликів. У 2023 році дві з них були успішно відновлені та оснащені автономними системами енергоживлення на території Радіоастрономічної обсерваторії ім. С. Я. Брауде РІ НАНУ. Це дало змогу відновити систематичні спостереження Сонця, а також реалізувати двохелементний інтерферометр для дослідження космічних радіоджерел.

Третю секцію було перенесено та відновлено на території Полтавської гравіметричної обсерваторії НАНУ. Основною перешкодою для її функціонування стала сильна радіочастотна завада (RFI), спричинена системою безперебійного живлення самої обсерваторії. Цю проблему вдалося ефективно вирішити завдяки розробці та встановленню спеціального зовнішнього мережевого фільтра.

Зусилля, спрямовані на відновлення цих наукових інструментів, демонструють, що наукова діяльність може тривати навіть у складних умовах воєнного часу завдяки інженерним інноваціям та наполегливості дослідницької команди.

Ключові слова: радіоастрономія, низькочастотний радіотелескоп, антенні решітки, космічні дослідження.

1. Introduction

The Giant Ukrainian Radio Telescope (GURT) is a next-generation radio astronomical instrument designed to operate in the 8–80 MHz frequency range (Konovalenko et al., 2016; Tokarsky et al., 2019a; 2019b). Its development began in 2001 at the S.Ya. Braude Radio Astronomical Observatory in Kharkiv's region, Ukraine.

The GURT antenna system is modular and composed of identical 25-element subarrays, ten of which were operational as of early 2022. Each subarray includes five main components: the antenna array, phasing system, amplification system, beam control system and AC-DC power supply units. Signals from each subarray are transferred by and RF cables to a central registration system based on digital receivers ADR (Zakharenko et al., 2016), where they are digitized, processed, and stored on hard drives. These subarrays have been used to form two interferometric baselines of 56 m and 89 m. Since 2018, the implementation of an automatic and remote control system has enabled systematic daily solar monitoring observations.

In addition to solar observations, GURT has been employed to study pulsar radio emission, decametric emissions from Jupiter, Galactic background, and the supernova remnant Cassiopeia A. More than 20 scientific publications have addressed the modeling, design principles, and technical characteristics of various GURT subsystems, while over 10 papers have reported astrophysical results based on its observational data.

Figure 1: Damaged antenna elements of the GURT radio telescope.

Following the Kharkiv counteroffensive conducted by the Armed Forces of Ukraine in September–October 2022, the territory of Kharkiv's region containing the S.Ya. Braude Radio Astronomical Observatory was liberated. Preparations for restoring the observatory's infrastructure and equipment began shortly thereafter. However, the initial phase of the effort was significantly delayed due to the need for thorough de-mining of the site.

After a comprehensive safety inspection, it was decided to begin the restoration process with the GURT radio telescope. Despite the relocation of the frontline to approximately 40 km from the observatory, the risk to both personnel and equipment remained substantial. Nonetheless, the strategic importance of resuming scientific operations motivated the initiation of phased restoration activities under these constrained and potentially hazardous conditions.

Unfortunately, due to military hostilities, the GURT antenna system sustained extensive damage. Over 80% of the antenna elements became non-functional. Blast waves destroyed the arms of many elements, and the majority of low-noise amplifiers were damaged. The force of the explosions caused electronic components to lose contact with printed circuit boards, and RF transformer windings were broken. Shrapnel severely damaged the supporting stands of the antenna elements, as well as equipment cabinets and their internal systems. In some areas, the density of shrapnel was so high that even 16 mm diameter metal-plastic pipes were repeatedly pierced (see Figure 1). In most cases, the electronic equipment damaged by shrapnel was beyond repair.

2. Restoration of GURT Radio Telescope Subarrays at S. Braude Observatory

The restoration of two subarrays of the GURT radio telescope at the S.Ya. Braude Radio Astronomical Observatory in Kharkiv's region marked the first and one of the most crucial steps in resuming the instrument's operation. LiFePO4The recovery process began with key prerequisites: de-mining of the observatory site and establishing an autonomous power supply system, as the centralized electrical grid had been completely destroyed due to hostilities.

To power the equipment of the observatory, a self-sustained power system was designed and implemented, consisting of ten solar panels supplemented by a backup gasoline generator. This hybrid energy solution provided a stable and reliable power supply, essential for operating the restored GURT subarrays and supporting other observatory infrastructure. The solar power plant thus became a vital component in ensuring the continuity of scientific observations under wartime conditions.

Key Parameters of the Autonomous Power System:

Inverter: Altek Atlas 6 kW – 48 V.

Solar Panels: 10 mono-crystalline panels (model UL-550M-144HV), each rated at 500 W, providing a total peak power output of 5 kW.

Battery System: Atlas 48 V B3 LiFePO4Lithium-Fe-Polymer battery with a nominal capacity of 200 A·h and a nominal voltage of 48 V.

Power Consumption: Each GURT subarray of 2 linear polarizations consumes up to 1 kW of power. Linear regulated DC power suppliers provide power for phase shifters, RF high-linear amplifiers, beam control unit in the subarray cabinet. Additional power is consumed by ADR receiver and preamplifier in the receiving equipment room.

This configuration was specifically designed to power two GURT subarrays simultaneously while enabling extended nighttime observations. During daylight hours, the high-efficiency solar panels not only meet the system's real-time energy requirements but also charge the high-capacity battery. Consequently, the system ensures uninterrupted radio astronomy operations for up to seven hours after sunset. The invertor gasoline generator supplies energy in case the sky is cloudy and does not allow fully charge the batteries with solar power during the light day, which is most usual in winter.

2.1. Diagnostics and maintenance

Following the restoration of the power supply, diagnostic and repair work on the damaged systems commenced. One of the first subsystems to be restored was the frequency standard module (ADC clock generator), which is essential for ensuring the precision of astrophysical measurements. A lot of equipment was lost and some systems were replaced with spare ones or older models used when the GURT systems were developed. Considerable effort was dedicated to resolving instabilities in the control system. Investigation revealed that data exchange issues between the control unit and the new PC were caused by conflicts with the OS firewall and microcontroller software incompatibilities. These issues were resolved by updating the firmware and optimizing network protection settings, thereby restoring stable operation of the control infrastructure.

Direct field work on the subarray restoration began only in September 2023. The first subarray was repaired in a relatively short time: dipoles of one linear polarization

were restored till September 21, followed by the complete antenna system on September 28. Over 50% of the antenna elements were replaced to the new ones. On October 12, the first solar observations were successfully conducted using the restored subarray. Leveraging the experience gained, the team was able to quickly restore the second subarray, which was brought into operation on November 20, 2023.

2.2. Scientific Results

The restoration of the initial subarrays of the GURT radio telescope enabled the resumption of systematic scientific observations, which began in 2024 under the framework of the "Favorit-Astro" projectfunded by NAS of Ukraine. Preliminary test observations of solar radio emission revealed heightened solar activity, characterized by a variety of radio burst types. The GURT data correlated well with optical observations from the SDO and SOHO satellites, confirming the association of the detected radio bursts with solar flares and coronal mass ejections.

Observations were conducted monthly in week-long campaigns, during which up to 34 GB of data were collected per day, which provided unique valuable data for solar astronomers of IRA NASU. This allowed the detection and analysis of bursts originating from specific active regions on the solar disk.

In addition to solar observations, the two restored subarrays were successfully configured as a two-element short-base correlation interferometer. This configuration facilitated the initiation of monthly monitoring of the secular decrease in the flux density of Cassiopeia A, using the radio galaxy Cygnus A as a calibration source (see Figure 2). Owing to the narrow beam pattern of the interferometer, measurements were significantly less affected by background radio emission.

The data acquired during these sessions enriched and continued long-term set of measurements on this instrument, demonstrated high stability and enabled precise tracking of the flux ratio between these two prominent astronomical sources, confirming the interferometric system's sensitivity and robustness.

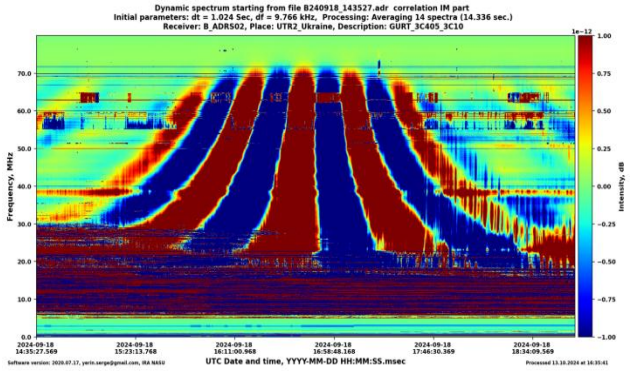

Figure 2: Dynamic spectrum of the real part of the cross-power spectral density between the two GURT subarrays during the transit of the radio source *Cygnus A* through the interferometer's beam pattern as observed 18 September 2024.

3. Relocation of GURT subarray to Poltava region and its Restoration

Another strategically significant step was to relocate at least one GURT subarray to a safer place to provide safe uninterrupted restoration and observations. As such a place the Poltava Gravimetrical Observatory of NASU site in Stepanivka village of Poltava's region was chosen.

The restoration process was divided into two parallel workflows: component preparation in Kharkiv at IRA NASU and field deployment in Stepanivka. In Kharkiv, the team focused on restoring and modernizing the radio telescope's hardware, while simultaneous earthworks and installation activities were conducted at the new site. Final assembly commenced on 29 October 2024, beginning with the installation of cross-dipoles. By 1 November, the full antenna field had been installed.

The first successful test of one polarization was achieved on 6 November 2024, and solar radio bursts were detected the following day confirming the full operability of the restored subarray. Final assembly concluded on 20 December 2024, with the launch of the second polarization subarray equipment. From that point onward, the third GURT subarray entered regular operation.

3.1. The Problem of Electromagnetic Interference

Following the successful deployment of the GURT subarray in Stepanivka, the team encountered two major challenges: frequent power outages and high levels of radio frequency interference (RFI). To maintain uninterrupted observational capabilities, an uninterruptible power supply (UPS) system was developed and installed. However, this very system was identified as the primary source of conducted RFI, propagating along the 230 V power line.

To diagnose the issue, a dedicated test setup for measuring conducted RFI was assembled. Measurements revealed that at a frequency of 7 MHz, the interference level reached 37 dBμV – an intensity that rendered astronomical observations unfeasible. The root cause was traced to inadequate built-in filtering within the UPS unit. This is attributable to the fact that most inverter systems are engineered to comply with general household electromagnetic compatibility standards (e.g., CISPR, 2015), which do not account for the stringent sensitivity requirements of radio astronomical instrumentation and observatories sites.

3.2. Engineering Solution

Conventional simple mitigation techniques such as shortening cable lengths, shielding conductors, and installing ferrite rings proved insufficient to eliminate the conducted RFI. A more comprehensive engineering approach was required, involving both precise measurement and targeted suppression of interference at its source. Based on the diagnostic data obtained from the custom-built conducted RFI test stand, a specialized external mains filter was designed and installed. This filter was optimized to operate across the 100 kHz to 80 MHz frequency band and demonstrated high suppression efficiency.

Following its installation, the interference level at 7 MHz was reduced from 37 dBμV to 20 dBμV, enabling

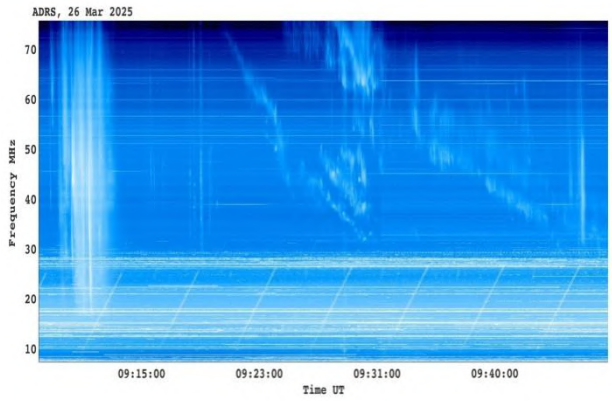

Figure 3: Example of Solar sporadic radio emission, obtained on 26.03.2025.

successful radio astronomical observations. Although some residual interference was still detectable in the test setup, the team hypothesized that it stemmed from the absence of a high-quality high-frequency grounding system at the site.

Once the power supply issue was resolved and RFI had been sufficiently minimized, continuous monitoring of solar radio emission was initiated. Figure 3 presents an example of sporadic solar radio emission received by the GURT subarray in Stepanivka. This observation represents the first scientific dataset obtained at the new location, confirming the telescope's full operational readiness.

4. Conclusion

The experience of restoring the GURT radio telescope subarrays in both Kharkiv and Poltava region marks a new chapter in the operational history of the instrument. In Kharkiv, efforts were primarily focused on rebuilding the infrastructure and establishing a reliable, autonomous power supply via a solar power plant. This enabled the resumption of systematic radioastronomical observations, including the successful operation of two restored subarrays as a two-element correlation interferometer.

In contrast, the primary challenge in Poltava region was not the physical restoration itself, but rather the mitigation of complex radio-frequency interference. Through an innovative engineering approach, the team developed a custom-designed external filter, successfully adapting commercially available equipment for use with highly sensitive scientific instrumentation.

The successful outcomes of both restoration efforts demonstrate that meaningful scientific research can continue even under adverse and unstable conditions. These achievements stand as a testament to the perseverance, ingenuity, and technical excellence of the research team, ensuring the continuity of radio astronomical observations despite significant logistical and environmental challenges.

Acknowledgements. The authors are grateful to the National Research Foundation of Ukraine for financial and organizational support under the call "Excellent Science in Ukraine" (2024–2026), Grant No. 2023.03/0007. The work was also partially carried out in the framework of the projects "Signal" (4.1/25 − П) and "Favorit-vidnovlennia" (No. 0125U000563).

References

Konovalenko A., Sodin L., Zakharenko V. et al.: 2016, *ExA*, **42**, 11.

Tokarsky P. L., Konovalenko A. A., Yerin S. N. et al.: 2019, *ITAP*, **67**, 7304.

Tokarsky P. L., Konovalenko A. A., Yerin S. N. et al.: 2019, *ITAP*, **67**, 7312.

Zakharenko V., Konovalenko A., Zarka P. et al.: 2016, *JAI*, **05**, 04, id1641010. DOI: 10.1142/S2251171716410105

International Special Committee on Radio Interference: 2015, CISPR 11.

https://doi.org/10.18524/1810-4215.2025.38.341471

SPECTRAL FEATURES OF A SINGLE TYPE III BURST OBSERVED BY PSP ON 04.06.2020

V. M. Melnik[1], V.V. Dorovskyy[2]

[1] Institute of Radio Astronomy, National Academy of Sciences of Ukraine, Kharkiv, Ukraine, *melnik@rian.kharkov.ua*

[2] Institute of Radio Astronomy, National Academy of Sciences of Ukraine, Kharkiv, Ukraine

ABSTRACT. Spectral features of single Type III burst observed by PSP on 4 June 2020 in the frequency range 1.4–19 MHz are studied. This burst was also observed by radio telescopes URAN-2 and GURT in the frequency band 10–70 MHz (Melnik et al., 2024). At the first time the velocity spectrum of electrons, which responsible for the radio emission of different bursts levels, was found in the wide frequency band because this Type III burst was fairly powerful. The duration dependence as well as the flux dependence on frequency was analyzed in the frequency band of 10–70 MHz. This paper is the extension of the previous paper with the aim to expand essentially the frequency band using PSP observations. The discussed burst is also fairly powerful one at the frequencies 1.4–19 MHz so the analyzing procedure can be repeated for these frequencies as well. Comparing the obtained results with previous ones shows that the velocity spectrum is practically unchanged. The duration-frequency dependence is almost the same too. At the same time behavior of the burst flux at the frequencies of 1.4–19 MHz is essentially differed of it in the common band of 10–19 MHz even. According to PSP data the burst flux is decreased with decreasing frequency in this band, but not increased as follow to URAN-2 – GURT data. We associate it with the fact that PSP and URAN-2 – GURT observed this burst from different directions.

Keywords: PSP, URAN-2, GURT, Type III burst, drift rate, duration, flux, electron velocity, beam-plasma struc-ture.

АНОТАЦІЯ. В роботі вивчаються спектральні характеристики поодинокого сплеску III типу, що спостерігався космічною місією PSP 4 червня 2020 року в частотному діапазоні 1,4–19 МГц. Цей сплеск також спостерігався, але в діапазоні 10–70 МГц, українськими радіотелескопами УРАН-2 та ГУРТ (Melnik et al., 2024). З тієї причини, що він достатньо потужний, вдалось вперше знайти швидкісний спектр електронів, які відповідають за радіовипромінювання на передньому та задньому фронтах, а також в максимумі сплеску в широкому діапазоні частот. Також була досліджена залежність тривалості сплеску та його інтенсивність від частоти в полосі частот 10–70 МГц. Дана робота є продовженням попередньої роботи з метою суттєво розширити частотний діапазон аналізу, використовуючи дані отримані PSP. В діапазоні частот 1,4–19 МГц сплеск також досить потужний, тому вдається практично повністю повторити процедуру і для цього діапазону. Порівняння отриманих результатів з попередніми показує, що швидкісний спектр електронів практично не змінюється. Це ж стосується залежності тривалості від частоти. В той самий час потік сплеску на частотах 1,4–19 МГц значно відрізняється від поведінки навіть в загальній полосі 10–19 МГц. За даними PSP потік не тільки не збільшується із зменшенням частоти як було за даними УРАН-2 та ГУРТ, а повільно зменшується. Ми пов'язуємо це з тим, що цей сплеск спостерігався PSP та радіотелескопами УРАН-2 та ГУРТ з різних напрямків.

Ключові слова: PSP, УРАН-2, ГУРТ, сплеск III типу, швидкість дрейфу, тривалість сплеску, потік сплеску, швидкість рухуелектронів, пучково-плазмове утворення.

1. Introduction

Solar Type III bursts are the important part of sporadic radio emission of the Sun (Suzuki & Dulk, 1985). They have be studied for decades since 1950 (Wild, 1950) both experimentally and theoretically. It is generally agreed that fast electron beams propagating through coronal plasma with velocities from 0.2c to 0.6c are responsible for their radio emission (Suzuki & Dulk, 1985). Fast electrons generate Langmuir waves at every point and these waves are transformed into fundamental and harmonic of electromagnetic waves (Ginzburg & Zheleznyakov, 1958). Propagation of fast electrons through coronal plasma and generation of Langmuir waves are multi-level and essentially nonlinear processes because these Langmuir waves absorbed by fast electrons too, that affects the motion of these electrons in the plasma (Ryutov & Sagdeev, 1970). It was shown analytically (Melnik, 1995) and numerically (Kontar et al.,1998; Mel'Nik et al.,1999) that such nonlinear process leads to formation of a nonlinear object, beam-plasma structure, which consists of fast electrons and Langmuir waves, and moves with a constant velocity as a soliton. Because this object consists of Langmuir waves it can generate electromagnetic waves, which manifest themselves in the solar corona as Type III bursts (Melnik & Kontar, 2003). Therefore, Type III bursts have properties of beam-plasma structures: every level propagates with very own velocity, where greater velocities correspond to the burst front and smaller velocities correspond to the burst tail (Reid & Kontar, 2018;

Zhang et al., 2019). At the same time velocity of the burst maximum is constant and equals average velocity between maximum and minimum velocities of beam-plasma structure (Kontar et al., 1998). So the learning of Type III burst velocity spectrum is very important for the confirmation of the theory of beam-plasma structure. Radio telescopes of new generation, LOFAR, NenuFAR, GURT and modernized with new registered facilities, UTR-2 and URAN-2, with high sensitivity and with high frequency-time resolutions allow to register and analyze fine spectral features of Type III bursts in a wide frequency band. New cosmic mission, PSP, gives an opportunity to expand frequency range in the low frequency band: from 20 kHz to 19 MHz.

First such observations and data analysis (Melnik et al., 2024) show that, really, electrons with different velocities are responsible for the different burst phases: fast and slow electrons are responsible for the front and the back of burst, accordingly. Also for the first time the spectrum of velocities corresponding different levels of Type III burst, 0.1, 1/e, 0.5, 0.7 at the front and back of the burst as well as for maximum flux, was found (Melnik et al., 2024). It was shown that Type III burst observed on 4 June 2020 was generated at the second harmonic in Newkirk corona (Newkirk, 1961). It was turned out that velocity associated with the maximum was equal to 0.6 of the velocity, which was associated with 0.1 level on the front. This is precisely the value obtained in the theory of beam-plasma structure (Kontar et al.,1998). It was shown also that the Type III burst duration τ dependence on frequency was close to Elgaroy-Lingstad law (Elgaroy & Lingstad, 1972) $\tau = 6.21(f/30)^{-2/3}$. The Type III flux was increased with decreasing frequency as $I \sim f^{-1.63}$ and $I \sim f^{-1.74}$ in frequency bands of 30-70 MHz and 10-30 MHz respectively. This result confirmed earlier obtained results (Suzuki & Dulk,1985).

In this paper available PSP data of observations of single Type III burst in the frequency band of 1.4-19 MHz registered on 4 June 2020 by radio telescopes URAN-2 and GURT are used. It allowed studying spectral features of a single burst in unprecedentedly wide frequency band from 1.4 up to 70 MHz. We found the velocity spectrum of this Type III burst and the dependence of the latter's duration on frequency. We also obtained the changeability of burst flux with frequency in the frequency band of 1.4-19 MHz and discussed the divergence with results got with radio telescopes URAN-2 and GURT earlier.

2. Observations

Observations of solar radio emissions with radio mission PSP are conducted with the help of two receivers, Low Frequency Receiver (LFR) and High Frequency Receiver (HFR). In this paper we shall use data obtained with HFR. This Receiver module onboard the Parker Solar Probe mission (Bale at al., 2016) receives radio emission in the frequency band of 1.275 – 19.17 MHz. This band is unprecedentedly wide in terms of overlap ratio (the ratio of the highest frequency of the range to the lowest one), which equals 15. For this reason, frequency resolution of the equipment is frequency dependent maintaining constant relative frequency resolution (df/f) of about 0.04

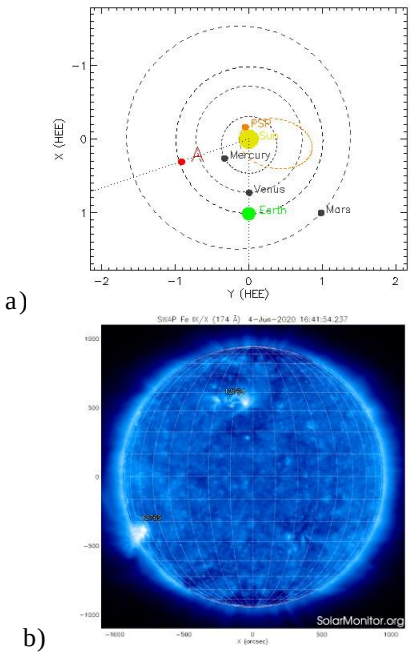

Figure 1: a) Location of cosmic mission PSP relatively to the Sun and the Earth. b) Active region NOAA 2765 on the solar disk on 4 June 2020.

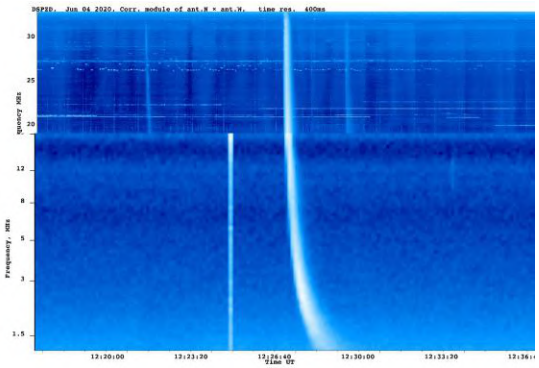

Figure 2: United dynamic spectrum of the Type III burst observed by URAN-2 (19-32 MHz) and PSP (1.4-19 MHz) on 4 June 2020.

throughout the whole frequency band. This provides absolute frequency resolutions from 0.8 MHz at 19MHz up to 47kHz at 1.3 MHz. Time resolution is also variable depending on the spacecraft orbital position. It changes from 3-7s during 12 days around the perihelion down to 56 s during the rest of the orbit. Observations on 4 June 2020 were conducted during 5 perihelion (Figure 1a) and time resolution that time was 7 s. This time PSP was situated practically beyond the Sun of the east side. Discussed Type III burst was initiated with active region NOAA 2765 (Figure 1b) which was at the east side of the solar limb practically in picture plane and this burst was observed with URAN-2 and GURT under the angle of 90°.

The dynamic spectrum of Type III burst according to PSP and URAN-2 data it the frequency range 1.4 – 32 MHz is shown in Figure 2. The time synchronization of observations on the Earth and cosmic mission PSP takes

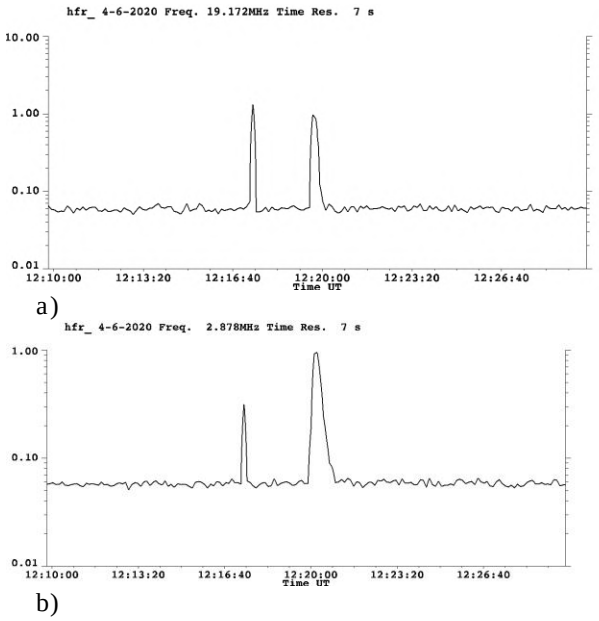

Figure 3: Profiles of Type III burst at frequencies 19.17 MHz (a) and 2.87 MHz (b) at 12.20 UT according to PSP data.

into account the different time of arrival. This burst disappears at frequencies lower than 1.4 MHz.

Profiles of the Type III burst are shown in Figure 3. We see that this burst is enough strong (its maximum flux is more than 10 times larger than the background flux) so it is possible to measure drift rates of different levels of the burst practically in the whole frequency band of 1.4 – 19 MHz.

This burst was not registered by LFR of PSP because the solar corona could not let its radio emission through at such low frequencies in the direction "back".

We measured drift rates with the method used in (Melnik et al., 2024). We found arrival time of corresponding burst level in the dependence of frequency $t = t(f) = A \cdot f^{-\alpha}$ and then found drift rate $df/dt = -B(f/30)^{\beta}$ from this equation, where $B = 30^{\beta}/A\alpha$ and $\beta = 1+\alpha$. Values for B and β for the whole frequency range 1.4-70 MHz are presented in the Table in the second and the third columns. In the fourth column corresponding velocities are presented. They were obtained in the assumption of harmonic generation in the Newkirk coronal plasma ($n(r) = 4.2 \cdot 10^4 \cdot 10^{4.32/r}$, $r = R/R_S$) (Newkirk, 1961). B, β and v from (Melnik et al., 2024) are shown in the fifth, sixth and seventh columns for comparison. We see that all values differed slightly, and the velocities obtained in wider band are some larger only for the front part.

The examples of approximations for the observed drift rates for levels $0.5\pm$ and maximum (1) for Newkirk coronal plasma are presented in the Figure 4. Here "+" and "-" denote the burst front and tail respectively. For other levels the situation is approximately the same. The velocity spectra obtained for the frequency bands of 1.4-70 MHz and 10-70 MHz (Melnik et al., 2024) are shown in Figure 5. These spectra are very close and similar. It is

Table

levels of flux	B	β	v, c	B	β	v, c
0.1+	6.3	1.75	0.55	5.6	1.89	0.5
1/e+	5.8	1.74	0.47	4.5	1.94	0.42
0.5+	5.2	1.76	0.43	4.2	1.97	0.39
0.7+	5.1	1.74	0.42	4	1.95	0.37
1	4.4	1.69	0.34	3.5	1.85	0.31
0.7-	3.7	1.64	0.29	3.2	1.74	0.27
0.5-	3.2	1.67	0.25	3	1.71	0.25
1/e-	3.2	1.62	0.24	2.9	1.67	0.24
0.1-	2.3	1.68	0.18	2.8	1.56	0.23

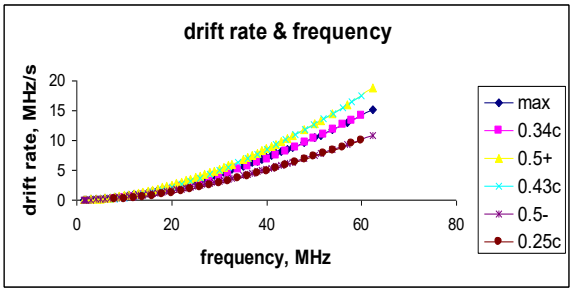

Figure 4: Drift rates dependence on frequency for levels $0.5\pm$ and maximum (1) and approximations for the harmonic radio emission in the Newkirk model.

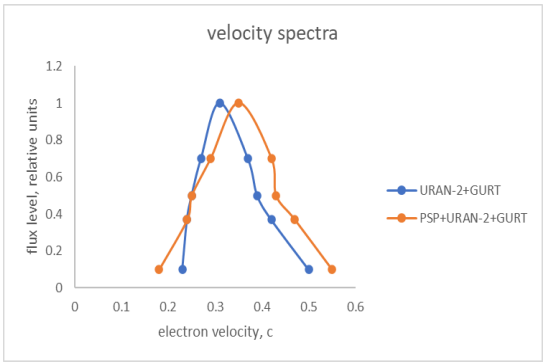

Figure 5: Velocity spectra of Type III burst for the cases for the frequency bands of 10-70 MHz and of 1.4-70 MHz.

important that despite the difference in the velocity values the maximum to minimum velocities ratio is the same and equal 0.62.

The duration of discussed Type III burst increased with decreasing of frequency according to PSP data. This dependence including data obtained with URAN-2 and GURT is shown in Figure 6. The corresponding equation for this dependence is $\tau = 6.22(f/30)^{-0.59}$ and it agrees with

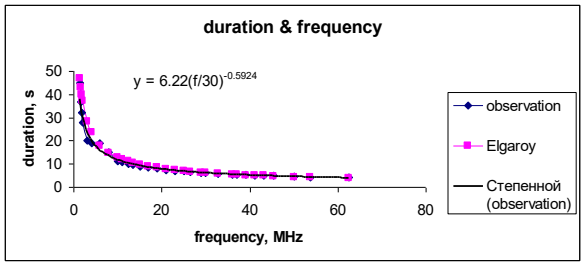

Figure 6: The duration dependence on frequency for Type III burst in the frequency band 1.4-70 MHz and Elgaroy-Lingstad dependence.

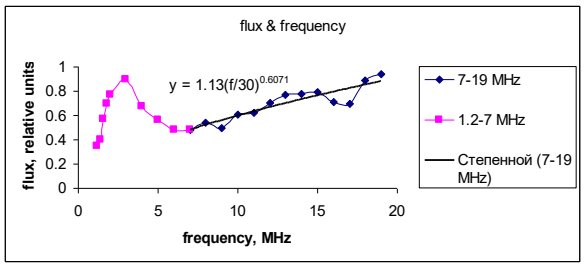

Figure 7: Radio emission flux of Type III burst in the frequency band of 1.4-19 MHz according PSP observations.

that for the URAN-2 – GURT data $\tau = 6.17(f/30)^{-0.53}$. The well-known dependence of Elgaroy-Lingstad (Elgaroy & Lingstad, 1972) is shown also. We see that our dependence is very close to it but is a little below. According to PSP observations the flux of discussed Type III burst behaves significantly differently than that according to URAN-2 – GURT data. The last one was and followed the laws, $I \sim f^{-1.63}$ in the frequency band 30-70 MHz and $I \sim f^{-1.74}$ at frequencies 10-30 MHz. For PSP data the flux frequency dependence is shown in Figure 7 and demonstrates a twofold decrease when frequency decreases from 19 MHz to 6 MHz with the equation of $I = 1.13(f/30)^{0.61}$. Starting from 5 MHz the flux increased two times to frequency 3 MHz. Below this frequency the flux decreased again very quickly and at frequency 1.2 MHz it equals the background flux.

3. Discussion

Observations of Type III burst with PSP on 4 June 2020 gave an opportunity to expand frequency band of analysis to 1.4 – 70 MHz. For this particular burst PSP data obtained in frequency band of 1.4-19MHz supplement data obtained with URAN-2 and GURT in frequencies 8-32MHz and 8-70 MHz respectively (Melnik et al., 2024). Frequency bands overlap allows combining these data in the wide frequency band of 1.4 – 70 MHz in a correct way. Concerning drift rates of the burst different levels we have very nice correspondence of the results obtained with different radio telescopes. The drift rate dependences on frequency in the expanded frequency band of 1.4-70 MHz are very close to those in the frequency band of 10-70 MHz. The assumption that fast electrons propagate in the Newkirk solar corona and that they generate radio emission at the second harmonic allows finding their velocities. The corresponding spectra for both frequency bands, 1.4 -70 MHz and 10-70 MHz, are practically identical (Fig. 5). The only difference is the spectrum in the first case shifted toward a little higher velocity. In our opinion there is a very important point, that the velocity for burst maximum equals about 0.62 of maximum velocity, $v_1 = 0.62 \cdot v_{0.1+}$. This value is close to that in the theory of beam-plasma structure, which propagates through coronal plasma. In this theory beam-plasma structure consists of fast electrons and Langmuir waves, generated by these electrons and absorbed by them. This structure moves through plasma with constant velocity and it can be a source of electromagnetic waves, t, by means of transformation of Langmuir waves, l, in the processes of scattering on ions, i, $l + i = t + i$, and coalescence of Langmuir waves, $l + l = t$ (Ginzburg & Zheleznyakov, 1958). The velocity of beam-plasma structure equals the mean velocity of electrons $(v_{\max} + v_{\min})/2 = 0.36c$, where $v_{\max} = v_{0.1+} = 0.55c$ and $v_{\min} = v_{0.1-} = 0.18c$ in our case. Different parts of beam-plasma structure move with different velocity as different levels of Type III burst. The density of fast electrons can be found from the equation (Vedenov & Ryutov, 1975)

$$v_{\max}/v_{\min} + \ln(v_{\min}/v_0) = 1 + \frac{\pi}{\Lambda}\omega_{pe}\frac{n'}{n}\tau$$

which connects the minimal and the maximum electron velocity and the duration of the burst. It equals about $n'/n \approx 10^{-7}$. It gives the energy density of Langmuir waves $W/nkT = \frac{n'}{n}(\frac{v_0}{v_{Te}})^2 < 10^{-4}$ $(v_{Te} = 5 \cdot 10^8 cm/s)$ in beam-plasma structure. This value is the necessary condition for the regime of weak turbulence $(W/nkT \approx n' \cdot mv_0^2/nkT \approx (n'/n)(v_{\max}/v_{Te})^2 \approx 10^{-4})$ (Tsytovich, 1970) and namely in this regime beam-plasma structure can only exist. Thus we can conclude that existence of beam-plasma structure is confirmed by observations.

The duration of Type III burst can be connected with the passage of fast electrons across the given plasma level in the solar corona (Melnik et al., 2017; Melnik et al., 2024) and be defined with the velocity dispersion of different levels of beam-plasma structure (Melnik et al., 2024). In this case the duration can be found from the equation

$$\Delta t = (\frac{4.32}{\lg\frac{\pi m f^2}{1.6 \cdot 10^5 e^2}} - 1) \cdot R_S \cdot \frac{v_{0.5+} - v_{0.5-}}{v_{0.5+} v_{0.5-}}$$

assuming generation at generation at the second harmonic. This dependence for this burst is shown in Figure 8 as well as observational dependence for the comparison. It is seen that for frequencies > 10 MHz they are practically coincided but at frequencies <10 MHz the settlement curve is higher. It connected with the fact that radio emission at the frequency 10 MHz is generated at the distance of about R=5Rs, where the local plasma frequency is 5 MHz and approximately at these distances the Newkirk law for coronal plasma ceases to be correct (Newkirk, 1961; Suzuki & Dulk, 1985). So we conclude that for this burst at frequencies >10 MHz the burst duration is defined by longitudinal size of beam-plasma structure.

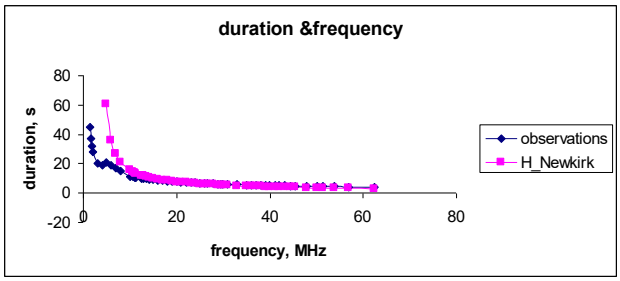

Figure 8: Duration dependencies on frequency, observational and calculated in assumptions that duration is determined by electron velocity dispersion in Newkirk plasma.

Flux dependence on frequency is also an interesting result. In spite of a similarity and closeness of the results on drift rates of different burst levels and burst duration obtained by URAN-2 – GURT and PSP in different frequency ranges, the flux dependencies in common frequency band of 10-19 MHz are essentially different. We explain this by different angles at which the source of the burst was visible from the URAN-2 and PSP (Figure 1). It is well-known (Zheleznyakov, 1977) that directivity pattern of the harmonic radio emission has 4 lobes, two lobes in the direction of electron propagation and two other different in the opposite direction moreover their values and directions depend on the phase velocity of electromagnetic waves. Besides the radio emission registered by PSP was under influence of solar corona because of scattering and even partial absorption. The latter is the possible cause of abrupt stop of radio emission lower than 1.4 MHz.

4. Conclusion

Frequency band broadening (up to 1.4-70 MHz) of spectral properties analyzes of Type III burst observed on 4 June 2020 by radio telescopes URAN-2, GURT and PSP confirmed the main results obtained in the tighter frequency band of 10-70 MHz.

The first, each level of the burst has its own velocity at that this velocity for the front is higher than for the back. The velocity for the burst maximum equals 0.6 of maximum velocity (level 0.1+). This result is weighty argument in favor of the theory of beam-plasma structure, specific composite soliton, which appears at nonlinear propagation of fast electrons in plasma.

The second, the duration-frequency dependence for this burst is very close to the Elgaroy-Lingstad law in the whole frequency band of 1.4-70 MHz. We show that the duration of this Type III burst is defined by the velocity dispersion in the beam-plasma structure in the Newkirk coronal plasma. This is correct for the distances not exceeding approximately $5R_S$, where the Newkirk law can be used.

The third, the difference of flux-frequency dependences for the band of 10-19 MHz according to URAN-2 and PSP data is connected with different sight angles of observations.

Acknowledgements. All authors acknowledge funding from the NASU (National Academy of Sciences of Ukraine) project “Complex researches of sporadic radio emission of the Sun during 25 cycle of solar activity” (RADIUS) 0122U000616.

References

Bale S.D., Goetz K., Harvey P.R. and 81 co-authors: 2016, *Space Science Reviews*, **204**, 49.
Ginzburg V.L. and Zheleznyakov V.V.: 1958, *Astron. Zh.*, **35**, 694.
Elgaroy O., Lingstad E.: 1972, *AAP*, **16**, 1.
Kontar E.P., Lapshin V.I., Mel'nik V.N.: 1998, *Plasma Physics Reports*, **24**, 772.
Melnik V., Brazhenko A., Dorovskyy V. et al.: 2024, *FrASS*, **11**, id. 1396326.
Mel'Nik V.N.: 1995, *Plasma Physics Reports*, **21**, 89.
Mel'Nik V.N., Lapshin V., Kontar E.: 1999, *Sol. Phys.*, **184**, 353.
Mel'Nik V.N., Kontar E.P.: 2003, *Sol. Phys.*, **215**, 335.
Melnik V., Shepelev V., Brazhenko A., Dorovskyy V., Rucker H., Poedts S.: 2017, *Sun and Geosphere*, **12**, 105.
Newkirk G.Jr.: 1961, *ApJ* , **133**, 983.
Reid H.A.S., Kontar E.P.: 2018, *AAP*, **614**, A69.
Ryutov D. D., Sagdeev R. Z.: 1970, *JETP* **58**, 739.
Suzuki S., Dulk G.A.: 1985, In: McLean, D.J., Labrum, N.R. (eds.) Solar Radiophysics: Studies of Emission from the Sun at Metre Wavelengths, 289. (Cambridge: Cambridge Univ. Press).
Tsytovich V.N.: 1970, Nonlinear Effects in Plasma. (New York: Plenum Press).
Vedenov A.A., Ryutov D.D.: 1975, Reviews of Plasma Physics, 6. ed. M. A. Leontovich. (MD USA. Published by Consultants Bureau, New York).
Wild J.P.: 1950, *AuSRA*, **3**, 541.
Zhang P., Yu S., Kontar E.P., Wang C.: 2019, *ApJ*, **885**, id. 140.
Zheleznyakov V.V.: 1977 Electromagnetic waves in cosmic plasma. Generation and propagation. (Moskva: Nauka).

.

https://doi.org/10.18524/1810-4215.2025.38.340381

VISUALIZATION AND ANALYSIS OF VECTOR NETWORK ANALYZER DATA FOR THE EXPERIMENTAL MODEL OF THE ACTIVE ANTENNA SECTION OF THE GURT RADIO TELESCOPE

V. I. Myrhorod, I. M. Bubnov, V. Yu. Selin

Institute of Radio Astronomy, National Academy of Sciences of Ukraine,
Kharkiv, Ukraine

ABSTRACT. **Subject and purpose of the work.** During the development and testing of radio engineering devices, in particular the active antenna sections of the GURT radio telescope, there is a need for prompt and efficient processing of experimental data. Large volumes of measurements obtained from vector network analyzers require tools for fast interpretation and statistical analysis. The purpose of this work is to create software that ensures high-quality processing and visualization of such data, contributing to improved accuracy in the evaluation of antenna system parameters.

Methods and methodology. To achieve this goal, the Graphics v.1.9 software was developed, functioning in the Windows environment on the .NET Framework 4.8 platform. The program employs the ScottPlot library for building interactive plots and ClosedXML for handling Excel data. The architecture of the solution is designed according to a modular principle, which facilitates the integration of new functionality. The main methods include parsing data from the Obzor-103 analyzer, generating plots, performing statistical averaging of results, and exporting data into formats suitable for publications and presentations.

Results of the work. The Graphics v.1.9 program enables advanced visualization of measurements, the creation of high-quality graphical reports, as well as the averaging of data of the same type to detect statistical deviations and assess the repeatability of results. This makes it possible to obtain generalized characteristics of the studied devices, quickly detect instabilities in individual elements, and perform comparative analysis within a series of identical components. Practical application of the program in the testing of GURT antenna sections has confirmed its efficiency and feasibility for scientific research.

Conclusions. The developed software significantly increases the efficiency of experimental data analysis in radio astronomy and radio engineering. Graphics v.1.9 not only reduces the time required for data processing but also provides deeper insight into system characteristics and contributes to its optimization. Prospects for further development of the program include support for new input data formats, expansion of processing tools, and the implementation of advanced visualization features, making it a universal tool for a wide range of scientific and applied tasks.

Keywords: GURT radio telescope, active antenna, data processing, visualization, statistical analysis, averaging.

АНОТАЦІЯ. **Предмет і мета роботи.** Під час розробки та випробування радіотехнічних пристроїв, зокрема активних антенних секцій радіотелескопа ГУРТ, виникає потреба в оперативній та ефективній обробці експериментальних даних. Значні обсяги вимірювань, отриманих з векторних аналізаторів мереж, потребують інструментів для швидкої інтерпретації та статистичного аналізу. Метою роботи є створення програмного забезпечення, яке забезпечує якісну обробку та візуалізацію таких даних, сприяючи підвищенню точності оцінки параметрів антенних систем.

Методи та методологія. Для реалізації поставленої мети було розроблено програму Graphics v.1.9, яка функціонує у середовищі Windows на базі платформи .NET Framework 4.8. У програмі використано бібліотеку ScottPlot для побудови інтерактивних графіків та ClosedXML для роботи з Excel-даними. Архітектура рішення побудована за модульним принципом, що забезпечує зручність додавання нового функціоналу. Основні методи включають парсинг даних з аналізатора Obzor-103, побудову графіків, статистичне усереднення результатів і експорт даних у формати, придатні для публікацій та презентацій.

Результати роботи. Програма Graphics v.1.9 дозволяє виконувати розширену візуалізацію вимірювань, створювати графічні звіти високої якості, а також здійснювати усереднення даних одного типу для виявлення статистичних відхилень і оцінки повторюваності результатів. Це дає змогу отримати узагальнені характеристики досліджуваних пристроїв, швидко виявляти нестабільності в окремих елементах та проводити порівняльний аналіз у межах серії ідентичних компонентів. Практичне застосування програми у випробуваннях антенних секцій ГУРТ підтвердило її ефективність та доцільність використання в наукових дослідженнях.

Висновки. Розроблене програмне забезпечення значно підвищує ефективність аналізу експериментальних даних у радіоастрономії та радіотехніці. Graphics v.1.9 не лише скорочує час на обробку вимірювань, але й забезпечує глибше розуміння характеристик системи та сприяє її оптимізації. Перспективи подальшого розвитку програми полягають у підтримці нових форматів вхідних даних, розширенні інструментарію для

програми полягають у підтримці нових форматів вхідних даних, розширенні інструментарію для обробки та реалізації додаткових можливостей візуалізації, що робить її універсальним засобом для широкого спектра наукових і прикладних завдань.
Ключові слова: радіотелескоп ГУРТ, активна антена, обробка даних, візуалізація даних, статистичний аналіз, усереднення.

1. Introduction

New-generation radio telescopes play a key role in modern radio astronomy, enabling high-sensitivity observations across a wide frequency range. One such instrument is the Ukrainian radio telescope GURT, built on the principle of a phased array antenna (PAA). Its design is based on the use of active antenna elements, in which the amplifier is integrated directly into the dipole structure. This approach provides preliminary signal amplification at the reception stage, reduces losses, and increases the overall sensitivity of the system.

Each section of the GURT consists of 25 cross-oriented dipoles (Fig. 1), forming 50 independent active channels for two mutually perpendicular polarizations. For the telescope to work effectively, all channels must be highly identical. Even slight differences in parameters, such as impedance, gain coefficient, or phase characteristics, can cause distortion of the directional pattern and deterioration of observation quality.

The analysis of such multichannel systems requires obtaining a large amount of experimental data from vector network analyzers, such as Obzor-103. However, manual processing of dozens and hundreds of measurement files is difficult, time-consuming, and prone to errors. In these conditions, there is a need for specialized software capable of automating the processing, visualization, and statistical analysis of results.

For this purpose, Graphics v.1.9 software was developed to provide comprehensive processing of experimental data. Its use reduces analysis time, minimizes the risk of errors in manual processing, and improves the accuracy of active antenna system parameter estimation.

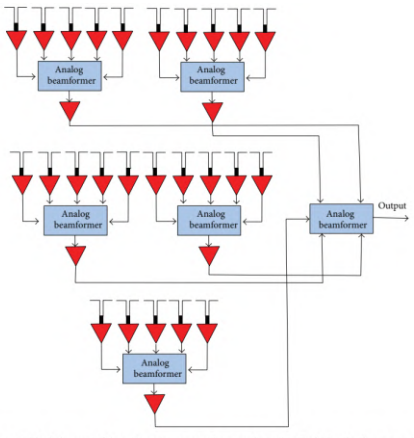

FIGURE 2: Block diagram of the active antenna array in one polarization. Red triangles denote amplifiers.

Figure 1: Diagram of a single polarization of the GURT sublattice

2. Implementation of Graphics v.1.9

Graphics v.1.9 software was created as a tool for efficient processing of experimental data obtained in the course of research on the active antenna sections of the GURT radio telescope. The main task was to ensure the possibility of quick interpretation of measurements with minimal time expenditure by the researcher. The choice of the Windows development environment in combination with the .NET Framework 4.8 platform was dictated by both technical and practical reasons. This solution made it possible to combine performance, a wide range of libraries, and ease of integration with hardware.

The key implementation language was C#, which is the standard for creating modern desktop applications in the Windows environment. The language provides both an object-oriented code structure and advanced capabilities for working with graphics, multithreading, and interfaces. The program has a modular architecture: each component performs its own set of functions, but they interact closely with each other, allowing the user to obtain a complete result without the need for complex additional settings.

Among the main elements of the architecture, it is worth highlighting the data loading and pre-processing module, the analysis module, the visualization block, and the export module. This structure allows users to flexibly manage the processing process: from opening source files from the Obzor-103 device to creating reports in the form of graphic materials or spreadsheets.

Special attention was paid to working with input data. As is well known, files generated by measuring equipment may contain not only arrays of useful values, but also service information, uneven measurement intervals, or formatting errors. Graphics v.1.9 takes these factors into account and automatically converts the data into a unified format suitable for further analysis. This eliminates the need for manual editing and significantly reduces the risk of errors.

3. Features and functional characteristics

One of the key advantages of the program is the function of averaging measurement results. When studying antenna channels, where each element must have the same characteristics, averaging allows you to obtain generalized indicators and evaluate repeatability. This is especially relevant when the results of different measurements differ slightly due to external factors such as electromagnetic interference, temperature changes, or equipment errors. Using the averaging function makes it possible to identify systematic deviations and form a more reliable model of the device's operation.

The program provides extensive data visualization capabilities. Graphing is implemented in such a way that the user can not only see static curves, but also interact with them. Zooming, scrolling, highlighting individual sections of the spectrum, and overlaying multiple graphs on a single screen create a flexible working environment that far exceeds the standard capabilities of measuring instruments. For example, when analyzing antenna channel parameters, you can simultaneously display amplitude and phase graphs, allowing you to quickly assess compliance with

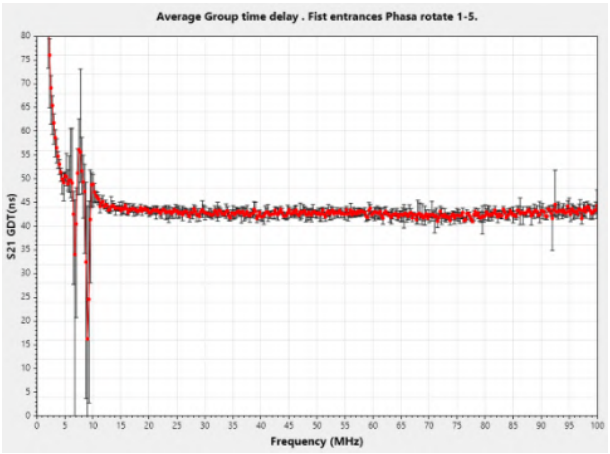

Figure 2: Example of data visualization on a plot

requirements. There are a significant number of settings for graph axes, axis value limits, etc. Figure 2 shows an example of data visualization on a plot.

The input file does not always contain all the necessary parameters. The functionality for calculating additional values was developed specifically to solve this problem. Thanks to this, even with only a few parameters from the input file, the program allows the user to access a much larger set of physical quantities. All calculations are performed automatically while reading the files, after which these new parameters can be used for statistical research and visualization.

The user interface (Fig. 3) was designed with the needs of engineers and researchers in mind, who do not always have extensive programming experience. Therefore, the main functions are displayed on the control panel in the form of buttons and drop-down menus, allowing key operations to be performed quickly. At the same time, more complex parameters remain accessible through the settings system, allowing the program to be adapted to specific tasks. Selecting data for visualization is simplified by convenient filters, sorting, and search functions. All names, captions, and titles on the graphs are dynamic, so the user can customize them to their needs at any time.

The export module is equally important. Saving data in Excel spreadsheets simplifies further processing using statistical methods and report generation. In addition, the ability to save graphs in PNG, JPEG, SVG, and other formats allows you to prepare materials for scientific publications and presentations without additional effort. In this way, Graphics v.1.9 effectively integrates all stages of processing: from obtaining raw measurements to the final result, ready for presentation.

4. Practical application

The Graphics v.1.9 program found its main application during testing of the active antenna sections of the GURT radio telescope. When working with a large number of channels, each with its own characteristics, researchers needed to quickly assess the quality of the identity. Using traditional manual processing methods, this process took many hours, and sometimes days, especially when analyzing tens of thousands of measurement points. The use

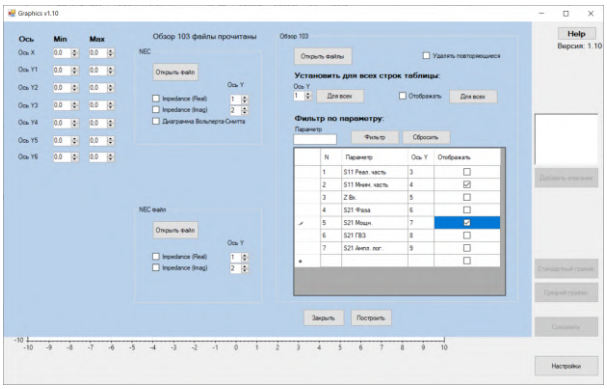

Figure 3: Graphical user interface

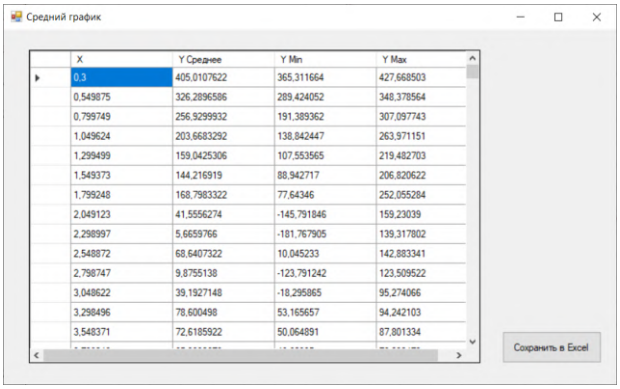

Figure 4: Average data and error bars

of Graphics v.1.9 reduced this time several times over and also reduced the likelihood of human error.

The actual use of the program has proven its effectiveness in tasks such as determining the average characteristics of group delay time, as well as identifying errors in the measurements of this parameter on individual components. For this purpose, the average values and error bars were calculated (Fig. 4). These data make it possible to find phase shifters whose settings need to be adjusted.

Although Graphics v.1.9 was primarily developed for the needs of the GURT radio telescope, its functionality is universal. The program can be used to study and test other radio engineering devices: amplifiers, antennas of various configurations, filters, and resonant systems. Thanks to its ability to process large amounts of data and support various formats, it is a universal tool for engineers and scientists working in related fields.

5. Conclusions

The developed Graphics v.1.9 software has proven its effectiveness in analyzing experimental data obtained during research on the active antenna sections of the GURT radio telescope. It reduces the time required to process results, minimizes the risk of errors that arise during manual analysis, and provides a deeper understanding of the system's characteristics.

The program will be useful for a wide range of users:

• scientific laboratories engaged in research in the field of radio astronomy and radio engineering;

• educational institutions, where it can be used as a teaching tool for training future engineers and researchers;

• engineering companies engaged in the development and testing of antenna systems and radio engineering devices.

Future development plans for Graphics v.1.9 include expanding the range of supported input formats, integrating new processing algorithms, improving the interface, and adding advanced visualization capabilities. This will make the program a universal platform for analyzing large amounts of experimental data not only in radio astronomy, but also in related scientific and engineering disciplines.

References

Esposito D., and Saltarello F.: 2018, Microsoft.NET: Architecture and Application Programming. (Moscow: Dialektika), 624 p.

Falkovich I.S., Konovalenko A.A., Gridin A.A. et al.: 2011, *ExA*, **32**, 2, 127. DOI: 10.1007/s10686-011-9256-z

Konovalenko A., Sodin L., Zakharenko V. et al.: 2016, *ExA*, **42**, 11, 11. DOI: 10.1007/s10686-016-9498-x

Paliichuk O.V.: 2020, Development of Application Programs Using the .NET Framework Platform. (Lviv: LNU Publishing), 312 p.

Richter J.: 2012, CLR via C#, 4th ed. (Microsoft Press), 826 p.

Tokarsky P.L., Konovalenko A.A., Yerin S.N., Bubnov I.N.: 2016, *RPRA*, **21**, 1, 48. DOI: 10.15407/rpra21.01.048

Tokarsky P.L., Konovalenko A.A., Yerin S.N., Bubnov I.N.: 2019, *ITAP*, **67**, 12. DOI: 10.1109/TAP.2019.2927841

https://doi.org/10.18524/1810-4215.2025.38.344822

PREPARING RADIO AND OPTICAL DATA FOR COMPARING BINARY BLACK HOLE CANDIDATES: THE CASE OF OJ 287

D. A. Zabora[1,2], M. I. Ryabov[2], A. L. Sukharev[2]

[1] Odesa I. I. Mechnikov National University, Odesa, Ukraine, *zaboradaniil@gmail.com*

[2] Institute of Radio Astronomy of the National Academy of Sciences of Ukraine (IRA NASU), Kharkiv, Ukraine, *rian@rian.kharkov.ua*

ABSTRACT.

Background. In light of recent discoveries, in particular the appearance in the literature of strong evidence in favor of a binary supermassive black hole (SMBH) in the core of OJ 287, interest in the search for such objects has revived. Therefore, the issue of detecting candidates has gained considerable relevance. The variability of the radio flux of Active Galactic Nuclei (AGN) in the optical, radio and spatial dimensions provides significant insights into the complex structure of physical phenomena in the immediate vicinity of the black hole and the conditions for launching jets. In particular, these manifestations may indicate the presence of a binary SMBH in the center of such a system.

Data & methods. The paper uses multi-filter optical observations (aggregated by AAVSO) and radio observations of the MOJAVE project at 15 GHz, given in Lister et al. (2019), in the form of radio fluxes and bright component positions (obtained from the VizieR database). Time-frequency analysis methods (including wavelet analysis, LombScargle, and cross-correlation) as well as clustering and regression methods of machine learning and analysis are used for processing.

Results. The intersections of the accretion disk by the companion black hole in the core of OJ 287 cause characteristic optical flares and affect the jet morphology. The latter is manifested in the change in the angles of the bright features (components). It is found that these changes in the case of OJ 287 exhibit noticeable patterns that can be used as indicators for binary black hole candidates (SMBBHs) in active nuclei.

Conclusions. The established connection between optical flares (with potential X-ray verification) and changes in the orientation of jet components with a characteristic pattern can serve as a criterion for detecting binary black hole candidates in AGN.

Keywords: binary supermassive black hole (BSMBH), AGN, blazar, optical flares, jet morphology, quasi-periodicity.

АНОТАЦІЯ.

Передісторія. У світлі нещодавніх відкриттів, зокрема появу у літературі вагомих доказів на користь подвійної надмасивної чорної діри (SMBH) у ядрі OJ 287, інтерес до пошуку подібних об'єктів пожвавився. Відтак, питання виявлення кандидатів набуло значної актуальності. Змінність радіопотоку Активних ядер галактик (АЯГ) в оптичному, радіо та просторовому вимірах надає суттєві інсайти стосовно складної структури фізичних явищ у безпосередньому оточенні чорної діри та умов запуску джетів. Зокрема, ці прояви можуть свідчити про наявність подвійної SMBH у центрі такої системи.

Дані та методи. У статті використовуються багатофільтрові оптичні спостереження (агреговані AAVSO) та радіоспостереження проєкту MOJAVE на частоті 15 GHz, наведені в Lister et. al. (2019), у вигляді радіопотоків та положень яскравих компонент (отриманих із бази VizieR). Для обробки застосовуються методи часово-частотного аналізу (зокрема вейвлет-аналіз, LombScargle та крос-кореляція), а також кластеризаційні та регресійні методи машинного навчання та аналізу.

Результати. Перетини акреційного диску чорною дірою-компаньйоном у ядрі OJ 287 спричиняють характерні спалахи у оптичному діапазоні та впливають на морфологію джета. Останнє виявляється у зміні позиційних кутів яскравих особливостей (компонент). Виявлено, що ці зміни у кейсі OJ 287 демонструють помітні патерни, які можна використовувати як індикатори для кандидатів на подвійну SMBH у активних ядрах.

Висновки. Встановлений зв'язок між оптичними спалахами (з потенційною рентгенівською верифікацією) та змінами орієнтації компонентів джетів із характерним патерном може слугувати критерієм виявлення кандидатів у подвійні чорні діри в АЯГ.

Ключові слова: подвійна надмасивна чорна діра, АЯГ, блазар, оптичні спалахи, морфологія джета, квазіперіодичність.

1. Introduction

Active Galactic Nuclei (AGN) are objects located in the central regions of some galaxies and are characterized by extreme luminosity in almost the entire wavelength range: from radio waves to gamma rays, which makes them one of the most powerful sources of electromagnetic radiation in the Universe. According to the current Standard Model (Marscher, 2009), energy supply is provided by the release of gravitational and rotational energy as a result of the accretion of matter onto a supermassive black hole in the center.

The accretion disk surrounding a supermassive black hole is the primary source of optical and ultraviolet radiation. In it, matter falling onto the black hole is heated to high temperatures, releasing gravitational energy in the form of the electromagnetic continuum.

Surrounding the disk is a dust torus, a structure of cooler matter that partially shields the central region. The torus intercepts some of the ultraviolet and optical radiation, heats up, and radiates in the infrared range, forming the characteristic IR component of the spectrum.

Many active nuclei exhibit relativistic jets, collimated plasma streams ejected from the black hole's surroundings in directions close to the polar axis (perpendicular to the disk plane) and observed at distances of tens to hundreds of kpc from the nucleus. These jets emit in a wide range of wavelengths, from radio to X-rays, as a result of synchrotron and inverse Compton processes.

It is possible that the supermassive black hole at the center of a galactic system is not a single one, but multiple—for example, a double or even a triple. According to recent studies, this is exactly the configuration exhibited by the object OJ 287, which is considered one of the most convincing candidates for the presence of a double supermassive black hole.

OJ 287 is classified as a BL Lacertae object, a high-luminosity type of AGN with a relativistic jet directed almost into the observer's line of sight, resulting in significant Doppler beaming and making the object very bright despite its considerable distance. It is located at a cosmological distance corresponding to a redshift of $z = 0.3056$ (ASA/IPAC Extragalactic Database, 2008) in the constellation Cancer. OJ 287 is exceptional in its proximity to the ecliptic plane (it has been accidentally captured on a large number of photographic plates) and, as a result, in the unprecedentedly long series of historical observational data available: over 120 years (Alachkar et al., 2023), which is critical for identifying long-term orbital effects.

The initial hypothesis of the presence of a double SMBH in the OJ 287 system first appeared in Sillanpaa et al. (1988), where periodic flares ($\sim 11.65\,\mathrm{yr}$) were observed in the optical curve of the AGN. They were associated with a tidal perturbation of the accretion disk of the primary BH by the companion as it passed the pericenter. This perturbation would cause increased accretion towards the center and would lead to a flare in the optics. The masses of the companions were estimated at $\sim 5\cdot10^9 M_\odot$ and $\sim 2\cdot10^7 M_\odot$, with a semi-major axis of $\sim 0.1\,\mathrm{pc}$. The lifetime of such a system (due to the energy loss to gravitational radiation) was also estimated to be $\sim 10^5\,\mathrm{yr}$. The observed pattern allowed for the prediction of the outburst, which was later confirmed in 1994.

Further development (or even rethinking of the model), which is already closer to modern ideas, is presented in the Lehto and Valtonen (1996). In it, the authors noticed that: the flares are not strictly periodic — the time intervals between them change; the structure of the flares is often double (two peaks separated by an interval of 1–2 years); the change in the brightness of the base level and the flares hinted at the modulation of the light curve with a period of 60 years. Another mechanism has been proposed: the flares arise as a result of the collision of a secondary black hole (moving at an angle to the accretion disk) with the radiation-dominated optically thick and geometrically thin accretion disk of the primary at supersonic speed (twice per period), which leads to a shock wave at the collision site, the subsequent formation of optically thick hotter bubbles, their cooling and bremsstrahlung radiation (which are observed as flares); a relativistic precession of the secondary's orbital semi-axis and the amplification of the flares by gravitational waves have been introduced (to explain their irregularity). The following parameters were refined: the eccentricity of the secondary black hole's orbit (0.685), the orbital period ($\sim 12.07\,\mathrm{yr}$), an upper estimate of the decay rate of the orbital period ($\sim 10^{-3}$), the precession period of the system's semi-major axis (130 years), and the properties of the accretion disk.

Sundelius et al. (1997) performed a multi-particle simulation of the disk within the framework of a restricted three-body problem with previously calculated BH orbits: large outbursts were identified with the passage of the pericenter by the companion black hole and induced mass flows from the perturbed accretion disk to the main black hole. Superflares superimposed on longer outbursts are associated with the crossing of the accretion disk by the companion (as in Lehto and Valtonen, 1996). The gas perturbed by the shock wave leaves the disk for a certain time, after which it cools to a temperature at which it becomes capable of radiating. This causes a delay between the moment of impact and the appearance of the optical flare. As a result, the model allowed the authors to calculate the onset of the 1995 superflare quite accurately. The simulation reproduced with good accuracy slow flares ($\sim 1\,\mathrm{yr}$) associated with the increase in the accretion period and faster ones

($\sim$ 0.1 yr) associated with the crossing of the accretion disk, as well as brightness modulation (60-year cycle) associated with the precession of the semi-major axis and strong flares (when the companion's semi-major axis was almost perpendicular to the disk).

Subsequent works (Valtonen and Lehto, 1997, Valtonen et al. 2006, 2010, 2016, Dey et al., 2019) showed the importance of taking into account gravitational waves and the associated energy losses, expanded the model to take into account the spin of black holes and spin-orbit interaction, and refined the model parameters: the mass of the primary black hole $\sim 18.35 \cdot 10^{10} M_{\odot}$, the mass of the secondary black hole $\sim 150 \cdot 10^{6} M_{\odot}$, the Kerr parameter for the primary BH $\chi_1 \sim 0.381$, the eccentricity of the orbit ~ 0.657, the period ~ 12.06 yr, etc. As a result, a super-accurate prediction of the flare caused by the intersection of the accretion disk was observed by the Spitzer telescope in 2019 with an accuracy of up to 4 hours (Laine et al., 2020).

In general, we are talking about tidally induced outbursts, which are associated with the influence of a secondary black hole, which manifests itself in the destabilization of the accretion disk (especially when it passes the pericenter), accelerating the accretion rate and can last for years; and shock flares - sharp short-lived and powerful events (flares and superflares) associated with crossings of the accretion disk twice (once on the way to the pericenter and once after per orbital cycle) with an interval of about a year between flares and subsequent afterflares in the jet in ~ 2 months.

Table 1: Summary table of OJ 287 activity events

Date	Description	References
Nov 1995 – Jan 1996	The second flare of the 1994–1996 pair	Sillanpaa et al. (1996)
2005 – 2008	Tidal-induced period of activity	Valtonen et al. (2009)
Nov 2005	First flare from 2005-2008	Valtonen et al. (2006)
Sep 2007	Second flare from 2005-2008 (giant flare)	Valtonen et al. (2009)
Nov 2015	First flare from 2015-2019	Valtonen et al. (2016)
Oct 2016	Unexpected double flare recorded in X-rays and optics explained as disk afterflare	Komossa et al. (2021)
Jul 2019	Second flare from 2015-2019	Laine et al. (2020)

We are interested in events in the period 1995–2020, for which there is data on the movement of bright components in jets, so will provide a table of activity events with their descriptions and links (Table 1.).

2. Data and methods

This paper uses AAVSO and MOJAVE data to highlight the connection between optical and radio flares and changes in the morphology of the OJ 287 jet. AAVSO (American Association of Variable Star Observers) is an international non-profit organization that brings together professional and amateur astronomers to coordinate observations of variable stars and other astronomical objects. The corresponding AAVSO International Database is one of the largest archives of photometric observations. MOJAVE (MOJAVE Team, 2025, Lister et al., 2018) is a program of long-term monitoring observations of AGN jets using the VLBA radio interferometer. The MOJAVE project also has an open database (MOJAVE/2cm Survey Data Archive) for a sample of over 500 AGN, which provides access to radio fluxes, radio images of nuclei and jets, polarization maps, and data on the positions of bright components in jets with time intervals ranging from 5-10 days to a year between observation sessions.

In particular, the work uses data on radio fluxes (Fig. 1) and positions (Fig. 2) of bright components in the MOJAVE project jets with a resolution of up to 0.47 mas at a frequency of 15 GHz, which are presented in works of Lister et. al. (2019, 2021) and obtained from the VizieR database (Ochsenbein, 1996).

Previous works related to the study of AGN using MOJAVE data are presented in works of Zabora et al. (2022, 2023) and Zabora, Ryabov, and Sukharev (2025), which investigate the variability of radio fluxes and spatial variability of jet morphology of AGN samples.

As can be seen, the available data is in the range from 1995-04-07 to 2019-06-29, accordingly (despite the significantly longer duration of the time series), the AAVSO data was taken for the same interval (Fig. 3).

The most complete are the observations in the Johnson V filter, but they are often missing on key event dates. To ensure maximum completeness of the time series, we also include data from other photometric filters — Johnson B, Cousins I and R, Sloan i, r, g, etc.

Since we are primarily interested in the shape of the light curve during the flare, rather than the absolute magnitude values, we convert all observations to the Johnson V scale. Typically, this conversion requires color indices and spectral approximations that take into account the physical properties of the source. However, in our case, absolute accuracy is not critical—it is the structure of the light curve that matters.

Therefore, we build separate regression models of the

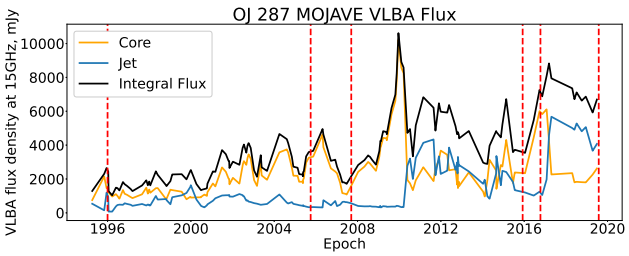

Figure 1: Radio fluxes of the core (orange), jet (blue), and total (black)

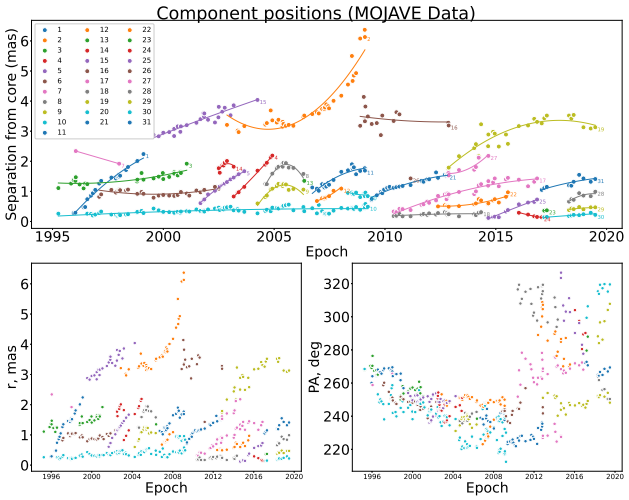

Figure 2: Position of bright components over time: sep vs time plot, distance from nucleus in mas (bottom left) and position angles in degrees (bottom right)

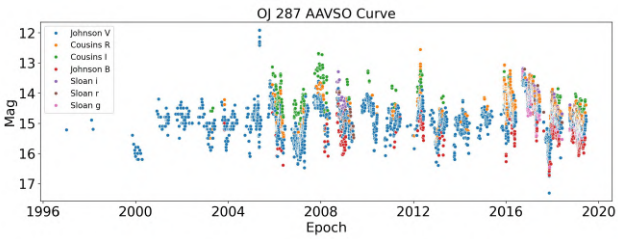

Figure 3: Light curve according to AAVSO data in Johnson V, B, Cousins I, R, B, Sloan i, r and g filters

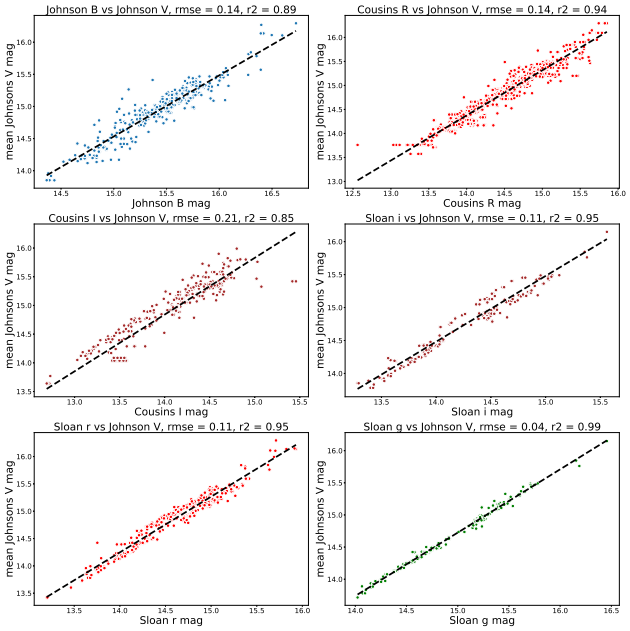

Figure 4: Calibration diagrams of the transition from alternative filters to Johnsons V and corresponding regressions

transition from each filter to Johnson V, independently of the others. This allows us to use even single observations on individual dates when only one filter is available, and to preserve maximum temporal density for subsequent paternalization.

Fortunately, the physical nature of the emission can be partially accounted for by constructing these calibration models based on data from OJ 287 itself — using those dates for which simultaneous observations are available in Johnson V and the corresponding alternative filter. For now, we limit ourselves to simple linear models and to moving from each alternative filter to Johnsons V separately, but in the future this approach can be refined or expanded (by taking into account approximated observations in additional filters and using real ones where they are available). A comparison of observations in other filters and Johnsons V, as well as regression model metrics, is given in Fig. 4, the full light curve is given in Fig. 5, and its wavelet periodogram is given in Fig. 6.

To analyze the temporal structure of periodicity in the optical and radio bands, wavelet analysis based on the Weighted Wavelet Z-Transform (WWZ) was applied, which is proposed by Foster (1996) as a wavelet transformation method for non-uniform time series. The Wavelet Transform allows to localize periods not only in frequency domain, but also in time (in contrast to the spatially/temporally global Fourier analysis). The python library libwwz (ISLA Group, University of Hawaii, 2025), which provides a robust interface for WWZ computation, was used to perform the transformation. In general, this allows to study both stable (constantly present in the signal) and temporary or evolving periods, which is critically important when studying stochastic signals such as radio fluxes or AGN light curves.

As an additional validation metric in the time-frequency analysis, the Lomb–Scargle method was used, which is a classic method for detecting periodic-

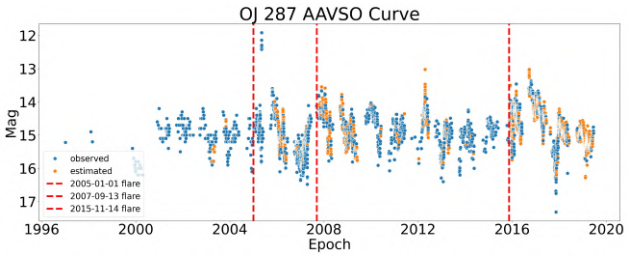

Figure 5: The full light curve, including actual observations in Johnson V (blue), approximate values based on other filters (orange), and dates of flares that fall within the corresponding range of observations (red).

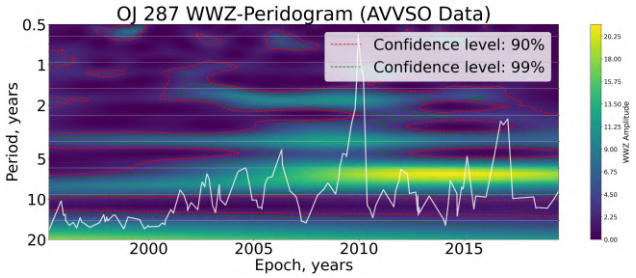

Figure 6: Wavelet periodogram of the radio nucleus OJ 287 with the radio flux curve superimposed (in white).

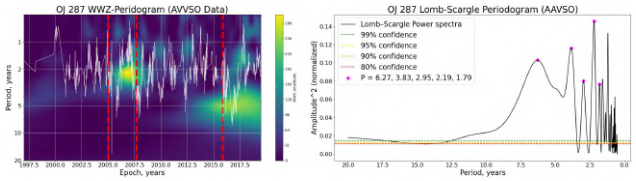

Figure 7: Periodograms: Wavelet with marked flare dates (red lines) — left and Lomb-Scargle with confidence levels (right).

ity in signals in non-uniformly distributed time series. Lomb–Scargle is a generalized Fourier transform based on a weighted harmonic approximation with a correction to the mean value (Lomb, 1976 and Scargle, 1982). In this work, the timeseries.LombScargle implementation (Astropy Collaboration, 2025) of the astropy library (Astropy Collaboration et al., 2022) was used. Cross-correlation is used to find time delays and shifts between flares.

For clustering purposes, the work uses the KMeans model, a machine learning algorithm that allows dividing data into a predetermined number of clusters with minimal internal variation by minimizing a loss function known as inertia, the sum of the distances between points in the data and their centroid (Sculley, 2010). For implementation, an implementation using the scikit-learn (2025) python library (sklearn.cluster.KMeans) is used.

3. Results

The wavelet periodogram of the core radio flux (Fig. 6) shows variability over a wide range of periods. In particular, there is a broad and long-lasting peak near $\sim 12\,\mathrm{yr}$, which is consistent with the main orbital period of the binary supermassive black hole according to the model described above. The peak at $\sim 6-7\,\mathrm{yr}$ is likely a harmonic of this main period. The $\sim 2-3\,\mathrm{yr}$ periods correspond to the intervals between flares, particularly in 2005–2007, and have resumed since ~ 2016, which is consistent with the temporal localization of the corresponding flares. The shorter periods are likely related to stochastic processes in the jet or accretion disk.

In this paper, we discuss the identification of patterns that could hint at a binary black hole in AGN. Thus, we must continue with the analysis of the optical variability, which was the first to hypothesize a binary black hole in OJ 287.

Fig. 7 shows periodograms obtained using the wavelet transform (WWZ) and the Lomb-Scargle method, based on AAVSO optical observations, reduced to a single filter and averaged daily. The detected quasi-periods of variability alone, without additional context, provide limited interpretation. However, in combination with the already known main period ($\sim 12\,\mathrm{yr}$), which manifests itself in both periodograms as a harmonic with a period of $\sim 6\,\mathrm{yr}$, the picture becomes obvious. In particular, it is worth noting the peaks in the wavelet periodogram — bursts with a period of $\sim 2-3\,\mathrm{yr}$, which are well consistent in time between consecutive OJ 287 flares and their dates. All this is also well confirmed by the Lomb-Scargle periodogram.

The light curves corresponding to the flares in the time interval considered in this work are shown in Fig. 8. Fig. 5 shows that the flare of late 2015 is the best described, so we will choose it as the basis for patterning. However, to validate the repeatability of the pattern, we will compare the corresponding light curve with two others using cross-correlation. The result of optimal superposition in this way can be seen in Fig. 9.

Thus (Fig. 9) the pattern of flares is at least approximately repeatable: all the curves considered exhibit a characteristic asymmetric morphology: rapid growth, a secondary (weaker) peak and a long slow decline within approximately the same time scales. This highlights the possibility of finding similar patterns in other binary black hole candidates in AGN, although the final verification of OJ 287-like systems will of course require

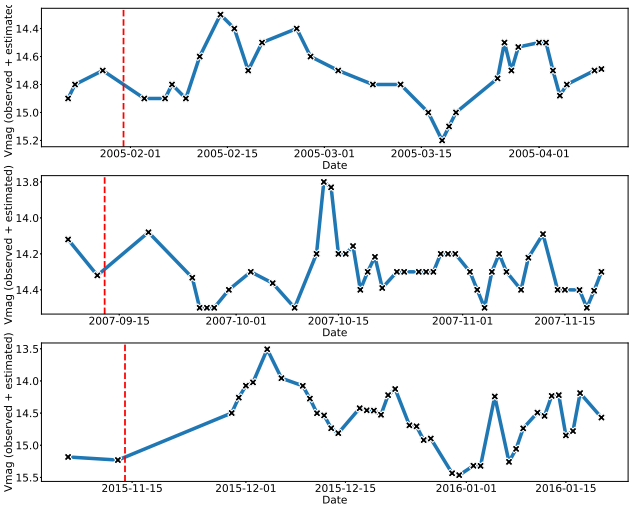

Figure 8: Light curves for the 2005, 2007, and 2015 flares, with daily averages of the data.

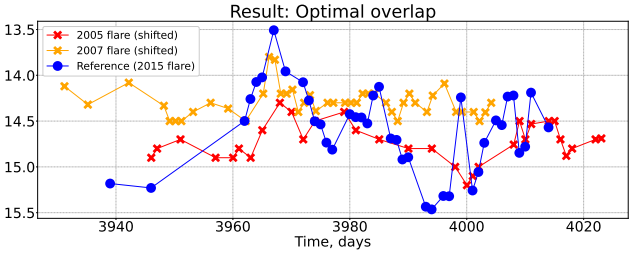

Figure 9: Optimal overlap of the 2015 reference flare (blue) and the 2005 and 2007 flares (red and orange, respectively).

additional statistical tests and simulations.

After the 2007 optical event, a radio-band flare was detected at the end of 2009 (Figs. 1 and 6). As shown in Fig. 10, the range of component position angles becomes markedly chaotic following this flare — exhibiting a significant expansion. This behavior suggests the onset of strong perturbations within the jet, likely triggered by the close passage of the secondary black hole and its gravitational impact on both the jet structure and the accretion disk.

To visualize the evolution of the jet component position angles, we employed a polar diagram (Fig. 11), where the radial coordinate corresponds to the observation index (ordered by date), and the angular coordinate represents the component's position angle. This approach enables tracking the spatiotemporal dynamics of jet morphology. In Fig. 11 (left), the time–angle diagram displays component observations grouped relative to the date of the 2009 radio flare. The same panel (right) also presents automatic clustering in the space $(n, \cos(PA), \sin(PA))$, where

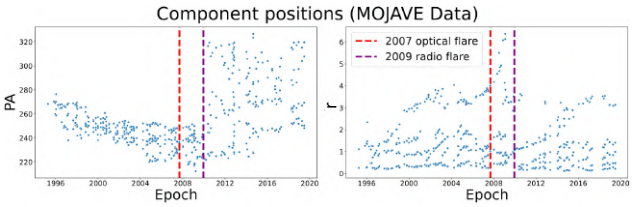

Figure 10: Diagrams of component position angles over time (left) and distances from the nucleus (right) with dates of optical (red) and radio (purple) flares.

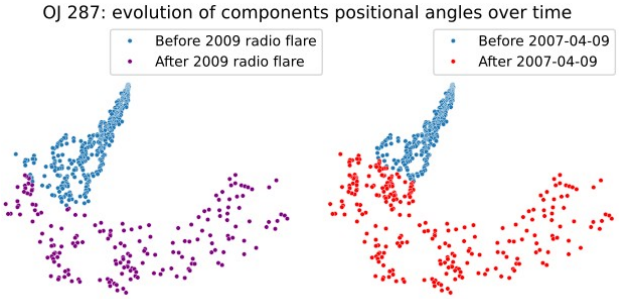

Figure 11: Time-angular visualization of the evolution of position angles of the components of the OJ 287 jet. Left: components grouped by the date of the 2009 radio burst. Right: automatic clustering.

n is the observation index. This clustering reveals the temporal location (distance on the diagram) of jet perturbation — preceding the 2007 flare, which corresponds to the approach of the secondary black hole near the accretion disk. Such a method allows the detection of structural changes in jet morphology without prior assumptions about event timing, and facilitates correlation with optical and radio features.

4. Discussion

We observe the results that we would expect: a clear connection between the temporal dynamics of optical flares, radio emission, and changes in the spatial morphology of the OJ 287 jet. Our analysis is consistent with the key tenets of the double SMBH model in OJ 287. In particular, the detection of a quasi-periodicity of about 12 years in the core radio flux is consistent with the orbital period of the secondary black hole. The peaks at 6–7 years are likely to be harmonics or related to the modulation of the accretion disk, as described in the literature.

A critically important result is the detection of a repeating asymmetric pattern of optical flares. This morphology (rapid rise, secondary peak, slow decline) is not typical of stochastic AGN variability, but is con-

sistent with the mechanism of a secondary black hole collision with an accretion disk (superflares) and subsequent accelerated accretion (tidal-induced outbursts). The repeatability of this pattern makes it a powerful indicator for searching for similar systems.

On the other hand, the analysis of changes in the position angles of the jet components (Fig. 10, 11) demonstrates a clear connection between optical events and spatial perturbations in the jet. The expansion of the range of position angles after the 2007/2009 flares indicates a significant gravitational influence of the secondary BH, which changes the conditions for launching and/or collimation of the jet. The clustering result (Fig. 11), which highlights the moment of perturbation before the 2007 optical flare, is particularly indicative. This indicates that the jet dynamics can respond to the approach of the BH companion to the accretion disk earlier than the impact/flare itself occurs in the optical range.

This time lag between the change in jet morphology, optical flare, and radio burst confirms a complex cascade of physical processes: companion approach/impact, perturbation of the accretion disk and jet; gas perturbed by the impact cools: optical flare occurs (with a delay); accretion onto the main black hole intensifies; jet activation occurs (delayed radio burst).

Limitations: The established correlations are based on a phenomenological analysis of a single object (OJ 287). To verify the reliability of these indicators (asymmetric optical pattern + characteristic change in jet angles), their application to a wider sample of AGN with signs of binarity (e.g. light curves with a periodicity of 1-10 years) is necessary. In addition, for a more accurate modeling of the transition between filters in AAVSO, nonlinear regression models or color indices should be considered.

5. Conclusions

1. Key periods of variability have been confirmed: the WWZ and Lomb–Scargle methods have detected quasi-periods of about 12 years in the radio fluxes and optical light curve of OJ 287 and its harmonics, which is consistent with the orbital period of the secondary BH.

2. A repeating pattern of optical flares is shown: light curves corresponding to periods of activity exhibit a clear asymmetric morphology (rapid rise, secondary peak, slow decline). This pattern is a characteristic manifestation of a BH companion collision with an accretion disk.

3. The relationship between optical and radio flares and jet morphology is shown: the period of optical and radio flares correlates with the appearance of significant, chaotic perturbations in the OJ 287 jet, which manifest themselves in the expansion of the range of position angles of bright components.

4. A criterion for identifying candidates has been formulated: the presence of periodicity in optics and radio with corresponding periods, characteristic asymmetric flashes in optics, a change in the orientation of components, and corresponding radio flares.

Acknowledgements. We acknowledge with thanks the variable star observations from the AAVSO International Database contributed by observers worldwide and used in this research. This research has made use of data from the MOJAVE database that is maintained by the MOJAVE team [Lister et al. 2018]. This research has made use of the VizieR catalogue access tool, CDS, Strasbourg, France (DOI: 10.26093/cds/vizier). The original description of the VizieR service was published in 2000, A&AS 143, 23.

References

Alachkar A., Ellis J., Fairbairn M.: 2023, *Phys. Rev. D*, **107**, 103033.

American Association of Variable Star Observers (AAVSO): 2025, *https://www.aavso.org/*

Astropy Collaboration: 2025, *https://docs.astropy.org/en/stable/api/astropy.timeseries.LombScargle.html*

Astropy Collaboration, Price-Whelan A.M., Lim P.L. et al.: 2022, *Astrophys. J.*, **935**, 167.

Dey L., Gopakumar A., Valtonen M. et al.: 2019, *Universe*, **5**, 108.

Foster G.: 1996, *Astron. J.*, **112**, 1709.

ISLA Group, University of Hawaii: 2025, *https://github.com/ISLA-UH/libwwz*

Komossa S., Grupe D., Parker M.L. et al.: 2021, *Mon. Not. R. Astron. Soc.*, **504**, 5575–5587.

Laine S., Dey L., Valtonen M. et al.: 2020, *Astrophys. J. Lett.*, **894**, L1.

Lehto H.J., Valtonen M.J.: 1996, *Astrophys. J.*, **460**, 207.

Lister M.L., Aller M.F., Aller H.D. et al.: 2018, *Astrophys. J. Suppl. Ser.*, **234**, 12.

Lister M.L., Homan D.C., Hovatta T. et al.: 2019, *Astrophys. J.*, **874**, 43.

Lister M.L., Homan D.C., Kellermann K.I. et al.: 2021, *Astrophys. J.*, **923**, 30.

Lomb N.R.: 1976, *Astrophys. Space Sci.*, **39**, 447–462.

Marscher A.P.: 2009, *https://arxiv.org/abs/0909.2576*

MOJAVE Team: 2025, *https://www.cv.nrao.edu/MOJAVE/allsources.html*

NASA/IPAC Extragalactic Database: 2008, *http://ned.ipac.caltech.edu/cgi-bin/objsearch?objname=OJ+287*

Ochsenbein F.: 1996, *https://vizier.cds.unistra.fr*

Scargle J.D.: 1982, *Astrophys. J.*, **263**, 835.

Scikit-learn developers: 2025, *https://scikit-learn.org/stable/modules/generated/sklearn.cluster.KMeans.html*

Sculley D.: 2010, *Proc. 19th Int. Conf. World Wide Web*, 1177–1178.

Sillanpaa A., Haarala S., Valtonen M.J. et al.: 1988, *Astrophys. J.*, **325**, 628.
Sillanpaa A., Takalo L.O., Pursimo T. et al.: 1996, *Astron. Astrophys.*, **315**, L13–L16.
Sundelius B., Wahde M., Lehto H.J. et al.: 1997, *Astrophys. J.*, **484**, 180–185.
Valtonen M.J., Lehto H.J.: 1997, *Astrophys. J.*, **481**, L5–L7.
Valtonen M.J., Lehto H.J., Sillanpaa A. et al.: 2006, *Astrophys. J.*, **646**, 36–48.
Valtonen M.J., Mikkola S., Merritt D. et al.: 2010, *Astrophys. J.*, **709**, 725–732.
Valtonen M.J., Nilsson K., Villforth C. et al.: 2009, *Astrophys. J.*, **698**, 781–785.
Valtonen M.J., Zola S., Ciprini S. et al.: 2016, *Astrophys. J. Lett.*, **819**, L37.
Zabora D., Ryabov M., Sukharev A. et al.: 2022, *Astron. Astrophys. Trans.*, **33**, 89–100.
Zabora D., Ryabov M., Sukharev A. et al.: 2023, *Odessa Astron. Publ.*, **36**, 154–160.
Zabora D., Ryabov M., Sukharev A.: 2025, *Astron. Astrophys. Trans.*, **34**, 343–362.

SUN, SOLAR ACTIVITY, SOLAR-TERRESTRIAL RELATIONS AND ASTROBIOLOGY

https://doi.org/10.18524/1810-4215.2025.38.340497

MORPHOLOGICAL FEATURES OF EXTREME GEOMAGNETIC STORM SOURCES

N. N. Kondrashova, M. N. Pasechnik

Main Astronomical Observatory, NASU, Kyiv, Ukraine,
kondr@mao.kiev.ua, rita@mao.kiev.ua

ABSTRACT. The modern world is becoming increasingly vulnerable to geomagnetic storms due to the rapid development of new technologies and technical systems. This applies to all areas of human activity where power grids, GPS, the Internet, and digital communications are used.

Storms can cause damage to the energy sector, aviation, navigation, satellite electronics, communication systems, industry, and the agro-industrial complex. Extreme geomagnetic storms can cause enormous economic damage and endanger to human health. Their prediction is very important, but not yet perfect enough.

Extreme geomagnetic storms are typically caused by coronal mass ejections (CMEs) during powerful flares. A detailed study of their sources is very important. To study the conditions that favor the occurrence of extreme storms, we selected six active regions (ARs) that were their sources in the period from 2000 to 2024. We have analyzed the spatial and temporal evolution, morphological characteristics, magnetic field structure, and flare activity of NOAA 09393, 10484, 10486, 10501, 10696, 13664. Some ARs were located in large activity complexes.

The ARs studied developed rapidly, their area and number of spots increased, their magnetic structure became more complex, and the flare activity increased. Many of these ARs had very large maximum areas exceeding 2000 millionths of a solar hemisphere. On the days when the eruptions occurred the ARs were located near the central meridian, and the Bz-component of the interplanetary magnetic field was directed south. Their area and spot number were close to their maximum, the magnetic configuration was βγδ in most cases. The sources of the CMEs were M and X class flares, which were preceded by the rapid emergence of new magnetic fluxes and their reconnection with the existing magnetic field of the region.

The most powerful geomagnetic storms during the considered period with a minimum DST index less than -400 nT were observed on November 20, 2003 and May 10–11, 2024. These storms were caused by CMEs from flares occurred in ARs 10501 and 13664. These ARs were characterized by complex magnetic topology and rapid magnetic flux emergence. The storm on May 10–11, 2024, was preceded by cannibal CMEs that enhanced its strength and duration. The most powerful storm of the period under review, on November 20, 2003, with a peak Dst index of -422 nT, was caused by a CME from an M3.9 flare in the AR NOAA 10501. During the storm's peak, auroras were observed as far south as Florida, Michigan, and Wisconsin in the United States and Greece in Europe. It was found that AR with a small area and moderate flares can produce extreme storms, while ARs with large areas and with powerful flares do not always.

Keywords: Sun, active regions, sunspots, solar flares, coronal mass ejections, geomagnetic storms.

АНОТАЦІЯ. Сучасний світ стає дедалі вразливішим до геомагнітних бур через швидкий розвиток нових технологій та технічних систем. Це стосується всіх сфер людської діяльності, де використовуються енергетичні мережі, GPS, Інтернет та цифровий зв'язок. Бурі можуть завдати шкоди енергетиці, авіації, навігації, супутниковій електроніці, системам зв'язку, промисловості та агропромисловому комплексу. Екстремальні геомагнітні бурі можуть завдати величезної економічної шкоди та загрожувати здоров'ю людини. Їх прогнозування дуже важливе, але ще недостатньо досконале.

Екстремальні геомагнітні бурі зазвичай спричинені викидами корональної маси (КВМ) під час потужних спалахів. Детальне дослідження їх джерел є дуже важливим. Для вивчення умов, що сприяють виникненню екстремальних штормів, ми вибрали шість активних областей (АО), які були їх джерелами у період з 2000 по 2024 рік. Ми проаналізували просторову та часову еволюцію, морфологічні характеристики, структуру магнітного поля та спалахову активність АО NOAA 09393, 10484, 10486, 10501, 10696, 13664. Деякі АО знаходилися у великих комплексах активності.

Досліджувані АО розвивалися швидко, їхня площа та кількість плям збільшувалися, магнітна структура ставала складнішою, а спалахова активність зростала. Багато з цих АО мали дуже велику максимальну площу, що перевищувала 2000 мільйонних часток сонячної півкулі. У дні виверження АО розташовувалися поблизу центрального меридіана, а Bz-компонент міжпланетного магнітного поля був спрямований на південь. Їхня площа та кількість плям були близькими до максимуму, магнітна конфігурація в більшості випадків була βγδ. Джерелами КВМ були спалахи класу M та X, яким передував швидкий вихід нових магнітних потоків та їх перез'єднання з уже існуючим магнітним полем області.

Найпотужніші геомагнітні бурі за розглянутий період з індексом геомагнітної активності Dst менше -400 нТл спостерігалися 20 листопада 2003 року та 10–11 травня

2024 року. Бурі були спричинені корональними викидами маси від спалахів, що сталися в АО NOAA 10501 та 13664. Ці АО характеризувалися складною магнітною топологією та швидким виходом магнітного потоку. Бурі 10–11 травня 2024 року передували КВМ типу «канібалізм», які посилили її силу та тривалість. Найпотужніший шторм розглянутого періоду, 20 листопада 2003 року, з піковим індексом Dst = -422 нТл, був спричинений КВМ від спалаху M3.9 в АО NOAA 10501. Під час піку шторму полярні сяйва спостерігалися аж до Флориди, Мічигану та Вісконсина у Сполучених Штатах та Греції в Європі. Було виявлено, що АО з невеликою площею та помірними спалахами можуть спричиняти екстремальні шторми, тоді як АО з великою площею та потужними спалахами не завжди їх викликають.

Ключові слова: Сонце, активні області, сонячні плями, сонячні спалахи, викиди корональної маси, геомагнітні бурі.

1. Introduction

Extreme geomagnetic storms can cause enormous economic damage and threaten human health. The modern world is becoming increasingly vulnerable to geomagnetic storms due to the rapid development of new technologies and technical systems. The first extreme space weather event was observed in early September 1859 by Carrington (Carrington, 1859) and Hodgson (Hodgson, 1859). A very powerful flare on September 1, 1859, caused a severe geomagnetic storm that disrupted telegraph communications in Europe and North America. Auroras were observed all over the world. The Dst (Disturbance Storm Time Index) peak, which provides information about the strength of the ring current around the Earth, was estimated to have ranged from -900 nT to -1640 nT. The X-ray class of the flare that caused the storm is estimated to be X64.4 or ≈X80. Other extreme events were the event of May 13, 1921 (peak Dst=-907 nT), the Fatima geomagnetic storm of January 25-26, 1938. Since 1957, the beginning of the space era, extreme storms with a peak Dst index below -400 nT, were the events of September 13, 1957 (peak Dst = -427 nT), February 11, 1958 (peak Dst = -426 nT), July 15, 1959 (peak Dst = -429 nT). The most powerful geomagnetic storm since that time was the Quebec March 13-14, 1989 (peak Dst = -589 nT).

Forecasting extreme geomagnetic storms is very important, but not yet perfect. To study the conditions that contribute to the occurrence of extreme storms, we selected six active regions that were their sources between 2000 and 2024. We analyzed the spatial and temporal evolution, morphological characteristics, magnetic field structure, and flare activity of NOAA ARs 09393, 10484, 10486, 10501, 10696, 13664. These ARs were the sources of geomagnetic storms with a minimum Dst index near -400 nT.

Magnetograms, continuum images of these ARs were provided by the Solar and Heliospheric Observatory (SOHO) Michelson Doppler Imager (MDI) and the Solar Dynamics Observatory (SDO) Helioseismic and Magnetic Imager (HMI). X-ray data were acquired on the Geostationary Operational Environmental Satellite (GOES). Data on the solar flares are taken from the site https://www.lmsal.com/solarsoft/latest_events_archive.html and data on SMEs and their impact on Earth from the site https://www.swpc.noaa.gov. NOAA's Space Weather Prediction Center (SWPC) is a division of the National Weather Service. Dst indexes of geomagnetic activity are taken from the site of Kyoto geophysical observatory https://wdc.kugi.kyoto-u.ac.jp/dst_final/index.html.

2. Extreme geomagnetic storms of November 20, 2003 and May 10-11, 2024

The most powerful geomagnetic storms since 2000 were the storms on November 20, 2003 and May 10-11, 2024. The geomagnetic storm of May 10-11, 2024, with a peak Dst index of -412 nT, was the most powerful storm since the 2003. This storm was produced by a Carrington-type active region NOAA 13664. The topology of the magnetic field of the active region based on data from the SDO observatory was studied in (Jarolim et al., 2024, Jaswal et al., 2024, Mac Taggart et al., 2024, Romano et al., 2024). The evolution of coronal mass ejections (CMEs) and their geoeffectiveness are reviewed in (Hayakawa et al., 2024, Liu et al., 2024, Wang et al., 2024).

Super active region NOAA 13664 appeared in the southern hemisphere of the solar disk on May 1, 2024, during the phase of increasing solar activity near the maximum of the 25th solar activity cycle. AR 13664 developed very quickly until May 8, 2024. The number of sunspots and the area of AR increased rapidly. From May 4th to 8th, the area of the AR increased from 240 to 630 millionths of the solar hemisphere (designation in the figures – m. s. h.), and the number of sunspots increased from 16 to 37 (Fig. 1b). The maximum area of 2400 millionths of the solar hemisphere was observed on May 11, and the maximum number of sunspots was 81 on May 10.

HMI magnetograms AR 13664, obtained by the SDO on May 6, 7 and 8, 2024, show that the structure of the AR magnetic field changed during this period and became very complicated, of βγδ class (Fig. 1a). On May 6, a new bipole emerged on the AR eastern side, and to the east of it, a small bipolar AR NOAA 13668 appeared nearby. An active complex was formed from these two regions. Fig. 1a also shows the emergence of a bipole with different polarities in the southern and central parts of the AR. Magnetic reconnections began, which caused the powerful flares. On May 8 a series of M- and X-class flares occurred in the AR (Fig. 1c), causing coronal mass ejections, which resulted the extreme geomagnetic storm began on May 10. MacTaggart et al. (2024) showed that an emerging bipole of twisted magnetic field was the source of the X1 flare and the first halo CME. As the authors established, it was a twisted magnetic tube, which subsequently erupted. The event was classified as a G5 geomagnetic storm. The storm became sixth extreme since the beginning of the space age. Proton storm with intensity S2 began on May 10 too. Some CMEs catching up and merged with previous ones to form a cannibal CME, which intensified and prolonged the storm (Liu et al., 2024; Wang et al., 2024). Other cases of cannibal CMEs formation have been studied, for example, in (Soni

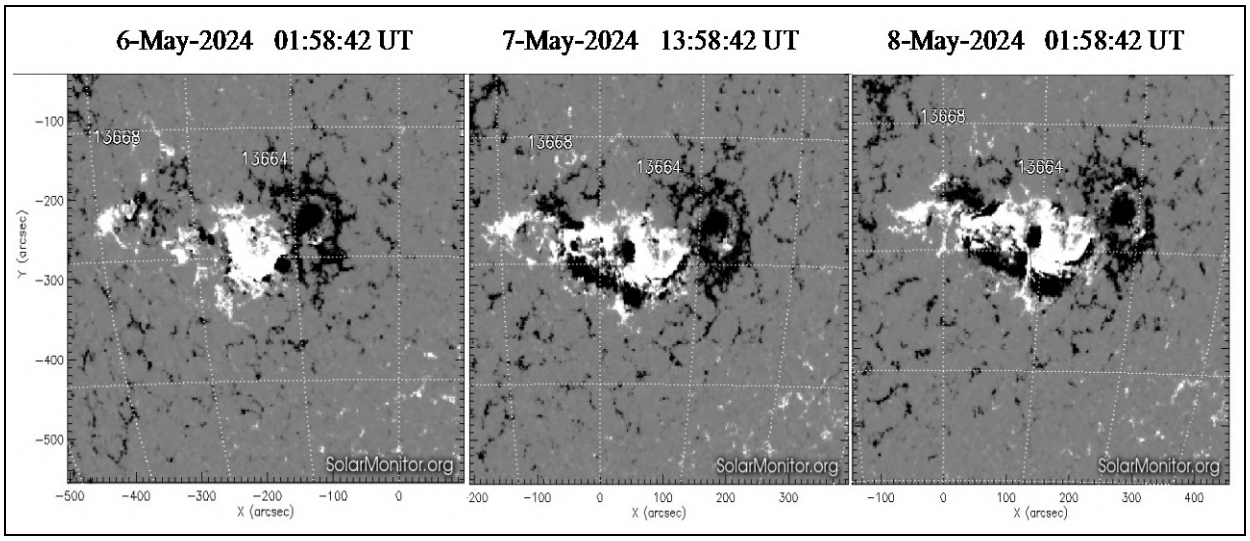

Figure 1a: AR13664 magnetograms obtained with the SDO/HMI instrument on May 6, 7 and 8, 2024. The positive and negative polarities are indicated by white and black colors, respectively.

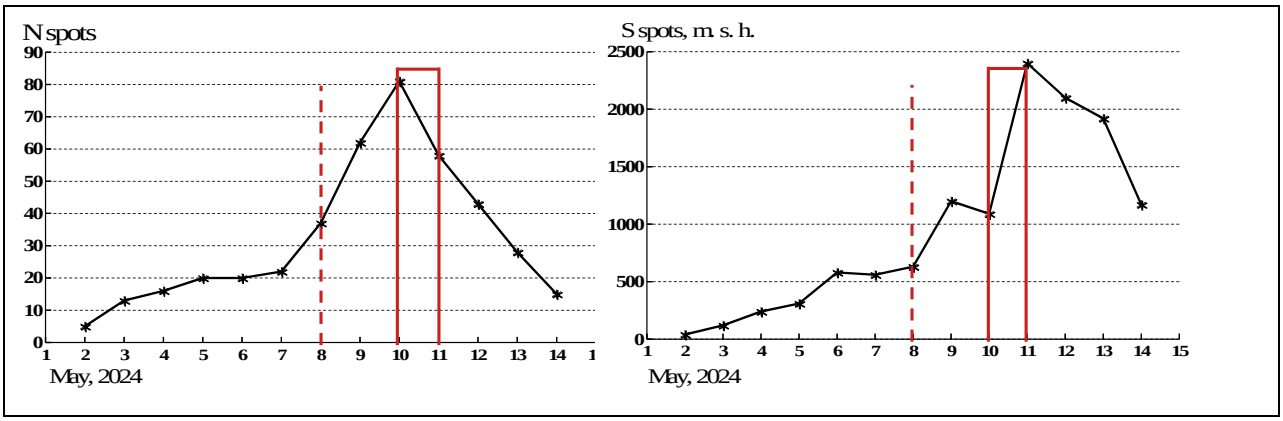

Figure 1b: Change in the number of sunspots (N) and the area occupied by them (S, m. s. h. is S, millionths of the solar hemisphere) during the first passage of AR13664 across the Sun's disk. The start time of the CME is marked by vertical dashed lines, the time of the storm by solid lines.

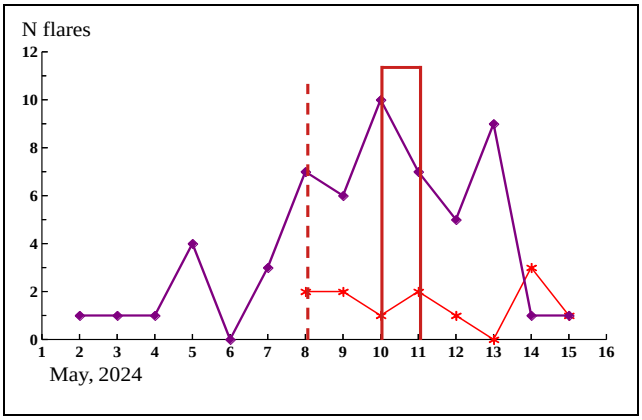

Figure 1c: Change in the number of M (purple curve) and X (red curve) class flares (N flares) over time in AR 13664. The start time of the CME is marked by vertical dashed lines, the time of the storm by solid lines

et al., 2024). The authors found that cannibal CMEs from AR 12887 interacting with CME from AR 12891 demonstrated increased geoeffectiveness compared to individual CMEs.

The geomagnetic storm ended on May, 12. It caused power outages and disrupted GPS and high-frequency radio communications. Auroras were seen in Europe, Asia, Mexico, and all 50 U. S. states, including Hawaii. Auroras were seen as far away as London and near San Francisco, California, as well as in many parts of Ukraine. AR 13664 passed across the solar disk two more times, but there were no more powerful ejections from it towards Earth. The development of the region in subsequent passages across the solar disk is described in (Kondrashova et al., 2024).

The most powerful geomagnetic storm since 2000 with a peak Dst index of -422 nT was on November 20, 2003. Its source was AR NOAA 10484 in its second pass across the Sun's disk. AR 10484 appeared on October 18, 2003

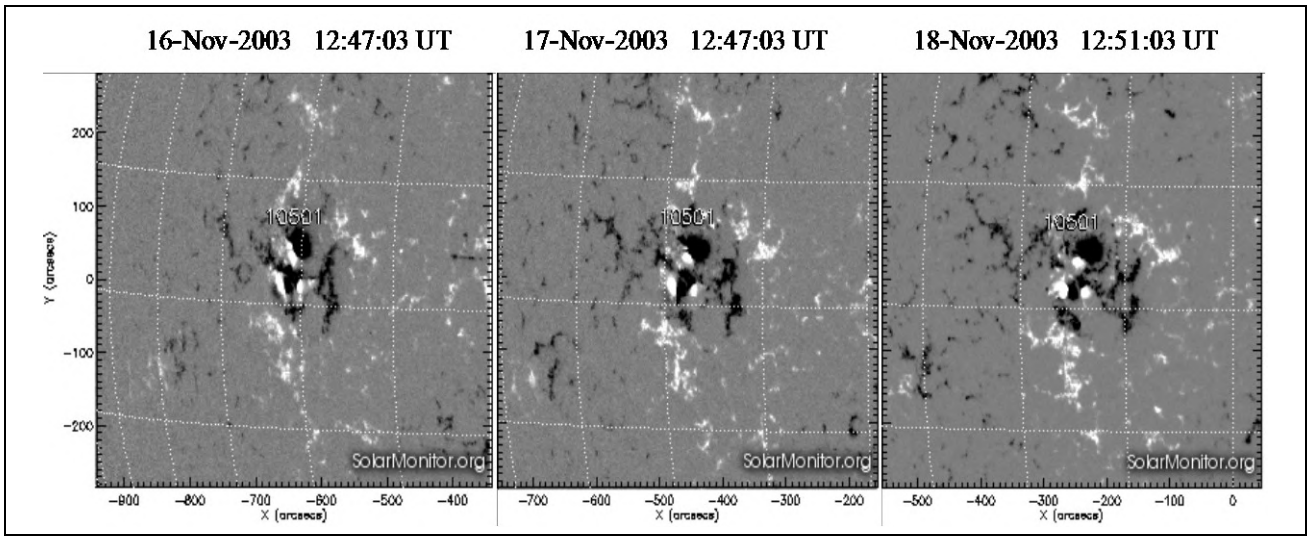

Figure 2a: MDI magnetograms for AR10501 on November 16, 17 and 18, 2003.

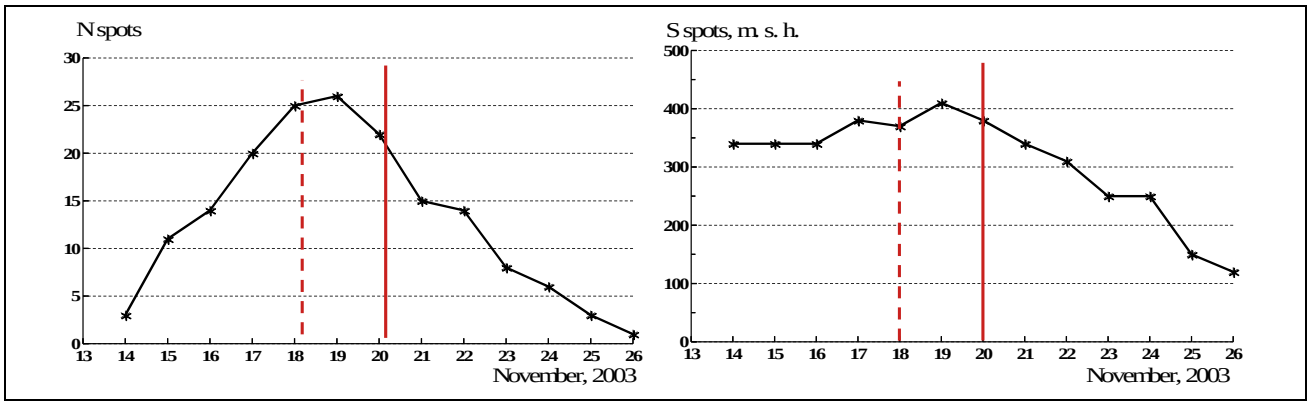

Figure 2b: the same as in Figure 1a, but in AR10501.

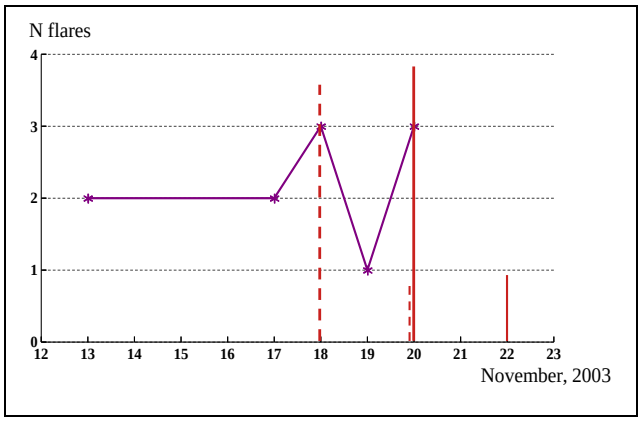

Figure 2c: Change in the number of M (purple curve) class flares (N flares) over time in AR10501.

during the declining phase of the 23rd solar cycle in the northern hemisphere of the solar disk and passed across the disk until October 31, 2003. Its maximum area was 1750 millionths of the hemisphere, and the maximum number of sunspots was 69. It had a complex magnetic configuration of the βγδ class. On October 19, 22, and 26, powerful X and M flares occurred in the AR, triggering CMEs. Despite this, no major geomagnetic storms occurred. On October 19 and 26, the region was located at the edges of the disk, and the ejections were directed past Earth. On October 22, the Bz component of the interplanetary magnetic field was directed north.

In the second pass through the disk, AR 10484 was renumbered as NOAA 10501. The AR 10501 passed across the solar disk from November 13 to November 26, 2003. On November 18, it experienced an M3.9 flare, which caused a powerful CME. Fig 2a shows the magnetograms obtained with the SOHO/MDI instrument on November 16-18, 2003, before the storm on November 20. The magnetic field configuration of the region was of βγ class, and became more complex on November 19 to the βγδ class. Fig. 2b, and Fig. 2c shows the changes in the number of sunspots, area, and the number of M class flares over time in AR 10501. The maximum number of sunspots was 26 and the area maximum was 410 millionths of the solar hemisphere on November 19. On November 18, the number of sunspots was 25 and the area was 370 millionths of the solar hemisphere. The flares of M1.8, M3.2 and M3.9 occurred in AR 10501 on this day.

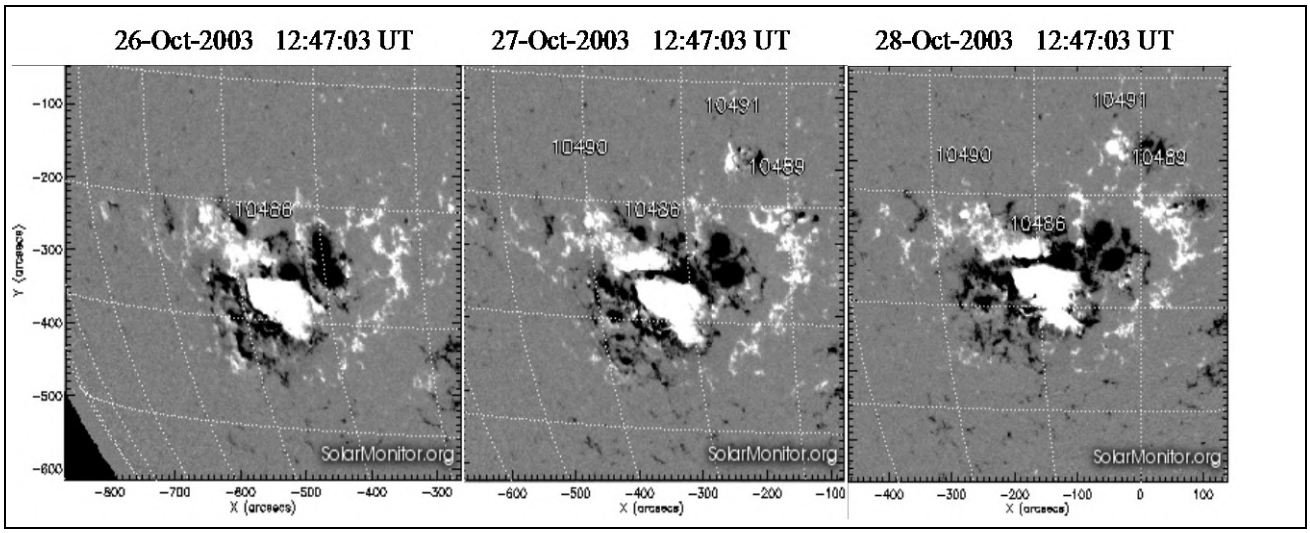

Figure 3a: MDI magnetograms for AR10486 on October 26, 27 and 28, 2003.

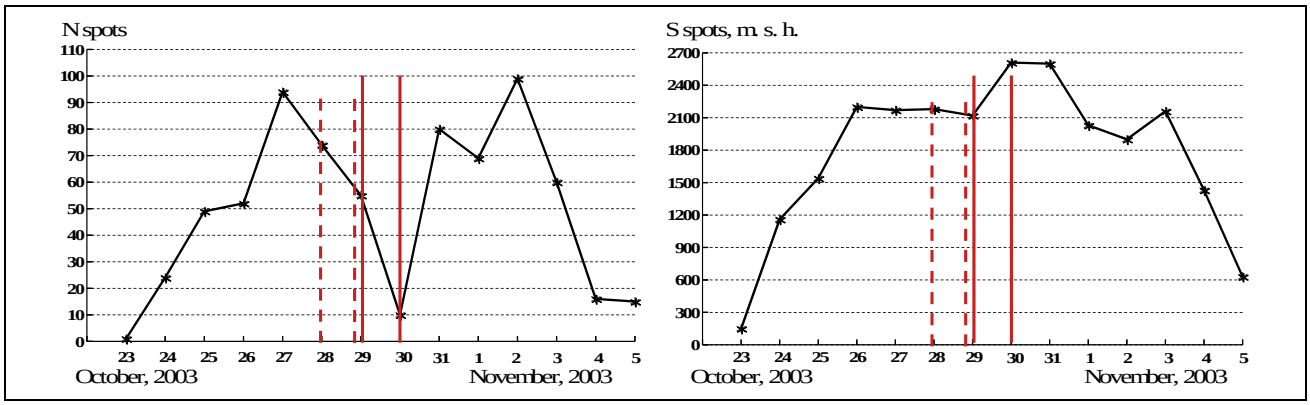

Figure 3b: the same as in Figure 1b, but in AR10486.

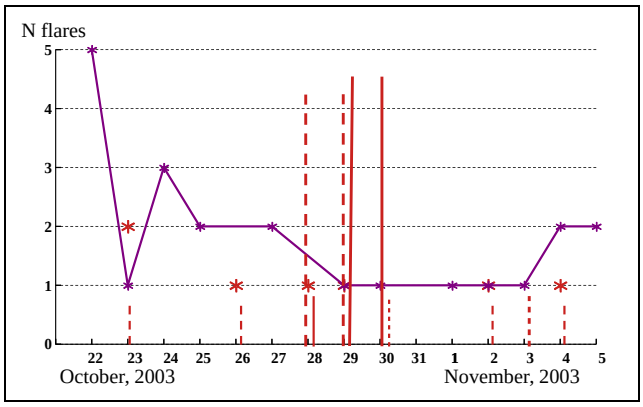

Figure 3c: Change in the number of M (purple curve) and X (red stars) class flares (N flares) over time in AR10486.

The extreme geomagnetic storm on November 20, 2003 became the fifth since 1957, the beginning of the space age. It was accompanied by a proton storm. During the peak of the storm, auroras were seen as far south as Florida, Michigan, and Wisconsin in the United States and Greece in Europe. In the days leading up to the storm, the solar wind stream affected the Earth's magnetic field, causing weak geomagnetic storms. The magnetosphere was already agitated, which may have intensified the extreme storm. Raghav et al. (2023) suggested that the CME that led to the November 20 event had an extremely flattened structure. It had less adiabatic expansion than usual in the compressed direction, which led to a strong magnetic field strength, high plasma density, high solar wind speed, high dynamic pressure, and a strong interplanetary electric field to the east. This may have contributed to the efficient transfer of plasma and energy to the Earth's magnetosphere.

3. Other extreme geomagnetic storms that occurred during the study period

NOAA 10486 was the most active region of Cycle 23 and was characterized by high flare activity. During its passage across the solar disk, it produced 7 X-class flares, about two dozen M-class flares, and 6 CMEs. The most powerful flares ever recorded occurred in it. It passed across the solar disk from October 23 to November 4, 2003 in the declining phase of the 23rd solar cycle. AR 10486 was part of a large active complex. The structure of the region was rapidly changing and becoming more complex. Its area and sunspot number increased rapidly

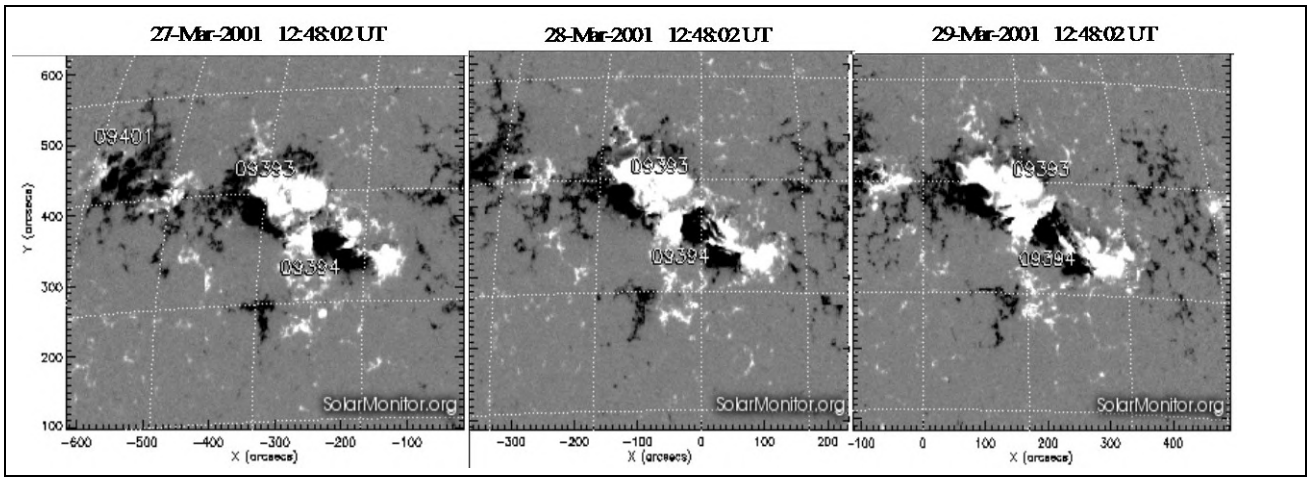

Figure 4a: MDI magnetograms for AR09393 on March 27, 28 and 29, 2001.

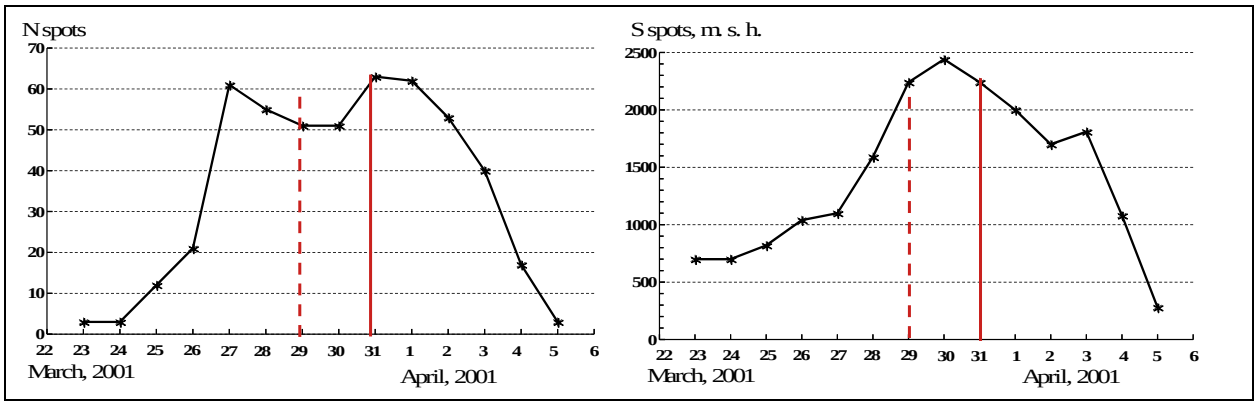

Figure 4b: the same as in Figure 1b, but in AR09393.

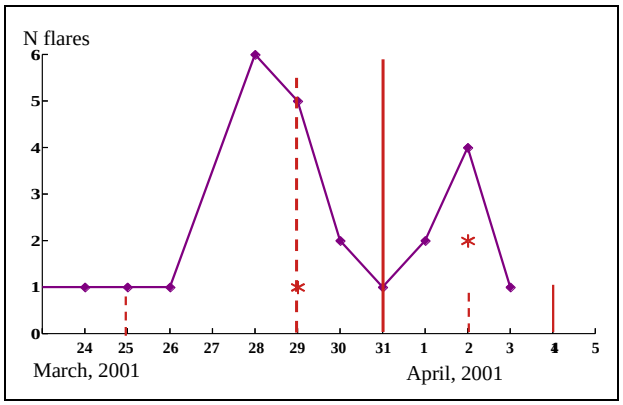

Figure 4c: the same as in Figure 3c, but for AR09393.

over time. The magnetic field structure changed over time and became increasingly complex. Magnetograms of the AR 10486 show the penetration of negative polarity to positive (Fig. 3a). The magnetic field configuration of the region was of class βγδ. The activity of the AR has increased with the appearance of δ-sunspots. On October 28, a flare X17 class occurred in the region, and on October 29, a flare X10 class. CMEs from these flares caused two geomagnetic storms with the minima Dst index of -353 nT and -383 nT on October 30. The changes in the number of sunspots, area, and the number of M and X class flares over time in AR 10486 are presented in Fig 3b and Fig 3c. The maximum number of sunspots was 99 and the area maximum was 2610 millionths of the solar hemisphere. On November 4, 2003 the X18+ flare caused a powerful CME, but there was no geomagnetic storm because the region was at the edge of the solar disk.

The AR 09393 was also very active. 24 M-class flares and 3 X-class flares occurred in it. It appeared on March 23, 2001 near the maximum of the 23rd solar cycle in the north hemisphere of the solar disk and passed along the disk to April 5, 2001. The region was part of a very large active complex. The magnetic field configuration of the region by March 25th had become more complex, from βγ to βγδ. Magnetograms of the AR obtained on March 27-29, 2001, before the CME, show penetration of negative polarity into positive polarity in several places (Fig. 4a). It is known that when δ-sunspots containing opposite polarities appear, powerful flares can occur. On March 28 the number of powerful flares has increased sharply. The powerful flares M4.3 on March 28 and X1.7 on March 29

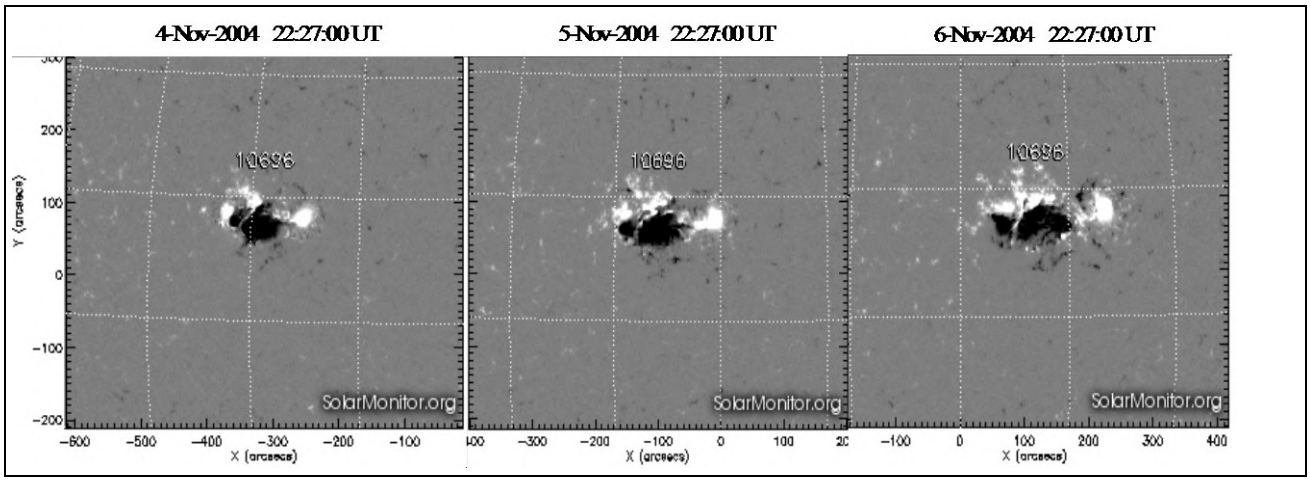

Figure 5a: MDI magnetograms for AR10696 on November 4, 5 and 6, 2004.

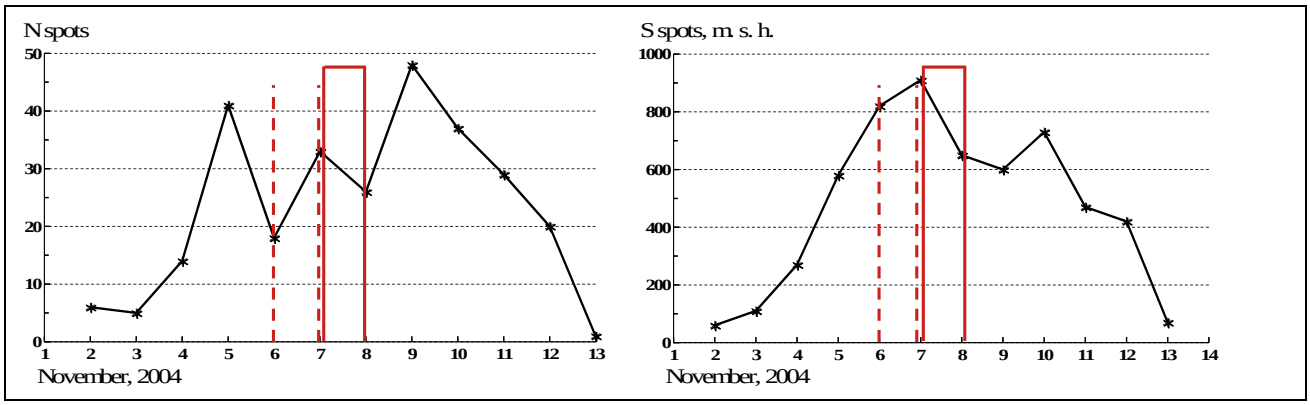

Figure 5b: the same as in Figure 1b, but in AR10696.

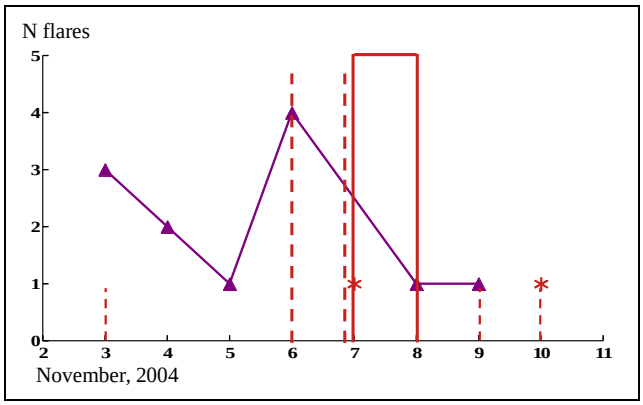

Figure 5c: the same as in Figure 3c but for AR10696.

in AR caused CMEs. The extreme storm with a minimum Dst of -387 nT began at 01:00 UT on March 31st when the first CME struck Earth's magnetosphere. A second CME struck magnetosphere at ~22.00 UT on March 31th and caused less strong storm with a peak Dst index of -284 nT. As the CME passed Earth, the interplanetary magnetic field suddenly turned north. X1.7 flare triggered a day-long S1-class proton storm. Changes in the number of sunspots, area and flares number in the AR 09393 region are shown in Fig. 4b and Fig. 4c. The maximum number of sunspots was 63 on March 31 and the area maximum was 2440 millionths of the solar hemisphere on March 30. On April 2, 2001, the most powerful X20-class solar flare since 1976 occurred, causing a powerful CME, but this region was at the edge of the disk, and a storm did not occur.

The AR 10696 produced 14 powerful flares of M and X class and six CMEs. It passed across the solar disk from November 1 to November 13, 2004, during the declining phase of the 23rd solar cycle, in the northem hemisphere. The region was growing rapidly. The structure of the magnetic field gradually became more complex. In the first days of the AR passage across the solar disk, the configuration of its magnetic field was of β class, and by November 5 it was already of βγδ class (Fig. 5a). The area and the number of sunspots were increasing (Fig 5b and Fig. 5c). The maximum number of sunspots was 48 and the area maximum was 910 millionths of the solar hemisphere. The number of powerful flares increased on November 6. On this day AR 10696 produced four powerful flares. M9.3-class flare erupted by CME, which caused extreme geomagnetic storm. The storm began at 22:00 UT on November 7, and Dst index reached a minimum of -374 nT on November 8. Auroras were observed as far south as Alabama and California in the United States.

4. Conclusion

Although extreme geomagnetic storms are rare, they cause enormous economic losses and pose a threat to human health. Their study and prediction is extremely important. In this work, we identified typical features of active regions where coronal mass ejections occurred, causing extreme geomagnetic storms, as follows:

– Active regions studied developed very quickly, their area and the number of sunspots increased rapidly.

– These ARs typically had a complex magnetic field configuration of βγδ class.

– They were often part of activity complexes.

– Their area, the number of sunspots and flares, on the day when a coronal mass ejection occurred were, close to the maximum.

– The flare activity of the ARs, caused by the emergence of new magnetic fluxes and their reconnection with the magnetic field of these regions, increased several days before the ejections. The ARs became the source of high-intensity flares of classes M and X. Whole series of powerful flares often occurred. Powerful flares created the largest CMEs and associated extreme geomagnetic storms.

– Cannibal CMEs increased the power and duration of the geomagnetic storms.

– The AR location near the central meridian contributes to greater geoeffectiveness of the CME.

– ARs with a small area and moderate flares can sometimes produce extreme storm.

Forecasting CMEs and storms is complicated by the many factors that contribute to their occurrence and determine their powerful. Improving the quality of forecasts requires improved ground-based and space-based observation techniques, as well as a comprehensive and detailed study of the magnetic field and morphological characteristics of the active regions, including those discussed in this paper. They can be useful in the extreme storms forecasting modeling, including using machine learning.

Acknowledgments. The authors are grateful to the referee for providing useful comments, which helped improve the quality of the manuscript. We thank the observing teams at the Kyoto geophysical observatory, SOHO, SDO, and GOES for providing free access to their results.

References

Carrington R. C.: 1859, *MNRAS*, **20**, 13.

Hayakawa H., Ebihara Y., Mishev A. et al.: 2025, *ApJ*, **979**, 49.

Hodgson R. M.: 1859, *MNRAS*, **20**, 15.

Jarolim R., Veronig A., Purkhart S. et al.: 2024, preprint (arXiv:2409.08124).

Jaswal P., Sinha S., Nandy D.: 2024, preprint (arXiv:2409.14752).

Kondrashova N. M., Pasechnik M. M., Osipov S. M. et al.: 2024, *OAP*, **37**, 112.

Liu Y. D., Hu H., Zhao X. et al.: 2024, *ApJ L*, **974**, L8.

MacTaggart D., Williams T., Aslam O.P.M.: 2024, preprint (arXiv:2410.15964)

Romano P., Elmhamdi A., Marassi A. et al.: 2024, *ApJ L*, **973**, L31.

Raghav A., Shaikh Z., Vemareddy P. et al.: 2023, *SoPh*, **298**, 64.

Soni S. L., Maharana A., Guerrero A. et al.: 2024, *A&A*, **686**, A23.

Wang R., Liu Y. D., Zhao X. et al.: 2024, *A&A*, **692**, A112.

https://doi.org/10.18524/1810-4215.2025.38.341400

NORTH-SOUTH ASYMMETRY OF SUNSPOT ACTIVITY DURING THE MAUNDER MINIMUM

V. N. Krivodubskij

Astronomical Observatory, Taras Shevchenko National University of Kyiv, Kyiv, Ukraine
krivod2@ukr.net

ABSTRACT. An important key to studying the impact of solar activity variations on the Earth's climate is the Maunder Minimum (late 17th century), during which extremely little sunspots were observed. Applying the rare event analysis method to these observations led the researchers to conclude that the appearance of sunspots during the Maunder minimum had a weak amplitude 22-year cycle. The concept of continuity of magnetic cycles at this time is also confirmed by measurements of cosmogenic radionuclides in natural terrestrial archives. Therefore, today it is believed that during the Maunder Minimum, the cyclic magnetic activity of the Sun did not stop, although the amplitude of the cycles was quite low. In the αΩ dynamo model, this may be due to the fact that the magnitude of the magnetic induction of the toroidal field, excited by radial differential rotation in the solar convection zone (SCZ), at this time did not reach the threshold value required for lifting magnetic power tubes to the solar surface (nonlinear dynamo mode). Possible physical mechanisms describing the suppression of the dynamo process at time intervals, when no sunspots were observed, are analysed. A scenario for explaining the north-south asymmetry of magnetic activity during the Maunder Minimum is proposed. A key role in the proposed scenario is played by the special nature of the internal rotation of the Sun, revealed in the helioseismological experiments. According to helioseismology data, the SCZ is naturally divided into polar and equatorial domains with opposite signs of the radial angular velocity gradient. In addition, the radial angular velocity gradient penetrates into the deep layers of the stable radiant zone below the SCZ. It is shown that, taking into account these helioseismology data, the αΩ dynamo excites two harmonics (dipole and quadrupole) of the toroidal magnetic field in the SCZ, which cyclically change their direction. The αΩ dynamo excites two harmonics (dipole and quadrupole) of the toroidal field in the RMS, which cyclically change their direction. At the same time, the deep Ω effect in the radiant zone creates the toroidal field of stationary orientation. The summary toroidal magnetic field (the dynamo-field of the SCZ + the field of the radiant zone) rising to the Sun's surface due to magnetic buoyancy may contribute to the north-south asymmetry in sunspot activity.

Key words: sunspots, the Sun's magnetic cycle, the convection zone, differential rotation, dynamo, the radiant zone, helioseismological data.

АНОТАЦІЯ. Важливим ключем до вивчення впливу варіацій сонячної активності на клімат Землі є мінімум Маундера (кінець XVII століття), під час якого спостерігалося надзвичайно мало сонячних плям. Застосування методу аналізу рідкісних подій до цих спостережень призвело дослідників до висновку, що появі сонячних плям у мінімумі Маундера був притаманний слабкий за амплітудою 22-річний цикл. Концепція безперервності магнітних циклів у цей час також підтверджується вимірюваннями космогенних радіонуклідів у природних наземних архівах. Тому сьогодні вважається, що впродовж мінімуму Маундера циклічна магнітна активність Сонця не припинялася, хоча амплітуда циклів була досить низькою. У моделі αΩ-динамо це може бути пов'язано з тим, що величина магнітної індукції тороїдального поля, збудженого радіальним диференціальним обертанням у сонячній конвективній зоні (СКЗ), у цей час не досягла порогового значення, необхідного для підйому магнітних силових трубок на поверхню Сонця (нелінійний режим динамо). Проаналізовано можливі фізичні механізми, що описують пригнічення процесу динамо в інтервали часу, коли сонячних плям не спостерігалося. Запропоновано сценарій для пояснення північно-південної асиметрії магнітної активності впродовж мінімуму Маундера. Ключову роль у запропонованому сценарії відіграє особливий характер внутрішнього обертання Сонця, виявлений в геліосейсмологічних експериментах. Згідно з даними геліосейсмології СКЗ природно поділена на полярні і екваторіальні домени з протилежними знаками радіального градієнта кутової швидкості. Крім того, радіальний градієнт кутової швидкості проникає у глибинні шари стабільної променистої зони нижче СКЗ. Врахувавши ці дані показано, що αΩ-динамо збуджує дві гармоніки (дипольну та квадрупольну) тороїдального поля в СКЗ, які циклічно змінюють свій напрямок. Водночас глибинний Ω-ефект у променистій зоні створює тороїдальне поле стаціонарної орієнтації. Сумарне магнітне тороїдальне поле (динамо-поле СКЗ + поле променистої зони), що піднімається до поверхні Сонця завдяки магнітній плавучості, може сприяти північно-південній асиметрії активності сонячних плям.

Ключові слова: сонячні плями, магнітний цикл Сонця, конвективна зона, диференційне обертання, динамо, променista зона, геліосейсмологічні дані.

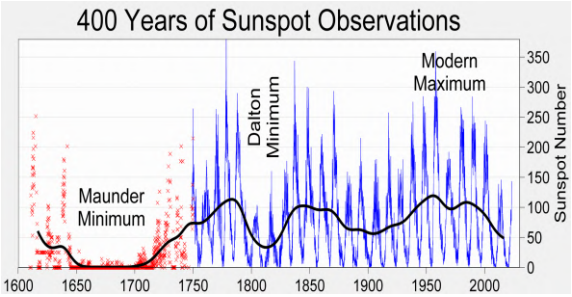

Figure 1: Long-term variations in solar activity.

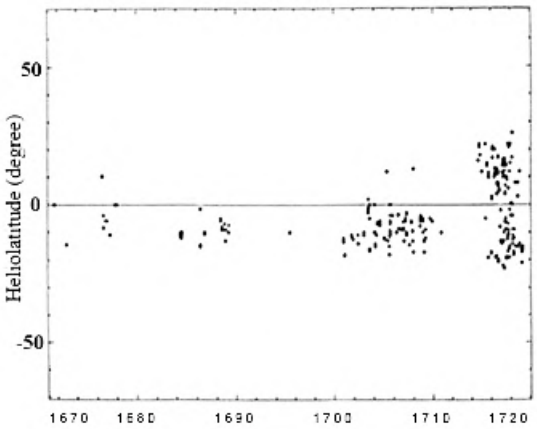

Figure 2: Butterfly diagram of sunspot, Paris archives: 1670-1719 (Sokoloff & Nesme-Ribes, 1994).

The Maunder Minimum was a period of long-term decrease in the number of sunspots from approximately 1645 to 1715 (Fig. 1). This was first noted by F. Spörer (1887) while processing the observational data of R. Wolf (1868). Spörer's work was soon summarized by E. Maunder (1894) and Clerke A. M. (1894).

For a long time, the anomaly of solar activity did not arouse the keen interest of researchers. And only almost a century later, interest in the problem was revived by John Eddy (1976), who published a number of additional evidence regarding the sharp weakening of the solar activity in the period 1645–1715, calling it the Maunder Minimum.

(In honor of the couple Annie (1868–1947) and Edward (1851–1928) Maunder, who studied archives of solar observations on changes in the location of sunspots on the solar surface over time). According to Maunder calculations, only about 50 sunspots were observed during this period instead of the usual 40-50 thousand. The decrease in solar activity during the Maunder period was later confirmed by analysis of the radionuclides ^{10}Be (in trees) and ^{14}C (in glaciers) whose origin is associated with the penetration of cosmic rays into the Earth's atmosphere. Using the rare event analysis method during these observations, Sokoloff (2004) concluded that the appearance of sunspots during the Maunder Minimum had a weak amplitude 22-year cycle. The concept of the continuity of magnetic cycles is also confirmed by measurements of cosmogenic radioisotope proxies ^{10}Be and ^{14}C in natural terrestrial archives. Therefore, it is generally accepted that during the Maunder Minimum, the cyclic magnetic activity of the Sun did not stop, although the amplitude of the cycles was quite low (Wang & Sheeley, 2003). The most widespread belief among researchers is that the solar magnetic cycle is triggered by the $\alpha\Omega$ dynamo process (Vainshtein, Zeldovich & Ruzmaikin, 1980). For the $\alpha\Omega$ dynamo model, the Maunder Minimum explanation may be the fact that the magnitude of the magnetic induction of the toroidal field, excited by the radial differential rotation in the SCZ, did not reach the threshold value necessary for the lifting of the magnetic force tubes to the solar surface (nonlinear dynamo mode) at this time. Research over the past decade has shown that modern dynamo models can reproduce the Maunder Minimum under specific initial conditions. It can be assumed, for example, that the absence of sunspots at this time is mainly due to changes in the field configuration and its latitudinal and radial redistribution, rather than a decrease in the magnetic field amplitude itself (Pipin, Sokoloff & Usoskin, 2012). Eddy, Gilman &Trotter (1976) processed observational data on sunspot displacements across the solar disk. It was found that 20 years before the onset of the Maunder Minimum, the latitudinal differential rotation was the same as in the modern era. However, it is important that later (in the initial phase of the Minimum), the equatorial velocity became 3-5% higher, and the latitudinal gradient of angular velocity increased three times. If we assume that these changes were accompanied by a decrease in the radial gradient of angular velocity due to the redistribution of angular momentum, then the magnitude of the magnetic induction of the toroidal field excited by this radial differential rotation could not reach the threshold value required in dynamo models for the lifting of magnetic force tubes to the solar surface. The presence of long-term suppression of the dynamo process is often explained in terms of the α effect, which may contain a fluctuation part associated with chaotic turbulent motions (Ossendrijver, 2000), leading to irregular large minima (Brandenburg &Spiegel, 2008).

A very important feature of the solar activity during the Maunder Minimum was its strong north-south asymmetry (Fig. 2), when sunspots were observed mainly only in the southern hemisphere of the Sun.

Sokoloff & Nesme-Ribes (1994) suggest that this asymmetry can be interpreted within the framework of the nonlinear $\alpha\Omega$-dynamo theory. It has been shown that sunspot activity results from the action off a nonlinear rotation on a general magnetic field exhibition two mixed-parity solutions: a dipole and a quadrupole component. One mixed-parity solution is relevant to modern Schwabe cycles while the other could account for peculiar sunspot activity during the Maunder Minimum.

We suggest that the observed north-south asymmetry of sunspot surface magnetism may be related to the north-south asymmetry of the structure of the deep magnetic field of the Sun. Therefore, it is necessary to look for ways to detect this asymmetry. To explain the phenomenon, we in the paper (Krivodubskij, 2021) proposed a dynamo scenario in which the superposition of the cyclic dynamo-component of the toroidal field of the SCZ and the stationary toroidal field of the radiant zone may lead to

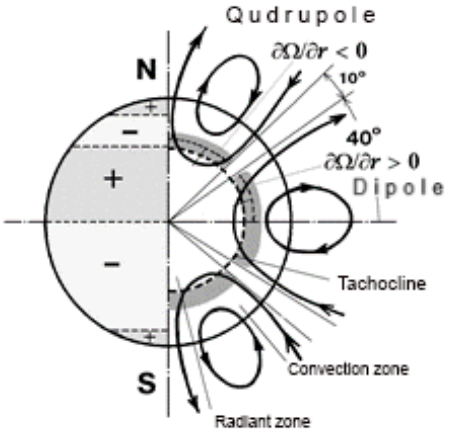

Figure 3: The structure of the global magnetic field excited by the $\alpha\Omega$ dynamo mechanism in the deep layers of the solar convection zone near the tachocline.

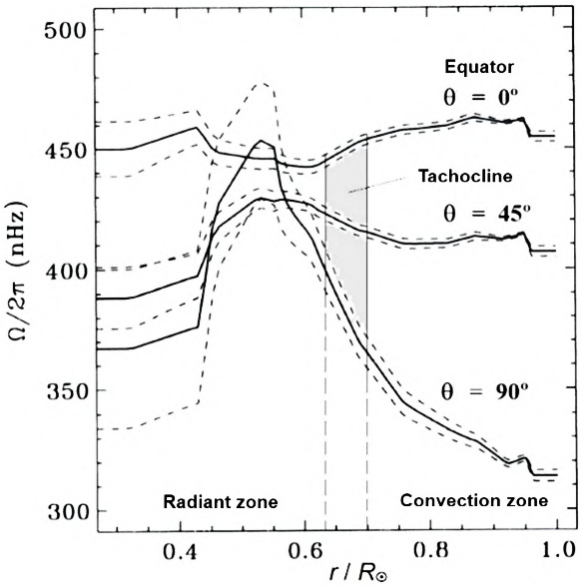

Figure 4: Radial profiles of the Sun's internal rotation velocity for three heliolatitudes θ, $\Omega/2\pi$ is the rotation frequency in nanohertz, $r/R_\odot$ is the relative heliocentric radius. It is relevant that $\partial\Omega/\partial r \neq 0$ in the radiant zone.

a predominance of the intensity of sunspot formation in one of the hemispheres of the Sun.

A key role in the proposed scenario is played by the special mode of the Sun's internal rotation, revealed as a result of helioseismological experiments. According to helioseismological data, the SCZ is divided into polar and near-equatorial regions with opposite signs of the radial angular velocity gradient $\partial\Omega/\partial r$ (Howe, 2009). If we take into account helioseismological data on $\partial\Omega/\partial r$, the $\alpha\Omega$ dynamo excites two harmonics of the toroidal field in the SCZ (including the tachocline). The first harmonic is a dipole (polar region $\partial\Omega/\partial r > 0$), the second is a quadrupole (near-equatorial region $\partial\Omega/\partial r < 0$) (Fig. 3). These dynamo toroidal magnetic harmonics change their direction with the period of the solar cycle.

It is relevant that the radial angular velocity gradient $\partial\Omega/\partial r$ penetrates into the deep layers of the stable radiant zone (Howe, 2009), below the SCZ and the tachocline (Fig. 4).

The radial gradient of the angular velocity $\partial\Omega/\partial r$ acts on the primary poloidal magnetic field, and thereby excites a toroidal magnetic field of constant direction in time (deep Ω effect of the radiant zone). This second toroidal component penetrates to the SCZ due to magnetic buoyancy. Then the summary toroidal field in the SCZ will consist of two components: variable (the dynamo-field of the SCZ) and stationary (the field rising from the radiant zone).

Conclusion. The first toroidal magnetic component (which consists two dynamo harmonics) is excited by the dynamo process in the convection zone. This component ***cyclically changes its direction (polarity)***. The second toroidal magnetic component is excited by deep Ω effect in the radiant zone. This component ***has a constant direction in time***. The deep magnetic component, rising to the convective zone, can lead here to a predominance of the summary toroidal magnetic field in one of the hemispheres of the Sun. The summary toroidal field, when rising onto the solar surface, can contribute to the north-south asymmetry of the sunspot formation process. Thus, continuous "feeding" of the dynamo process in the solar convection zone by additional toroidal flow emanating from the deep radiant zone can lead to the north-south asymmetry of the sunspot distribution on the surface, which was characteristic of the Maunder Minimum.

Funding: The work was carried out with the support of the Ministry of Education and Science of Ukraine, state budget grant for the prospective development of the scientific direction “Mathematical Sciences and Natural Sciences” at Taras Shevchenko National University of Kyiv.

References

Brandenburg A., Spiegel E.A.: 2008, *Astron. Nachr.*, **329**, 351.
Clerke A. M.*:* 1894, *Knowledge*, **17**, 206.
Eddy J. A.: 1976, *Science*, **192**, 1189.
Eddy J. A., Gilman P. A., Trotter D. E.: 1976. *Solar Phys.*, **46**, 3.
Howe R.: 2009, *Liv. Rev. Solar Phys.*, **6(1)**, 1.
Krivodubskij V.: 2021, *Visnyk Kyiv University, Astronomija*, **64(2)**, 26 [in Ukrainian].
Maunder E. W.*:* 1894, *Knowledge*, **17**, 173.
Ossendrijver M. A. J. H.: 2000, *Astron. Astrophys.*, **359**, 364.
Pipin V.V., Sokoloff D.D., Usoskin I.G.: 2012, *Astron. Astrophys.*, **542**, A26.
Spörer F. W. G.: 1887, *Vierteljahrsschr. Astron. Gesellschaft (Leipzig)*, **22**, 323.
Sokoloff D. D.: 2004, *Solar Phys.*, **224**, 145.
Sokoloff D. D., Nesme-Ribes E.: 1994, *Astron. Astrophys.*, **288**, 293.
Vainshtein S. I., Zel’dovich Ya. B., Ruzmaikin A. A.: 1980, Turbulent Dynamo in Astrophysics. Moscow: Nauka [in Russian].
Wang Y.-M., Sheeley N. R.. Jr.: 2003, *Astrophys. J.*, **591**, 1248.
Wolf R.: 1868, *Astronomische Mittheilungen der Eidgenössischen Sternwarte Zürich XXIV*, **3**, 103.

https://doi.org/10.18524/1810-4215.2025.38.340927

MAGNETIC FIELD WEAKENING IN DEEP LAYERS OF A SUNSPOT

V. G. Lozitsky[1], I. I. Yakovkin[1,2,3], U. O. Pavlichenko[3], V. A. Sheminova[4]

[1] Astronomical Observatory of Taras Shevchenko National University of Kyiv, Kyiv, Ukraine

[2] Institute of Physics of the National Academy of Sciences of Ukraine, Kyiv, Ukraine

[3] Faculty of Physics, Taras Shevchenko National University of Kyiv, Kyiv, Ukraine

[4] Main Astronomical Observatory of the National Academy of Sciences of Ukraine, Kyiv, Ukraine

vsevolod.lozitsky@knu.ua, yakovkinii@knu.ua, kitiketkotova@gmail.com, shem@mao.kiev.ua

ABSTRACT. The preliminary results of spectral-polarization observations of a large sunspot on August 17, 2024, observed on the Echelle spectrograph of the horizontal solar telescope of the Astronomical Observatory of Taras Shevchenko National University of Kyiv are presented. Direct measurements of the magnetic field in this spot were performed by splitting the bisectors of the profiles of ten spectral lines, mainly the Fe I lines, as well as three lines of Fe II, Cr II, and Sc II ions. The magnetic field, measured by splitting the sigma components of the Fe I 5250.2 line, reached 3400 G, however, the field magnitude by other lines with smaller Landé factors was significantly smaller, apparently reflecting the longitudinal component $B_{\rm LOS}$ of the magnetic field, rather than its intensity modulus. The shape of the bisectors of the $I \pm V$ profiles generally corresponds to a homogeneous field only for the Fe I lines, while for the ion lines these bisectors have a rather peculiar appearance, with a minimum splitting at approximately half the depth of the profiles and a maximum in the core of such lines or in their wings. If the magnetic field averaged over the entire profile is determined based on the average splitting of the bisectors at different depths of each spectral line, the following main effects are revealed: (a) the ion lines show 300–1200 G weaker magnetic fields than the neutral atom lines, (b) the measured $B_{\rm LOS}$ value increases with the Landé factor for the neutral atom lines, but for ions, the corresponding dependence is obviously the opposite, (c) for the neutral atom lines the $B_{\rm LOS}$ value decreases with increasing excitation potential EP of the lower term of the line. Effect (b) for the neutral atoms can be explained by the significant inclination of the field lines to the line of sight, while effects (a) and (c) indicate that the magnetic field strength in the spot decreased with depth. However, it remains unclear what role thermodynamic effects and the subtelescopic structure of the magnetic field might play here.

Keywords: Sun, solar activity, sunspots, magnetic fields, spectral lines, the Zeeman effect, altitudinal inhomogeneity of the magnetic field.

АНОТАЦІЯ. Представлені попередні результати спектрально-поляризаційних спостережень великої сонячної плями 17 серпня 2024 р., яка спостерігалась на ешельному спектрографі горизонтального сонячного телескопа Астрономічної обсерваторії Київського національного університету імені Тараса Шевченка. Прямі вимірювання магнітного поля у цій плямі були виконані по розщепленню бісекторів профілів 10 спектральних ліній, в основному ліній Fe I, а також трьох ліній іонів Fe II, Cr II та Sc II. Магнітне поле, виміряне по розщепленню сігма-компонент лінії Fe I 5250.2, досягало 3400 Гс, однак величина поля по інших лініях з меншими факторами Ланде була значно меншою, відображаючи, очевидно, поздовжню компоненту магнітного поля $B_{\rm LOS}$, а не його модуль напруженості. Форма бісекторів профілів $I \pm V$ в основному відповідає однорідному полю лише для ліній Fe I, тоді як для ліній іонів ці бісектори мають досить своєрідний вигляд, з мінімальним розщепленням приблизно на половинній глибині лінії, а максимальним – в ядрі таких ліній або в їх крилах. Якщо визначати усереднене по всьому профілю магнітне поле, виходячи з середнього розщеплення бісекторів на різних глибинах кожної спектральної лінії, то виявляються такі основні ефекти: (а) лінії іонів показують на 300-1200 Гс слабші магнітні поля, ніж лінії нейтральних атомів, (б) виміряна величина $B_{\rm LOS}$ зростає з фактором Ланде для ліній нейтральних атомів, але для іонів, очевидно, відповідна залежність є протилежною, (в) для ліній нейтральних атомів величина $B_{\rm LOS}$ зменшується при збільшенні потенціалу збудження нижнього терма EP. Ефект (б) стосовно ліній нейтральних атомів можна пояснити значним нахилом силових ліній до променя зору, тоді як ефекти (а) і (в), вказують на те, що напруженість магнітного поля у плямі зменшувалась з глибиною. Однак наразі залишається неясним, якою тут може бути роль термодинамічних ефектів а також субтелескопічної структури магнітного поля.

Ключові слова: Сонце, сонячна активність, сонячні плями, магнітні поля, спектральні лінії, ефект Зеємана, висотна неоднорідність магнітного поля.

1. Introduction

Magnetic fields in sunspots are generally measured using spectral lines with the largest Lande factors. It was by these lines that it was found that the typical magnetic field strength in developed sunspots is 2000-3000 G and reaches 5000-6000 G on very rare occasions (see, e.g., Livingston et al., 2006; Solanki, 2003). A significant advantage of such spectral lines is that they are suitable for direct measurements of an important characteristic of the magnetic field – the modulus (absolute value) of the intensity vector. This possibility can be realized due to the fact that at magnetic fields of B ≥ 2.5-3 kG, the Zeeman splitting $\Delta\lambda_H$ is complete in some narrow lines of neutral iron Fe I, which have a half-width $\Delta\lambda_{1/2}$ of about 0.1 Å and large Lande factors (g_{eff} = 2.5-3). In this case, the Zeeman π- and σ-components are completely separated in spectra. In solar magnetometry, this splitting mode is called the strong-field mode (SFM). In terms of physical content, the specified SFM differs from the same-name mode in atomic physics, where the latter is realized when the Zeeman splitting in magnitude significantly exceeds the multiplet splitting of the fine structure of atomic terms. In this case, the Paschen-Back effect occurs, when in spectral lines with complex (non-triplet) splitting, the anomalous splitting pattern (with several Zeeman subcomponents) gradually disappears, and this pattern in appearance approaches a simple Zeeman triplet, which has only three splitting components – one central π-component and two side σ-components (Frisch, 2010).

In the vast majority of spectral lines, the Landé factor is close to unity, i.e. close to the value that should theoretically be for a classical Lorentz triplet. In this case, at magnetic fields of several kilogauss, incomplete Zeeman splitting occurs by which it is possible to measure (with a circular polarization analyzer) not the modulus of the magnetic field strength *B*, but only its longitudinal component $B_\parallel \equiv B_{LOS}$ (Unno, 1956). This splitting mode in solar magnetometry is called as the weak-field mode (WFM), which formally corresponds to the condition $\Delta\lambda_H << \Delta\lambda_{1/2S}$. More precisely, this condition corresponds to a truly weak field only when this field is homogeneous (single-component), and the corresponding filling factor *f* is close to unity, i.e. $f \approx 1$. If the magnetic field is inhomogeneous and contains, for example, two components, one of which corresponds to $f << 1$, then the observed case $\Delta\lambda_H << \Delta\lambda_{1/2}$ may mask the situation when a strong Zeeman splitting actually occurs in the component with a small filling factor, i.e. when $\Delta\lambda_H \approx \Delta\lambda_{1/2}$ (Stenflo, 1973, 2011).

It is worth noting the fundamental difference between the values of the longitudinal component of the magnetic field B_{LOS} measured from spectral-polarization and magnetographic measurements. In the first case, this component is measured directly by the shift of the spectral lines, without any reference to the atmospheric model or standard line profile. In the second case, it is not the Zeeman splitting that is measured directly, but the amplitude of the circular polarization measured at the steepest parts of the profile (Babcock, 1953; Scherrer et al., 1995). This amplitude is compared with a similar polarization signal from the "average" profile corresponding to locations on the Sun outside the active regions. The ratio of these amplitudes is multiplied by a certain calibration factor, which gives the correct value of the magnetic field for the "average" line profile. However, in active regions, especially in solar flares and spots, this "average" profile can differ significantly from the real one, and the corresponding magnetic field magnitude can differ from its true magnitude. This is the main reason why it was not possible to carry out a satisfactory empirical calibration of the solar magnetograph, using direct measurements by visual and photographic methods for comparison (Severny, 1967). The corresponding empirical calibration curve turned out to be very scattered and indicated the possibility of quite large measurement errors, up to 200-300%.

Another type of instrument measures solar magnetic fields more realistically - the lambda meter (Semel, 1980; 1981). It does not use any assumptions about the standard line profile. As a result, weakening of the line profile, for example, does not affect the measured magnetic field magnitude. The only parameter used to calibrate the measurements is the Lande line factor – as in the spectral-polarization measurements analyzed below.

According to measurements with a lambda meter, the magnetic field in a sunspot was found to be almost the same by 12 spectral lines with Lande factors in the range of 0.93 – 3.00; the corresponding discrepancy was within 10% (Semel, 1981). This was considered in the mentioned work as a positive result of testing the use of such a measurement technique, which gives only the longitudinal component $B_\parallel$. In addition, this result, in the author's opinion, indicates that in a sunspot the spatially unresolved structure is less pronounced than in a solar plage. For a solar plage, the discrepancy of the magnetic field values was found by different lines turned out to be almost an order of magnitude larger and depended mainly on the equivalent line width. In particular, strong lines like Fe I 5233 showed 3-6 times greater intensities than weaker lines like FeI 5250.2.

These results for sunspots differ somewhat from similar data obtained by Venglinsky and Lozitsky (2012). Mentioned authors studied two large sunspots, which were observed on March 25, 1991 and July 22, 2004 at the HST of the AO KNU. The magnetic field was measured by the Zeeman splitting of many (≈ 150) spectral lines of various chemical elements - mainly Fe I, as well as Fe II. It turned out that the results by the Fe I and Fe II lines differ significantly. It is especially interesting that although in the sunspot umbra the magnetic field by the Fe I lines was stronger than the field by the Fe II lines, in the sunspot penumbra and in the surrounding photosphere an inverse relationship was found. Moreover, in the middle of the studied spots a significant "dip" in the magnitude of the magnetic field by the Fe II lines was recorded; no such result has been found in the scientific literature. Perhaps, it indicates the spatial heterogeneity of the field and the influence of thermodynamic effects on the measurement results. It is also possible that different sunspots differ greatly in their magnetic and thermodynamic properties, and therefore new research in this area has significant scientific value.

The purpose of our research was to verify the above-mentioned patterns on new observational material obtained in Kyiv during the war, in 2024.

2. Observations and data processing

Observational material for our study was obtained with the Echelle spectrograph of the horizontal solar telescope (HST) of the Astronomical Observatory of Taras Shevchenko National University of Kyiv (Lozitsky, 2016). The main value of observations with named spectrograph is that a wide spectrum interval, from 3800 to 6600 Å, can be recorded simultaneously where many thousands of spectral lines can be observed. Another advantage of our observations is that $I + V$ and $I - V$ spectra were obtained simultaneously, on separate adjacent bands of the spectrograms. This was made thanks to the fact that the circular polarization analyzer consisted of a λ/4 plate in front of the entrance slit of the spectrograph and a beam splitting prism (analogous to the Wollaston prism) behind the entrance slit. Therefore, $I + V$ and $I - V$ spectra relate to the same moment of time and to the same locations on the Sun.

The sunspot under study was observed 17 August 2024 in active region NOAA 3784 and had diameter of penumbra about 40 Mm. Observers were Vsevolod Lozitsky and Ulyana Pavlichenko. This sunspot was located from the disk center at a distance $\rho/R \approx 0.54$. According to visual magnetic field measurements made in Fe I 5250.2 Å line, peak magnetic field intensity in this sunspot was 3700 G, polarity was N. Echelle Zeeman-spectrogram of the sunspot was obtained at 6:24 UT using the ORWO WP3 photo-plates; exposure was 30 sec.

The spectrogram of the sunspot was scanned using an Epson Perfection V 550 scanner, which allows to obtain two-dimensional scans of images recorded on transparent films or on photo-plates. Methodological details of processing such scanograms for the scientific analysis are described by Yakovkin and Lozitsky (2022).

3. Selected spectral lines

Table 1 lists the selected spectral lines which were used. In this Table, λ is the wavelength in angstroms (Å), *EP* is the excitation potential of the lower term in electron-volts (eV), by (Moore et al., 1966), g_{eff} is the effective Landé factor. These factors for lines Nos. 1, 2, 6, 7, 9, and 10 correspond to those empirically determined in laboratory conditions (Zemanek and Stefanov, 1976). For the other lines, theoretical factors for the case of a *LS* coupling are given. This choice of spectral lines is useful for diagnosing the magnetic field in the vertical and horizontal directions. In particular, ion lines are generally formed deeper than neutral atom lines, while lines with smaller Lande factors are more suitable for diagnosing particularly strong magnetic fields (Lozitsky, 2015). The pair of lines 5247.1-5250.2 is suitable for study the spatially unresolved magnetic field by the line ratio method (Stenflo, 1973).

Table 1. Some characteristics of selected spectral lines

No.	Element, multiplet number, wavelength (Å)	*EP*, eV	g_{eff}
1	Fe I-383 5232.952	2.94	1.261
2	Fe II-49 5234.630	3.22	0.869
3	Cr II-43 5237.325	4.07	1.33
4	Sc II-26 5239.893	1.45	1.00
5	Fe I-843 5242.495	3.63	1.00
6	Fe I-1089 5243.783	4.26	1.509
7	Fe I-1 5247.058	0.09	1.998
8	Cr I-18 5247.574	0.96	2.50
9	Fe I-1 5250.216	0.12	2.999
10	Fe I-66 5250.654	2.20	1.502

4. Results and their discussion

Line profiles and their bisectors. Since the equivalent length of the entrance slit of the spectrograph was approximately 27 Mm on the Sun, it was possible to study individual adjacent photometric sections with a width of 1 Mm each. In this way, we could compare the photometric profiles in individual areas on the Sun along the direction of the entrance slit, along which we introduce a horizontal coordinate L with a discreteness also of 1 Mm. In this preliminary study, we present results only for $L = 18$ Mm, which corresponds to the middle part of the sunspot umbra.

For example, in Fig. 1 we present the profiles of line No. 5 from the list in Table 1, which has a rather small Landé factor (1.0) and exhibits a relatively weak splitting in the core of the spot. This splitting can be regarded as a weak field regime (WFA), in which, at a uniform field, only the longitudinal component B_{LOS} of the intensity vector can be determined.

It can be seen from the figure that the bisectors of the $I + V$ and $I - V$ profiles are almost parallel to each other, and have a sharp deviation to the right in the wings of the line. Such parallelism of the bisectors is theoretically quite expected for the regime of weak splitting in a homogeneous field. As for the named sharp deviation of the bisectors to the right, this effect is repeated in all lines

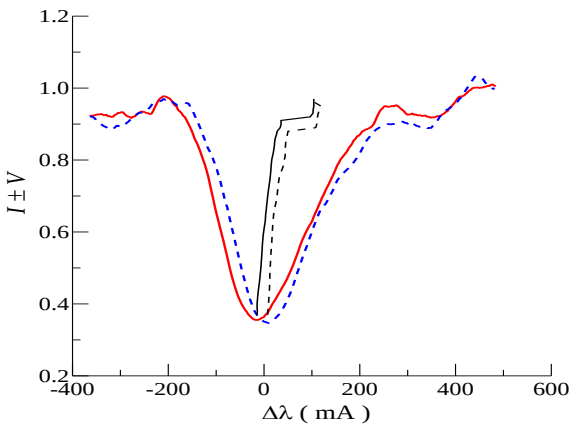

Figure 1: Stokes $I \pm V$ profiles and bisectors of Fe I 5242.495 line in sunspot umbra for $L = 18$ Mm.

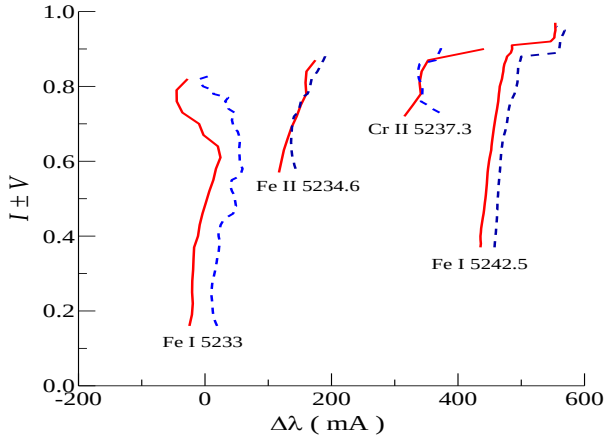

Figure 2: Comparison of the bisectors for some spectral lines. The position of the bisectors for the Fe I 5233 is original, while ones for the other lines are artificially shifted in the horizontal direction for better comparison of the data.

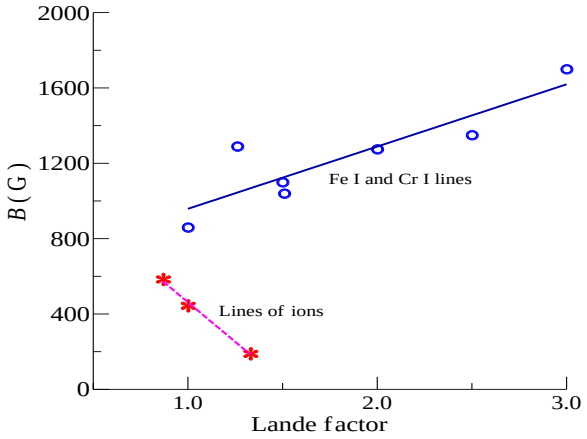

Figure 3: Comparison of measured magnetic fields with Landé factors of lines. Typical measurement errors are ± 100 G.

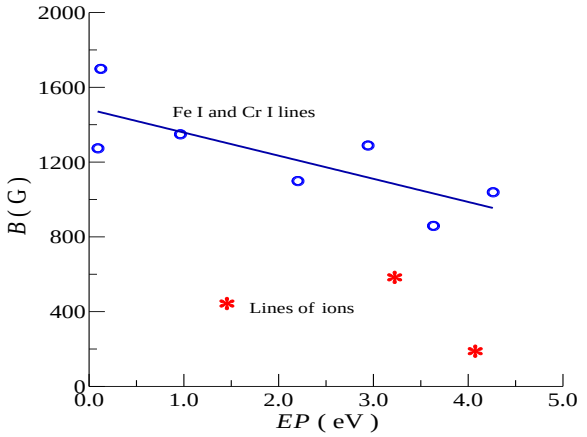

Figure 4: Measured magnetic fields B vs. excitation potential EP of the lower term.

of neutral atoms and is associated with a weak component located in the red wing at a distance of about 350 mÅ from the center of the lines. This indicates that the velocity field in the studied spot was inhomogeneous: in addition to the main component with a large filling factor, there was another component with a smaller factor, which had a positive velocity (plasma descent) of 20 km/sec.

A more interesting case is presented in Fig. 2, where the bisectors for the four lines are compared. It can be seen that the strong line Fe I 5233 has almost parallel bisectors too, while the ion lines have a rather peculiar shape, similar to the letter "X". To the best of our knowledge, such a case of bisector crossing is reported here for the first time. The mentioned bisector crossing cannot be explained within uniform magnetic field models, and likely reflects the different the magnetic field sign at the locations where the core and the wings are formed, similar to the magnetic field sign reversal along the line of sight reported in a different sunspot by Franz & Schlichenmaier (2013).

It can also be noticed that Fe I 5233 line has in its wings a local deviation of the bisectors to the left, i.e. in the opposite direction relative to FeI 5242 line. This means that areas of relatively slow plasma rise are detected at the level of formation of this line.

Averaged magnetic fields. Since the bisectors behave very differently in different parts of the line profiles, we determined the average splitting of the bisectors for the entire profile of each line to estimate the corresponding magnitude of the averaged magnetic field. These data are presented in Figs. 3 and 4 in comparison with the Landé factor of the lines and the excitation potential of the lower term.

The dependence "B vs. g" for lines of neutral atoms presented in Fig. 3 is quite expected theoretically. After all, when using a circular polarization analyzer, the value of the Zeeman splitting gives $B_{\rm LOS}$ only in the case when this splitting is significantly less than the half-width of the spectral line (Unno, 1956). If the Zeeman splitting $\Delta\lambda_H$ increases so much that it is comparable to the half-width $\Delta\lambda_{1/2}$ of the line, then from the measurements we obtain a value intermediate between the longitudinal component and the modulus of the magnetic field strength. So, then, one would expect that the larger the Lande factor, the larger the measured magnetic field should be if the angle between the line of sight and the field line is significantly different from 0 or 180 degrees. However, what is incomprehensible from this point of view is the dependence for ions, which has the opposite character (here the measured field is probably anticorrelated with the Landé factor). However, the observational data for ions in this case are not enough to draw more confident conclusions.

However, from Fig. 3 and 4, another more obvious effect is evident: the ion lines give 300-1200 G fields weaker than the neutral atom lines. Calculations of the heights of spectral line formations in the spot showed that this feature reflects the effect of the height of spectral line formations. In particular, if we compare the heights of formations of Nos. 2, 3 and 4 lines (-17.51, 12.59 and 81.01 km, respectively) with the magnetic fields measured by them (290, 320 and 940 G), it is clear that the higher the spectral line is formed, the stronger the magnetic field it shows. We plan to provide more detailed observational data and data on calculations of the heights of line formations in a separate, more detailed article.

We checked whether this result could not be random, that is, only for one point of the sunspot. It turned out that also in other places of the sunspot along the cross-section of its image by the entrance slit of the spectrograph, the magnetic field measured by the lines of ions, in general, is systematically weaker than by the lines of neutral elements. Thus, we cannot explain this difference by the different inclination of the lines of force, and therefore the only possibility remains in the frame one-component field: the magnetic field strength really weakens when deepening into the sunspot.

This, however, seems paradoxical because the pressure, temperature and concentration of the plasma increase with depth (Maltby et al., 1986), and, therefore, the magnitude of the equilibrium magnetic field in the flux tube should also increase. Perhaps, different sunspots can have significantly different magnetic field topology, ranging from homogeneous to significantly inhomogeneous ones (Franz & Schlichenmaier, 2013).

The observed weakening of the magnetic field with depth may indicate that the sunspot is a relatively shallow formation resembling a thin disk, rather than a deep long force tube. In this regard, different authors have come to different conclusions. In particular, based on the study of the torsional oscillations of the spots, it was concluded that the sunspot is a rather deep formation: the length of the corresponding flux tube is several times greater than its thickness (Gopasyuk and Gopasyuk, 2005). However, some theoretical studies, as well as helioseismological data, indicate that the spots, on the contrary, are relatively shallow formations (Kosovichev, 2012). It is possible, however, that in this case not only the height of the line formation plays a role, but also their different temperature sensitivity to changes in thermodynamic conditions at different depths in the spot, as well as the subtelescopic structure of the field, which contains both very strong magnetic fields and opposite magnetic polarities. It seems possible to find the correct answer to this question using the modeling profiles for the case of a significantly inhomogeneous solar atmosphere, which may contain several discrete components with different intensities, polarities, filling factors, Doppler velocities, and thermodynamic parameters.

Probably, it is worth paying attention not only to the effects of the shape of the "X" bisectors (Fig. 2), but also to the subtle effects in the splitting of the bisectors of the type of local maximum, similar to that found in line FeI 5233. As can be seen from this figure, at the intensity level of 0.7- 0.8 this line has a local maximum of splitting, which should not be at a homogeneous magnetic field. A similar effect is found not only for $L = 18$ Mm, but also in neighboring photometric sections. A possible reason for this effect is the subtelescopic structure of the magnetic field, in which the actual local magnetic field intensities can be much larger than those obtained directly from direct measurements (Lozitsky, 2015).

5. Conclusions

The main result of our work is that the ion lines in the studied sunspot demonstrate significantly lower magnetic field strengths than the lines of neutral atoms. This is probably due to the significant altitudinal gradient of the magnetic field. If this is the case, then a paradoxical situation arises: the magnetic field strength weakens with depth in the spot, while the gas pressure, as is known, increases (Maltby et al., 1986). Our results confirm the previously obtained data of Venglinsky and Lozitsky (2012) that in the sunspot umbra there can be a sharp "dip" of the strengths measured by the ion lines. Although the results of our study do not agree with the measurements of Semel (1981), it cannot be ruled out that different sunspots have very different patterns of spatial inhomogeneity of the magnetic field. In this respect, sunspots may be no less interesting objects for research than solar flares. However, it should be noted that sunspots are much more convenient objects for observation than solar flares.

Acknowledgements. This study was partly funded by the Ministry of Education and Science of Ukraine, projects Nos. 22БФ023-03 and 25БФ051-04.

References

Babcock H. W.: 1953, *ApJ*. **118**, 387.
Franz, M., Schlichenmaier, R.: 2013, *A&A*, 550, id A97.
Frish S.E.: 2010, Optical atom spectra. St.-Peterburg. Moscow. Krasnodar. 656 p.
Gopasyuk, S. I., Gopasyuk, O. S.: 2005, *SoPh*, **231**, 11.
Kosovichev A.G.: 2012, *SoPh*, **279**, 323.
Livingston W., Harvey J.W., Malanushenko O.V.: 2006, *SoPh*, **239**, 41.
Lozitsky V.G.: 2015. *AdSpR*, **55**, 958.
Lozitsky V.G.: 2016, *AdSpR*, **57**, 398.
Maltby P., Avrett E. H., Carlsson M. et al.: 1986, *ApJ*. **306**, 284.
Moore Ch.E., Minnaert M.G.J., Houtgast J.: 1966, The spectrum 2935 Å to 8770 Å. Second revision of Rowland's Table of solar spectrum wave lengths (Nat. Bureau Stand., Monogr.), 61. 349 p.
Scherrer P. H., Bogart R. S., Bush R. I. et al.: 1995, *SoPh*, **162**, 129.
Semel M.: 1980, *A&A*, **91**, 369.
Semel M.: 1981, *A&A*, **97**, 75.
Severny A.B.: 1967, *BCrAO*, **36**, 22.
Solanki S.: 2003, *A&ARv*, **11** (2-3), 153.
Stenflo J. O.: 1973, *SoPh*, **32**, 41.
Stenflo, J. O.: 2011, *A&A*, **529**, id.A42, 20.
Unno W.:1956, *PASJ*, **8**, 108.
Venglinsky E.R., Lozitsky V.G.: 2012. *BTSNU*, **49**, 26.
Yakovkin I. I., Lozitsky V. G. *AdSpR*, **69**, 4408.
Zemanek E.N., Stefanov A.P.: 1976, *VeKie*. **18**, 20.

https://doi.org/10.18524/1810-4215.2025.38.341022

JUPITER'S DAM RADIO EMISSION AND SOLAR ACTIVITY: IO-DEPENDENT AND NON-IO SOURCES

N. O. Tsvyk

Institute of Radio Astronomy of the NAS of Ukraine, Kharkiv, Ukraine
natalitsv69@gmail.com

ABSTRACT. We study Jupiter's DAM radio storms to identify the features that may correlate with solar wind and coronal mass ejections (CME). We investigate the dynamics of DAM storms and burst features, and explain them by considering MHD processes associated with Io and the presence of gas in Jupiter's lower magnetosphere.

DAM radio storms occur when plasma injected by Io or by solar wind propagating along Jupiter's magnetic field lines into the auroral zone of Jupiter's lower magnetosphere together with low-frequency Alfvén wave. Those MHD oscillations in low magnetosphere can trigger ionization processes and create streamers, activating maser instabilities in the electron plasma. This can occur under the influence of dense solar wind and CME that penetrate to Jupiter's magnetosphere, creating high-latitude currents with non-Io radio storms, and enhancing Io-dependent sources of DAM radio emissions.

We found that dynamics of development of Io-dependent and non-Io DAM radio storms have similar features and evolutionary peculiarities. That time periodicities (5 min and 20 min durations) may connected with MHD instabilities activated by Io, that modulate the current sheets system in all auroral zone. The power of Io-dependent storms is modulated by the solar wind pressure on the magnetosphere of Jupiter. On the other hand, in non-Io radio sources associated with solar plasma injections, due to the content of high-energy ions which scatter on the gas fluids, a number of specific radio bursts are formed, for example, having zebra structures on high-resolution dynamic spectra.

Keywords: DAM radio emission, Alfven waves, magnetosphere, solar wind, Jupiter.

АНОТАЦІЯ. В цій роботі буде вивчено декаметрові (ДКМ) радіобурі Юпітера, для того, щоб виявити особливості, які можуть бути пов'язані із впливом сонячного вітру та корональних викидів маси (CME) на утворення радіобур та сплесків ДКМ радіо випромінювання. Ми розглядаємо динаміку бур та особливості окремих ДКМ сплесків, та пояснюємо їх з урахуванням МГД процесів, пов'язаних з Io, та процесів, що відбуваються за наявності нейтрального газу в нижній магнітосфері Юпітера.

Вважаємо, що бурі ДКМ радіовипромінювання виникають, коли плазма, інжектована на Io, або плазма сонячного вітру проникає до авроральної зони нижньої магнітосфери Юпітера, поширюючись вздовж ліній магнітного поля Юпітера разом з альвенівськими хвилями низької частоти. Ці МГД коливання в нижній магнітосфері можуть запускати процеси іонізації плазми і формувати стримери, та будуть активувати Мазерні нестійкості на електронах. Під впливом щільного сонячного вітру і корональних викидів маси змінюється структура магнітосфери Юпітера, з'являються високоширотні плазмові течії, дотичні до появи не-Io ДКМ штормів, та посилюється ДКМ радіовипромінювання, яке контролюється Io.

Враховано, що динаміка розвитку ДКМ радіобур, залежних від Io та незалежних від Io, мають схожі риси та еволюційні особливості. Так, їх спільні періодичності у часі (5 хвилин та 20 хвилин тривалості) можуть бути пов'язаними з МГД нестійкостями, активованими Io, які модулюють систему струмових шарів у всій авроральній зоні. Потужність бур, залежних від Io, модулюється динамічним тиском сонячного вітру на магнітосферу Юпітера. З іншого боку, в радіоджерелах незалежних від Io, і пов'язаних з інжекціями сонячної плазми, завдяки вмісту високоенергетичних іонів, що стикаються з газовим середовищем, формується ряд специфічних радіо сплесків, наприклад, такі, що мають зебра-структури на динамічних спектрах високої роздільної здатності.

Ключові слова: ДКМ радіовипромінювання, альвенівські хвилі, магнітосфера, сонячний вітер, Юпітер.

1. Introduction: the Io-dependent and non-Io sources observed in DAM radio storms

Jupiter's DAM radio storms were observed in radio telescopes in Ukraine, France, USA (Florida) and others (see: Ryabov & Gerasimova, 1990; Ryabov, 2001; Ryabov et al. 2014; Marques et al., 2017; Flagg et al., 1991), as well as during the mission's observation by Voyager-1,2, Juno and others (e.g., see: Genova, 1985; Barrow et al., 1986; Liu et al., 2021) on time-scale of low resolution (hour, min, second) and high resolution (millisecond scale). In Ukraine such observations have been made at the UTR-2 and URAN-4 telescopes. We can see on them the different types of sources: dusk-side (A, C) sources and down-side (B, D) sources, for Io-dependent and non-Io sources. We also made and presented in Table 1 a comparison of the observed properties of these dynamic spectra for DAM storms (on a large scale and with higher resolution), such as storm evolution, temporal and frequency modulation of the burst pattern, observed high-resolution features of the dynamic spectrum in DAM bursts using UTR-2 and URAN-4 data and a thorough analysis of data from a telescope in France, which was carried out by Marques et al. (2017).

Table 1: Compare of Io-dependent and non-Io storms

	Io-dependent sources	*Non-Io-storms*
Arcs forms	Dusk Io-A,C: „late" arcs Down Io-B,D: „early" arcs	Dusk non-Io-A,C: „late" arcs Down non-Io-B,D.: „early" arcs
Storm duration	50 min – 1.5 hr A number of Dusk storm cases are grater then in Down cases	40 min – 1.2 hr A number of the storms cases are grater then in Io-depended storm cases
Position: λ_{CML} and λ_S	λ_{CML}~ 240° ±40° (Io-A); ~ 140° ±40° (Io-B); ~ 320° ±40°(Io-C); ~ 125° ±90° (Io-D). (λ_S +30°)~ Λ_{Io} ~ 195° ±80° (Io-A,B)	λ_{CML} ~ 80-190° (non-Io B); ~ 200-340° (non-Io A, C); λ_{CML} ~ 60-320° (non-Io D)
Intensity	The intensity Io- and non-Io storms are compared; have the finest bursts	Non-Io storms have some much power, and some less durations
Max-frequency	Io-A,B (N-sph,): 39 MHz; Io-C,D (S-sph.): 27 MHz	Non-Io: up to 28 MHz
Polarization	Io-A,B (N-sph.): RH dominated; Io-C,D (S-sph.): LH dominated	(N-sph.): RH dominated; (S-sph.): LH dominated
UV, IR	UV, IR brightness in N-pole oval is grater then in S-pole	UV spots observed in auroral zones. A number of UV spots are grater at N-pole then at S-pole
Solar wind	A number of storm cases and storm power depends on SW kinetic power	A number of storm cases increase with solar wind kinetic power

We are interested in what are the common properties and differences in the dynamic spectra, in order to explain the mechanism of activation of Jupiter's DAM radio emission, and they possible connection with Solar wind ejections. So, we see such main periodicities for Io-dependent sources: the storm duration of 1-3 hr, the periodicity of 20-40 min with arcs structure (be seen the early-arc modulation for Down sources, and the late-arcs for Dusk sources); and the periodicity of 5 min of common cases of storm spectrum (see: Dessler & Hill, 1979; Ryabov, 2001; Marques et al., 2017). In addition, we see the lanes modulation (~ 0.1-1 MHz), and in the dynamical spectra of high resolution there is the L- or S-bursts with slow or fast drift; and with periodicity of about 1s for L-bursts, and of 0.1s, 0.03s, 0.003-0.01s for S-bursts (see: Flagg et al., 1991; Ryabov & Gerasimova 1990; Ryabov, 2001; Ryabov et al., 2014).

Many models of the Io correlation mechanism propose that the 5-minute modulations are associated with Io-generated Alfvén waves with a 10-minute period, which further activate DAM bursts with fast S-drift in the dynamical spectra (see: Su et al., 2006; Hess et al., 2007). However, only in Io-dependent storms we registry the many fine structures of S-bursts in the dynamic spectrum, together with L- and Narrow-band bursts. These storms also correlate with infrared and far-ultraviolet data obtained with the Hubble Space Telescope (Gerard et al., 2014). The Io flux tube draws a main oval in the Jupiter's surface, which corresponds to the locations where Io-dependent radio sources radiate. Considering a pole tilt, a region with maximum magnetic fields is formed at λ_{CML}~ 165° for N and at ~240° for S-hemisphere, which is responsible for the maximum number of DAM storm occurrences with (λ_S+30°)~Λ_{Io}~195° (Marques et al., 2017).

Similar periodicities we can also observe in the non-Io storms, for example, we observe storms with duration of about ~1 hr, and we see modulation with periods of 5 minutes within the arc structures of 20-30 minutes duration (Barrow et al., 1986; Marques et al., 2017). In high-resolution dynamic spectra, we most often observe L-bursts, or in some rare cases, we observe Zebra-type and Narrow-band bursts (Ryabov & Gerasimova, 1990; Marques et al., 2017; Panchenko et al., 2018). The fact of similar modulation with 5-minute periods in non-Io sources is unexpected.

On the other hand, high-latitude non-Io storms can be activated directly by the solar wind. So, Barrow et al. (1986) find from Voyager-1 data that correlation of DAM storms with solar wind kinetic power of P_{SW} ~ $(m_p n_{ei} v_{s\omega}{}^2)$, and a number of that storm cases is increased when solar wind fluctuation and CME reach the Jupiter's magnetosphere. Incidentally, Barrow et al. found that the correlation with the solar wind works for both non-Io and Io-dependent storms. This fact convinces us to search a general mechanism to explain these types of low-frequency modulations in the DAM radiation of Io-dependent and non-Io storms. How this mechanism works in the Jupiter magnetosphere and how the solar wind affects the DAM radio emission will be seen below.

2. The activation mechanism for Jupiter DAM Radio Emission in Io-dependent sources

2.1. Io-Jupiter interaction

The Io-dependent DAM radio storms of Jupiter are associated with the satellite Io, which generates Alfvén waves (with a period of ~10 minutes) in the region of Jupiter's

magnetosphere with a strong magnetic field, under the influence of which the "rotational energy" of Jupiter is converted into DAM radio energy and non-thermal acceleration of plasma particles.

This Io – Jupiter interaction mechanism have been proposed and developed by Gold-reich &Lynden-Bell, (1969), Dessler &Hill, (1979), Su, et al. (2006), Hess, et al. (2007), and others. They studied how the Alfvén wave is generated and transported from Io, and how it interacts with Jupiter's lower magnetosphere, which consists of plasma and gas fluids.

The plasma density in the auroral zones is very low, so the active plasma is mainly injected into the DAM sources from Io torus, transported along the Io-Jupiter flux tube into this zone with electric currents (see Su, et al. 2006, Hess, et al. 2007). Moreover, since this zone contains high-density neutral gas fluids, ionization can begin under the influence of low-frequency Alfvén waves generated by Io, which also adds plasma particles to these zones (see Boev, et al. 2001, Boev, 2005; Tsvyk, 2019, 2023, 2024). All these processes lead to the emergence of Io-dependent DAM radiation sources with S- and L-bursts.

The plasma in Io's torus is forced into co-rotation with Jupiter, meaning to share the same period of rotation. The Io torus fundamentally alters the dynamics of the Jovian magnetosphere when Io moves through the magnetosphere, and it generates the Alfvén wave electric fields of with periods of $T_{A0} \sim 10$ min, which may be connected with the torus curvature and depend on how that Alfvén instability works.

The Alfvén wave pattern is formed in the magnetosphere by the interaction of Io and Jupiter, when Alfvén energy is transported to Jupiter along magnetic field lines and this involve the Io-torus plasma to move along the flux tube. The Alfvén waves are directed almost along the lines of Jupiter's rotation (along the torus), so Alfvén waves and Io-torus fluid are transported both to and away from Jupiter (into the outer magnetosphere) when the wave-vector k_A rotates in a period of 20-40 min. Thus, the current sheets and a magnetic disk have being formed in Jupiter's magnetosphere, sharing it into tubes or sheets with a width of $2R_{tor} \sim 6\ R_{io} \sim 0.15\ R_j$, and Alfvén waves may transform to kinetic modes.

2.2. MHD waves in Io vicinity

Let us consider in a vicinity of Io the plasma and MHD wave parameters corresponding to a plasma torus. So, these are: $n_{ei} \sim 200$ cm^{-3}; $T_{ei} \sim 10^5$-10^6 K (very dense and hot plasma, see: Krupp et al. 2004, Su et al. 2006), and this gives us: $c_{Afx} \sim v_{ti} \sim 5 \cdot 10^4$ m/s; $v_{te} \sim 3 \cdot 10^6$ m/s= 0.01 c ($c_{Afx} < v_{te} < c_A$). Such MHD instabilities, due to the rotation of Io in a strong magnetic field, generate the low-frequency (LF) Alfvén waves with a period of $T_{A0} \sim 600$ s ($k_A = 2\pi/\lambda_A$); the Alfvén velocity on the orbit of Io ($z_j \sim 6$, $\varphi \sim 0$) is: $c_A \sim 0.25$ c (z_j in R_j units). Therefore, this velocity corresponds to the transfer of wave energy along the magnetic field lines from Io (at $z_j \sim 5$) to the mirror point in the ionosphere ($z_j \sim 0.014$), which lasts of ~ 7 s by time.

The model parameters of Alfvén waves are presented in Table 2. So, using the typical MHD theory (see: Akhiezer, et al. 1974, Kadomtsev, 1988), we find the following magnetic and electric fields for these Alfvén waves: $B_{\omega y} \propto \xi_\perp k_{Az} B_{0z}$, $E_{\omega z} \propto \omega (k_{Ax} c)^{-1} B_{\omega y}$, with oscillations of $\propto \exp(i\mathrm{k_A r} - i\omega t)$. The wave's current is: $j_z = e\, n_{ei} (v_{iz} - v_{ez}) \propto i k_A B_{\omega y}$ with phase shifted oscillations. For Alfvén modes with k_A directed almost along the rotation lines (in x-axis of perpendicularly to B_{0z}-magnetic lines, $\theta_{kB} \approx 0.4995\pi$) the phase velocities are: $c_{Afz} = c_A \cos^2 \theta_{kB} \approx 20$ m/s (along magnetic field); and $c_{Afx} = c_A \cos \theta_{kB} \sin \theta_{kB} \approx 10^4$ m/s (nearly along k_A). Therefore, those Alfvén wavelengths are: $\lambda_A = T_{A0}\, c_A \cos \theta_{kB}$ and $\lambda_{Az} = T_{A0}\, c_A$.

2.3. A transport of MHD waves

The Alfven wave velocity c_A depends on $n_e(z_j)$ and $B_{0z}(z_j, \phi)$ and varies along the magnetic field lines. It is specified as $n_e(z_j)$ in the model of like Su, et al. (2006) (see Fig. 1), and we have chosen the dipole approximation for the Jupiter's magnetic field, $B_{0z}(z_j, \phi) \approx 10$ G $(1 + 3 \sin^2 \phi)(1 + z_j)^{-3}$ (as for N-pole at $\lambda_{CML} \sim 165°$), where z_j is the altitude from the Jupiter's surface (in R_j units) and φ is the azimuthally angle of the observed point.

The plasma density at the foot of Io flux tube may increase from 0 to 10^3 -10^4 cm^{-3} as the Io-related magnetic field lines move above the aurora zone, and the Io-plasma flows and are transported with Alfven waves to the Jupiter surface along the magnetic field lines. Then, the presence of neutral gas fluids at the lower altitudes in the Jupiter magnetosphere leads to the low-frequency (LF) Alfven wave velocity decrease from c_A to c_{ALF} because the neutral gas particles move together with the plasma oscillations through particle

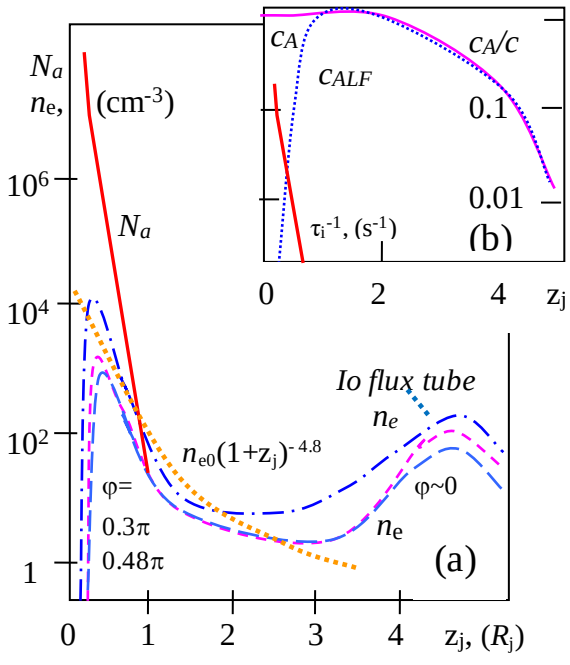

Figure 1: (a) The models for plasma n_e and gas N_a density variation at Jupiter magnetosphere along flux tube (altitudes z_j in Jupiter radius units). Curves are correspondent to the model like Su, et al. (2006) for Io flux tube and for other flux tubes at $\varphi = 0.48\pi$ and $\varphi = 0.3\pi$. (b) The dependence of τ_i time-scattering and $c_A(z_j)$ velocities along Io flux tube for HF and LF Alfven waves

Table 2: The Alfven wave model parameters at the Io orbit and at the foot of Io-Jupiter flux tube.
Here we take: B_{0z}, $k_A=(k_{AX}, k_{AZ})$; and $k_{AX}^2=k_{Ax}^2+k_{AY}^2 \approx k_{Ax}^2$.

	z_j=5 (Io orbit)		z_j=0.5		z_j=0.3 (atmosphere influence)	
c_A/c	0.25		0.95		0.25	
c_{AfX}	$4\cdot10^{-5}$ c		$5\cdot10^3$ m/s		$5\cdot10^3$ m/s	
c_{AfZ}	20 m/s		1 m/s		5 m/s	
θ_{kB}	0.4995π		0.49995π		0.4998π	
Wave length:	λ_A	k_A, m^{-1}	λ_A/R_j	k_A, m^{-1}	λ_A/R_j	k_A, m^{-1}
λ_A	4 R_{io}=0.1 R_j	10^{-6}	0.04	$2\cdot10^{-6}$	0.04	$2\cdot10^{-6}$
λ_{AZ}	~62 R_j	10^{-9}	2000	10^{-11}	~62	10^{-9}
λ_{AX}	0.1 R_j	10^{-6}	0.04	$2\cdot10^{-6}$	0.04	$2\cdot10^{-6}$
λ_{AY}	0.13 R_j	$7\cdot10^{-7}$	0.06	$1.4\cdot10^{-6}$	0.07	$1.3\cdot10^{-6}$
λ_{Ax}	4 R_{io} =0.15 R_j	$6\cdot10^{-7}$	0.05	$1.6\cdot10^{-6}$	0.05	$1.9\cdot10^{-6}$

collisions on LF Alfvén waves (see Tsvyk, 2023, 2024; and considering the equations for low-ionized plasma by Smirnov, 1995, Kadomtsev, 1963, Bragynskyi, 1963, Akhiezer, et al.1974):

$$c_A{}^2 \cong B_0{}^2/(4\pi n_i m_p),\ \omega > \tau_{ia}^{-1},$$

$$c_{A\_LF}{}^2 \cong B_0{}^2/(4\pi N_a m_p),\ \omega << \tau_{ia}^{-1}.$$

Here τ_{ia} is the ion scattering time in the presence of a neutral gas:

$$\tau_{ia} \cong 1/(v_{Ti} N_a a_\lambda{}^2) \approx 10^{14} cm^{-2}/(v_{Ti} N_a).$$

Alternatively, high-frequency (HF) Alfven waves moves with c_A-velocity, and they velocity reaches the light speed at low ionosphere altitudes ($z_j \to 0.014$, in R_j units) where the plasma density comes to Zero. At these altitudes the gas temperature is about T_a~ 1000 K, and the ionization processes can occur at higher altitudes, while the ion particles cool and recombine lower down. Ionization occurs mainly through collisions of high-energy particles with gaseous fluids, and to a lesser extent through the impact of energetic photons of solar radiation. Thus, in the lower magnetosphere of Jupiter at $z_j < 0.5$ we have T_a ~ 500 K for gaseous particles, the ep-temperature is $T_e > T_p$ ~2000 K, and here is the zone where DAM radio sources have been activated above the auroral zones (see: Boev, et al. 2001, Boev, 2005, Withers &Vogt, 2017).

Figure 1 shows the density variations for and outside the Io flux tube, using a model similar to Su et al. (2006), where N_a is the gas density and n_e is the plasma density ($n_e \approx n_p$, as well as some other impurity ions). And Fig. 1b shows the variation of c_A in the lower magnetosphere of Jupiter for HF and LF Alfvén waves. Thus, the ion-atom collision frequency began to affect the MHD waves at heights $z_j < 0.5$, where the atmospheric density is much higher than the plasma density.

2.4. MHD waves in lower magnetosphere and DAM storms

Now we can calculate the Alfvén wave parameters at (z_j~0.5, φ~π/3) using these magnetosphere data. The Alfven velocity here is high, $c_A \to c$, and corresponds to the fast transfer of MHD energy along the magnetic field lines. The phase velocity for Alfven wave-modes (T_{A0}) with θ_{kB}~0.49995π is: $c_{Afz} < 1$ m/s; $c_{Afx} \sim 5\ 10^3$ m/s. The current sheets shrink adiabatically because the B_0-magnetic field lines are focused at small z_j as in the dipole model: $\lambda_{Ax} = \lambda_{Ax0}(1+z_j)/6$. The plasma parameters in this zones are: n_{ei}~(30-10^4) cm^{-3}; T_{ei}~3000 K, that is give us: $c_{Afx} \sim v_{ti} \sim 4\cdot10^3$ m/s; v_{te}~$2\cdot10^5$ m/s~ 0.001 c ($c_{Afx} < v_{te} << c_A$). The magnetic field lines B_{0z} are curved as (dipole model); and the current sheets can be tilted towards the magnetic field lines under the of Jupiter's plasma rotation or by the influence of fast magneto sound (MS) waves, which are transported at a speed of c_A and have large length $\lambda_{fms} > 6\ R_j$ at T_{A0} wave-period.

At lower altitudes, e.g., at (z_j~0.3 and φ~π/3), it is necessary to take into account the presence of high-density neutral gas for the LF Alfvén wave, and we have its velocity of $c_{ALF} \sim 0.025c$, which corresponds to the anomalous increase in the Alfvén energy flux at $z_j \to 0$. And we get the following phase velocity of Alfven T_{A0}-modes (with θ_{kB}~0.4998π): $c_{Afz} \sim 3$ m/s; $c_{Afx} \sim 5\cdot10^3$ m/s, where the current sheets are compressed adiabatically in the x direction due to the coincidence of magnetic field lines at $z_j \to 0$.

The plasma parameters in this zone are: n_{ei}~(1-10^4) cm^{-3}; T_{ei}~3000 K, so we have: $c_{Afx} \sim v_{ti} \sim 4\ 10^3$ m/s; and v_{te}~$2\cdot10^5$ m/s~ 0.001 c. The MHD power (or wave energy density) increases with decreasing wave speed c_A, and when $c_A \to c_{ALF}$ (at $z_j \to 0$), this gives us a power increase of >100 factor compared to the MHD energy density at z_j=5. In the Io-dependent DAM sources this effect leads to the strong plasma hitting, which lead to the ionization begins at the wave-mirror point. In addition, the fast MS waves can affect to the current sheets at this mirror point, and the streamer-like structures appear in each of current sheet regions.

All these processes lead to the streamer-like stratification of the lower magnetosphere by MHD waves, and here the DAM radiation is activated with the observed bursts and modulation features which are presented in Table 3.

Table 3: *L* and *S* bursts: time periodicities and the storm shape in dynamical spectrum

Io-dependent storms	5 min, 20 min, arc-shaped structure	Alfven waves by Io generated: T_{A0} ~10 min. Due to k_A rotates and Io-plasma injection: T_{storm} ~ 20 min. The arcs correspond to the geometry of the Io – Jupiter flux tubes, where the plasma fluids move to Jupiter
L-bursts	1 s	This period may be associated with the τ_i-time scattering for ions with atoms of neutral gas in the lower magnetosphere
S-bursts (Io-dependent source)	0.002-0.01 s (with fast drift)	They may be connected with start of the ionization process, refraction process, so as connected with burst modulation of HF-Alfven waves within the streamers (T_{A1}~0.005-0.01 s, T_{A2}~ 0.03-0.1 s). They may be generated in the wave-mirror points at the Jupiter surface.
N-bursts	0.5-1 MHz (in bands)	They are associated with modulation of the plasma density, and the shape of the spectra is obtained due to refraction effects inside the DAM sources.
Bursts in non-Io storms	0.1-1s; 0.01 s (in 0.5 MHz bands)	They have a shorter duration and lover intensity. These bursts have dominantly L-shaped bursts, but in rare cases it appears zebra bursts with fine periodicity, ~ 0.01 s

3. Jupiter DAM radio emission of non-Io sources: a role of Solar wind and CME

We now consider the structure of Jupiter's magnetosphere, the role of Io in modulating the magnetic disk, and the influence of the solar wind on the activation of non-Io DAM radio sources in high-latitude auroral zones. We note that the activation of DAM sources requires the presence of plasma fluid in the auroral zone, and the Maser radiation mechanism arise due to the Alfvén waves working in current sheets.

So, when the solar wind (SW) interacts with Jupiter's magnetosphere, which has a strong magnetic field, a structure of bow shock – tail emerges in this magnetosphere (see: Khurana et al. 2004). Then, when the SW-pressure increases or a coronal mass ejection (CME) reaches Jupiter, the magnetic field reconnection occurs within the bow shock wave, or in the tail of Jupiter's magnetosphere at a distance of z_j~15, and solar plasma penetrates into Jupiter's auroral zones. We now consider the effects in solar wind turbulence on Jupiter's magnetosphere, leading to current reconstructions and tail fluctuations. We then review how these processes activate the non-Io DAM sources in Jupiter's high-latitude magnetosphere (e.g., for Ganymede-dependent DAM sources and others). We conclude this review by examining a number of special DAM bursts in non-Io storms (such as zebra pattern bursts) that can occur in the presence of solar wind plasma.

The feature of Jupiter's magnetosphere is a complex dynamical system of current sheets that are created in its various regions. In the tail of Jupiter's magnetosphere, a magneto-disk arises, consisting of a direct current and others, which may rebuild due to the pressure of Solar wind plasma that coming into Jupiter's magnetosphere. Thus, according to the Juno mission, several current sheets were observed in the magneto-disk region, which were located in the plane of Jupiter's equator with a diameter of 20 R_j and extended to a distance of z_j >20 (see: Liu et al., 2021). Then, this magneto-disk is stratified into radial elongated sheets with Io-correlated periods of T_{A0}≈10 min. The Juno mission also recorded the relativistic plasma particles with energies of 10-1000 keV ($\propto \varepsilon^{-2.3}$), which may be accelerated due to particle scattering on MHD-current sheets of been generated by Io.

Figure 2 presents the pressure dependences in Jupiter's magnetosphere, which vary in the range z_j = 0.1-100 and are approximated using spacecrafts data and models of Sentman et al. (1975), Khurana et al. (2004), Su et al. (2006). So, the solar wind plasma may penetrate to the Io torus, where we have the presser equilibrium of P_{ei}~ P_{SW}, and thus the Io – solar wind interaction will control a "machine" of Alfven wave productions.

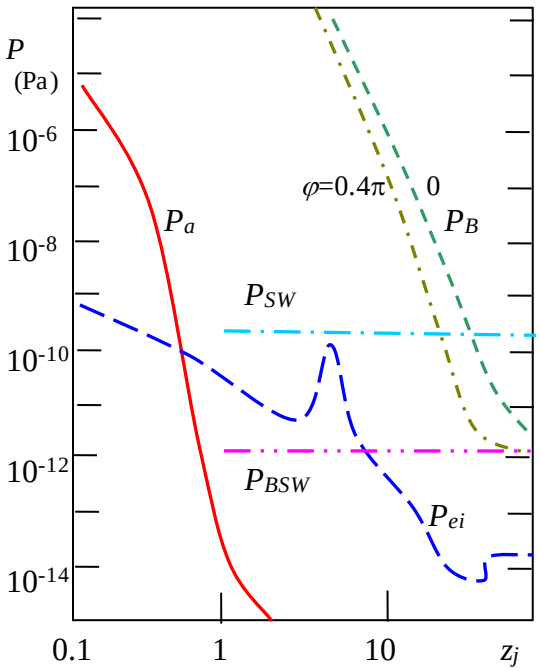

Figure 2: The models of presser variations in Jupiter magnetosphere. Here: P_B is Jupiter's magnetic field presser, P_a is the neutral gas presser, P_{ei} is the ep-plasma presser (with impurities of other ions); and they are comparison with typical solar wind dynamical (P_{sw}) and magnetic (P_{BSW}) pressers.

Firstly, the energetic SW plasma particles are frozen into the interplanetary magnetic field, and they penetrate through the bow shock to Jupiter's magnetosphere, which has a strong magnetic field that co-rotates with the planet. SW parameters at Jupiter's orbit (5 a.u.) are: n_{ei}~ 1 cm^{-3}; v_{ei}~ 280 km/s; B_{sw}≈10^{-5} G; T_e ≈ 10 T_i ≈ 10^5 K for a slow wind, and n_{ei}≈ 0.4 cm^{-3}; v_{ei}≈ 600 km/s; B_{sw}≈10^{-5} G; T_i ≈T_e ≈10^5 K, for a fast wind, correspondently. The bow shock temperature is about T_e >T_i ≈ 10^5 K , and magnetosphere parameters at z_j-distances in the tail region may be chosen: n_{ei} ≈ 0.3 cm^{-3}; v_{cor}≈ 200η km/s (carioles co-rotation velocity, where η >5); B_{0j} ≈4.5·10^{-3} G – for z_j=15; n_{ei}≈0.005 cm^{-3}; v_{cor}≈ 640η km/s; B_{0j}≈0.6 10^{-3} G – for z_j=50; and n_{ei}≈0.02 cm^{-3}; v_{cor}≈ 1200 η km/s; B_{0j}≈ 0.3 10^{-3} G – for z_j=100.

The SW fluxes with density fluctuation are transported and have the transformation by that way: firstly, from intra-planetary space into the Jupiter's bow shock (z_j~50); then, to the magnetopause (z_j<40, or trapped to the magneto-tail); to the magneto-disk (z_j~15, are in current sheets that transforms to the direct current); and to the return current (from z_j~15 to z_j~5); and finally they arrive to the auroral zones in the Jupiter's lower magnetosphere (z_j<0.5, φ≈0.3..0.5 π). The time of this transport is estimated to be about 10 hours or more, when solar particles move with diffusion and flux compression in the form of a hot non-thermal plasma flow (T_{ei} >10^5 K) with a velocity of about v_{ti}≈3·10^4 m/s, which is approximately equal to the Jupiter's co-rotation velocity with its magnetic field, in which the plasma particles are frozen.

At the reconnection point in Ganymede's orbit (z_j~15), electric field and current instabilities arise when the Alfvén theorem is breakdown in this region, $\frac{\partial E}{c\,\partial t} = rotB - \frac{4\pi}{c} j$. Thus, due to a strong fluctuation of the electric field, the Alfvén waves are generated along the magnetic field lines in the direction to Jupiter and in the direction of a radial current, respectively, forming a reverse current with new current sheets and the plasmoid ejections to magnetosphere tail. So, the reverse currents passing through the Io torus zone are modulated by its current sheets, and the solar fluids are transported to the auroral zone of Jupiter, being compressed by a factor of (z_j +1)/15. Thus, under the influence of the magnetic disk, we observe the duration of the DAM source activity of ~20-40 minutes in non-Io storms, the same as in Io-dependent sources.

Let we analyze now the non-Io DAM storm with Zebra-pattern bursts which was observed in URAN data by Panchenko**,** et al. (2018), to compare them with the zebra-like dynamical spectrum in the Io-C sources (storm at 8.09.1999, see: Ryabov, 2001). So, both non-Io and Io-C radio sources with zebra-bursts may be associated with ion plasma density fluctuation. For non-Io sources, these oscillations develop in the presence of high-density solar plasma with high-energy ions. Instead, for Io C sources, plasma fluctuations occur at the altitude where the plasma coming from Io interacts with the neutral gas of Jupiter's ionosphere.

So, if we observe a non-Io radio source when the solar plasma flux reaches Jupiter at z_j~0.1 and has a fluid compressed by (0.01-0.1) $(50/(1+z_j))^2$≈(20-200) times, then we can estimate the plasma density in this radio source as: 200 n_{sw} < 10^3 cm^{-3}. In the work of Panchenko et al. (2018), the emergence of Zebra-like spectra with observed frequency oscillations Δf ≈0.3-1.5 MHz in non-Io sources is explained by the resonance between ion cyclotron and electron plasma oscillations: f_{pi} =s f_{bi} ≈ 0.5 MHz (s= 5.. 10), where f_{bi} ≈ 0.01 MHz, and this is explained by the plasma density n_i ≈ 10^4 cm^{-3}. Therefore, this plasma density is very high for the SW fluid entering these sources. The other way, taking account an neutral gas influence into the SW plasma flux, that Zebra-like pattern can be explained also as the high-energy ions fluctuation in some LF-MHD waves, of T_A≈ 1s periods and $c_{ALF}/c \approx 10^{-3}$, taking account that scatter time of τ_{ia_sw}~0.03<<τ_{ia} for that SW-ions, that give us to Δf_{be} ~ 0.5 MHz fluctuation in altitude z_j ~0.1:

$$\lambda_{z\,A\,LF} \sim \lambda_{z\ FMS\,LF} \approx c_{ALF} T_A \approx 0.01\ R_j.$$

4. Conclusions

Both the Io-dependent and the non-Io DAM radio storms have similar time variation in the dynamical spectrum and shape structure, which is connected with current sheets that produced by Io in Jupiter magnetosphere.

To activate the Jupiter's DAM radio emission, both the presence of plasma in the lower magnetosphere and low-frequency Alfvén waves are necessary, which can support the mechanism for generating DAM radiation and their bursts (for example, due to the maser cyclotron instability).

The presence of plasma fluids within the magnetosphere help to save the magnetic rotation moments over large distances in Jupiter's magnetosphere. The same way, the plasma supports the processes of rotation moments exchange between Jupiter and its satellites. The atmosphere in the lower magnetosphere concentrates the energy of Alfven waves and helps to convert it into the DAM radio emission. Then, LF-Alfven waves arising due to the Io rotation lead to the streamer formations.

The Alfven waves generated by Io-Jupiter interaction convert the MHD energy into radio bursts, and produce the current sheets. The fast MS wave makes small changes to the structure of current sheet, may support the streamer formation, but they are insignificant in main storm structure.

Solar wind fluctuations and CMEs add the plasma fluids to the outer region of Jupiter's magnetosphere, and they produce the changes in current sheets due to the magnetic fields reconnection. Thus, the solar wind can influence the DAM radio emission by maintaining the MHD instabilities in the lower magnetosphere, and producing the non-Io DAM radio sources.

Acknowledgements. This work was carried out with the support of STCU "Crown" project No.6435.

References

Akhiezer A.I., et al.: 1974, *Plasma electrodynamics* (in Russian), 719. – Nauka, Gl. red. phys.-mat. Literatury/eds. Akhiezer A.I., Moscow.

Barrow C. H., Desch M.D., Genova F.: 1986, *A&A*, **165**, 244.

Behannon K. W., Burlaga L. F., Ness N. F.: 1981, *JGR*, **86**, A10, 8385-8401.

Boev A.G., Udal'tsova N.M., Yantsevich A.A.: 2001, *Radiophys. Radioastron.*, **6**, 252.

Boev A.G.: 2005, *Radiophys. Radioastron.*, **10**, 367.
Bragynskyi S.I.: 1963, *Questions of plasma theory* (in Russian), **1**, 183, Gos. izdatel'stvo literatury po nauke i tekhnike/eds. Leontovich M.A., Moscow.
Dessler A.J., Hill T.V.: 1979, *ApJ*, **227**, 664.
Flag R.S., Greenman W.B., Reyes F, Carr T.D.: 1991, *A Catalog of High Resolution Jovian Decametric Radio Noise Burst Spectra*, **1**, 199, – (University of Florida, Gainesville).
Hess S., Mottez F., Zarka P.: 2007, *JGR*, **112**, A11212.
Genova F.: 1985, *Planetary Radio Emission*, 51-71, Proc. of an international workshop, Graz, Austria, July 9–10, 1984).
Gerard J.C., Bonfond B., Grodent D. et al: 2014, *JGR Sp.Phys.*, **119**, 11, 9072-9088.
Goldreich P., Lynden-Bell B.: 1969, *ApJ*, **156**, 59.
Kadomtsev B.B.: 1963, *Questions of plasma theory* (in Russian), **2**, 132, Gos. izdatel'stvo literatury po nauke i tekhnike/eds. Leontovich M.A., Moscow.
Kadomtsev B.B.: 1988, *Collective phenomena in the plasma* (in Russian), 303, Nauka, Glav. red. phys.-mat. literatury, Moscow).
Khurana K. K., et al.: 2004, *Jupiter: The Planet, Satellites and Magnetosphere*, Cambridge University Press/eds. Bagenal, Fran, et al.
Leblanc Y., Bagenal F., Dalk J.A.: 1993, *A&A*, **276**, 603.
Liu Z.Y., Zong Q.G., Blanc M. et al.: 2021, *JGR Sp. Phys.*, **126**, 10.1029/2021JA029710.
Marques M.S., Zarka P. et al.: 2017, *A&A*, **604**, A17.
Panchenko M., Rosker S., Rucker H.O. et al.: 2018, *A&A*, **610**, 101.
Ryabov B.P., Gerasymova N.N.: 1990, *Decameter sporadic radioemission of Jupiter* (in Russian), 240, Kyev: Naukova dumka.
Ryabov V.B.: 2001, *Radiophys. Radioastron.*, **6**, 103.
Ryabov V.B. et al.: 2014, *A&A*, **568**, A53.
Sentman D.D., Allen J.A, Goerts C.K.: 1975, *GeoRL*, **2**, 465.
Smirnov B.M.: 1995, Physics of the low ionized gas (in Russian), 424, Nauka, Glav. red. phys.-mat. literatury, Moscow.
Su Y.J., Jones S.T., Ergun R.E. et al.: 2006, *JGR*, **111**, A06211.
Tsvyk N.O.: 2019, *OAP*, **32**, 105.
Tsvyk N.O.: 2023, *OAP*, **36**, 145.
Tsvyk N.O.: 2024, *OAP*, **37**, 94.
Withers P., Vogt M.F.: 2017, preprint (arXiv: 1702.07075v1).
Wu C.S.: 1985, *Space Sci. Rev.*, **41**, 215.

Наукове видання

Одеські Астрономічні Публікації

Том 38 (2025)

Англійською мовою

Технічний редактор та комп'ютерна верстка *С. Л. Страхова*

Підписано до друку 27.12.2025. Формат 60x84/8.
Ум. друк. арк. 20,5. Наклад 50 пр.
Зам. № 2890.

Видавець:
Одеський національний університет імені І. І. Мечникова
вул. Університетська, 12, м. Одеса, 65082, Україна
Свідоцтво суб'єкта видавничої справи
ДК № 4215 від 22.11.2011 р.
Тел.: (048) 723 28 39, e-mail: druk@onu.edu.ua

Виготовлювач:
Поліграфічний центр «ПромАрт» вул. Веснина,12, Харків, Україна
Тел.: +380 (50) 298 47 57, e-mail: promart.ua@gmail.com
https://promart.prom.ua/

Надруковано з готового оригінал-макета